

AD A113356

AD-A113356

2

READ INSTRUCTIONS
BEFORE COMPLETING FORM

1. Report Number EOARD-TR-82-7	2. Govt Accession No.	3. Recipient's Catalog Number
4. Title (and Subtitle) An investigation of the flow about an ogive cylinder at high angles of incidence	5. Type of Report & Period Covered Final Scientific Report 1 Feb 81 - 31 Jan 82	
7. Author(s) Bernard P. PAUL & E. WEDEMEYER	8. Contract or Grant Number Grant AFOSR 81-0118	
9. Performing Organization Name and Address von Karman Institute for Fluid Dynamics Chaussée de Waterloo, 72 B-1640 Rhode Saint Genèse, Belgium	10. Program Element, Project, Task Area & Work Unit Numbers P.E. 61102F Proj/Task 2301/D1 W.U. 122	
11. Controlling Office Name and Address European Office of Aerospace Research and Development/LNT Box 14 FPO New York 09510	12. Report Date March 1982	13. Number of Pages 178
14. Monitoring Agency Name and Address European Office of Aerospace Research and Development/LNT Box 14 FPO New York 09510	15.	
16. & 17. Distribution Statement Approved for public release; distribution unlimited.		
18. Supplementary Notes		
19. Key Words Flow visualization;Ogive cylinder body; Angle of attack;Subsonic flow;Transonic flow;Vortex pattern; Water tunnel		

20. Abstract
 The present work gives the results of flow visualization studies and six component force measurements on an ogive cylinder body at high angles of attack in the sub- and transonic flow regime. High angle of attack aerodynamic investigations had not been done before at the VKI, so a new wind tunnel model support system, six component force balance and water tunnel contraction and test section were designed and constructed to enable the present investigation to be performed. Force measurements and flow visualization studies were carried out on both a sharp nosed body and a blunt nosed body of $(x/d)_{TOT}=18$ and 17.4, respectively. The side force induced by the asymmetric vortex pattern which develops on the leeward side of an ogive cylinder was the primary focus of this investigation. A detailed review of previous investigations was performed. The results obtained in this investigation were found to agree quite well with previous results. The flow visualization studies were carried out in the VKI WT-1 water tunnel and the force measurements in the VKI S-1 transonic-supersonic wind tunnel.

DTIC FILE COPY

DTIC
ELECTE
APR 13 1982

82 04 12 141

E

EOARD-TR-82-7

This report has been reviewed by the EOARD Information Office and is releasable to the National Technical Information Service (NTIS). At NTIS it will be releasable to the general public, including foreign nations.

This technical report has been reviewed and is approved for publication.

Winston K. Pendleton

WINSTON K. PENDLETON

Lt Colonel, USAF

Chief Scientist

Gordon L. Hermann

GORDON L. HERMANN

Lt Colonel, USAF

Deputy Commander

DISCLAIMER NOTICE

THIS DOCUMENT IS BEST QUALITY PRACTICABLE. THE COPY FURNISHED TO DTIC CONTAINED A SIGNIFICANT NUMBER OF PAGES WHICH DO NOT REPRODUCE LEGIBLY.

ABSTRACT

The present work gives the results of flow visualization studies and six component force measurements on an ogive cylinder body at high angles of attack in the subsonic and transonic flow regime. High angle of attack aerodynamic investigations had not been done before at the von Karman Institute, so a new wind tunnel model support system, six component force balance and water tunnel contraction and test section were designed and constructed to enable the present investigation to be performed. Force measurements and flow visualization studies were carried out on both a sharp nosed body and a blunt nosed body of $(x/d)_{TOT} = 18$ and 17.4 respectively.

The side force induced by the asymmetric vortex pattern which develops on the leeward side of an ogive cylinder was the primary focus of this investigation. A detailed review of previous investigations was performed. The results obtained in this investigation were found to agree quite well with previous results.

The flow visualization studies were carried out in the VKI WT-1 water tunnel and the force measurements in the VKI S-1 transonic-supersonic wind tunnel.

DTIC
COPY
INSPECTED
2

Accession For	
NTIS GRA&I	<input checked="" type="checkbox"/>
DTIC TAB	<input type="checkbox"/>
Unannounced	<input type="checkbox"/>
Justification	
By	
Distribution/	
Availability Codes	
Dist	Avail and/or Special
A	23 G

TABLE OF CONTENTS

ABSTRACT	i
LIST OF SYMBOLS	ii
LIST OF FIGURES	iv
1. INTRODUCTION	1
2. PREVIOUS INVESTIGATIONS	2
3. EXPERIMENTAL FACILITIES AND EQUIPMENT	8
3.1 Wind tunnel	8
3.2 Wind tunnel models	8
3.3 Support system	9
3.4 The six component force balance	10
3.5 Water tunnel	10
3.6 Water tunnel models	11
3.7 Data acquisition	12
4. WATER TUNNEL RESULTS AND DISCUSSION	13
4.1 Experimental procedure	13
4.2 Results and discussion	14
5. WIND TUNNEL INVESTIGATIONS	16
5.1 Experimental procedure	16
5.2 Overall force measurement results	17
5.3 Discussion and results of the side force measurements	18
6. CONCLUSIONS	21
REFERENCES	22

APPENDICES :

I - DESIGN AND CALIBRATION OF A SIX COMPONENT FORCE BALANCE	27
II - DESIGN OF WATER TUNNEL CONTRACTION AND TEST SECTION	35
III - DATA REDUCTION PROGRAMS AND SAMPLE PLOTS AND OUTPUT	45
IV - SOURCES OF ERROR	65
FIGURES	67

ACKNOWLEDGEMENTS

I would like to deeply thank Dr. E. Wedemeyer for all of his patience, aid and guidance throughout the year. Without his help this project would not have been possible.

I would like to thank Mr. Connaisselle and his crew for their expert technical assistance. Working with Mr. Connaisselle made the completion of this project much easier and much more enjoyable too.

I want to thank Mr. Borres and his crew from the electronics shop for their expert workmanship concerning the construction of the six component force balance.

I want to thank Mr. Lejour and his crew of the metal shop for their excellent craftsmanship concerning the force balance, water tunnel contraction and other equipment.

I want to thank Mr. Toubeau and the drawing office for their aid in doing technical drawings.

I want to thank Jean Fourniols and Paul Van Westerhoven for their aid in the water tunnel investigations.

LIST OF SYMBOLS

x	length of component
x_b	length of model's body
d	body diameter
x/d	fineness ratio, length/diameter
$(x/d)_{nose}$	nose fineness ratio, nose length/body diameter
$(x/d)_{body}$	body fineness ratio, body model length/body diameter
$(x/d)_{TOT}$	total fineness ratio, total model length/body diameter
r_b	body radius
r_N	nose radius
x_1	distance from the model's tip to the point of vortex detachment from the body
A_1	$x_1/L * L/D * \tan \alpha$
C_L	rolling moment coefficients $\frac{L}{\frac{1}{2} \rho V_{\infty}^2 S \cdot d}$
C_M	pitching moment coefficient $\frac{M}{\frac{1}{2} \rho V_{\infty}^2 S \cdot d}$
C_N	yawing moment coefficient $\frac{N}{\frac{1}{2} \rho V_{\infty}^2 S \cdot d}$
C_y	side force coefficient $\frac{Y}{\frac{1}{2} \rho V_{\infty}^2 \cdot S}$
C_z	normal force coefficient $\frac{Z}{\frac{1}{2} \rho V_{\infty}^2 \cdot S}$
$ C_{y_{max}} $	Absolute value of maximum side force coefficient
D	body diameter
L	total model length

M	Mach number
Re _d or R _d	Reynolds number based on the diameter ; $\frac{\rho V_{\infty} D}{\mu}$
S	base area of model $\frac{\pi d^2}{4}$
x	center of pressure location/body diameter; XCP/D
α	angle of attack
α_{AV}	angle of attack at which the onset of asymmetry begins
$\left\{ \alpha_{AV} \right\}_{\text{weak}}$	angle of attack at which the generation of weak side forces begins
$\left\{ \alpha_{AV} \right\}_{\text{strong}}$	angle of attack at which the generation of strong side forces begins
α_{max}	angle of attack at which maximum side force occurs
α_{UAV}	angle of attack at which unsteady asymmetric vortex shedding occurs
x	$\text{tg} \bar{\xi} / \text{tg} \alpha$
$\bar{\xi}$	angle between the detached vortex and the body axis

LIST OF FIGURES

1. Flow types for increasing angle of attack on an ogive cylinder (Ref. 22).
2. Aerodynamic flow and onset boundaries for ogive cylinder (Ref. 22).
3. Leeward vortex structure in subsonic flow (Ref. 4).
4. Leeward flow regimes on a circular body, total length ~ 10 (Ref. 4).
5. Symmetric flow field viewed from the crossflow plane (Ref. 4).
6. Mach number effect on α_{AV} (Ref. 7).
7. Effect of Re_d and α_{AV} (Ref. 2).
8. Effect of roll orientation on α_{AV} (Ref. 6).
9. Effect of nose fineness ratio and body length on α_{AV} (Ref. 7).
10. Effect of total length on α_{AV} (Ref. 7).
11. Variation of side force with Reynolds number (Ref. 24).
12. Effect of Mach number on $|C_{y_{max}}|$ for ogive cylinders (Ref. 22).
13. Effect of Re_d on $|C_{y_{max}}|$ (Ref. 24).
14. Effect of forebody fineness ratio on $|C_{y_{max}}|$ (Ref. 7).
15. Effect of roll orientation on C_y and C_N (Ref. 22).
16. Sketch of rear section of wind tunnel model.
17. Sketch of middle section of wind tunnel model.
18. Sketch of sharp nosed forebody for wind tunnel model.
19. Sketch of blunt nosed forebody for wind tunnel model.
20. Sketch of low angle of attack support :
 $-5^\circ \leq \alpha \leq 30^\circ$.
21. Sketch of mid angle of attack support :
 $25^\circ \leq \alpha \leq 60^\circ$.
22. Sketch of high angle of attack support :
 $55^\circ \leq \alpha \leq 90^\circ$.
23. Sketch of the sting attachment component.
24. Detail for sting attachment component.
25. Sketch of the sting.
26. A picture of the water tunnel facility.
27. A sketch of the sharp nosed ogive cylinder water tunnel model $(L/d)_T = 18$, $d = 11$ mm.

28. A sketch of the blunt nosed ogive cylinder water tunnel model, $(\lambda/d)_{TOT} = 17.4$, $d = 11$ mm.
29. A sketch of the small sharp nosed ogive cylinder water tunnel model, $(\lambda/d)_{TOT} = 18$, $d = 8$ mm.
30. Flow visualization over a sharp nosed body for $\alpha = 15^\circ, 20^\circ, 25^\circ, 30^\circ$.
31. Flow visualization over a sharp nosed body for $\alpha = 35^\circ, 40^\circ, 45^\circ, 50^\circ$.
32. Flow visualization over a blunt nosed body for $\alpha = 15^\circ, 20^\circ, 25^\circ, 30^\circ$.
33. Flow visualization over a blunt nosed body for $\alpha = 35^\circ, 40^\circ, 45^\circ, 50^\circ$.
34. Investigation of the wall effect.
35. Parameter λ versus angle of attack as determined from water tunnel investigations (Ref. 45).
36. Parameter A_1 versus angle of attack as determined from water tunnel investigations (Ref. 45).
37. Parameter A_1 versus α ; Reynolds number effect (Ref. 45).
38. Parameter A_1 versus α ; Nose blunting effect (Ref. 45).
39. Parameter A_1 versus α ; Wall effect (Ref. 45)
40. Parameter A_1 versus α ; Rearward dye ejection holes effect (Ref. 24).
41. Problems encountered in flow visualization tests.
42. C_N versus α ; $M = .417$ sharp nosed body.
43. C_Z versus α ; $M = .417$ sharp nosed body.
44. C_M versus α ; $M = .417$ sharp nosed body.
45. $(XCP/D)_Z$ versus α ; $M = .417$ sharp nosed body.
46. C_L versus α ; $M = .417$ sharp nosed body.
47. C_N versus α ; $M = .617$ sharp nosed body.
48. C_Z versus α ; $M = .617$ sharp nosed body.
49. C_M versus α ; $M = .617$ sharp nosed body.
50. $(XCP/D)_Z$ versus α ; $M = .617$ sharp nosed body.
51. C_L versus α ; $M = .617$ sharp nosed body.
52. C_N versus α ; $M = .695$ sharp nosed body.
53. C_Z versus α ; $M = .695$ sharp nosed body.
54. C_M versus α ; $M = .695$ sharp nosed body.
55. $(XCP/D)_Z$ versus α ; $M = .695$ sharp nosed body.
56. C_L versus α ; $M = .695$ sharp nosed body.
57. C_N versus α ; $M = .796$ sharp nosed body.
58. C_Z versus α ; $M = .796$ sharp nosed body.
59. C_M versus α ; $M = .796$ sharp nosed body.

60. $(XCP/D)_Z$ versus α ; $M = .796$ sharp nosed body.
61. C_L versus α ; $M = .796$ sharp nosed body.
62. C_N versus α ; $M = .901$ sharp nosed body.
63. C_Z versus α ; $M = .901$ sharp nosed body.
64. C_M versus α ; $M = .901$ sharp nosed body.
65. $(XCP/D)_Z$ versus α ; $M = .901$ sharp nosed body.
66. C_L versus α ; $M = .901$ sharp nosed body.
67. C_N versus α ; $M = .395$ blunt nosed body.
68. C_Z versus α ; $M = .395$ blunt nosed body.
69. C_M versus α ; $M = .395$ blunt nosed body.
70. $(XCP/D)_Z$ versus α ; $M = .395$ blunt nosed body.
71. C_L versus α ; $M = .395$ blunt nosed body.
72. C_N versus α ; $M = .611$ blunt nosed body.
73. C_Z versus α ; $M = .611$ blunt nosed body.
74. C_M versus α ; $M = .611$ blunt nosed body.
75. $(XCP/D)_Z$ versus α ; $M = .611$ blunt nosed body.
76. C_L versus α ; $M = .611$ blunt nosed body.
77. C_N versus α ; $M = .698$ blunt nosed body.
78. C_Z versus α ; $M = .698$ blunt nosed body.
79. C_M versus α ; $M = .698$ blunt nosed body.
80. $(XCP/D)_Z$ versus α ; $M = .698$ blunt nosed body.
81. C_L versus α ; $M = .698$ blunt nosed body.
82. C_N versus α ; $M = .797$ blunt nosed body.
83. C_Z versus α ; $M = .797$ blunt nosed body.
84. C_M versus α ; $M = .797$ blunt nosed body.
85. $(XCP/D)_Z$ versus α ; $M = .797$ blunt nosed body.
86. C_L versus α ; $M = .797$ blunt nosed body.
87. C_Y versus α ; $M = .417$ sharp nosed body.
88. $(XCP/D)_Y$ versus α ; $M = .417$ sharp nosed body.
89. C_Y versus α ; $M = .617$ sharp nosed body.
90. $(XCP/D)_Y$ versus α ; $M = .617$ sharp nosed body.
91. C_Y versus α ; $M = .695$ sharp nosed body.
92. $(XCP/D)_Y$ versus α ; $M = .695$ sharp nosed body.
93. C_Y versus α ; $M = .796$ sharp nosed body.
94. $(XCP/D)_Y$ versus α ; $M = .796$ sharp nosed body.
95. C_Y versus α ; $M = .901$ sharp nosed body.
96. $(XCP/D)_Y$ versus α ; $M = .901$ sharp nosed body.

97. C_Y versus α ; $M = .395$ blunt nosed body.
98. $(XCP/D)_Y$ versus α ; $M = .395$ blunt nosed body.
99. C_Y versus α ; $M = .611$ blunt nosed body.
100. $(XCP/D)_Y$ versus α ; $M = .611$ blunt nosed body.
101. C_Y versus α ; $M = .698$ blunt nosed body.
102. $(XCP/D)_Y$ versus α ; $M = .698$ blunt nosed body.
103. C_Y versus α ; $M = .797$ blunt nosed body.
104. $(XCP/D)_Y$ versus α ; $M = .797$ blunt nosed body.
105. $|C_{Ymax}|$ versus Mach number for both nose shapes.
106. Different flow regimes as a function of Mach number.
107. Effect of Mach number on C_Y .
108. C_Y versus α for two nose shapes; $M = .407$.
109. C_Y versus α for two nose shapes; $M = .614$.

1. INTRODUCTION

Due to the increased maneuverability and performance requirements of modern day aircraft and missiles, high angle of attack aerodynamic design has become increasingly important. In the high angle of attack flight regime, two phenomena not encountered at lower angles of attack but which can drastically affect an aircraft's or missile's maneuverability or performance characteristics are vortex breakdown and the induced side force generated by asymmetric body vortices. Vortex breakdown, or bursting as it is sometimes called, involves the degeneration of the structured vortical flow formed at the leading edge of a wing. This can cause a sudden change in the lift and also exert unbalanced loads on the aircraft (Ref. 1). The second phenomenon, the formation of body vortices and their development into an asymmetric vortex pair, involves the generation of sudden side forces that can cause aircraft to spin or a missile to tumble. In flight, the vehicle's control system must be capable of coping with the loads generated by these phenomena. Presently the modelling of these flows mathematically is impossible, so a description of these phenomena must be based upon a large number of experimental measurements. It is the purpose of this investigation to explore the feasibility of making high angle of attack aerodynamic investigations using VKI facilities by experimentally studying the second phenomenon discussed, the side force generated by asymmetric body vortices. Several investigations of this phenomenon have already been conducted at other facilities and the results published (Refs. 5-11,13,15,17,18,20,23-28). Recently several excellent review articles of all present day information on various aspects of the asymmetric vortex phenomena have also been published (Refs. 1-4). A description of the phenomenon and a summary of the important results others have so far obtained will be given before a description of the present investigation and a comparison of its results with others is made.

2. PREVIOUS INVESTIGATIONS

In figures 1-4 an excellent illustration is given of the different flow regimes and their limits encountered by an ogive cylinder as its angle of attack changes from 0° - 90° (Refs. 4,22). In discussing these flow regimes, it is convenient to divide the flow into two components, the axial component and the crossflow component. At low angles of attack, $\alpha \leq 5^\circ$, the axial flow dominates. No separation occurs, no vortices form and the flow is essentially potential flow about a slender body. As the angle of attack increases beyond 5° , separation due to the crossflow begins to become important. As can be seen in figures 1b and 3a, the boundary layer is swept to the leeward side and separation occurs. The free shear layers formed roll up into two symmetric vortex sheets and a nonlinear normal force is generated. This flow regime is the symmetric vortex flow regime. It may last for angles of attack up to 40° , depending primarily upon body length. Since the vortices grow in size as they go towards the base of the body, they tend to interact sooner at a smaller angle of attack on a longer body and thus near 20° or even sooner, interaction between these vortices may occur and the symmetric vortices may begin to give away. The flow in this regime is well behaved and no undesirable increased loads occur on the body. In figure 5, an excellent view of how this flow appears in the crossflow plane is given. Note that perhaps in this flow regime, smaller, secondary vortices may occur.

Somewhere between 15° and 40° , depending on the body length and nose fineness, the flow field about the body begins to resemble that shown in figures 1c or 3b. The vortical flow begins to dominate and the shed vortices take on an asymmetric pattern, causing a side force to be generated. The exact mechanism by which this asymmetric vortex shedding and subsequent side force generation occurs is not really known. It is probably due to a combination of some change in the separation characteristics of the flow and an inviscid

interaction of the vortices which causes the symmetric vortex pattern to become unstable. The question is which process occurs first; do changes in the separation characteristics of the flow cause an inviscid interaction of the vortices and the subsequent asymmetric vortex pattern to form, or is it the other way around? Observation of both processes has been seen to occur, but it is not presently possible to say which process occurs first.

As the angle of attack continues to increase the side force steadily increases to a maximum and then begins to drop off rapidly. Continuing to increase the angle of attack further causes the flow to enter a regime where the separated flow completely dominates. Unsteadiness begins to set in from the body's base, and unsteady asymmetrical vortex shedding begins to occur. For longer bodies, this occurs at a much lower angle of attack, about 50° - 60° , when compared to shorter bodies for which this may not occur until an angle of attack of 80° .

As indicated before, this investigation will center on the third flow regime, that of steady asymmetric vortex shedding. It is in this regime where a substantial side force is generated and thus it is this regime which is of primary importance. In trying to understand and analyze this flow regime, there are four parameters of primary importance; the maximum induced side force $|C_{y_{max}}|$, the angle of attack at which this maximum induced side force occurs, α_{max} , the angle of attack at which the onset of asymmetry occurs, α_{AV} , and the angle of attack at which the onset of unsteady asymmetric vortex shedding occurs, α_{UAV} . These parameters have been investigated in some detail by many others (Refs. 5-28). It appears that they are influenced primarily by Mach number, Reynolds number, nose fineness and body length. These influences will now be discussed for each parameter.

The angle at which the asymmetry first appears is of first importance in determining the angle of attack range of asymmetric vortex effects. In figure 6, the independence of the angle of onset from Mach number in the subsonic and transonic ranges is shown (Ref. 7). It appears α_{AV} is not only independent of the Mach number, but the Reynolds number and roll orientation as well (Refs. 6-9,24). Indications of this can be seen in figures 7 and 8. However there appears to be a definite influence of the fineness ratio and body length on α_{AV} . In figures 9 and 10 these influences are readily apparent. As both the nose fineness ratio and total fineness ratio increase, the angle of onset decreases. A possible explanation of the first effect is given by Keener and Chapman (Ref. 9). As the nose fineness ratio increases, the nose angle will decrease. This may cause a crowding of the vortices which come off the missile nose at high angles of attack. This crowding may cause the vortices to interact and the symmetric pattern to become unstable leading to asymmetric vortical flow. Since the same effect is observed on delta wings, the argument seems very plausible. When the afterbody fineness ratio is large, however, the forebody fineness ratio does not influence the angle of onset so much. In this case, it appears the asymmetry sets in from the base of the body. As the separated vortical flow develops along the body, the vortices grow in size and strength towards the body's base. These larger vortices interact stronger than the vortices near the forebody, and thus the asymmetry first develops at the base. In the present investigation, the effect of body length will be extremely important, as the body examined will have a high total λ/d of 18.

The other important angles, α_{max} and α_{UAV} , appear to have the same dependencies as α_{AV} ; i.e., they are mainly influenced by body length and nose fineness. However, in some investigations, strong Reynold's number and Mach number effects on these parameters have been noted. In figure 6 and in figure 11, some of these effects may be observed.

Most works up to this point have concentrated more heavily on the angle of onset of asymmetric vortices, and thus much more investigation needs to be done on α_{max} and α_{UAV} before anything can be said about their true dependencies.

The above parameters are important in establishing the flight boundaries of asymmetric vortex effects. But by far the most important parameter concerning asymmetric vortex effects is the maximum induced side force. It is this parameter which must be known by aircraft designers and so it is the parameter which has received the most interest. In figure 12, the strong effect of Mach number on $|C_{y_{max}}|$ can be seen. A definite fall off in Mach number in the transonic regime can be observed. Two explanations have been suggested for this. Ericsson and Reding suggest that there is a purely three dimensional reason for this $|C_{y_{max}}|$ fall off: nose-induced flow separation (Ref. 2). Their argument is that at $M_{\infty} \sin \alpha > .5$, the supercritical/subcritical flow geometry necessary for vortex asymmetry cannot be established. Instead, a closed three dimensional separation bubble forms, preventing the nose from generating the vortices associated with more open separation regions, which play such an important role in the asymmetric vortex induced loads. Thus, the vortices can only be generated by the aft body, and since the corresponding side force in this case is usually small, $|C_{y_{max}}|$ falls off. On a slender nose tip, this nose induced separation phenomenon should not occur, and thus nose generated asymmetric vortices generate significant side forces even at supersonic speeds.

Wardlaw points out another possible explanation for this transonic fall off in $|C_{y_{max}}|$ (Ref. 4). As the crossflow Mach number becomes larger than the critical value (about .42 for a cylinder) parts of the flow near the cylinder's shoulders may become supersonic in the cross flow plane. Because of this, the influence of the leeward asymmetric vortex structures is not sensed on the surfaces near the cylinder shoulder. This explanation is well supported by experimental evidence.

Reynolds number also has a large effect on $|C_{y_{max}}|$. In several studies, this effect has been pointed out (Refs. 1,4,8,10,24). In figure 13, an example of this effect can be seen. It appears from this curve that as Re_d increases, the $|C_{y_{max}}|$ value increases. This is not always the case, however, and presently, no definite statement about the Reynolds number effect can be made, except that the maximum side force appears to occur at a Reynolds number where boundary layer transition can influence the flow separation asymmetry the most (Ref. 2).

Effects of body length and forebody fineness on $|C_{y_{max}}|$ are also definitely observed. In figure 12, the body length effect can easily be seen. It appears that the $|C_{y_{max}}|$ value increases as body length increases up to a point, and then it falls off again. The effect of the forebody fineness on $|C_{y_{max}}|$ can be seen in figure 14. As for afterbody length, an increase in the forebody fineness tends to increase the value of $|C_{y_{max}}|$. Both of these trends have been observed in many studies and so these trends are fairly well accepted now.

By far, the most puzzling of the effects on the side force is that of roll orientation. For an axisymmetric body, one would not expect the flow characteristics to change with roll orientation. This is not the case, however. In figure 15, the variation of side force and normal force with roll angle are shown. It can be seen that rolling the model does not really affect the magnitude of the side force, but the sign of the side force. The effect is similar for the normal force. At first, it was believed that this variation with roll angle was due to wind tunnel turbulence, but this has been shown not to be the case (Ref. 27). Probably, it is due to minute model asymmetries, but this is not known for certain and much more investigation into this problem needs to be done. The important point here is that when investigating the asymmetric vortex induced side force, data should be taken at several different roll orientations.

Up to this point, the discussion has centered on the side force and what parameters influence it. In practice, however, one would like to know for missile and airplane design purposes, how to alleviate this side force. This problem of side force alleviation has been the subject of some very recent investigations. Three primary models of asymmetric induced side force reduction have been observed; nose blunting, helical trips, and spinning the nose or the nose tip (Refs. 29-31). It is easily observed that all of these methods involve changing the flow characteristics about the nose. This is because of the dominant role of the nose shape and fineness ratio in determining the asymmetric flow field. In a large number of investigations, the general conclusion seemed to be that the flow separating from the nose played the dominant role in the asymmetric flow field development (Refs. 2,4-8,24,26). This is the primary reason for the success of the above side force alleviation methods. By blunting the nose, asymmetric vortex formation is delayed and the side force decreases (Ref. 27). By spinning the nose or nose tip, the side force again decreases possibly because the new vortices cannot change their positions, or perhaps fully establish their flow fields at new positions, fast enough to produce the full effect on the body (Ref. 31). And by using helical trips on the nose, separation at the nose is again affected and the side force decreases (Ref. 30). Further investigations must be conducted in order to determine the degree and range of these methods, but it appears practical ways of alleviating the induced side force are emerging.

3. EXPERIMENTAL FACILITIES AND EQUIPMENT

Since high angle of attack aerodynamic investigations had not been previously conducted at VKI, it was necessary to design several new pieces of equipment and modify some already existing equipment. A six component force balance was designed and built in order to carry out the necessary force measurements. A model support system was designed that enabled investigations to be made for an angle of attack range of 0° to 90° . A new contraction and test section were made for the existing water tunnel so that flow visualization studies could be made on missile bodies for up to an angle of attack of 60° . These and the other facilities used will be described.

3.1 Wind tunnel

The VKI S-1 supersonic wind tunnel facility was used for this investigation. The tests were performed using the 40 cm \times 40 cm transonic test section which has slotted top and bottom walls to reduce interference effects. This facility has a Mach number operating range of about .4 to 1.2 and a stagnation pressure of about 200 mm Hg. A typical unit Reynolds number is in the 5×10^6 per meter range. The stagnation temperature is approximately equal to room temperature. For the present investigation, the Mach number range was .4 to .9 and the Reynolds number was about 8.3×10^4 based on model diameters. The S-1 is a continuous closed circuit facility of the Ackeret type.

3.2 Wind tunnel models

Drawings of the models used in wind tunnel investigations are presented in figures 16-19. Figures 16 and 17 show the rear and front pieces of the cylindrical afterbody. This afterbody had an x_b/d ratio of 15, with the outer diameter

being 17 mm. The two nose shapes used are drawn in figures 18 and 19. The pointed nose has a fineness ratio of 3.0 and the blunted nose a fineness ratio of 2.4. The degree of bluntness, r_N/r_b , is 50%. The overall length of the sharp nosed body was 306 mm and that of the blunt nose 296.25 mm. These dimensions were chosen in order to minimize the wind tunnel wall effects on the measurements at high angles of attack and to allow a reasonable clearance between the internal force balance and the model's inner diameter. The reduction of the aft body's inner diameter to 13 mm was specifically done for this purpose. The attachment of the nose to the afterbody was also designed to allow for 4 roll orientations of the nose at angles of 90° , 180° , 270° and 360° .

3.3 Support System

The support system used is shown in figures 20-25. Angle of attack studies beyond 30° had never before been done at VKI so a new type of support system had to be designed in order to cover the angle of attack range from 0° to 90° . In order to do this, three separate supports needed to be designed since only a 35° sweep can be done with one support system. In figures 20-22, the three support systems are schematically shown. Figure 20 shows the support for low angles of attack, $-5^\circ \leq \alpha \leq 30^\circ$, figure 21 the support system for mid-angles of attack, $25^\circ \leq \alpha \leq 60^\circ$, and figure 22 the support system for high angles of attack $55^\circ \leq \alpha \leq 90^\circ$. The support system is of the sting type. This type of support was used because in studies of support interference effects on bodies at high incidence, this support was found to cause the least amount of interference in the transonic regime (Refs. 4,33,34). The sting support acts to increase the effective length of the model, which may result in a slightly higher C_z value. For this investigation only the first two support systems were used, as only angles of attack from 0° - 60° were investigated. The third support will be used in future high angle of attack studies. In figures 23 and 24, the sting attachment component for the supports is

shown. This component was designed to be removable from each of the supports in order to make the support changes easy to perform. In figure 25, the sting upon which the force balance and model were mounted, is shown. Its total length was chosen as to insure that the center of pressure of the model would fall between the two gage stations of the six component force balance. Its diameter was chosen as to be small within the model so that a reasonable amount of clearance existed between the sting and the model's inner diameter and larger beyond the model's base to insure strength and rigidity. A hole was put in the center of the sting for the passage of the force balances' wires.

3.4 The six component force balance

A six component internal strain gauge force balance was designed and constructed for use in this investigation. This type of balance had never before been built at VKI and thus it represented a major portion of this project's work. The balance's design, calibration and operation are discussed in Appendix I. At the time of the investigation the wiring of the axial component was not complete and so no axial force measurements were made.

3.5 Water tunnel

The water tunnel WT-1 was utilized for flow visualization studies on three ogive cylinder models of $(c/d)_{TOT} = 18$ and $(x/d)_{TOT} = 17.4$. It was felt that even though the flow is incompressible and the Reynolds number low, a qualitative understanding of the asymmetric vortex flow field could be obtained. A detailed sketch of this facility is given in figure 26. Water is pumped from a storage tank into an overhead reservoir and the velocity of the water through the test section is controlled by means of a valve and measured by a rotameter. Two possibilities exist for driving the tunnel : a continuously

driven mode with overflow and a blowdown mode after filling the overhead reservoir. In this study, only the blowdown mode was utilized as the pump used for the continuous mode tends to generate unwanted vibrations in the flow. Thirty to forty minutes were allowed between runs to reduce the amount of free stream turbulence the water acquires when it is pumped to the settling chamber. In order to investigate flows at high angles of attack, a new 24 cm x 12 cm rectangular test section was designed. Details of the design of this new section may be found in Appendix 2. For this investigation, Reynolds numbers based on the diameter of 750 and 1250 were achieved. The average run time was about 1.5 minutes.

In order to visualize the flow, dye of different colors was injected into the flow from small holes on the model. Then color pictures and video movies of the flow were taken in order to record any observed physical phenomena.

3.6 Water tunnel models

For this investigation, three different models were used. Schematics of these are shown in figures 27, 28 and 29. In figures 27 and 28, a sharp nosed ogive cylinder and a blunt nosed ogive cylinder are pictured. These models are geometrically similar to their counterparts used in the wind tunnel, having $(x/d)_{TOT}$'s of 18 and 17.4 respectively. A maximum allowable length of 200 mm was used to keep wall generated boundary layer effects small. Nevertheless to investigate whether there were any wall effects, a third model shown in figure 29, was built. This model also had an $(x/d)_{TOT}$ of 18, but its diameter was smaller (8 mm instead of 11 mm). The small model was used in order to compare its flow field with that of the longer model at high angles of attack. By observing any discrepancies in these two flow fields, it was thought that a wall effect might be observed.

The dye ejection holes were chosen as to be just upstream of the separation points of the body vortices. By doing this, the dye is taken by the vortical flow and forced to follow its path. Twelve dye ejection holes were used on the two larger models and only four holes on the smaller model. The holes were placed at the following locations :

$$\frac{x}{x} (\%) = 7; 11; 45; 50; 75; 80.$$

Three different colors of dye were used to further enhance the visualization.

3.7 Data acquisition

The data acquisition system used for the force balance measurements was a set of six strip chart recorders in conjunction with two voltage divider bridge circuit boxes which were able to handle three force components each. The recorded data was then reduced and plotted using the VKI VAX computer facilities.

4. WATER TUNNEL RESULTS AND DISCUSSION

4.1 Experimental procedure

As stated before three models were used in the water tunnel flow visualization studies. Using these three models and running the tunnel in the blowdown mode at Reynolds numbers of 750 and 1250 based on the model diameter, the following series of tests were performed :

(1) Test No. 1 : This test involved model 1 (Fig. 27) using six of the dye ejection holes :

$$\frac{x}{x_0} (\%) = 7; 50; 75.$$

An angle of attack range from 15°-55° was covered in 5° intervals as it is in this range where the asymmetric vortex phenomenon is observed. At each angle of attack 5°, a few pictures were taken during the course of each run. More than one test was usually done at each angle of attack to insure repeatability. The Reynolds number for this test was 750.

(2) Test No. 2 : Same procedure as test No. 1, but a Reynolds number of 1250.

(3) Test No. 3 : Same procedure as test No. 2, except only the four most forward dye ejection holes were used. This was done to see if the more rearward dye ejection affected the flowfields.

(4) Test No. 4 and Test No. 5 : These tests were done using the small sharp nosed body (Fig. 29). Test 4 was done at a Reynolds number of 750 and test No. 5 at a Reynolds number of 1250. Only angles of attack from 35°-55° were investigated, as it is here where a wall effect, if any should be observed.

(5) Test Nos. 6, 7 and 8 : These are the same as tests Nos. 1, 2 and 3, except the blunt body (Fig. 28) was used.

In total, 150 pictures were taken during the various tests.

4.2 Results and discussion

In figures 30-34 example pictures of the flow visualization tests are shown. Figures 30-31 constitute a series of pictures taken during test No. 3 showing the flowfield for the angle of attack range from 15° to 50° . One can clearly see the asymmetric flowfield's development from its onset near 20° to its full development at 30° and higher. The moving forward of the asymmetric vortex location as angle of attack increases is also observed along with the unsteadiness of the flow which can begin to be observed at 50° . In figures 32-33, a similar series of pictures is shown for the blunt body. Again similar trends as for the sharp body are visible, but the asymmetry does not appear to occur until about 25° - 30° . This was to be expected, as blunting the nose has been observed to delay asymmetric vortex formation (see Chapt. 2). In figure 34, a comparison between the flowfields about the long and short sharp nosed bodies is made. It appears that there may be a wall effect which changes the location of the vortex asymmetry on the body. In the upper set of pictures, the asymmetry appears to be more forward on the small body and in the lower pictures it appears to be more rearward on the small body. However, more investigation of this problem needs to be done before any firm conclusions can be made.

For this investigation, the water tunnel was primarily used to obtain a general qualitative idea of the asymmetrical vortical flowfield. In a related investigation though, a more detailed analytical study of the water tunnel results was performed (Ref. 45). Certain parameters involving vortex location (A_1 , A_2 etc.) and the angle the shed vortex makes with the body axis (χ) were determined and compared with the results of others. In figures 34-40, examples of the results obtained are presented. Good agreement was found for the parameter χ (Fig. 35) but the agreement for A_2 with others was not as good (Fig. 36). Also the effects of Reynolds

number (Fig. 37), blunting the nose (Fig. 38), the wall interference (Fig. 39) and the rearward dye ejection holes (Fig. 40) were not totally clear due to data scatter. These results were not totally unexpected, however. In the previous investigations of Thomson and Morrison (wind tunnel) and Clark (water tunnel), the tests were performed at Reynolds numbers one to two orders of magnitude higher. This is perhaps too large a difference in Reynolds number to expect the results to be comparable. Freestream turbulence, which may have been in the flow due to the pumping and mixing of water in the settling chamber, is known to cause data scatter (Ref. 19). It generally manifests itself by causing a constant switching or dancing of the vortices, a phenomenon observed during these tests. Also, minor problems shown in figures 41a-d were encountered which may have contributed to data scatter. These were ejected dye interference (Fig. 41a,b), support interference (Fig. 41c) and problems of dye dispersal which made some pictures difficult to interpret. A discussion of these problems and suggestions on how they may be avoided may be found in reference 45.

In summary then, two definite conclusions can be made from the water tunnel results :

- (1) The angle of onset of the asymmetry for the sharp nosed body was smaller than the angle of onset for the blunt nosed body; between 15° - 20° for the sharp nosed body and between 25° - 30° for the blunt nosed body. This agrees quite well with the results of other investigations.
- (2) The position of the asymmetry moves towards the nose as the angle of attack increases, which again agrees with previous investigations.

Further studies concerning Reynolds number effects, water tunnel wall effects and the values of λ and A_1 , A_2 , etc. must be made before any definite conclusions may be drawn. The suggestions were made and the test procedure outlined in reference 45 should greatly aid these investigations.

5. WIND TUNNEL INVESTIGATIONS

5.1 Experimental procedure

Force measurements were made on the two models previously discussed in the transonic test section of the VKI S-1 wind tunnel. Measurements were made at Mach numbers .4, .6, .7, .8 and .9 for both bodies, over an angle of attack range of 0°-60°. The Reynolds number was held reasonably constant at 8.3×10^4 based on the model's diameter. Due to the need for a support change to cover the full angle of attack range, the following procedure was utilized :

- (1) The low angle of attack support was installed and tests for all the various Mach numbers were conducted for the sharp nosed model. The angle of attack was varied from 0° to 30° with force measurements being taken every one or two degrees. The model was then returned to 0° with force measurements being taken every 5° to 10°. This was done in order to check the repeatability of the measurements and to observe if there was any hysteresis effect. The static pressure, the stagnation pressure, the atmospheric pressure and the temperature were recorded at the beginning and end of each Mach number run.
- (2) The high angle of attack support was installed and again tests were conducted for all the various Mach numbers on the sharp nosed body. The angle of attack was varied from 28° to 60° with force measurements being made every one or two degrees. The model was returned to 28° in larger increments of 5° or 10°, once again in order to check the repeatability and to observe if there was any hysteresis effect. The static pressure, the stagnation pressure, the atmospheric pressure and the temperature were recorded at the beginning and end of each Mach number run.
- (3) The above tests were repeated in exactly the same manner for the blunt nosed body.

All measurements were recorded using the data acquisition system described in section 3.8. The data reduction was done by utilizing VKI's VAX computer facility. All the data were reduced to coefficient form and referred to the body axis coordinate system. Since a six component force measurement data reduction program did not exist at VKI, one was developed and utilized for this investigation. A listing of this program and some example outputs may be found in Appendix III. It is again pointed out that no axial force measurements were made during this investigation.

5.2 Overall force measurement results

All the data obtained from the force measurements are plotted in figures 42-109. The first set of plots (Figs. 42-86) refers to the yawing moment, normal force, pitching moment, center of pressure for the normal force, and the rolling moment. The second set of plots (Figs. 87-109) refers to the main focus of this investigation, the side force.

Figures 42-86 are arranged in ascending order of Mach number for first the sharp nosed body and then the blunt nosed body. For each test, the yawing moment plot comes first followed by the normal force, pitching moment, the center of pressure for the normal force and the rolling moment. The yawing moment is seen to follow the same trends as the side force which was expected. The normal force coefficient ($-C_z$) is seen to decrease as Mach number increases for both nose shapes, but the blunt nose body's normal force is less than the sharp nose body's for $M = .4, .6$ and $.7$. Similar trends to these were pointed out in Wardlaw's article (Ref. 4). It should be noted that in the normal force curves there is a discontinuity in the data between $25-30^\circ$. This discontinuity is due to the support change and was expected to occur. The pitching moment and center of pressure curves also compare well with the results of others (Ref. 4). From the center of pressure curves (Figs. 45, 50, ...85) it can be seen that the center of pressure moves from

the tip (at small α) to the point $X = 8.6$ (large α) which agrees well with expected values. The rolling moment was observed to always be zero, which also was expected as these models had no added lifting surfaces or control surfaces that could induce a rolling moment. All the data indicate that the model support causes very little interference on the model. Therefore, it can be concluded that high angle of attack investigations, especially force measurements at high angles of attack can be accurately done using these new VKI facilities.

5.3 Discussion and results of the side force measurements

The main focus of the present investigation is the side force measurements. The results are shown in figures 87-109 with the sharp nose data coming first followed by the blunt nose data and then some comparative plots. The plots are in ascending order of Mach number, with the side force plot first and the side force center of pressure plot second. The data was found to be very repeatable and no hysteresis was found. Data scatter was small for the sharp nosed body at smaller transonic Mach numbers, but increased for the blunt nosed body and the higher Mach numbers (.8 and .9) for the sharp nosed bodies. From each plot, the angle of attack for the onset of small side forces $(\alpha_{AV})_{weak}$, large side forces $(\alpha_{AV})_{strong}$, maximum side force α_{max} , as well as α_{UAV} and $|C_{y_{max}}|$ was determined and plotted in figures 105 and 106.

In all plots of side forces for the sharp nosed body, there appears to be a small rise of the side force starting at an onset angle $(\alpha_{AV})_{weak}$ of about 13-15°, followed by a decrease back to zero near 25°. The side force remains to be zero up to about $(\alpha_{AV})_{strong} = 35^\circ$ and then increases sharply, reaching a maximum value at α_{max} . The peculiar hump of the side force curve between $(\alpha_{AV})_{weak}$ and $(\alpha_{AV})_{strong}$ which was also observed in other investigators results (example : Fig. 7, Ref. 7) can

possibly be explained as a Reynolds number effect. With increasing α , the type of separation changes from supercritical to transcritical to subcritical. This is because the path length of the boundary layer between stagnation point and separation decreases with increasing α . At small α , the boundary layer is turbulent at separation (supercritical separation) leading to the formation of the separated vortices which is different from that obtained for laminar separation. The turbulent separated vortices possibly interact stronger and therefore may become asymmetric sooner than in the case of laminar separation. With increasing α the separation becomes subcritical and asymmetry ceases until higher α 's are reached. Further work needs to be done investigating the above effect.

The above quantities are plotted in figures 105 and 106. Both curves compare very well with previous results. On figure 106, a line indicating the onset of a weak asymmetry has been added. In figure 107 the effect of Mach number on the side force can be seen. As Mach number was increased, the side force is shown to decrease. Above a Mach number of .7, a large fall off in C_y can be seen. Figures 108 and 109 show the effect of blunting the nose. The side force is definitely reduced and thus blunting the nose seems a very efficient way of alleviating the side force.

A few remarks should be made concerning the plots at the side force center of pressure versus angle of attack (Figs. 88,90,...104). For points where the side force is small, the calculations of $(XCP/D)_{side}$ is very inaccurate and these points should be ignored. For the points where this problem is not encountered the results show the definite movement of the asymmetry towards the nose with increasing α . For example, in figure 43, for $13^\circ \leq \alpha \leq 23^\circ-24^\circ$ and $32^\circ \leq \alpha \leq 59^\circ$, the forward movement of the asymmetry is clearly shown. For the angles of attack outside the above ranges, C_y is small and the calculation of $(XCP/D)_{side}$ is unreliable. This movement of the asymmetry towards the nose has been observed by other investigators and is thought to account for the increasing values of C_y (Refs. 2,4,7,etc.).

In summary, the phenomena associated with asymmetric vortex formation on ogive cylinder bodies are observed to occur in the same manner and magnitude on a body having a large $(x/d)_{TOT}$. The maximum side force varies in the same manner as for smaller bodies and the Mach number and nose blunting effects are shown to be the same as for shorter bodies. Future work should concentrate on the investigation of the effects of roll angle, to determine the exact unsteadiness boundaries, to do tests for different nose and body configurations, and investigate other side force alleviation techniques. Further, this investigation demonstrates that high angle of attack investigations at VKI are very feasible and that the induced side force and other high angle of attack phenomena can be investigated at VKI in the future.

6. CONCLUSIONS

Flow visualization studies and six component force measurements have been made on an ogive cylinder at high angles of attack in the transonic flow regime with good results. Force measurements were made up to an angle of attack of 60° but the possibility exists to extend these measurements up to 90° .

The water tunnel flow visualization studies gave an excellent qualitative view of the asymmetric vortex phenomenon. The previously recognized trends of the vortical flow field forming first a symmetric pair of vortices, then an asymmetric pair of vortices and finally a diffuse vorticity pattern and the tendency of the asymmetric vortex pair to move upwards the model's tip as α increased were shown to occur. Quantitative analysis of water tunnel results showed much scatter and further investigations need to be done before any firm conclusions can be made.

The force measurements for the two ogive cylinder bodies of $(x/d)_{TOT} = 18$ (sharp) and $(x/d)_{TOT} = 17.4$ (blunt) yielded the following results :

- (1) As Mach number increased $|C_{y_{max}}|$ and the side force in general decreased in value, falling-off sharply after $M = .7$.
- (2) Blunting of the nose was found to reduce the side force greatly, especially for $M \leq .7$.
- (3) A possible explanation for the onset of weak asymmetries is given. It may be due to a Reynolds number effect which causes the passage of the flow from the supercritical to subcritical flow regimes for $\alpha \leq 25^\circ$.

Further investigations for other model configurations, higher angles of attack and different roll orientations could now be considered in order to add to the present data base concerning the induced side force phenomena.

REFERENCES

Review articles

1. ERICSSON, L.E.: Steady and unsteady vortex-induced asymmetric loads, review and further analysis. AIAA Paper 79-1531, July 1979.
2. ERICSSON, L.E. & REDING, J.P.: Vortex-induced asymmetric loads in two dimensional and three dimensional flows. AIAA Paper 80-0181, Jan. 1980.
3. NIELSEN, J.N.: Missile aerodynamics - past, present and future. Journal of Spacecraft, Vol. 17, No. 3, May-June 1980.
4. WARDLAW, J.B. Jr.: High angle of attack aerodynamics, in "Missile Aerodynamics". AGARD LS 98, 1979, pp 5.1-5.53.

Detailed studies

5. WARDLAW, A.B. & MORRISON, A.M.: Induced side forces at high angles of attack. J. Spacecraft & Rockets, Vol. 13, No. 10, October 1976, pp 589-593.
6. KEENER, E.R. & CHAPMAN, G.T.: Onset of aerodynamic forces at zero sideslip on symmetric forebodies at high angles of attack. AIAA Paper 74-770, 1974.
7. KEENER, E.R.; CHAPMAN, G.T. & KRUSE, R.L.: Effects of Mach number and afterbody length on onset of asymmetric forces on bodies at zero sideslip and high angles of attack. AIAA Paper 76-66, 1976.
8. KEENER, E.R.; CHAPMAN, G.T.; COHEN, L. & TALEGHANI, J.: Side forces on a tangent ogive forebody with a fineness ratio of 3.5 at high angles of attack, Mach numbers from .1 to .7. NASA TM-X 3437, 1977.
9. KEENER, E.R. & CHAPMAN, G.T.: Similarity in vortex asymmetries over slender bodies and wings. AIAA Journal, Vol. 15, No. 9, Sept 1977, pp 1370-1372.
10. KEENER, E.R., CHAPMAN, G.T. & COHEN, L. & TALEGHANI, J.: Side forces on forebodies at high angles of attack and Mach numbers from .1 to .7 : Two tangent ogives, a paraboloid and a cone. NASA TM-X 3438, 1977.

11. KRUSE, R.L.; KEENER, E.R.; CHAPMAN, G.T. & CLASERS, G.: Investigation of the asymmetric aerodynamic characteristics of cylindrical bodies of revolution with variations in nose geometry and rotational orientation at high angles of attack to 58° and Mach number to 2.
NASA TM 78533, Sept. 1979.
12. KRUSE, R.L.: Influence of spin rate on side force of an axisymmetric body.
AIAA Journal, Vol. 16, No. 4, April 1978, pp 415-416.
13. ERICSSON, L.E. & REDING, J.P.: Maximum vortex-induced side force.
J. Spacecraft, Vol. 15, No. 4, July-August 1978, pp 201-207.
14. REDING, J.P. & ERICSSON, L.E.: Maximum side forces and associated yawing moments on slender bodies.
AIAA Paper 79-1647, August 1979.
15. LAMONT, P.J. & HUNT, B.L.: Prediction of aerodynamic out-of-plane forces on ogive-nosed circular cylinders.
J. Spacecraft & Rockets, Vol. 14, No. 1, Jan. 1977, pp 38-44.
16. LAMONT, P.J. & HUNT, B.L.: Pressure and force distributions on a sharp-nosed circular cylinder at large angles of attack in a uniform subsonic stream.
J. Fluid Mechanics, Vol. 76, Part 3, 1976, pp 519-559.
17. LAMONT, P.J.: Pressure measurements on a ogive-cylinder at high angles of attack with laminar, transition, or turbulent separation.
AIAA Paper 80-1556, August 1980.
18. MARSHALL, F.J. & DEFFENBAUGH, F.D.: Separated flow over a body of revolution.
J. Aircraft, Vol. 12, No. 2, 1975, pp 78-85.
19. DEXTER, P.C. & HUNT, B.L.: The effect of roll angle on the flow over a slender body of revolution at high angles of attack.
AIAA Paper 81-0358, 1981.
20. HUNT, B.L. & LAMONT, P.J.: Comment on induced side at high angles of attack.
J. Spacecraft & Rockets, Vol. 14, No. 6, 1977.
21. AGNONE, A.M.; ZAKKAY, V. & TONY, E.: Aerodynamics of slender finned bodies at large angles of attack.
AIAA Paper 77-666, 1977.
22. MALCOLM, G.N.: Impact of high- α aerodynamics on dynamic stability parameters of aircraft and missiles, in "Dynamic Stability Parameters",
AGARD LSP-114

23. DEFFENBAUGH, F.D. & KOERNER, W.G.: Asymmetric vortex wake development on missiles at high angles of attack.
J. Spacecraft, Vol. 14, No. 3, 1977, pp 155-162.
24. PRZIREMBEL, C.E.G. & SHEREDA, D.E.: Aerodynamics of slender bodies at high angles of attack.
J. Spacecraft, Vol. 16, No. 1, 1979, pp 10-14.
25. FAHERTY, J.I.: Experimental and analytical investigation of high angles of attack missile aerodynamics.
AIAA Paper 77-1156, August 1977.
26. YANTA, W.J. & WARDLAW, A.B.: Multi-stable vortex patterns on slender, circular bodies at high incidence.
AIAA Paper 81-0006, 1981.
27. HUNT, B.L. & DEXTER, P.C.: Pressure on a slender body at high angle of attack in a very low turbulence level airstream.
AGARD Symposium on High Angles of Attack Aerodynamics, Sandefjord, Norway, Paper No. 17, 4-6 Oct. 1978.
28. THOMSON, K.D. & MORRISON, D.F.: The spacing, position and strength of vortices in the wake of slender cylindrical bodies at large incidence.
J. Fluid Mechanics, Vol. 50, Part 4, 1971, pp 751-785.

Side Force Alleviation

29. ERICSSON, L.E. & REDING, J.P.: Alleviation of vortex-induced asymmetric loads.
J. of Spacecraft & Rockets, Vol. 17, No. 6, Nov.-Dec. 1980, pp 546-553.
30. RAO, D.M.: Side force alleviation on slender pointed forebodies at high angles of attack.
J. Aircraft, Vol. 16, No. 11, Nov. 1979, pp 763-767.
31. FIDLER, J.E.: Active control of asymmetric vortex effects.
AIAA Paper 80-0182, 1980.
32. PEAKE, D.J.; OWEN, F.K. & JOHNSON, D.A.: Control of forebody vortex orientation to alleviate side forces.
AIAA Paper 80-183, Jan. 1980.

Support Interference

33. DIETZ, W.E., Jr. & ALSTATT, M.C.: Experimental investigation of support interference of an ogive cylinder at high incidence.
AIAA Paper 78-165, Jan. 1978.

34. ERICSSON, L.E.: Support interference,
in "Dynamic Stability Parameters",
AGARD LSP-114, 1981, pp 8.1-8.26.

Force Balance Design and Calibration

35. POPE, A. & GOIN, K.L.: High-speed wind tunnel testing.
John Wiley & Sons, 1965.
36. ZARGHAMI, A.I.: Aerodynamic characteristics of a missile
configuration featuring a wing with various strakes
in subsonic and transonic flows up to high angles
of incidence.
VKI PR 1977-7.
37. GALWAY, R.D.: A comparison of methods for calibration
and use of multi-component strain gauge wind tunnel
balances.
NRC-LR-600, 1980.
38. COOK, T.A.: A note on the calibration of strain gauge
balances for wind tunnel models.
RAE TN Aero 2631, Dec. 1959.
39. HANSEN, R.M.: Evaluation and calibration of wire-strain-
gauge wind tunnel balances under load.
AGARD Report 13, Feb. 1956.
40. SMITH, D.L.: An efficient algorithm using matrix methods
to solve wind tunnel force balance equations.
NASA TN-D 6860, August 1972.

Water Tunnel Investigations

41. WERLE, M.H.: Tourbillons de corps fuselés aux
incidences élevées.
ONERA TP 1980-4.
42. CLARK, W.H.: Body vortex formation on missiles in
incompressible flows.
AIAA Paper 77-1154.
Paper presented at AIAA 4th Atmospheric Flight
Mechanics Conference, Hollywood, Florida,
August 8-10, 1977.
43. DEMURIE, F.; MUYLAERT, J. & WENDT, J.F.: Investigation
on the interaction between body vortices and the
strake-wing panels of a missile configuration.
VKI IN 63, June 1980.
44. DEMURIE, F.: Investigation of the interference effects
in the flowfield around a body-strake-wing
missile configuration.
VKI PR 1980-23.

45. FOURNIOLS, J.: Etude experimentale d'un missile à grande incidence en regime transsonique.
VKI SR 1981-05/AR, June 1981.

Others

46. GERALD, C.F.: Applied numerical analysis.
2nd Edition, Addison-Wesley Publishing Co., 1978.

APPENDIX I - DESIGN AND CALIBRATION OF A
SIX COMPONENT FORCE BALANCE

For this investigation, a six component force balance had to be designed, constructed and calibrated at VKI. Since this had not been done before at VKI, a considerable amount of effort was put into this undertaking. In order to design a force balance, certain factors concerning its use, maximum tolerable loads, adaptability, etc., must be first considered. The factors important in determining this balance overall dimensions are listed below.

(1) The balance was to be used mainly in VKI S-1 wind tunnel. This tunnel has a cross section of 36 cm x 40 cm. Thus in order to minimize wall effects, no model longer than 320 mm should be used. Since for this investigation bodies of $(x/d)_{TOT} = 18-20$ were to be investigated, the largest outer body diameter tolerable is 17 mm. Generally, a 2 mm model thickness is needed for the model manufacture, so the largest tolerable inside diameter is 13 mm. Thus, the balance must have a diameter < 13 mm.

(2) In order for the balance to be widely applicable, it must be able to work over the following force ranges :

Normal force - 0-100 Nt

Rolling moment - 0-200 Nt

Axial force - 0-25 Nt

For this investigation, the loads will be much less than this. However, it was felt that the balance should be designed to respond linearly in the above force ranges.

(3) Generally, the center of pressure on a body will move by as much as 10% when the body is not at an extreme aerodynamic condition. Thus, the distance between the gage stations should allow for at least a 10% movement of the center of pressure.

(4) When a model is placed at high angle of attack, $\alpha > 15^\circ$, deflection of the sting and balance becomes important. The sting and balance must not be deflected so as to touch the

model. At least 1-1.5 mm of deflection should be allowed for in the balance's design.

(5) The strength of the balance is very important. It must be safe from failure and must be very stiff so that large bending (which leads to a non linear response) does not occur. Thus a safety factor of at least 2-2.5 should be designed into the balance against failure and a very strong steel should be used for its construction.

In figure I-1, a sketch of the final balance design is given. Its largest outer diameter is 11 mm. This allows a 1 mm deflection tolerance for this investigation, which was calculated to be sufficient. A distance of 36 mm is found between the two gage stations, which should allow for the center of pressure movement. A safety factor of at least 2.0 in terms of strength exists for each cross section of the balance. It is constructed of a very high quality steel and should only suffer small deflections within its design force range. A brief discussion will now be given of each individual component design.

Rolling moment

The rolling moment is the cruciformed cross section part (section B, $L_{TOT} = 38$ mm) of the balance. A standard cruciform cross section is used as this type of section is uniformly responsive to a rolling moment. The strain gages are mounted in the center of this section, being crossed at 45° to obtain the most accurate and maximum response signal. A limit of 200 Nt cm was designed as the maximum rolling moment at which linear signal response will be obtained.

Normal and side forces and their associated moments

The two normal and side force stations are shown as sections C and F. They are 9 mm long and separated by a distance of 36 mm. A cross sectional area of 8.9 to 4.15 was

chosen as this makes the side force section twice as sensitive as the normal force section. This was done because for most applications the normal force is usually twice as large as the side force, if not more. Two gages are mounted on each surface of the gage station and a bridge circuit is formed between the upper and lower gages and the right and left side gages at each station. The normal force and side force is thus measured at each station and then by adding and subtracting them, the total normal and side forces and their respective moments are obtained.

Axial force

The axial force is by far the most difficult component to design, as it must be extremely sensitive but yet strong enough so as not to break. The axial component design for this balance is fairly standard and closely follows the design of a similar balance used at DFVLR. A maximum force of 25 Nt was calculated as the limit force for linear response of the axial component. This component is located between the two normal and side force gage stations.

A wiring schematic of the balance is shown in figures I-(2-5). For details of the theory of strain gage bridges, see either reference 35 or 36.

The calibration of the balance was carried out in the standard procedure of individually loading each component and determining the calibration constants for each component. Details of this procedure may be found in references 37-40. The balance was found to be relatively interference free and the tolerable maximum loads even higher than designed for. However, at the time of this investigation, the axial component was not constructed and so will be calibrated at a later date. The programs used for the determination of the calibration matrix and calculation of the forces and moments may be found in Appendix III.

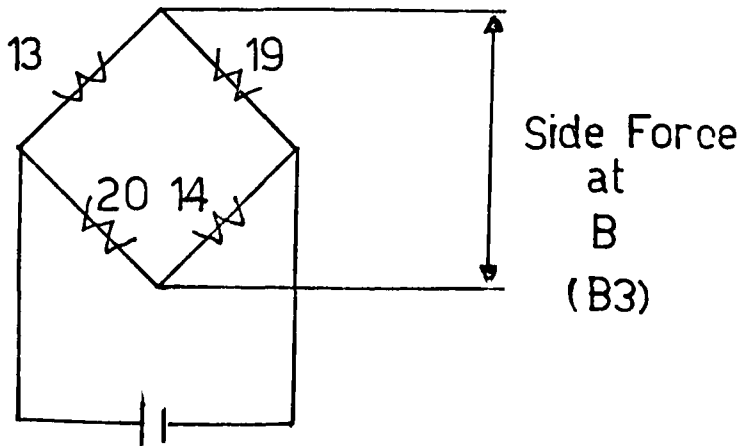
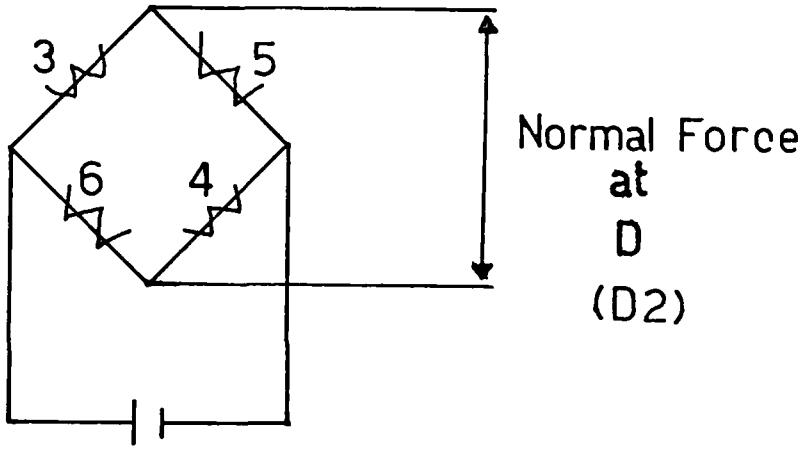
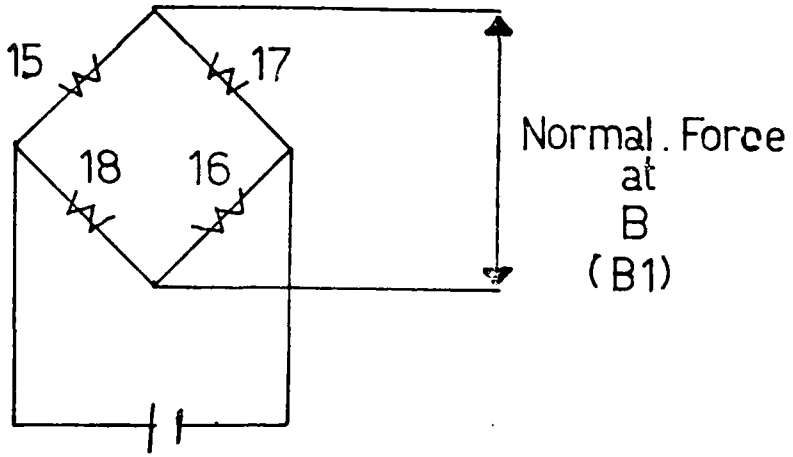
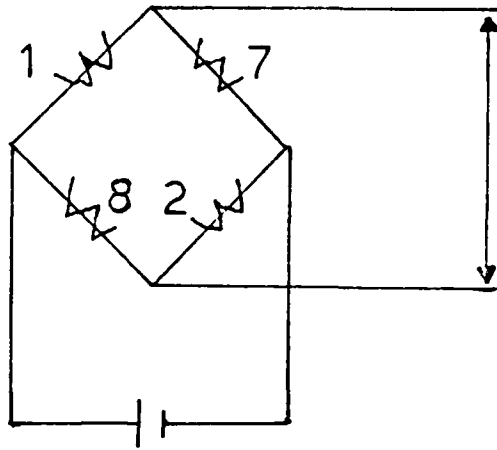
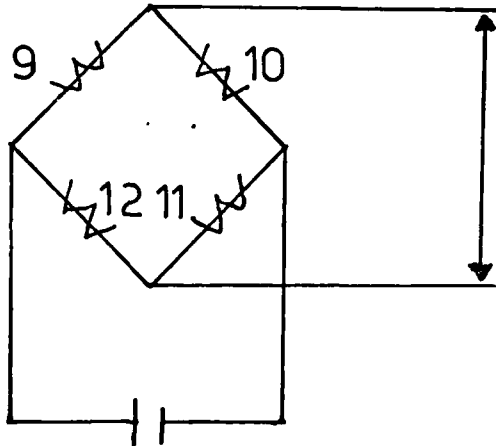


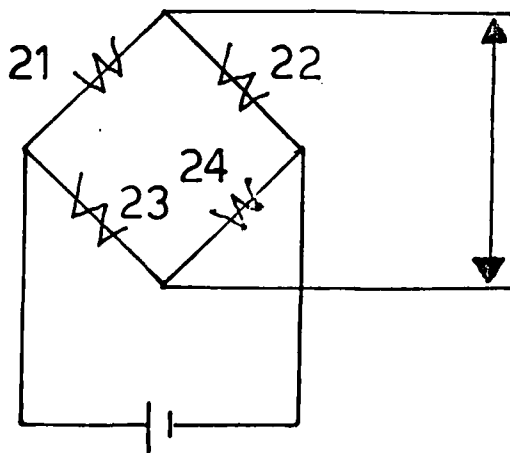
FIG. 1-3 - STRAIN GAGE BRIDGES



Side Force
at
D
(D 4)



Axial Force
(C 5)



Rolling Moment
(A 6)

FIG. I-3 - STRAIN GAGE BRIDGES

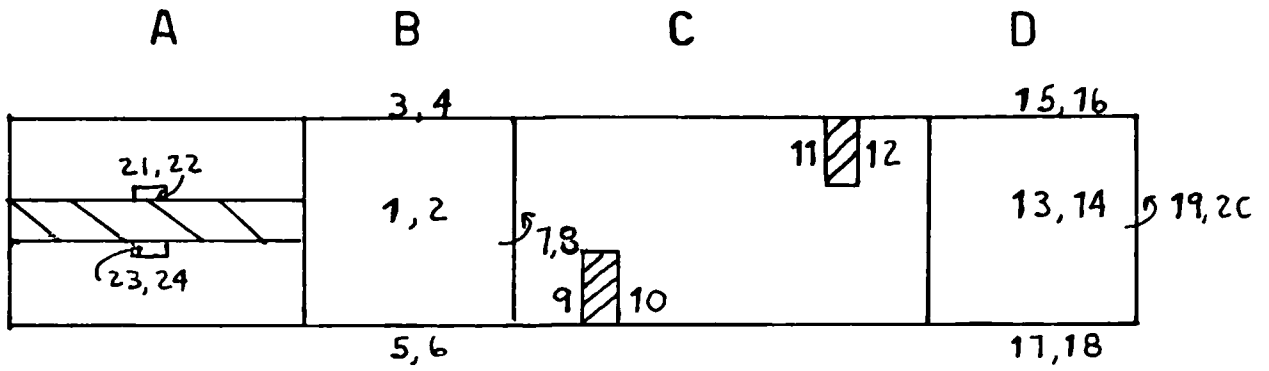


FIG. 1-4 - LOCATION OF STRAIN GAGES

Beam	Section	Location	Orientation
Beam 1	C1	Top	Vertical
Beam 1	B2	Bottom	Vertical
Beam 1	B1	Top	Horizontal

Beam	Section	Location	Orientation
Beam 2	A1	Top	Vertical
Beam 2	D1	Bottom	Vertical
Beam 2	B2	Top	Horizontal

FIG. 1-5 - TERMINAL CONNECTIONS ON THE BALANCE

APPENDIX II - DESIGN OF WATER TUNNEL CONTRACTION
AND TEST SECTION

In order to allow flow visualization studies at high angles of attack to be made, a new rectangular test section and nozzle contraction had to be designed. In designing the new test section, several factors had to be kept in mind :

- (1) One operates mostly in the blowdown mode (see Section 3 for water tunnel description). This puts a limit on the run time. In order to keep the existing run time and the same present range of Reynolds numbers, the new test section area must be approximately the same as the present test section area of 15×15 cm ($A = 225$ cm²).
- (2) An important factor in any test section design is the contraction ratio. This is the ratio of the settling chamber area to the test section area. Most tunnels have contraction ratios between 5 and 16.
- (3) The boundary layer along the test section wall also must be accounted for in the test section design. The model must be kept well away from this boundary layer as its effects on the flow field are not predictable. The approximate boundary layer thickness for the present test section is about 1-1.5 cm. Thus, the model should be kept at least 2 cm from the test section wall.
- (4) It was stated that the present investigation is concerned with bodies at high angles of attack. In fact, the bodies to be studied have a very high $(x/d)_{TOT}$ of about 18-20. Since angles of attack up to 70° want to be investigated and models 10-12 mm in diameter want to be used, the test section must be at least 20 cm in one of its dimensions.

Taking into account all of these factors, a test section of 12 cm × 24 cm was chosen. Its area, 288 cm², is not much larger than the present section area of 225 cm², so the run time is only slightly decreased. Its contraction

ratio of 8.8 is reasonable and should adequately reduce velocity fluctuations in the streamwise direction. Its dimension of 24 cm should allow a body of $(k/d)_{TOT} = 20$ with $d = 10$ mm to be studied at high angles of attack without the model's tip entering the wall's boundary layer. Thus, these dimensions for the new test section appear reasonable. Below, the calculation of the nozzle contour and the dimensions obtained is given. The formulas used below may be found in the report by A.F. Lehman, "The Garfield Thomas Water Tunnel", Navy Department of Ordnance, Contract No. 16597, 1959.

Calculation of the contour

In order to calculate the dimensions of the nozzle contour, the following formulas will be utilized :

$$d_1 = D_s - \frac{\theta_c}{2} L_1 \left(\frac{X_1}{L_1} \right)^3 \exp \left[\frac{1}{2} \left(1 - \frac{X_1}{L_1} \right)^2 \right]$$

$$d_2 = D_w + \frac{\theta_c}{2} L_2 \left(\frac{X_2}{L_2} \right)^3 \exp \left[\frac{1}{2} \left(1 - \frac{X_2}{L_2} \right)^2 \right]$$

where : θ_c = non dimensional parameter.

The other variables are defined in figure II-1. The problem in using these formulas is that they only apply for an axisymmetric contraction whereas our test section is rectangular, non axisymmetric. In order to utilize these formulas the following procedure is used :

- (1) The formulas are applied to an axisymmetric nozzle with the same A_s and A_w as the desired rectangular nozzle.
- (2) The dimensions obtained are then converted to their rectangular nozzle equivalents.

In figure II-2, an illustration of the process is shown. "a" is obtained from step 1 and then "b" and "c" are determined in step 2. Below, all the calculations are shown in detail. Tables listing the values a, b and c are given at the end.

$$\begin{aligned} \text{Desired Center} & : A_s = 2500 \text{ cm}^2 \\ & A_w = 288 \text{ cm}^2 \end{aligned}$$

$$\text{Equivalent contour} : \frac{\pi}{4} D_s^2 = A_s \rightarrow D_s = 56.42 \text{ cm}$$

$$\frac{\pi}{4} D_w^2 = A_w \rightarrow D_w = 19.15 \text{ cm}$$

Now at the inflection points :

$$(1) \quad d_1 = d_2$$

$$(2) \quad \left. \frac{\partial \begin{pmatrix} d_1 \\ D_s \end{pmatrix}}{\partial \xi_1} \right|_{\xi_1=1} = \left. \frac{\partial \begin{pmatrix} d_2 \\ D_w \end{pmatrix}}{\partial \xi_2} \right|_{\xi_2=1}$$

$$(3) \quad \left. \frac{\partial^2 \begin{pmatrix} d_1 \\ D_s \end{pmatrix}}{\partial \xi_1^2} \right|_{\xi_1=1} = 0 \quad \text{and} \quad \left. \frac{\partial^2 \begin{pmatrix} d_2 \\ D_w \end{pmatrix}}{\partial \xi_2^2} \right|_{\xi_2=1} = 0$$

$$\text{where : } \xi_1 = \frac{X_1}{L_1} \quad \text{and} \quad \xi_2 = \frac{X_2}{L_2}$$

Applying conditions (1) and (2) :

$$(1) \rightarrow D_S - D_W = \frac{\theta_C}{2} (L_1 + L_2)$$

$$(2) \rightarrow \frac{L_1}{L_2} = \frac{D_S}{D_W}$$

(3) Provides a check which is satisfied by (1) and (2).

Thus, the conditions at the inflection point are obtained.

$$(1) \quad D_S - D_W = \frac{\theta_C}{2} (L_1 + L_2)$$

$$(2) \quad \frac{L_1}{D_S} = \frac{L_2}{D_W}$$

Also : $L_1 + L_2 = 50$ cm.

Using all of the above, θ_C , L_1 and L_2 may be calculated.

$$(1) \quad \theta_C = \frac{56.42 - 19.15}{25} = 1.4908$$

$$(2) \quad \frac{L_1}{56.42} = \frac{L_2}{19.15} \Rightarrow L_1 = \frac{56.42}{19.15} L_2$$

$$(3) \quad L_1 = 50 - L_2$$

$$L_2 = 12.67 \text{ cm}$$

$$L_1 = 37.33 \text{ cm}$$

Substitution of these into the formula give :

$$d_1 = 56.42 - 27.826 \left(\frac{X}{37.33} \right)^3 \exp \left[\frac{1}{2} \left(1 - \left(\frac{X}{37.33} \right)^2 \right) \right]$$

$$d_2 = 19.15 + 9.444 \left(\frac{X}{12.67} \right)^3 \exp \left[\frac{1}{2} \left(1 - \left(\frac{X}{12.67} \right)^2 \right) \right]$$

Now the procedure outlined in figure 2 is utilized.

X	d ₁	a	b	c
cm	cm	cm	cm	cm
0	56.42	0	0	0
3	56.40	.01	.01	.007
4	56.36	.03	.031	.021
5	56.31	.055	.056	.038
6	56.23	.095	.097	.066
7	56.12	.15	.153	.105
8	55.98	.22	.224	.153
9	55.80	.31	.316	.216
10	55.57	.425	.433	.296
11	55.30	.56	.571	.391
12	54.97	.725	.739	.506
13	54.60	.91	.928	.635
14	54.16	1.13	1.15	.788
15	53.67	1.375	1.40	.959
16	53.12	1.65	1.682	1.15
17	52.51	1.96	2.00	1.37
18	51.84	2.29	2.33	1.60
19	51.11	2.66	2.71	1.86
20	50.31	3.06	3.12	2.13
21	49.45	3.49	3.56	2.43
22	48.53	3.95	4.03	2.75
23	47.54	4.44	4.53	3.10
24	46.50	4.96	5.06	3.46
25	45.41	5.50	5.61	3.84

X	d ₁	a	b	c
cm	cm	cm	cm	cm
26	44.26	6.08	6.20	4.24
27	43.06	6.68	6.81	4.66
28	41.81	7.31	7.45	5.10
29	40.51	7.96	8.11	5.55
30	39.18	8.62	8.79	6.01
31	37.81	9.31	9.49	6.49
32	36.41	10.01	10.20	6.98
33	34.98	10.72	10.93	7.48
34	33.53	11.45	11.67	7.99
35	32.06	12.18	12.42	8.49
36	30.57	12.93	13.18	9.02
37	29.09	13.67	13.93	9.53
38	27.60	14.41	14.69	10.05
39	26.14	15.14	15.43	10.56
40	24.76	15.83	16.14	11.04
41	23.49	16.47	16.79	11.49
42	22.36	17.03	17.36	11.88
43	21.40	17.51	17.85	12.21
44	20.63	17.90	18.25	12.48
45	20.04	18.19	18.54	12.69
46	19.62	18.40	18.76	12.83
47	19.35	18.54	18.90	12.93
48	19.21	18.61	18.97	12.98
49	19.16	18.63	18.99	12.99
50	19.15	18.64	19.00	13.00

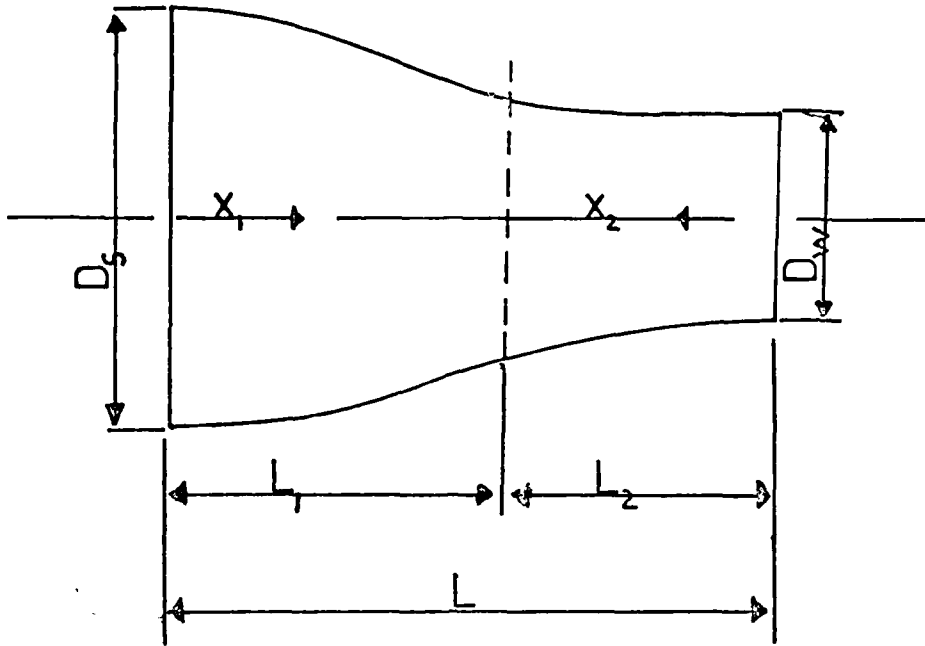
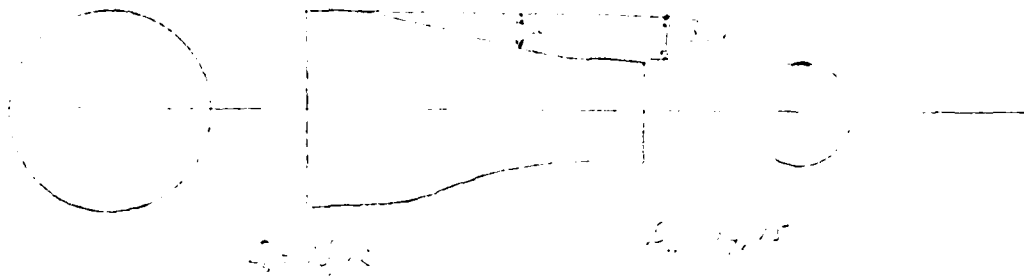
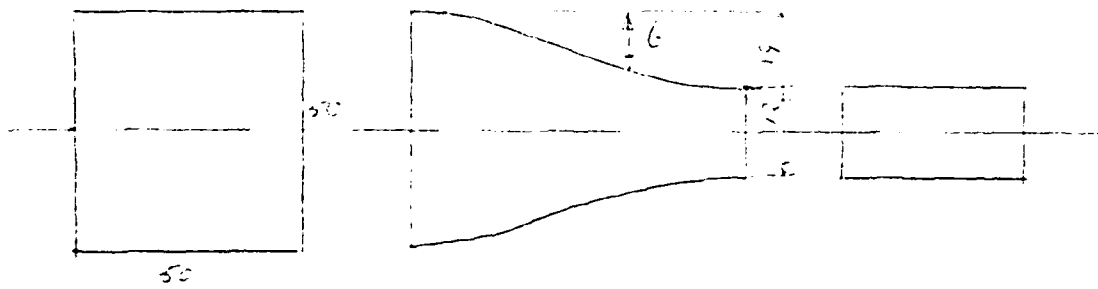


FIG. II-1 - SKETCH OF NOZZLE CONTOUR
AND IMPORTANT PARAMETERS

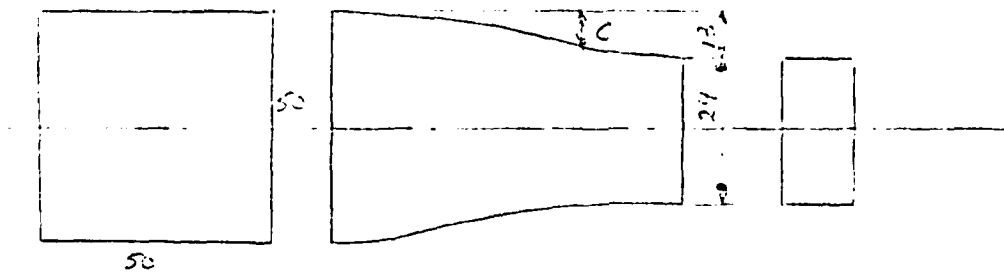


I)



$$\frac{a}{18,64} = \frac{b}{19}$$

II)



$$\frac{a}{18,64} = \frac{c}{13}$$

FIG. II-2 - CALCULATION PROCEDURE UTILIZED FOR CONTRACTION DESIGN

APPENDIX III - DATA REDUCTION PROGRAMS
AND SAMPLE PLOTS AND OUTPUT

```
4700 CALL SUBROUTINE(1,21,1,1,1)
4800 CALL SUBROUTINE(1,15,1,1,1)
4900 CALL SUBROUTINE(1,15,1,1,1)
5000 1 CALL SUBROUTINE(1,15,1,1,1)
5100 1 CALL SUBROUTINE(1,15,1,1,1)
5200 CALL SUBROUTINE(1,15,1,1,1)
5300 CALL SUBROUTINE(1,15,1,1,1)
5400 CALL SUBROUTINE(1,15,1,1,1)
5500 CALL SUBROUTINE(1,15,1,1,1)
5600 CALL SUBROUTINE(1,15,1,1,1)
5700 CALL SUBROUTINE(1,15,1,1,1)
5800 CALL SUBROUTINE(1,15,1,1,1)
5900 15 CALL SUBROUTINE(1,15,1,1,1)
6000 20 CALL SUBROUTINE(1,15,1,1,1)
6100 IF(1,15,1,1) CALL SUBROUTINE(1,15,1,1,1)
6200 C
6210 C
6220 C
6230 C
6300 C
6400 C
6500 C
6600 C
6700 C
6800 30 CALL SUBROUTINE(1,15,1,1,1)
6900 40 CALL SUBROUTINE(1,15,1,1,1)
7000 C
7100 C
7200 C
7300 C
7400 C
7500 50 CALL SUBROUTINE(1,15,1,1,1)
7600 IF(1,15,1,1) CALL SUBROUTINE(1,15,1,1,1)
7700 CALL SUBROUTINE(1,15,1,1,1)
7800 60 CALL SUBROUTINE(1,15,1,1,1)
7900 IF(1,15,1,1) CALL SUBROUTINE(1,15,1,1,1)
8000 IF(1,15,1,1) CALL SUBROUTINE(1,15,1,1,1)
8100 A(1,15)=A(1,15)+SCAL(1,15)
8200 70 CALL SUBROUTINE(1,15,1,1,1)
8300 80 CALL SUBROUTINE(1,15,1,1,1)
8310 C
8320 C
8330 C
8340 C
8400 C
8500 C
8600 110 CALL SUBROUTINE(1,15,1,1,1)
8700 CALL SUBROUTINE(1,15,1,1,1)
8800 IF(1,15,1,1) CALL SUBROUTINE(1,15,1,1,1)
8900 IF(1,15,1,1) CALL SUBROUTINE(1,15,1,1,1)
9000 A(1,15)=A(1,15)+SCAL(1,15)
9100 120 CALL SUBROUTINE(1,15,1,1,1)
9200 IF(1,15,1,1) CALL SUBROUTINE(1,15,1,1,1)
9300 IF(1,15,1,1) CALL SUBROUTINE(1,15,1,1,1)
9400 IF(1,15,1,1) CALL SUBROUTINE(1,15,1,1,1)
9500 IF(1,15,1,1) CALL SUBROUTINE(1,15,1,1,1)
9600 IF(1,15,1,1) CALL SUBROUTINE(1,15,1,1,1)
9700 IF(1,15,1,1) CALL SUBROUTINE(1,15,1,1,1)
9800 IF(1,15,1,1) CALL SUBROUTINE(1,15,1,1,1)
9900 130 CALL SUBROUTINE(1,15,1,1,1)
10000 A(1,15)=A(1,15)+SCAL(1,15)
10100 140 CALL SUBROUTINE(1,15,1,1,1)
```

```

10200      C(1)=C(1)+C(2)*A(1,1)+C(3)*A(1,2)+C(4)*A(1,3)
10300      IF(C(1).GT.0.0)C(1)=C(1)+5)GOTO 10400
10400      C(1)=0.0
10500      DO 150 I=1,3
10600      C(I)=C(I)+C(1)*C(I)
10700      C(I)=0.0
10800      DO 150 I=1,3
10900      S(I)=S(I)+C(1)*C(I)+C(1)*C(I)+C(1)*C(I)
11000      C(1)=0.0
11100      A(C(1),S(C(1)))=C(1)*C(1)+C(1)*C(1)+C(1)*C(1)
11200      C(1)=0.0
11300      S(1)=0.0
11400      C(1)=C(1)+C(1)*C(1)
11500      S(1)=S(1)+C(1)*C(1)+C(1)*C(1)+C(1)*C(1)
11600      C(1)=0.0
11700      A(C(1),S(C(1)))=C(1)*C(1)+C(1)*C(1)+C(1)*C(1)
11800      C(1)=0.0
11900      C(1)=0.0
11910      C(1)=0.0
11920      C(1)=0.0
11930      C(1)=0.0
12000      A(1,1)=C(1)*C(1)
2003      C(1)=C(1)+C(2)*A(1,1)+C(3)*A(1,2)+C(4)*A(1,3)
2004      C(1)=0.0
12300      C(1)=C(1)+C(2)*A(1,1)+C(3)*A(1,2)+C(4)*A(1,3)
12400      IF(C(1).GT.0.0)C(1)=C(1)+5)GOTO 12500
12500      C(1)=0.0
12600      DO 2007 I=1,3
12700      C(I)=C(I)+C(1)*C(I)
12800      C(I)=0.0
12900      DO 2007 I=1,3
13000      S(I)=S(I)+C(1)*C(I)+C(1)*C(I)+C(1)*C(I)
13100      C(1)=0.0
13200      A(C(1),S(C(1)))=C(1)*C(1)+C(1)*C(1)+C(1)*C(1)
13300      C(1)=0.0
13400      S(1)=0.0
13500      C(1)=C(1)+C(1)*C(1)
13600      S(1)=S(1)+C(1)*C(1)+C(1)*C(1)+C(1)*C(1)
13700      C(1)=0.0
13800      A(C(1),S(C(1)))=C(1)*C(1)+C(1)*C(1)+C(1)*C(1)
13900      C(1)=0.0
14000      C(1)=0.0
10      C(1)=0.0
14100      IF(C(1).GT.0.0)GOTO 14200
14200      C(1)=0.0
14300      S(1)=0.0
14400      A(C(1),S(C(1)))=C(1)*C(1)+C(1)*C(1)+C(1)*C(1)
14500      C(1)=0.0
14600      S(1)=0.0
20      C(1)=0.0
14700      A(C(1),S(C(1)))=C(1)*C(1)+C(1)*C(1)+C(1)*C(1)
14800      C(1)=0.0
14900      S(1)=0.0
25      C(1)=0.0
15000      C(1)=0.0
15100      C(1)=0.0
15200      C(1)=0.0

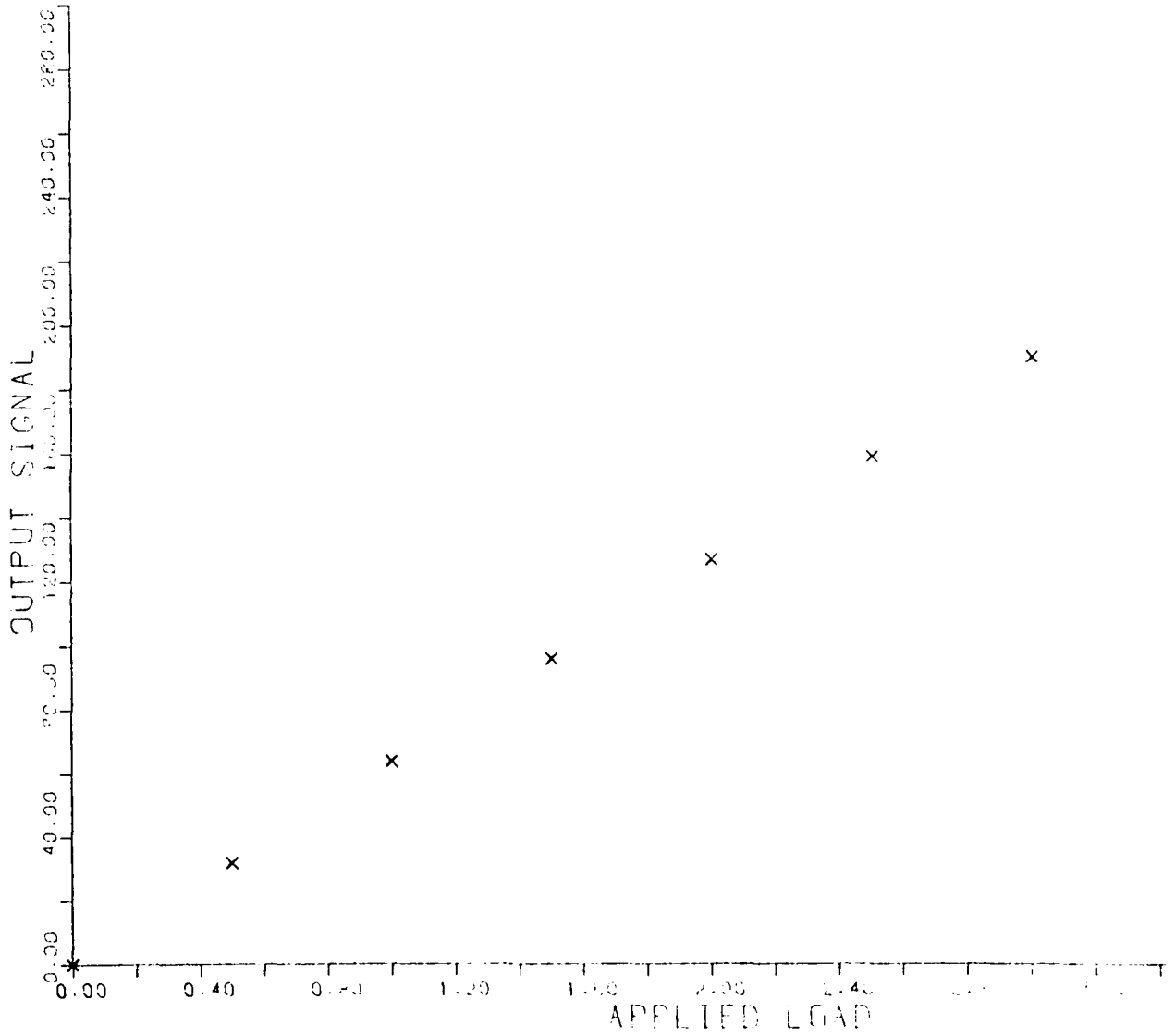
```

```

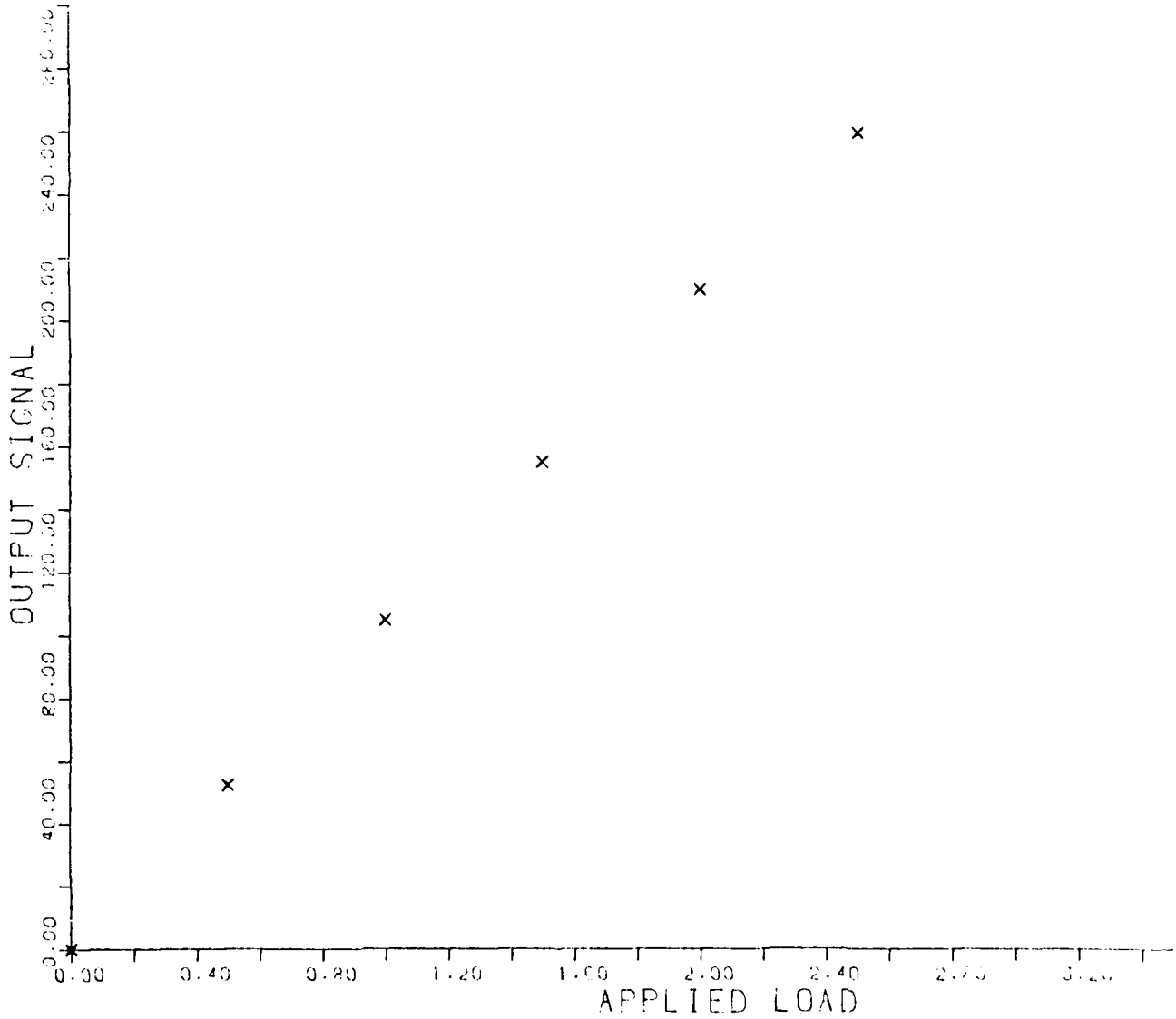
10      C
20      C
30      C           CALL SUBROUTINE TO CALCULATE THE
40      C           COEFFICIENTS OF THE CALIBRATION
50      C           EQUATION.
60      C
70      C
100     1      G1=61.7, L1=16.0, I1=AF10, A(1)=A(1), C(1)=C(1),
200     1      A(5)=5, ZC(5)=5
300     1      I1=600, I1=600
400     1      I1=600, I1=600
500     1      CALL FLSUB(0,0,7)
510     C
520     C           DATA I1, I1
530     C
600     C           NCO=25
700     C           I1=600, I1=600
800     C           I1=600, I1=600
900     C           I1=600, I1=600
1000    C           I1=600, I1=600
1100    C           I1=600, I1=600
1200    C           I1=600, I1=600
1300    C           I1=600, I1=600
1400    C           I1=600, I1=600
1500    C           I1=600, I1=600
1600    C           I1=600, I1=600
1700    C           I1=600, I1=600
1800    C           I1=600, I1=600
1900    C           I1=600, I1=600
2000    2000  I1=600, I1=600
2100    2001  I1=600, I1=600
2110    C
2120    C           DETERMINATION OF CALIBRATION CONSTANTS
2130    C
2200    C           S0X=0.0
2300    C           S0Y=0.0
2400    C           S0Z=0.0
2500    C           S0X1=0.0
2600    C           S0Y1=0.0
2700    C           I1=600, I1=600
2800    C           S0X=S0X+A(11)
2900    C           S0Y=S0Y+A(11)*A(11)
3000    C           S0Z=S0Z+A(11)*A(11)
3100    C           S0X1=S0X1+A(11)*A(11)
3200    C           S0Y1=S0Y1+A(11)*A(11)
3300    10    C           C0=1.0
3400    C           AA=(S0X1+S0Y1-S0Z)/S0X
3500    C           B=(S0X1-S0Y1+S0Z)/S0X
3600    C           C=(S0X1+S0Y1+S0Z)/S0X
3700    C           I1=600, I1=600
3800    C           C0=C0+AA*(S0X1-S0Y1+S0Z)/S0X
3900    C           C0=C0+B*(S0X1-S0Y1+S0Z)/S0X
4000    C           C0=C0+C*(S0X1-S0Y1+S0Z)/S0X
4100    C           I1=600, I1=600
4200    2004  I1=600, I1=600
4300    2005  I1=600, I1=600
4400    1      I1=600, I1=600
4405    C
4410    C           EQUATION OF CALIBRATION DATA
4420    C
4500    C           I1=600, I1=600
4600    C           CALL PR1(3.5,3.0,-3)

```

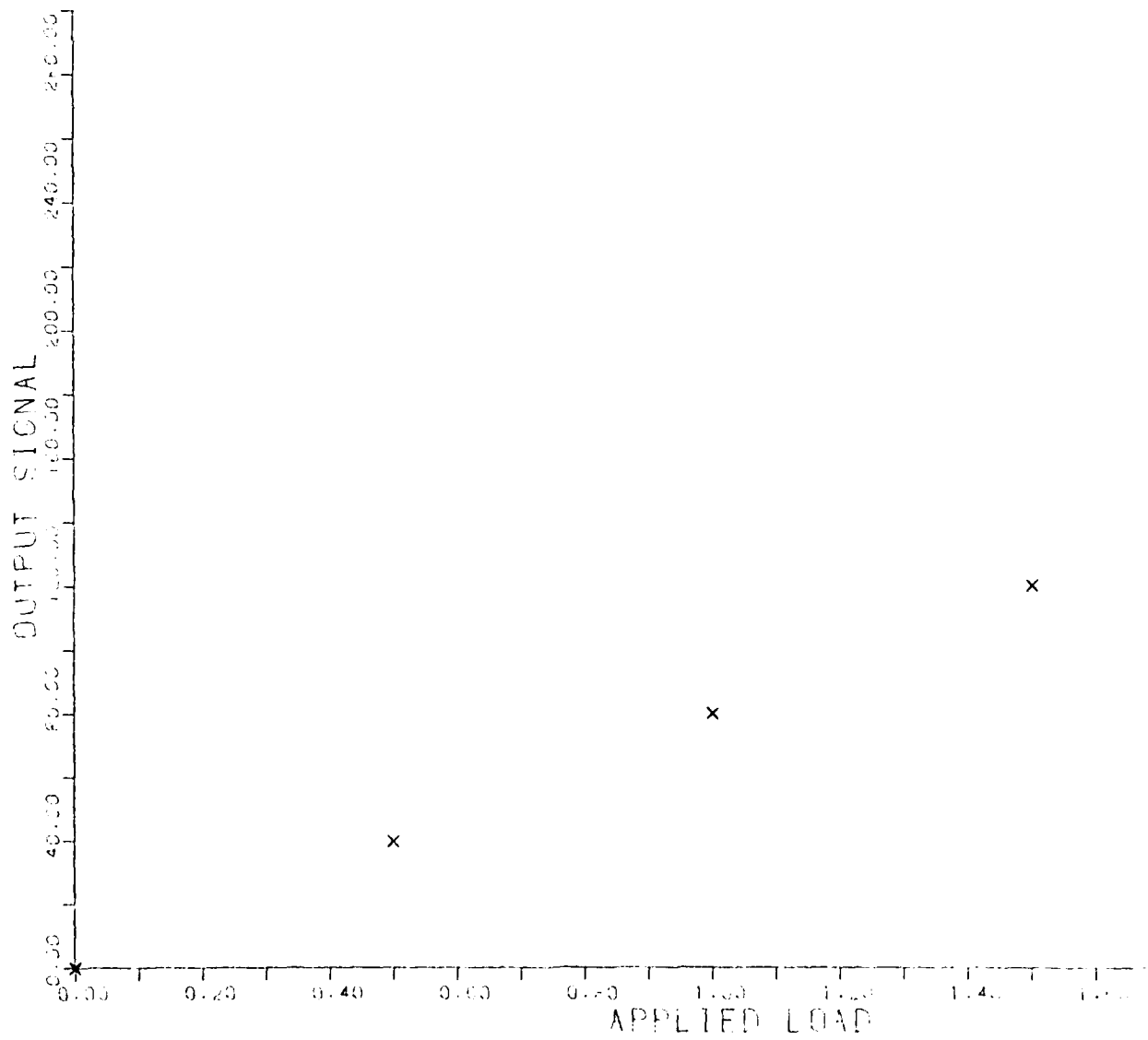
BRIDGE OUTPUT 1 VS. Z1
01-00-21



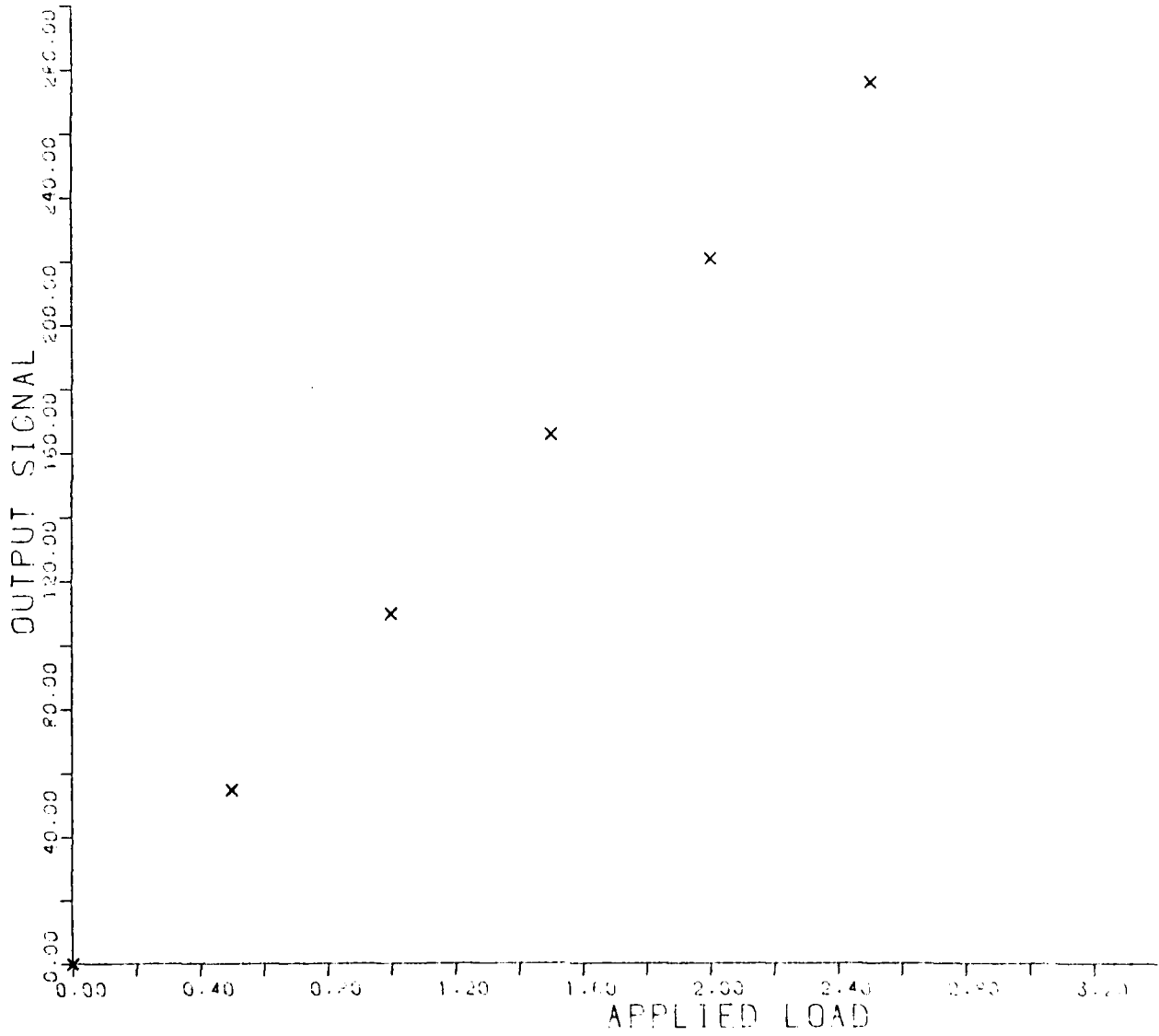
BRIDGE OUTPUT 2 VS. Z₂
01-00-81



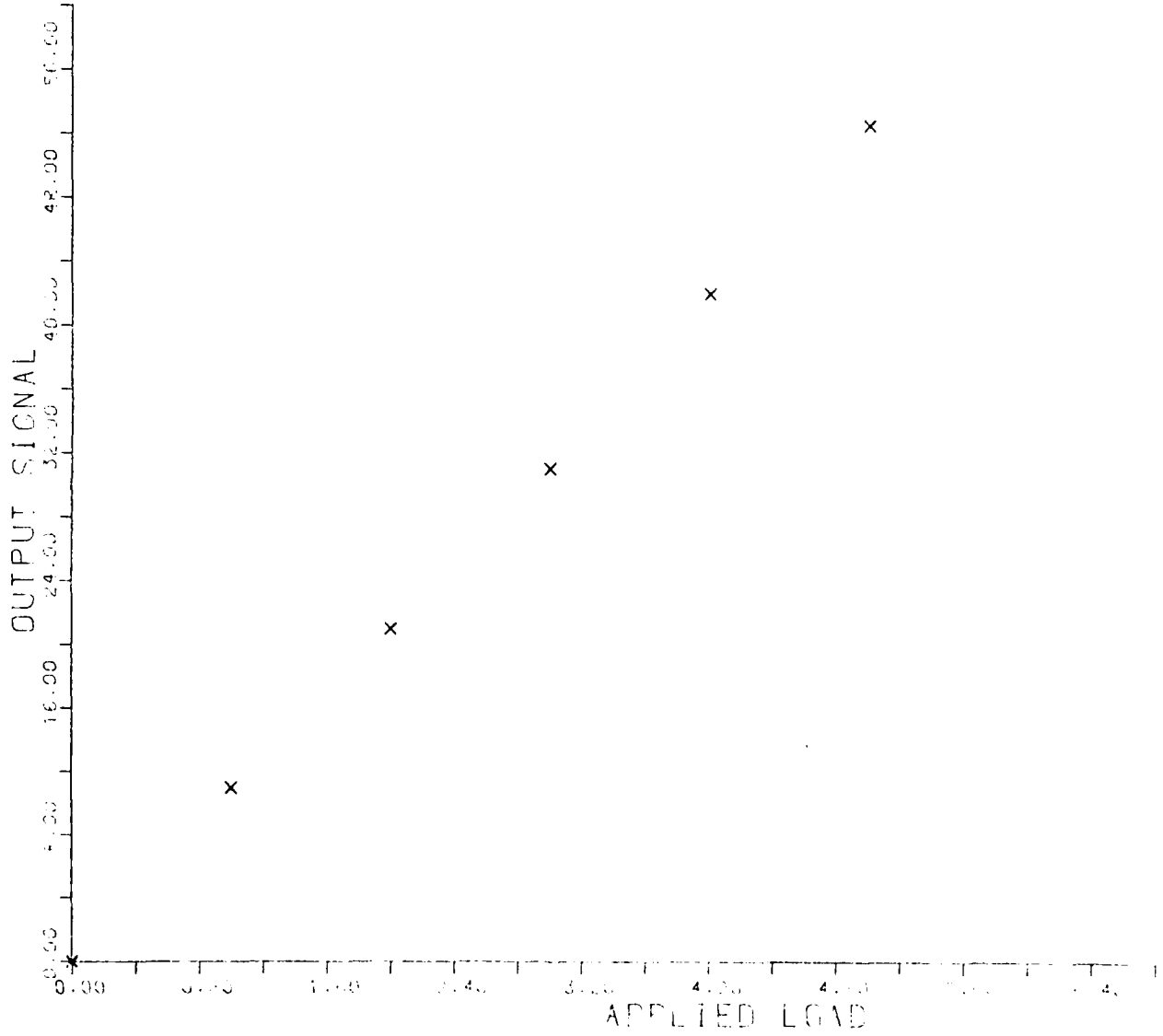
BRIDGE OUTPUT 3 VS. Y1
01-00-81



BRIDGE OUTPUT 4 VS. YZ
01-00-81



BRIDGE OUTPUT C.V. RM
01-07-61



DATE	TIME	COORDINATES	PRESSURE (mm Hg)	TEMPERATURE (°C)	WIND DIRECTION	WIND VELOCITY	SEA STATE
1952	0800	10° 00' N, 155° 00' W	1000	25	0	0	1
1952	0900	10° 00' N, 155° 00' W	1000	25	0	0	1
1952	1000	10° 00' N, 155° 00' W	1000	25	0	0	1
1952	1100	10° 00' N, 155° 00' W	1000	25	0	0	1
1952	1200	10° 00' N, 155° 00' W	1000	25	0	0	1
1952	1300	10° 00' N, 155° 00' W	1000	25	0	0	1
1952	1400	10° 00' N, 155° 00' W	1000	25	0	0	1
1952	1500	10° 00' N, 155° 00' W	1000	25	0	0	1
1952	1600	10° 00' N, 155° 00' W	1000	25	0	0	1
1952	1700	10° 00' N, 155° 00' W	1000	25	0	0	1
1952	1800	10° 00' N, 155° 00' W	1000	25	0	0	1
1952	1900	10° 00' N, 155° 00' W	1000	25	0	0	1
1952	2000	10° 00' N, 155° 00' W	1000	25	0	0	1
1952	2100	10° 00' N, 155° 00' W	1000	25	0	0	1
1952	2200	10° 00' N, 155° 00' W	1000	25	0	0	1
1952	2300	10° 00' N, 155° 00' W	1000	25	0	0	1
1952	2400	10° 00' N, 155° 00' W	1000	25	0	0	1
1952	2500	10° 00' N, 155° 00' W	1000	25	0	0	1
1952	2600	10° 00' N, 155° 00' W	1000	25	0	0	1
1952	2700	10° 00' N, 155° 00' W	1000	25	0	0	1
1952	2800	10° 00' N, 155° 00' W	1000	25	0	0	1
1952	2900	10° 00' N, 155° 00' W	1000	25	0	0	1
1952	3000	10° 00' N, 155° 00' W	1000	25	0	0	1

Analysis of Variance
 for the Effect of
 or for the Effect of

Source	SS	df	MS	F	P	MS Error
Between
Within
Total

SLA-COMPARISON OF FINDER WEIGHTS
 ELASORC-16 IS AN ACTIVE CYBERNETIC BODY
 OF 1/16" FOR THE FOLLOWING CHARACTERISTICS:

FINDER NUMBER	RUBB ORIENTATION		PRESSURE (CG/CS+D)		TENSION (CG/CS+D)		STOCK NUMBER
	CZ	CS	CZ	CS	CZ	CS	
31.000	1.04271E+01	-3.57873E+00	9.21640E-02	5.50434E-01	0.00000E+00	0.00000E+00	0.00000E+00
32.000	1.16095E+01	-3.87072E+00	5.80701E-02	7.92430E-01	0.00000E+00	0.00000E+00	0.00000E+00
33.000	1.24101E+01	-3.57220E+00	1.90018E-02	9.30417E-01	0.00000E+00	0.00000E+00	0.00000E+00
34.000	1.33003E+01	-3.56718E+00	2.25065E-02	1.26225E+00	0.00000E+00	0.00000E+00	0.00000E+00
35.000	1.43181E+01	-3.52350E+00	1.00709E-01	1.90230E+00	0.00000E+00	0.00000E+00	0.00000E+00
36.000	1.55021E+01	-4.18205E+00	9.49347E-02	4.17638E-01	0.00000E+00	0.00000E+00	0.00000E+00
37.000	1.64911E+01	-4.11193E+00	7.58402E-02	5.45013E-01	0.00000E+00	0.00000E+00	0.00000E+00
38.000	1.73318E+01	-5.23417E+00	-1.88359E-01	7.63110E-01	0.00000E+00	0.00000E+00	0.00000E+00
39.000	1.79926E+01	-6.04220E+00	1.93332E-01	2.11303E-01	0.00000E+00	0.00000E+00	0.00000E+00
40.000	1.81090E+01	-7.37550E+00	1.00162E-01	1.97030E-01	0.00000E+00	0.00000E+00	0.00000E+00
41.000	1.86223E+01	-8.94110E+00	1.27430E-02	2.27230E-01	0.00000E+00	0.00000E+00	0.00000E+00
42.000	1.93355E+01	-9.50720E+00	-4.13689E-01	2.30140E-01	0.00000E+00	0.00000E+00	0.00000E+00
43.000	2.08550E+01	-3.70625E+00	-4.13032E-01	-2.00538E-01	0.00000E+00	0.00000E+00	0.00000E+00
44.000	2.10547E+01	-9.03059E+00	-1.30248E-01	-1.16119E-01	0.00000E+00	0.00000E+00	0.00000E+00

SLA-Component of Force and Torque
 Calculated with the Assumed Conditions
 of 1/20=10 for the Following Conditions:

Angle of Force	Vertical Reaction	Horizontal Reaction	Vertical Force (F _v)	Horizontal Force (F _h)	60° Shear
4.2500E+01	0.00000E+00	1.00000E+01	4.90000E+02	3.90000E+02	8.25025E+02
1.0000E+00	0.00000E+00	1.00000E+01	1.00000E+02	1.00000E+02	1.41421E+02
51.000	-9.00179E+00	5.97713E+02	1.02630E+01	0.00000E+00	8.25025E+02
51.000	-9.20775E+00	5.40495E+02	2.76562E+01	0.00000E+00	8.32116E+02
51.000	-9.13305E+00	4.83042E+02	4.02512E+01	0.00000E+00	8.20991E+02
50.000	-9.10222E+00	5.00077E+02	7.02300E+01	0.00000E+00	8.10020E+02
51.000	-9.01063E+00	5.11752E+02	5.00000E+01	0.00000E+00	8.07530E+02
50.000	-9.05270E+00	4.99300E+02	3.10101E+01	0.00000E+00	8.00451E+02

SIX-COMPONENT FORCE BALANCE

MEASUREMENTS ON AN OBTUSE CRUISE BODY
 OF L/D=16 FOR THE FOLLOWING CONDITIONS:

ANGLE OF ATTACK	Cx	Cy	Cz	ROLL OF REFLECTION	PRESSURE (CG/C+2)	TEMPERATURE (F)	WIND VELOCITY
0.000	0.00000E+00	0.00000E+00	0.00000E+00	0.00000E+00	0.00000E+00	7.01950E+02	50.0
2.000	3.77725E-01	4.70228E-03	-4.99923E-01	1.00000E+00	0.00000E+00	2.95380E+02	50.0
5.000	3.77720E-01	4.70228E-03	-4.99923E-01	0.00000E+00	0.00000E+00	2.95380E+02	50.0
9.000	1.65931E+00	1.35000E-02	-1.22256E+00	0.00000E+00	0.00000E+00	2.95380E+02	50.0
13.000	1.65931E+00	3.20537E-02	-0.37022E-01	1.37905E-02	0.00000E+00	2.95380E+02	50.0
15.000	2.46737E+00	1.07077E-01	-1.13069E+00	-1.03433E-01	0.00000E+00	2.95380E+02	50.0
17.000	2.93941E+00	2.07397E-01	-1.04959E+00	-2.00093E-01	0.00000E+00	2.95380E+02	50.0
21.000	4.16941E+00	4.31040E-01	-1.65426E+00	-5.01120E-01	0.00000E+00	2.95380E+02	50.0
23.000	4.72116E+00	6.33019E-01	-9.7310E-01	-6.23618E-02	0.00000E+00	2.95380E+02	50.0
25.000	5.59555E+00	1.14005E-01	-4.51671E-01	2.32311E-02	0.00000E+00	2.95380E+02	50.0
27.000	6.52771E+00	7.12850E-01	-5.20666E-01	-6.00130E-02	0.00000E+00	2.95380E+02	50.0
30.000	7.60302E+00	1.00000E-01	-6.90271E-01	-1.31603E+00	0.00000E+00	2.95380E+02	50.0
35.000	1.10911E+00	6.31050E-01	-1.65926E+00	-5.01120E-01	0.00000E+00	2.95380E+02	50.0
41.000	1.70942E+00	2.74809E-02	-1.05577E+00	3.00000E-03	0.00000E+00	2.95380E+02	50.0

SIX-COMPONENT FORCE BALANCE
 MEASUREMENTS ON A POSITIVE CYCLING BODY
 OF SIZE 18 FOR THE FOLLOWING CONDITIONS:

AXIS NUMBER	ROLL ORIENTATION	PRESSURE (KG/CM ²)	TEMPERATURE (K)	SIZE (mm)
31.000	0.00000E+00	2.83000E+01	2.97900E+02	11.5
31.000	0.00000E+00	7.76200E+01	2.90050E+02	11.5
31.000	6.99566E+00			
31.000	6.27302E+00			
31.000	-1.38269E-01	-2.39907E-01	-1.93901E+02	0.00274E+00
31.000	8.81928E-02	-2.52901E-01	-1.93701E+02	0.00274E+00

APPENDIX IV - SOURCES OF ERROR

Below are listed possible error sources for this project and values of their approximate magnitude.

- (1) Tunnel blockage : $\leq .15\%$
- (2) Error in angle of attack : $\leq \pm .5^\circ$
- (3) Mach number : $\leq \pm 3-4\%$
- (4) Wind tunnel interference : Negligible
- (5) Support interference : Small
- (6) Repeatability of data : Excellent
- (7) Error in force measurements due to the zero drift : $\leq 3-4\%$
- (8) Hysteresis : Negligible

PRECEDING PAGE BLANK-NOT FILMED

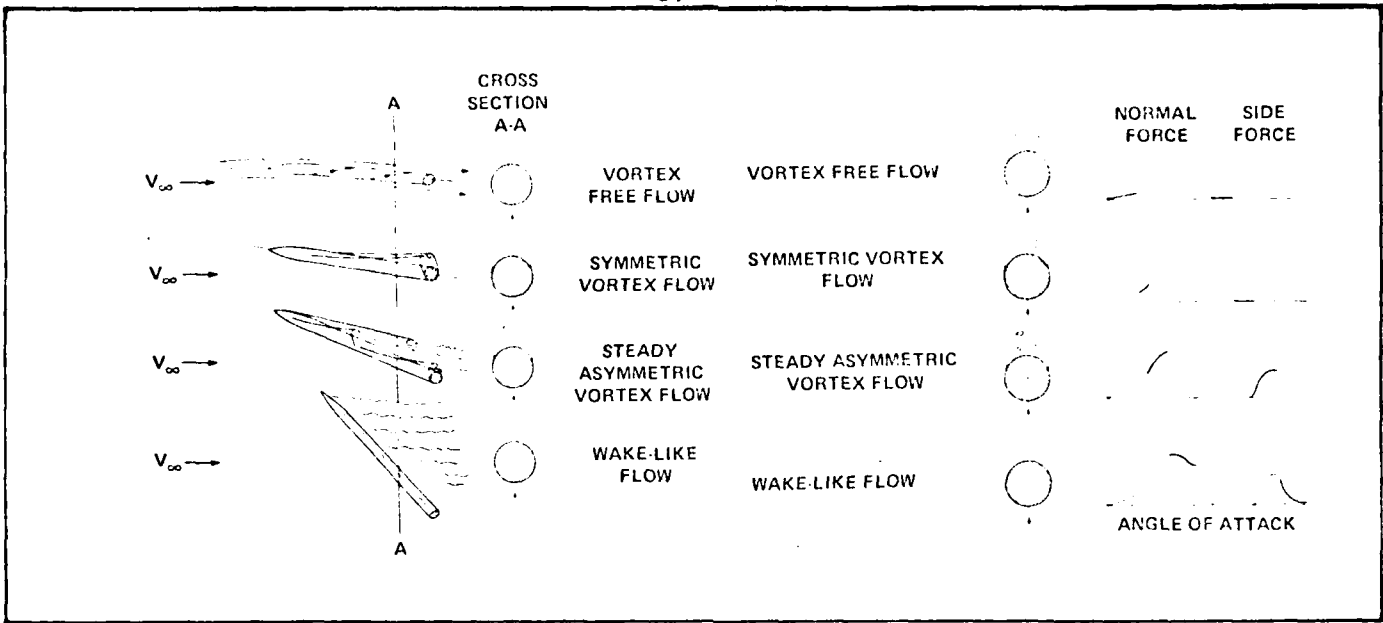


FIG 1 - FLOW TYPES FOR INCREASING ANGLE OF ATTACK ON AN OGIVE CYLINDER (Ref. 22).

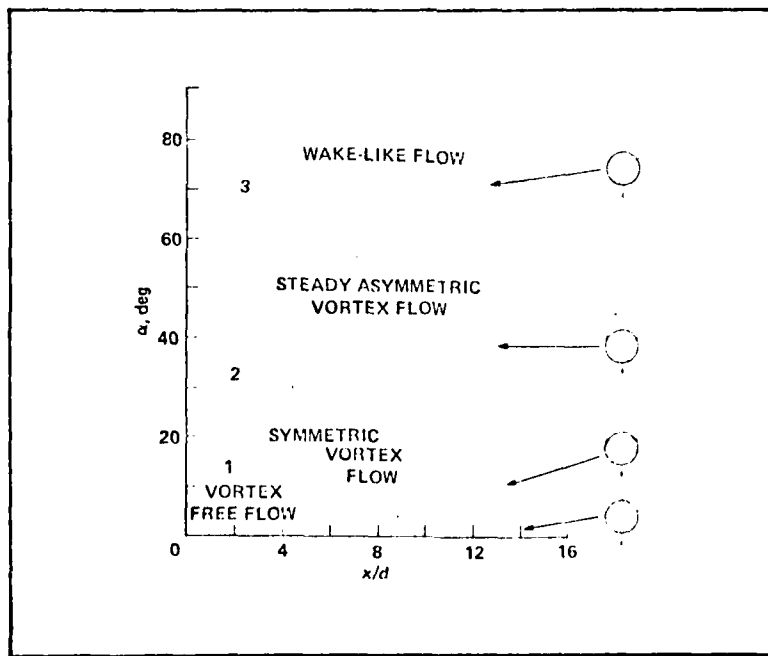


FIG. 2 - AERODYNAMIC FLOW AND ONSET BOUNDARIES FOR OGIVE CYLINDER (Ref. 22).

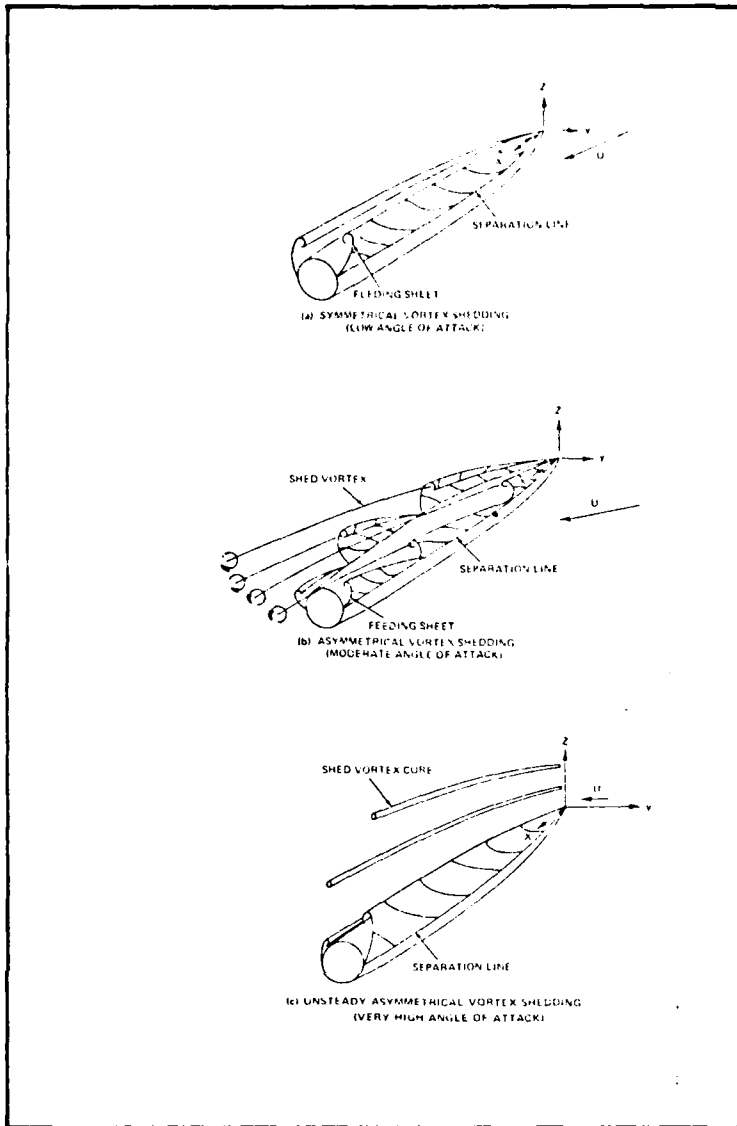
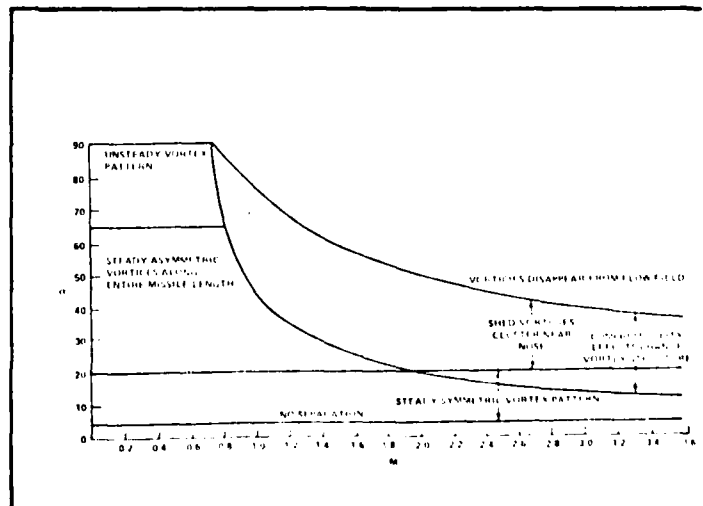


FIG. 3 - LEEWARD VORTEX STRUCTURE IN SUBSONIC FLOW (Ref. 4).

FIG. 4 - LEEWARD FLOW REGIMES ON A CIRCULAR BODY, TOTAL LENGTH ~ 10 . (Ref. 4).



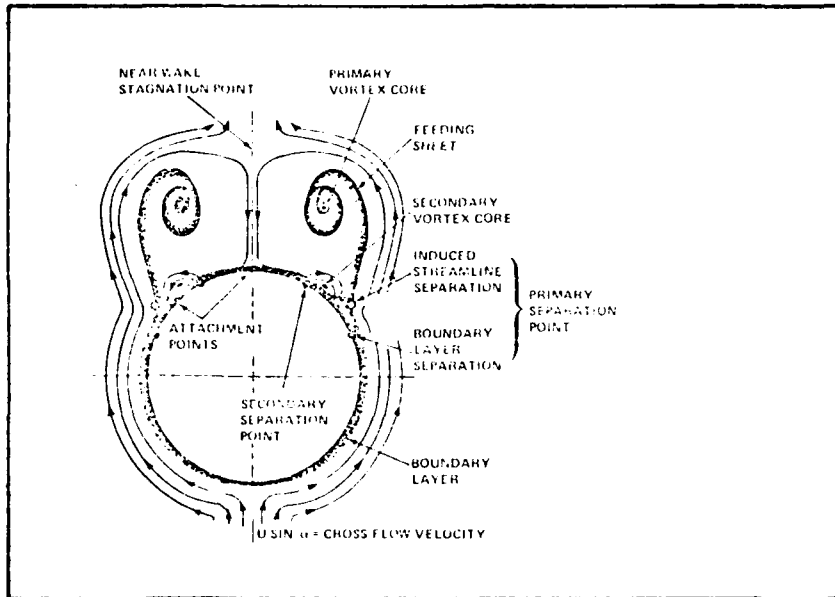


FIG. 5 - SYMMETRIC FLOW FIELD VIEWED FROM THE CROSSFLOW PLANE (Ref. 4).

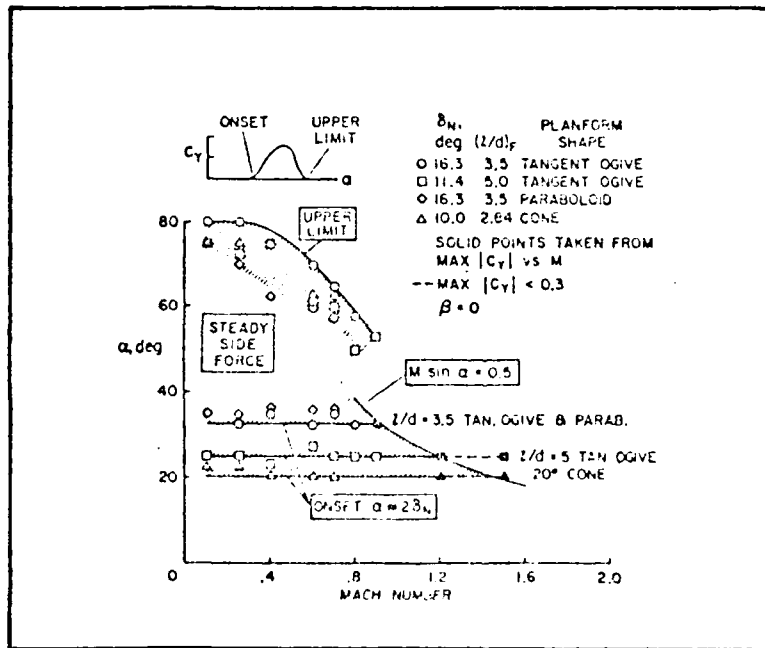


FIG. 6 - MACH NUMBER EFFECT ON α_{AV} (Ref. 7).

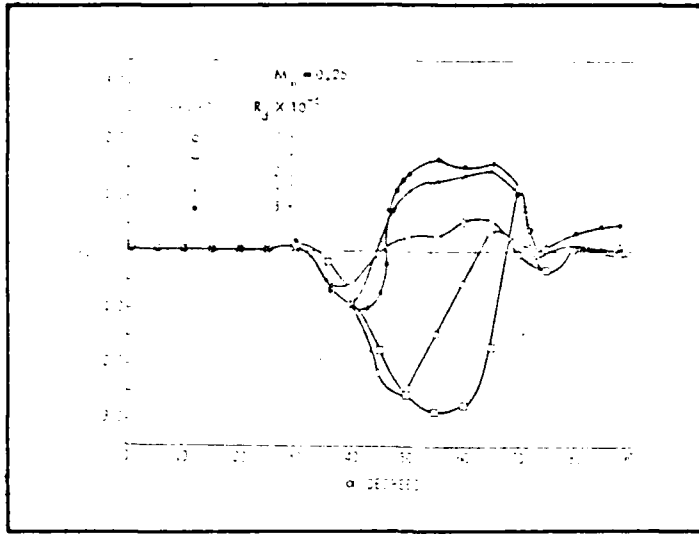


FIG. 7 - EFFECT OF Re_d and α_{AV} (Ref. 2).

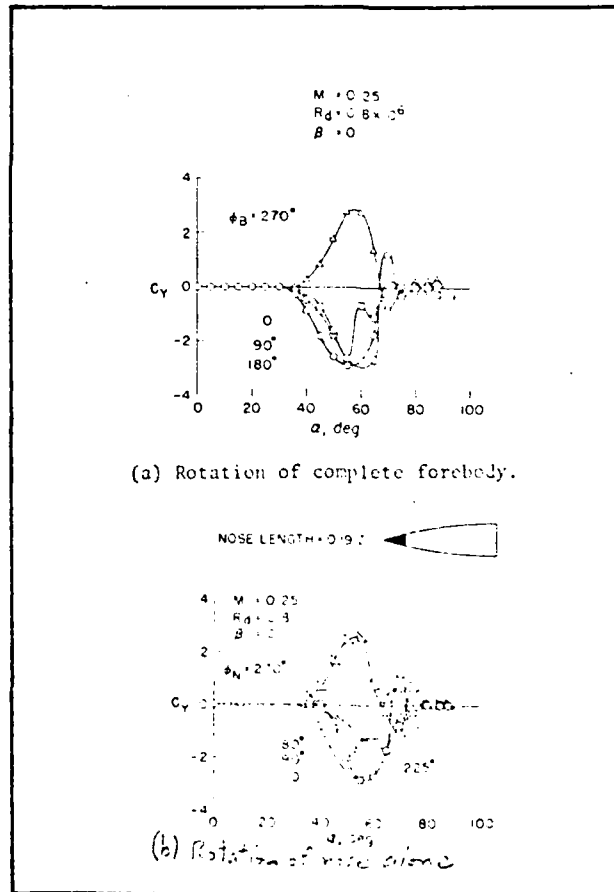


FIG. 8 - EFFECT OF ROLL ORIENTATION ON α_{AV} (Ref. 6).

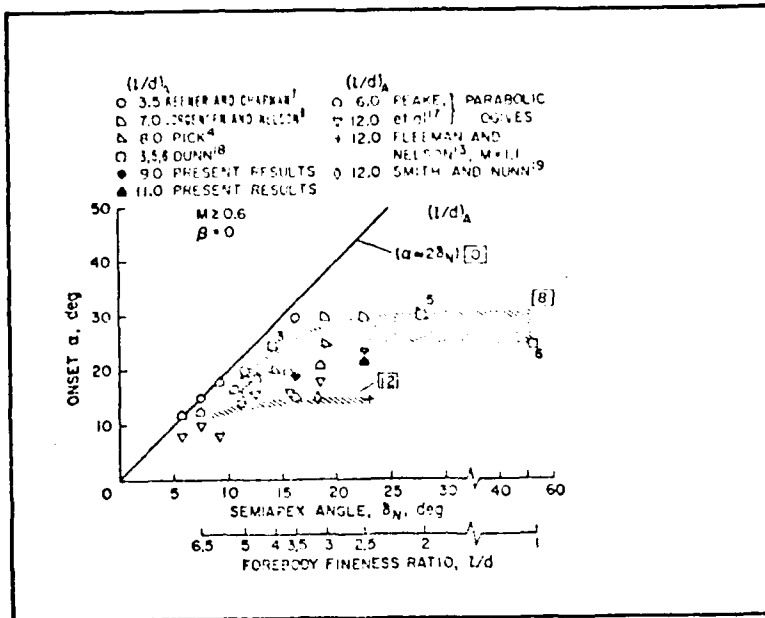


FIG. 9 - EFFECT OF NOSE FINENESS RATIO AND BODY LENGTH ON α_{AV} (Ref. 7).

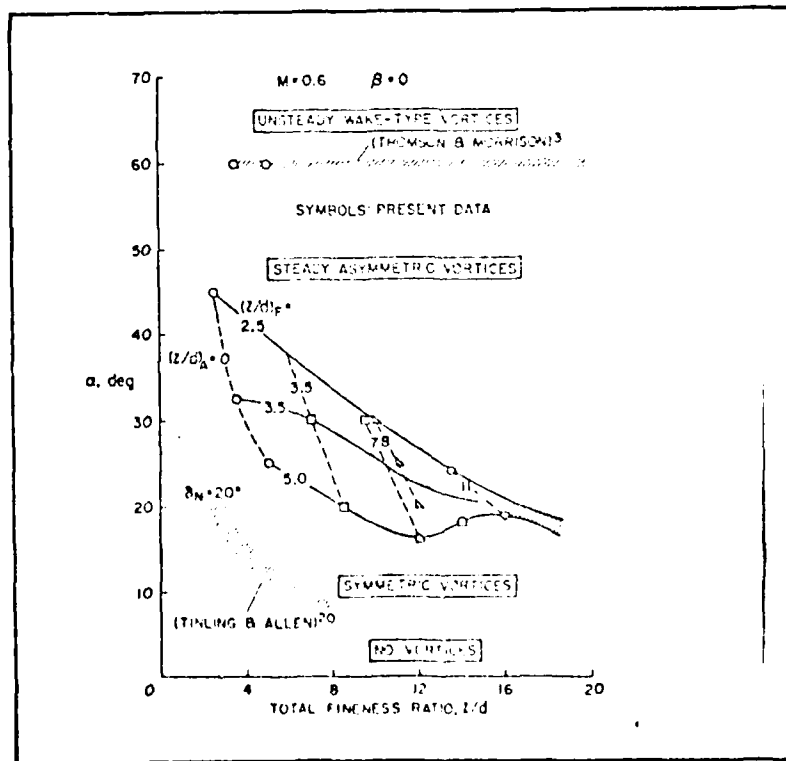


FIG. 10 - EFFECT OF TOTAL LENGTH ON α_{AV} (Ref. 7).

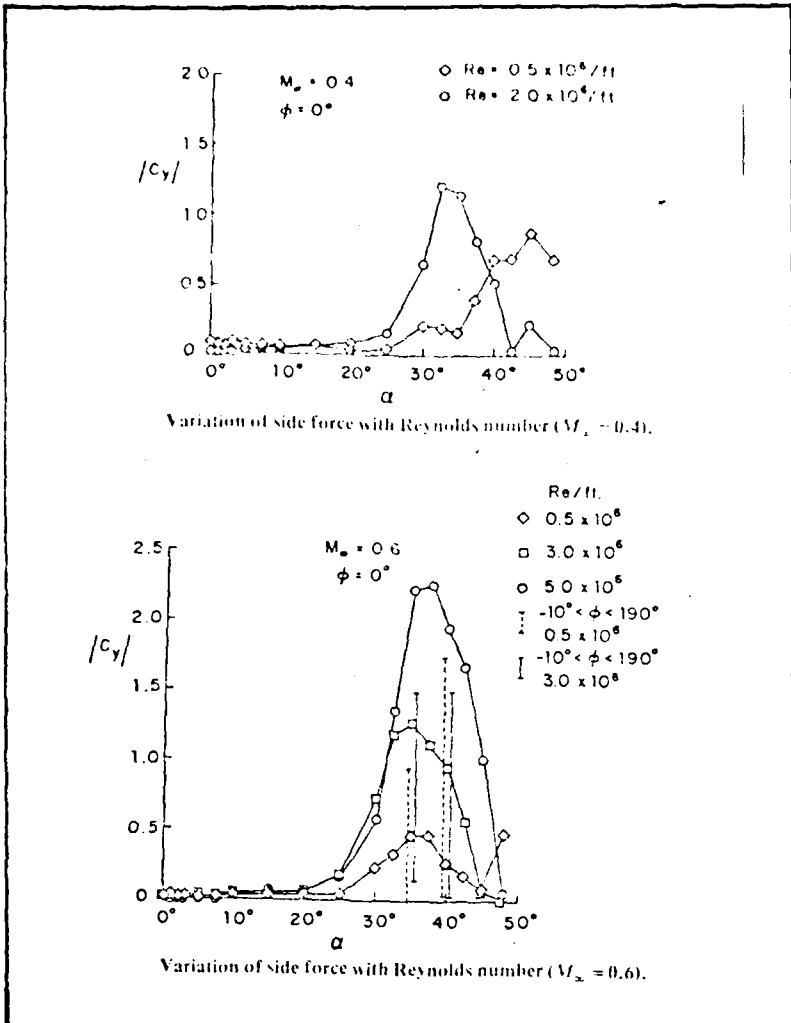
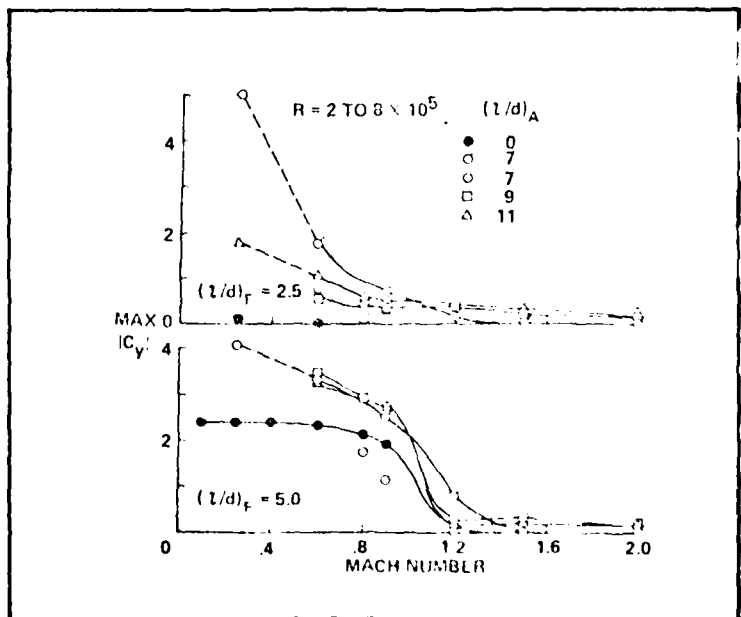


FIG. 11 - VARIATION OF SIDE FORCE WITH REYNOLDS NUMBER (Ref. 24).

FIG. 12 - EFFECT OF MACH NUMBER ON $|C_{y_{max}}|$ FOR OGIVE CYLINDERS (Ref. 22).



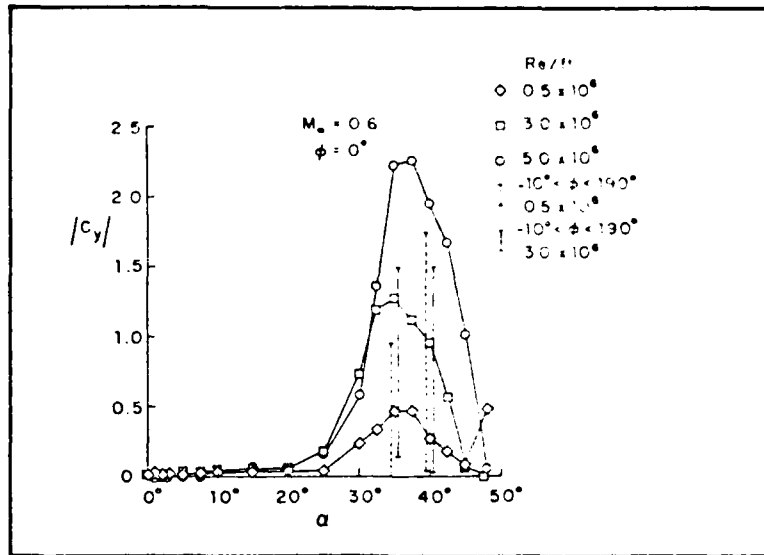


FIG. 13 - EFFECT OF Re_d on $|C_{y_{max}}|$ (Ref. 24).

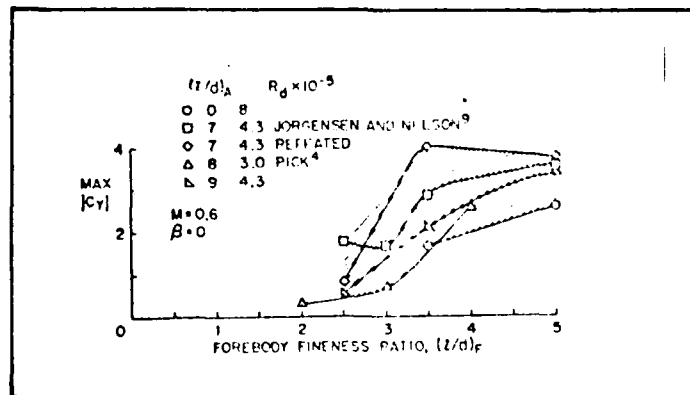


FIG. 14 - EFFECT OF FOREBODY FINENESS RATIO ON $|C_{y_{max}}|$ (Ref. 7).

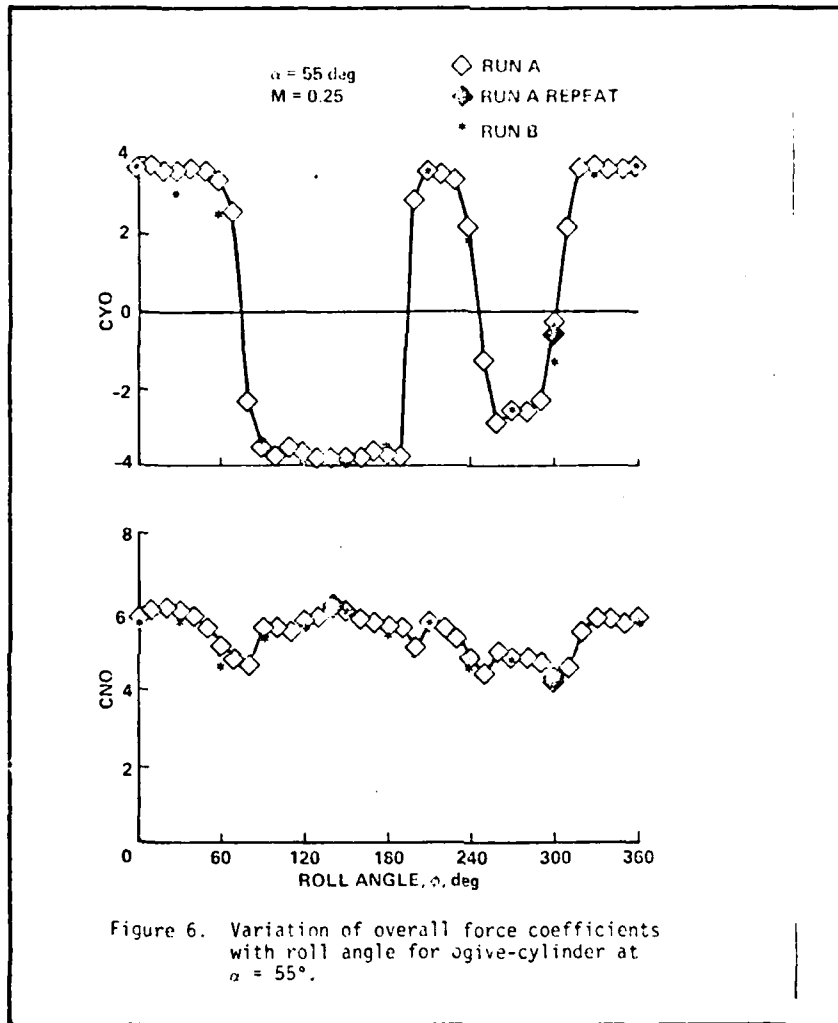


FIG. 15 - EFFECT OF ROLL ORIENTATION
ON C_y AND C_N (Ref. 22).

4 trous. M3 à 90°

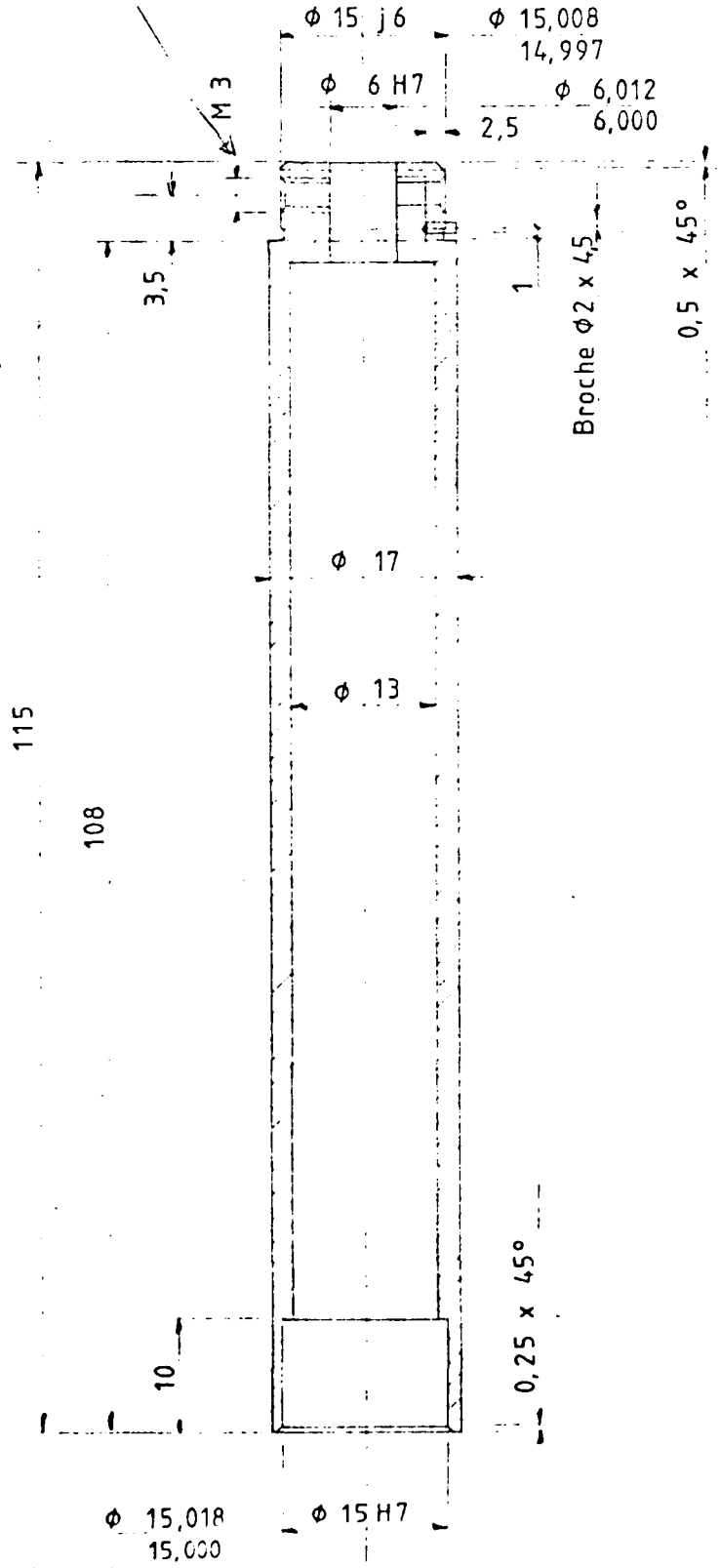
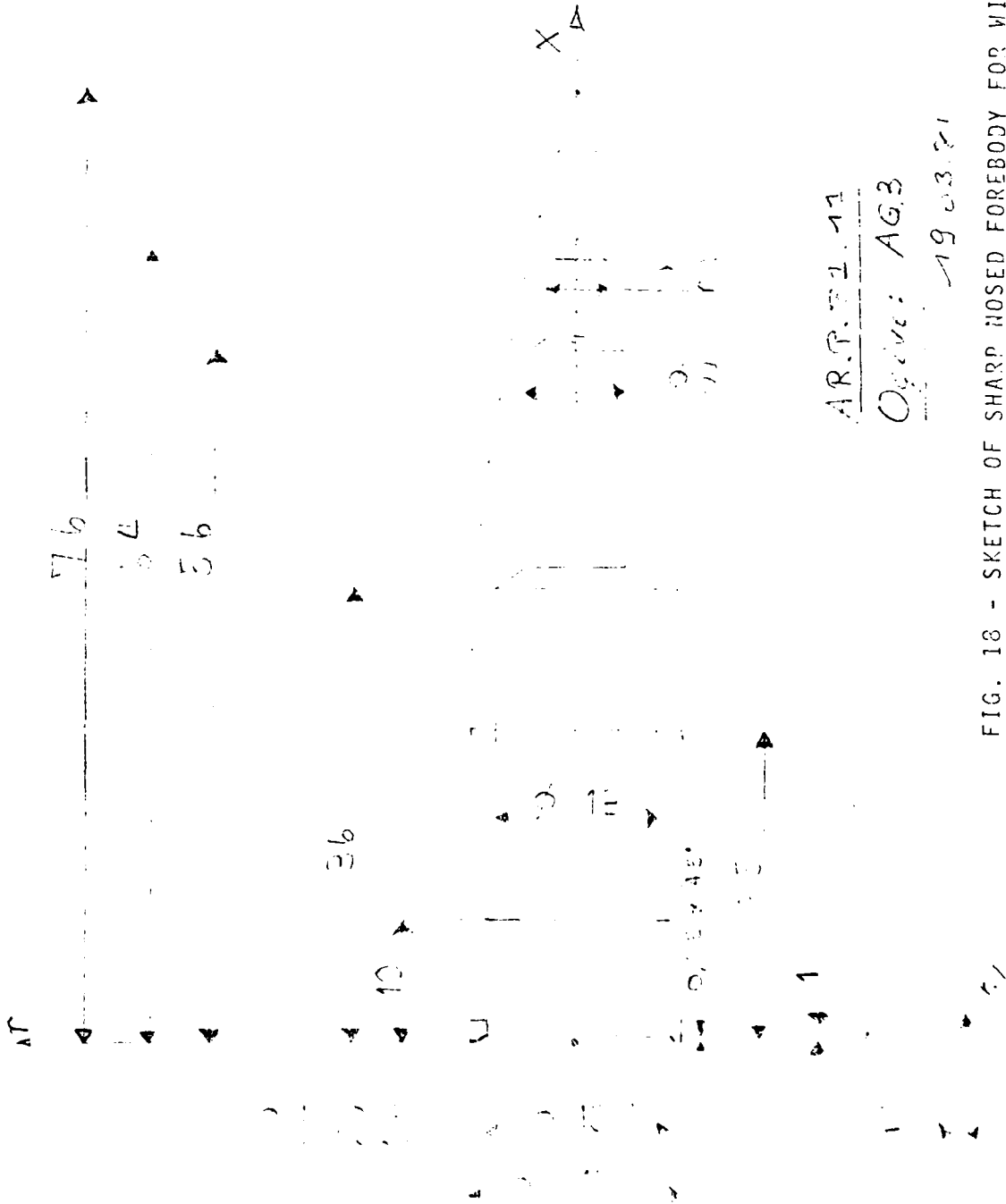


FIG. 17 - SKETCH OF MIDDLE SECTION OF WIND TUNNEL MODEL.

100



X	65 75 77 78 79 80 81 82 83 84 85 86 87 88 89 90 91 92 93 94 95 96 97 98 99 100
R	101 102 103 104 105 106 107 108 109 110 111 112 113 114 115 116 117 118 119 120 121 122 123 124 125 126 127 128 129 130 131 132 133 134 135 136 137 138 139 140 141 142 143 144 145 146 147 148 149 150

AR.P. 71.11

Opener: AG3

19 03 21

FIG. 18 - SKETCH OF SHARP NOSED FOREBODY FOR WIND TUNNEL.

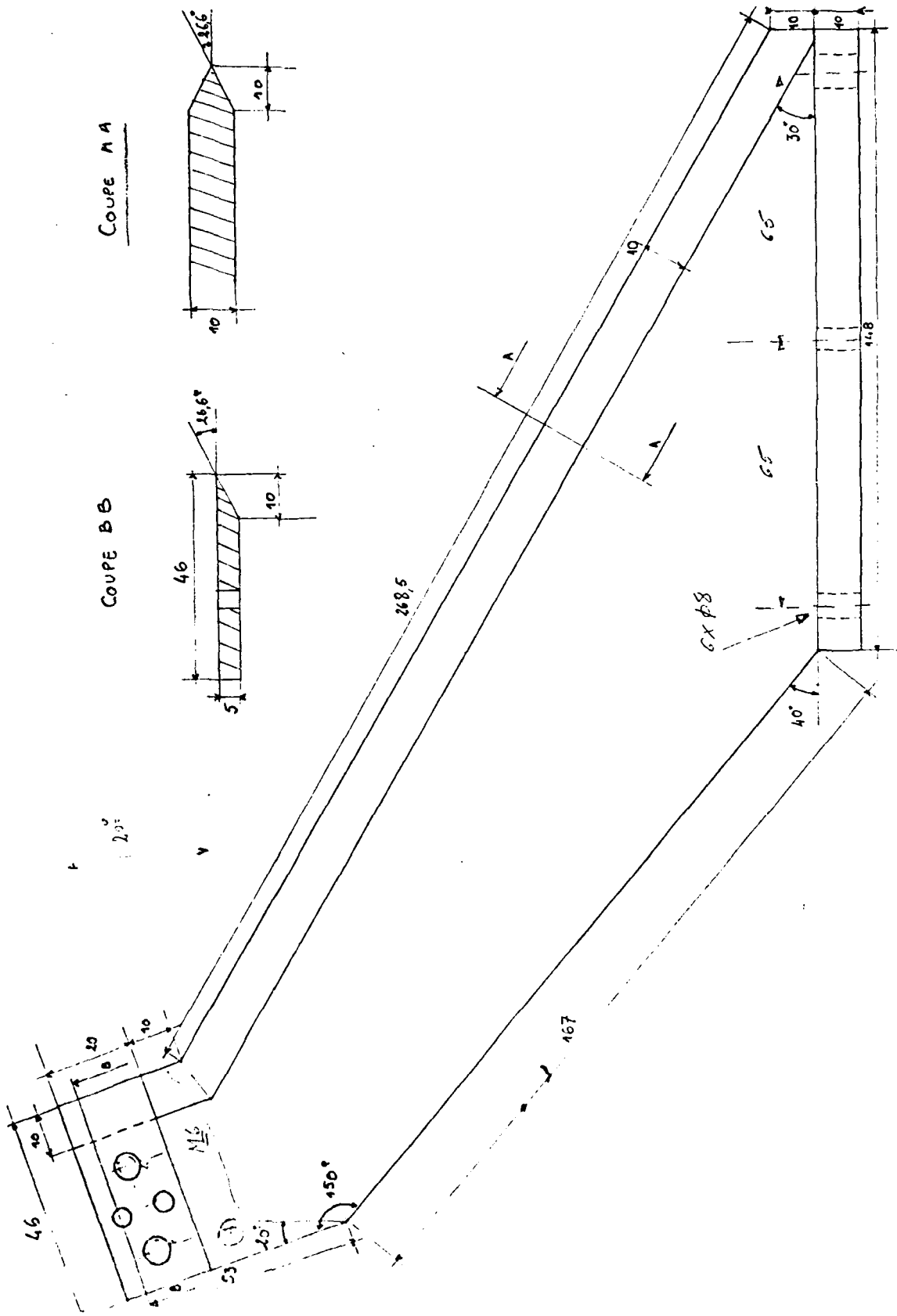


FIG. 20 - SKETCH OF LOW ANGLE OF ATTACK SUPPORT : $-5^\circ \leq \alpha \leq 30^\circ$.

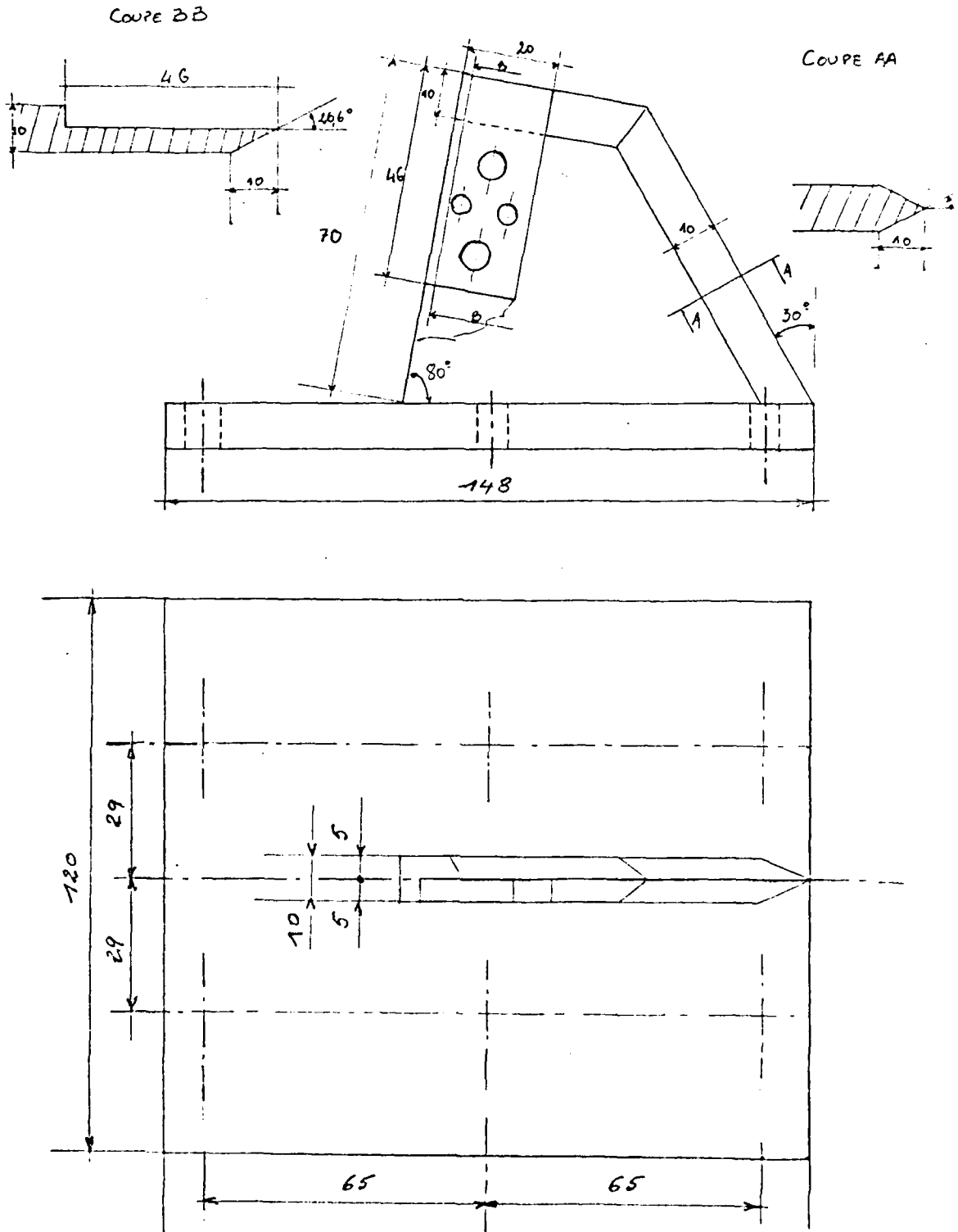


FIG. 22 - SKETCH OF HIGH ANGLE OF ATTACK SUPPORT : $55^\circ \leq \alpha \leq 90^\circ$.

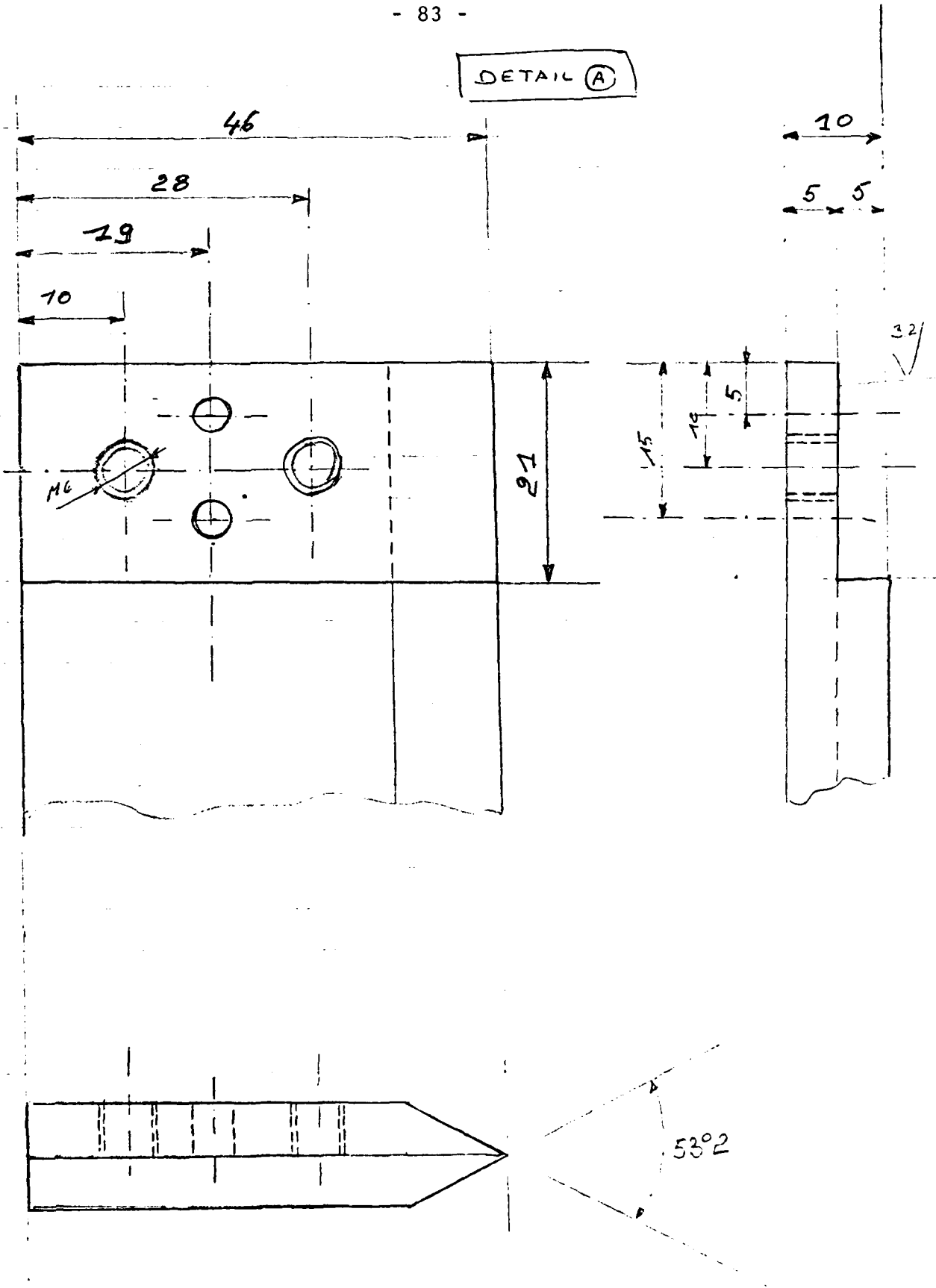


FIG. 24 - DETAIL FOR STING ATTACHMENT COMPONENT.

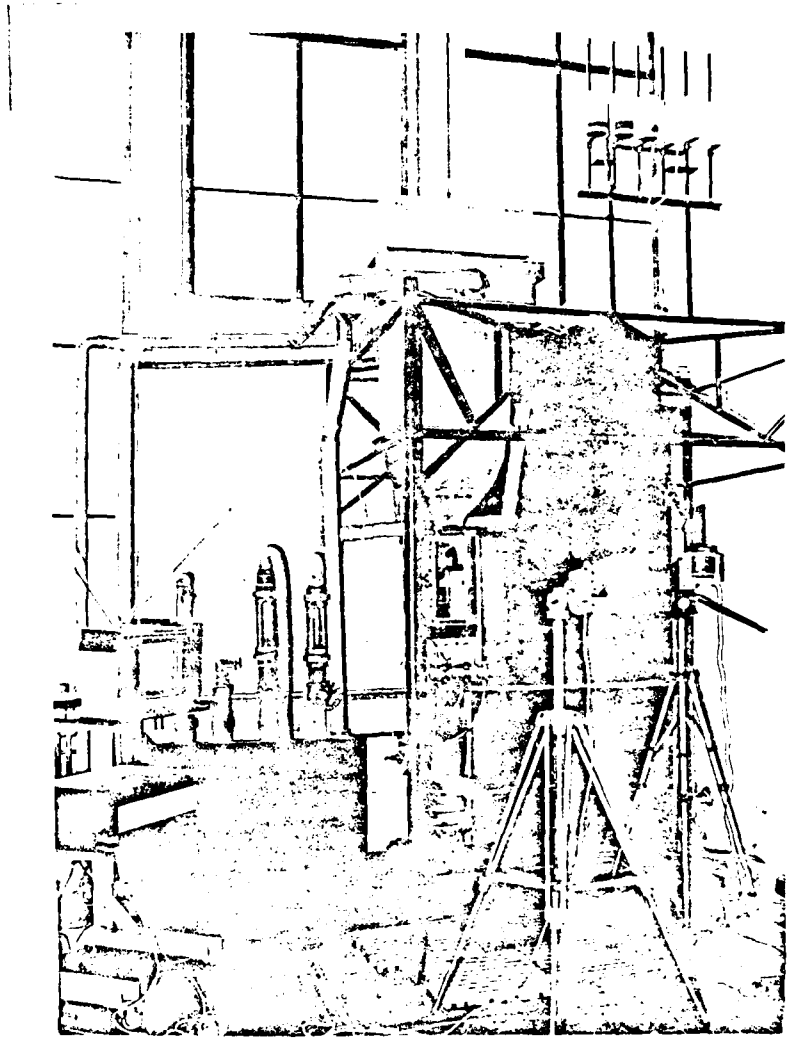


FIG. 26 - A PICTURE OF THE WATER TUNNEL FACILITY

X 0 5 10 15 20 23.872 24 25 26 26.044
 R 5.5 5.37 5 4.36 3.418 2.617 2.638 2.157 0.411 0

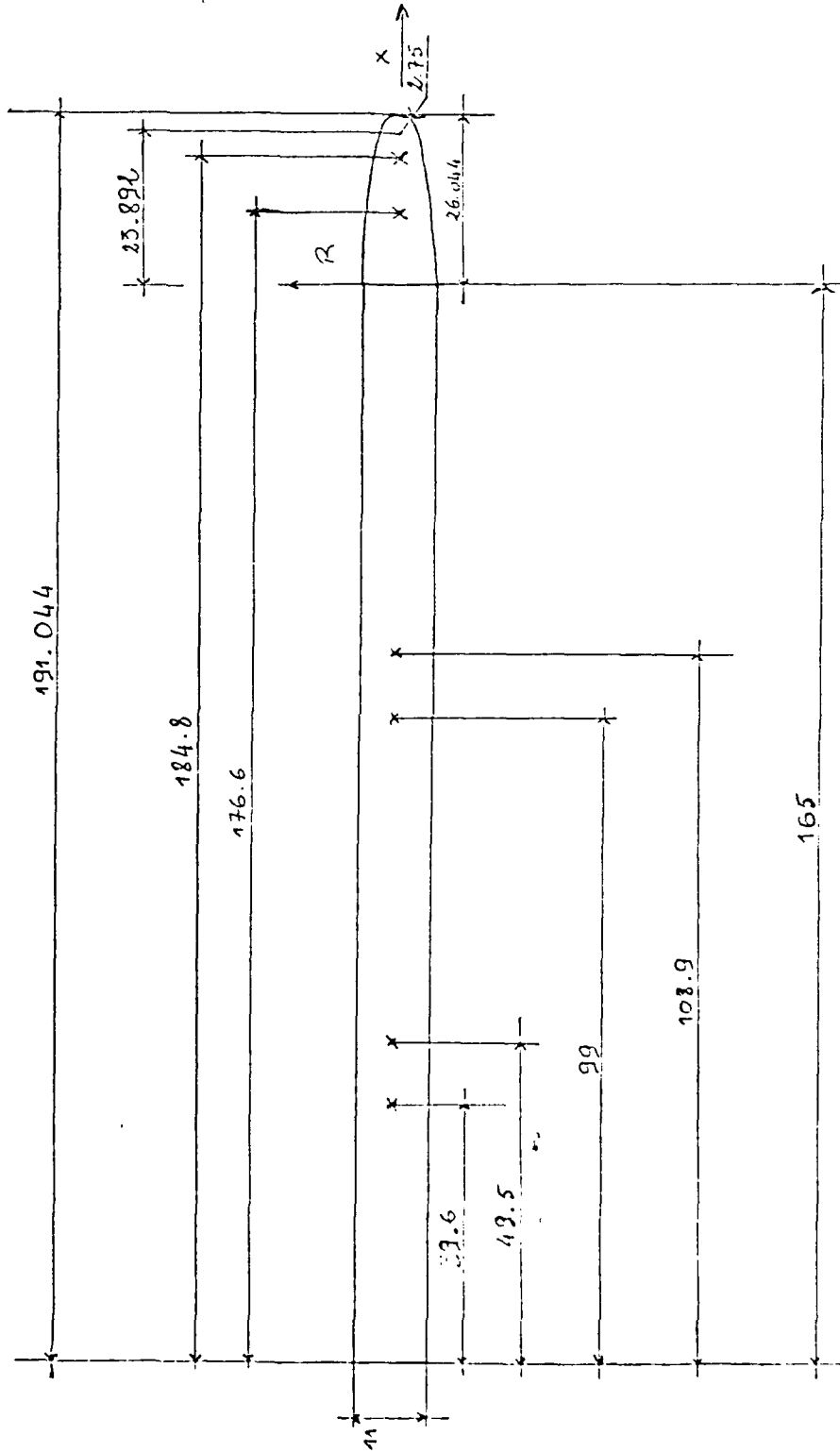


FIG. 22 - A SKETCH OF THE BLUNT NOSED OGIVE CYLINDER WATER TUNNEL MODEL.

$(r/d)_{TOT} = 17.4, d = 11 \text{ mm.}$

X 0 4 8 12 16 20 24
R 4 3.89 3.56 3 2.22 1.22 0

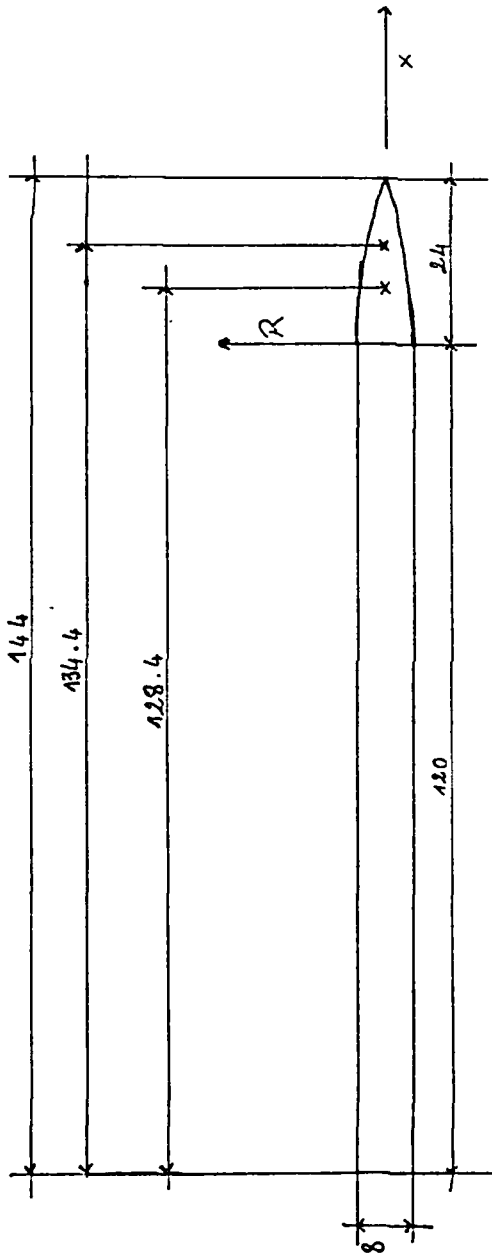


FIG. 29 - A SKETCH OF THE SMALL SHARP NOSED OGIVE CYLINDER WATER TUNNEL MODEL, $(x/d)_{TOT} = 18$, $d = 8$ mm.

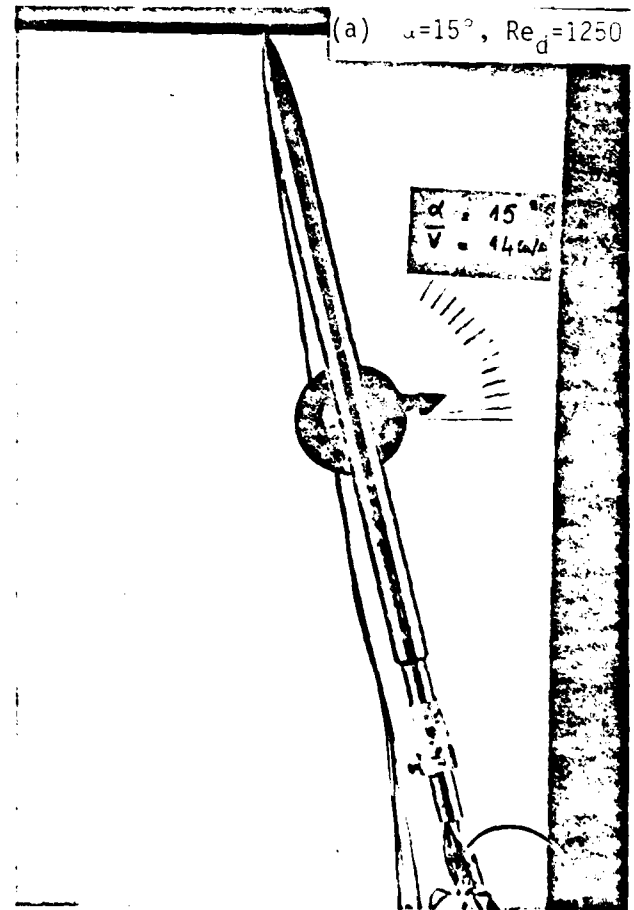
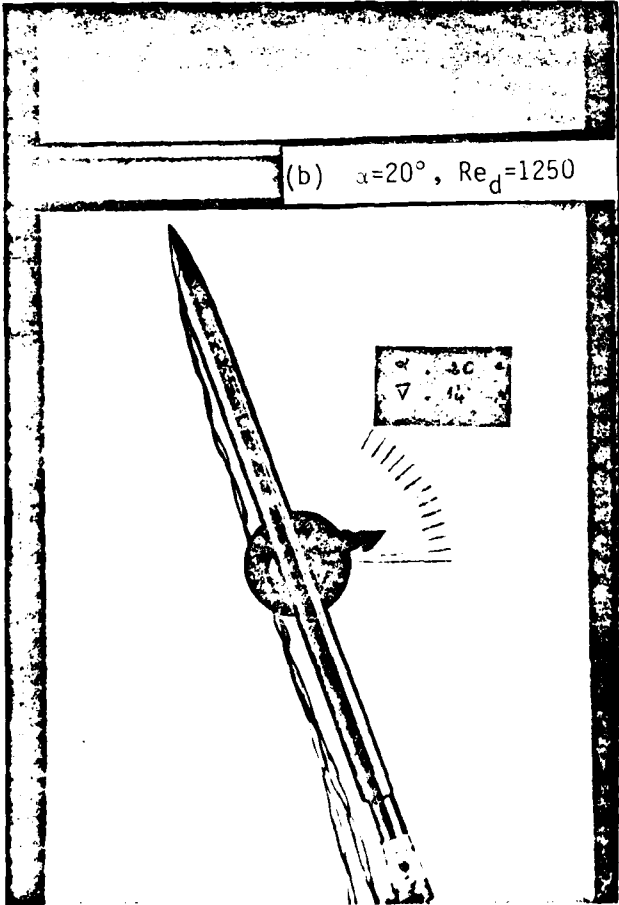
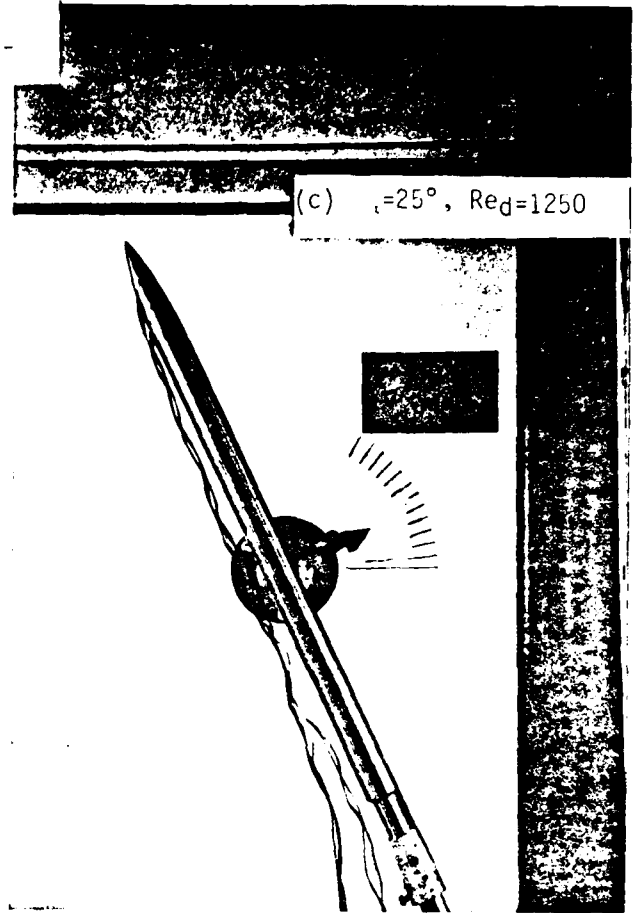
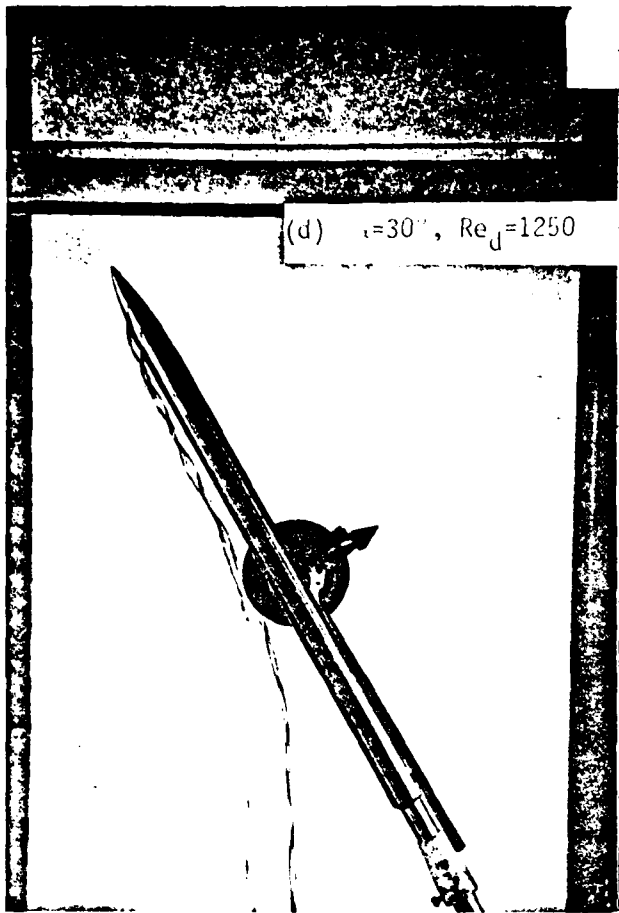
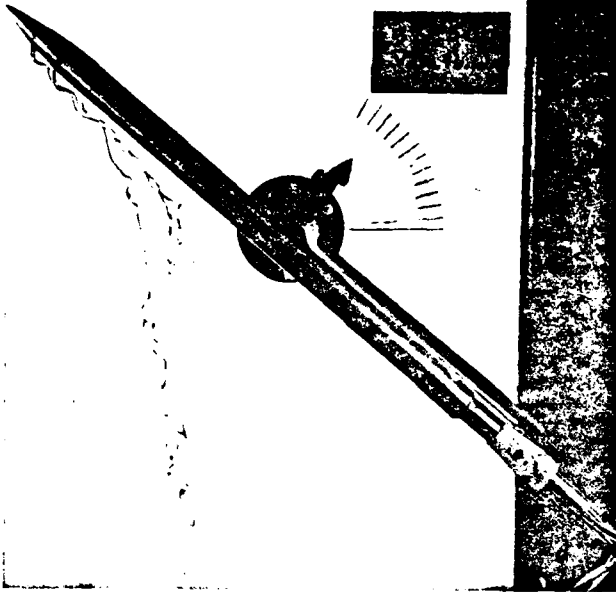
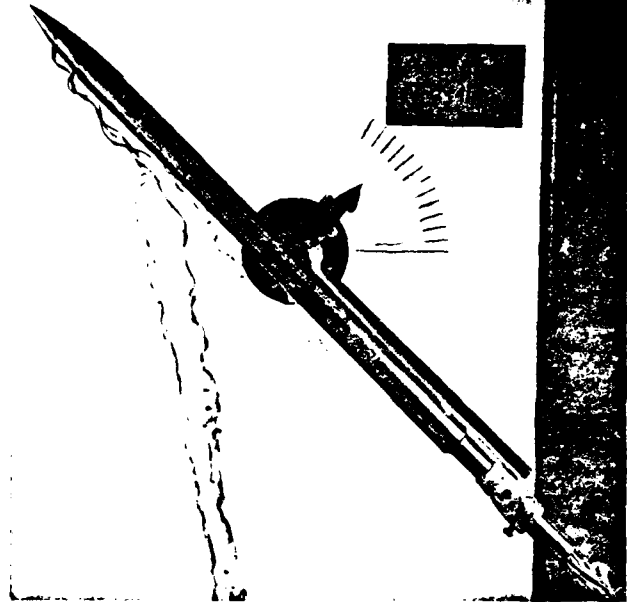


FIG. 30 - FLOW VISUALIZATION OVER A SHARP NOSED BODY FOR $\alpha=15^\circ, 20^\circ, 25^\circ, 30^\circ$

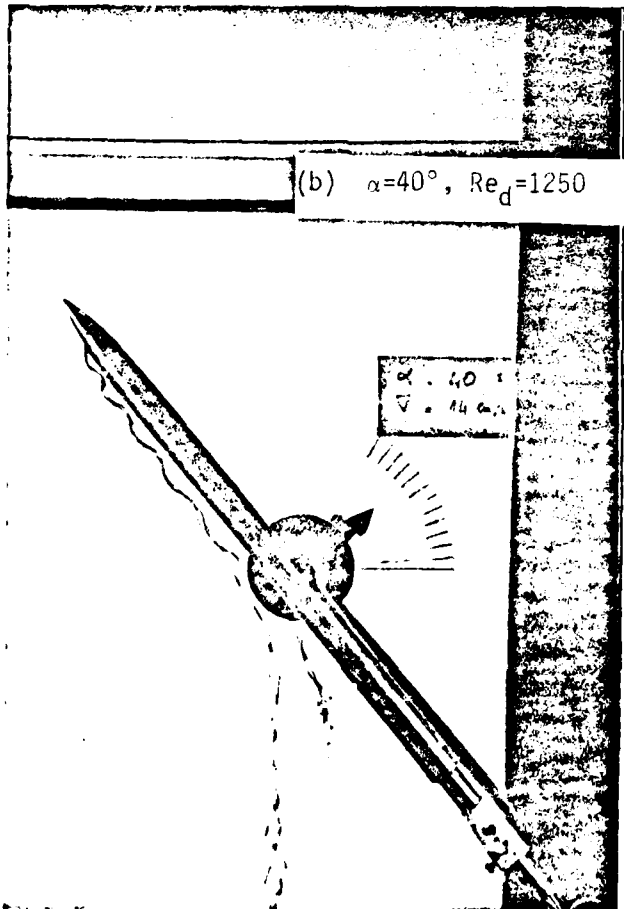
(d) $\alpha=50^\circ$, $Re_d=1250$



(c) $\alpha=45^\circ$, $Re_d=1250$



(b) $\alpha=40^\circ$, $Re_d=1250$



(a) $\alpha=35^\circ$, $Re_d=1250$

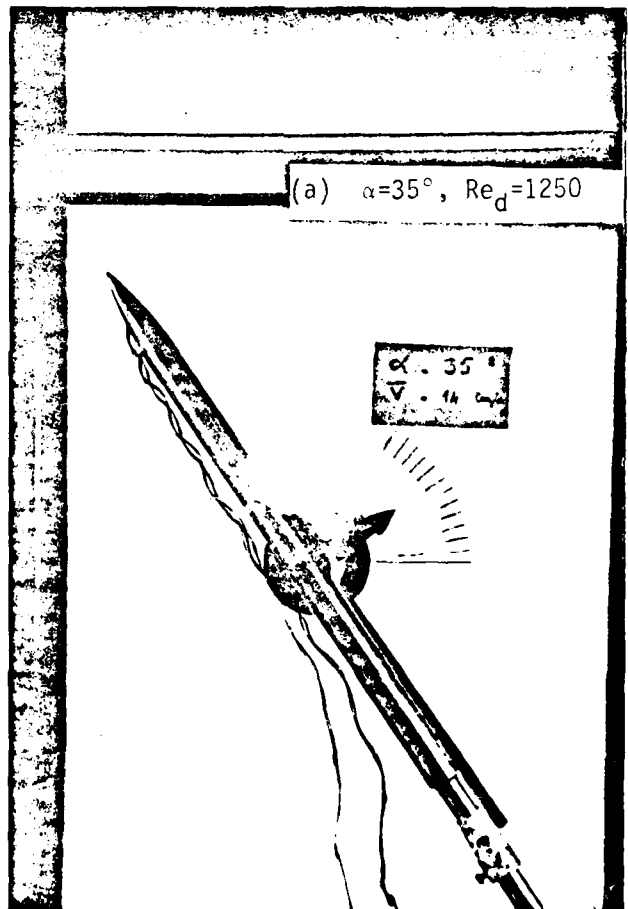


FIG. 31 - FLOW VISUALIZATION OVER A SHARP NOSED BODY FOR $\alpha=35^\circ, 40^\circ, 45^\circ, 50^\circ$

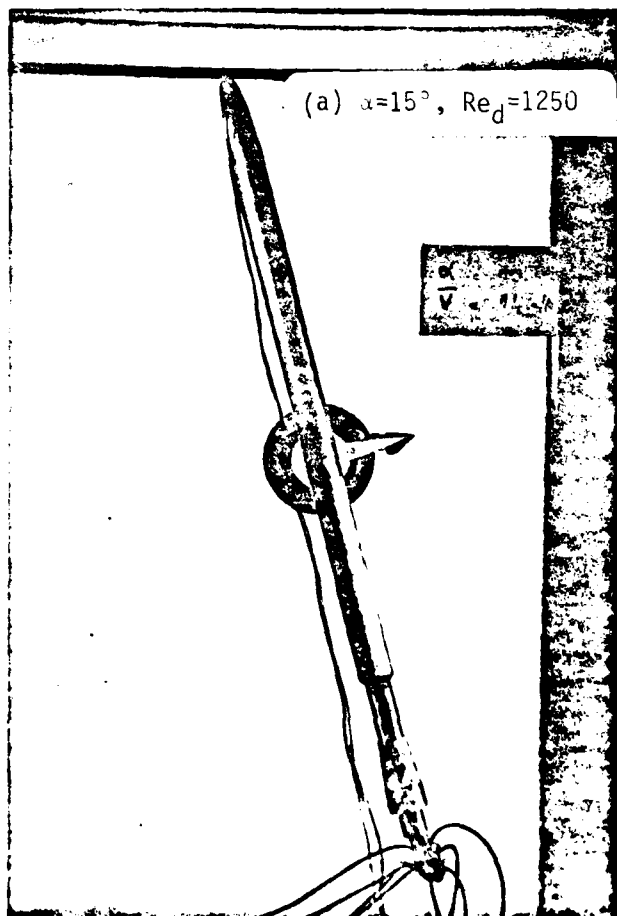
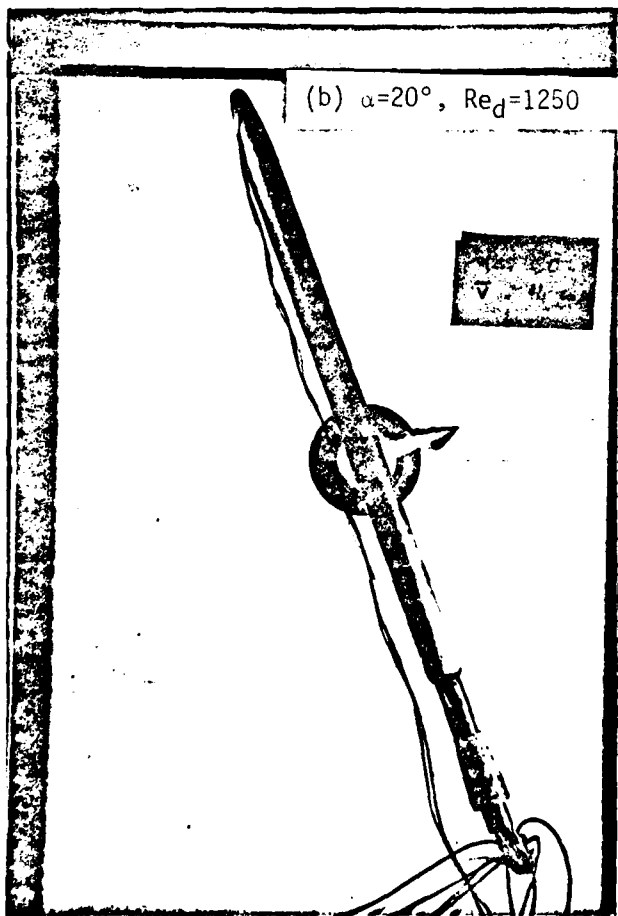
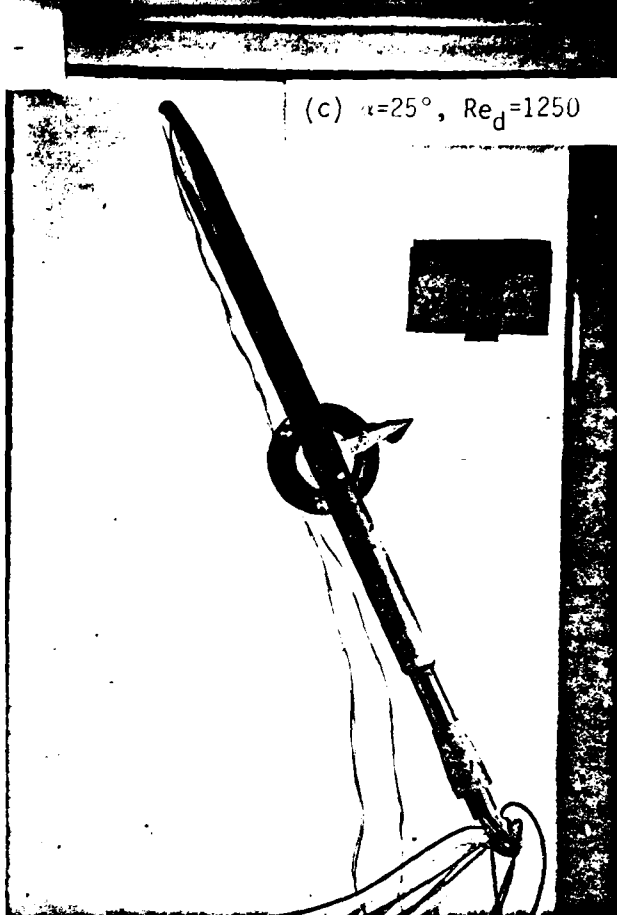
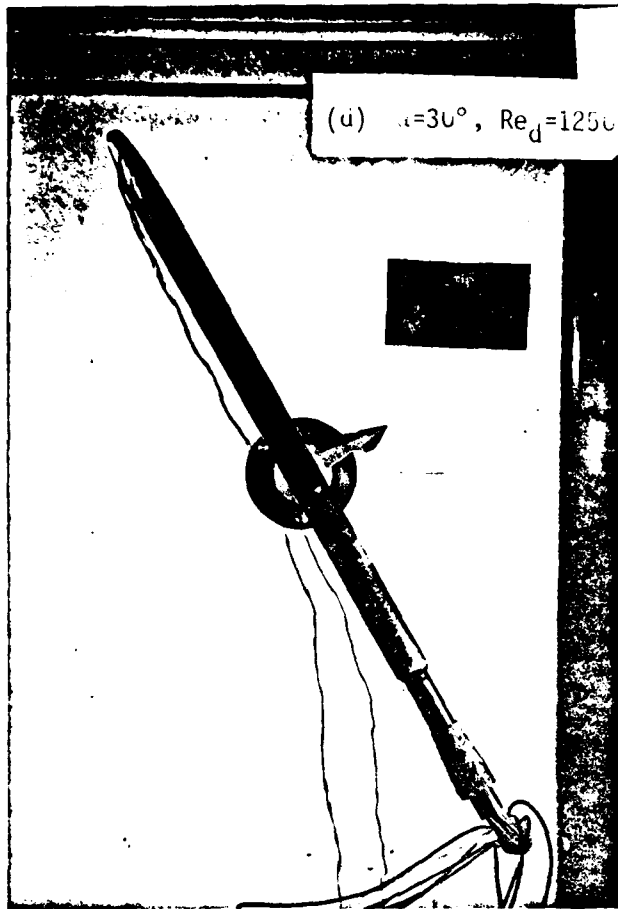
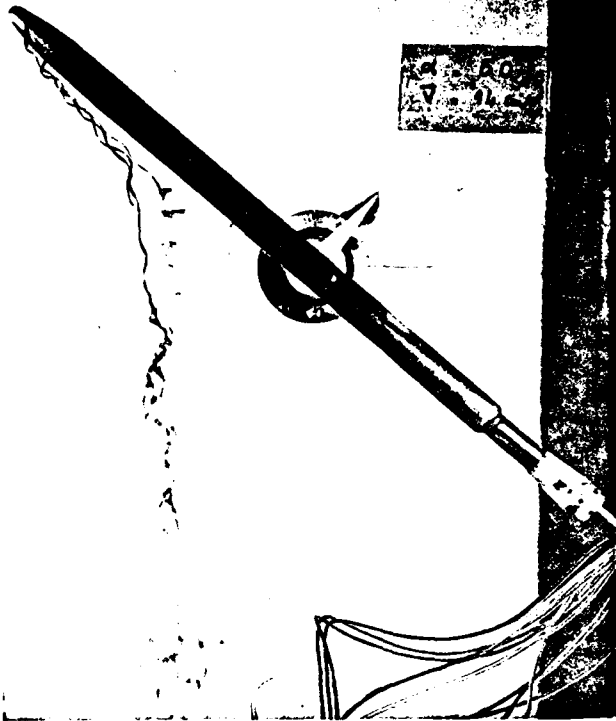
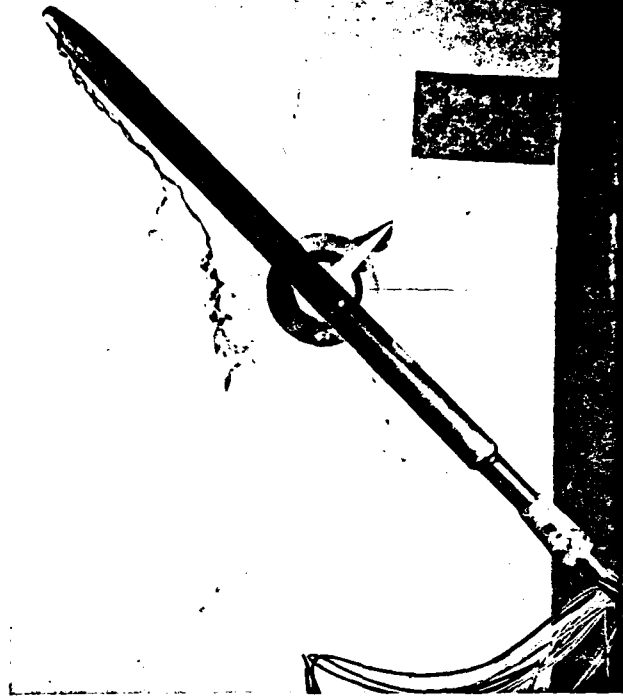


FIG. 32 - FLOW VISUALIZATION OVER A BLUNT NOSED BODY FOR $\alpha=15^\circ, 20^\circ, 25^\circ, 30^\circ$

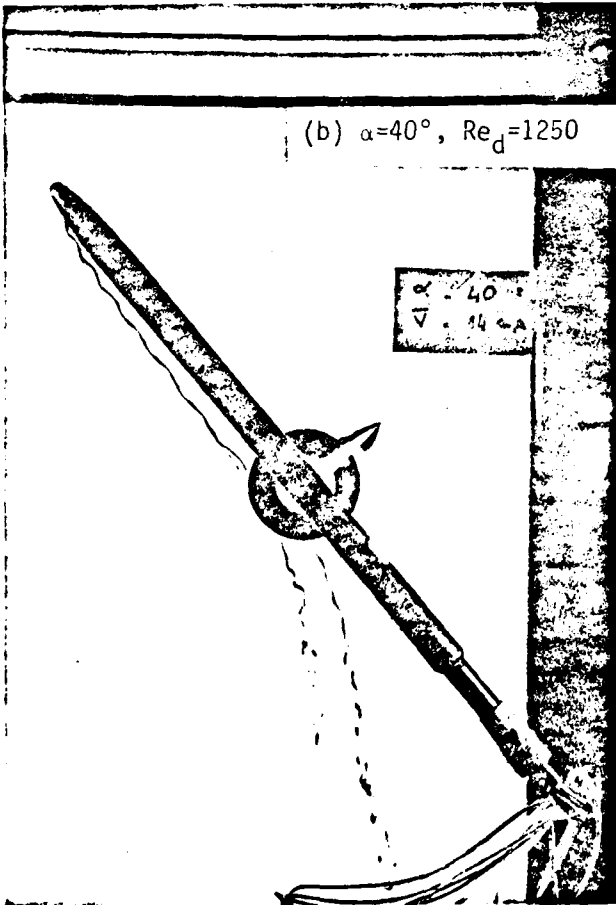
(d) $\alpha=50^\circ$, $Re_d=1250$



(c) $\alpha=45^\circ$, $Re_d=1250$



(b) $\alpha=40^\circ$, $Re_d=1250$



(a) $\alpha=35^\circ$, $Re_d=1250$

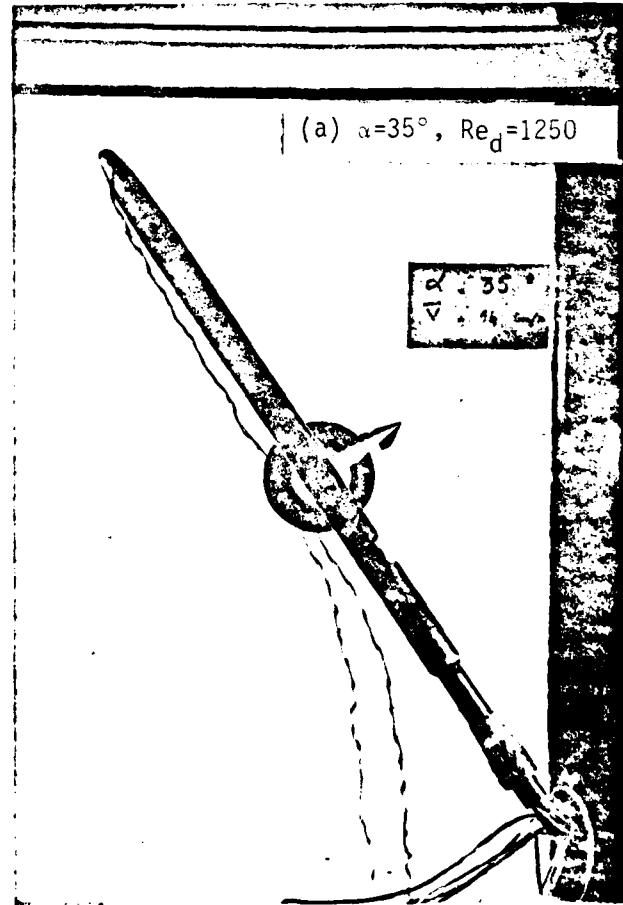
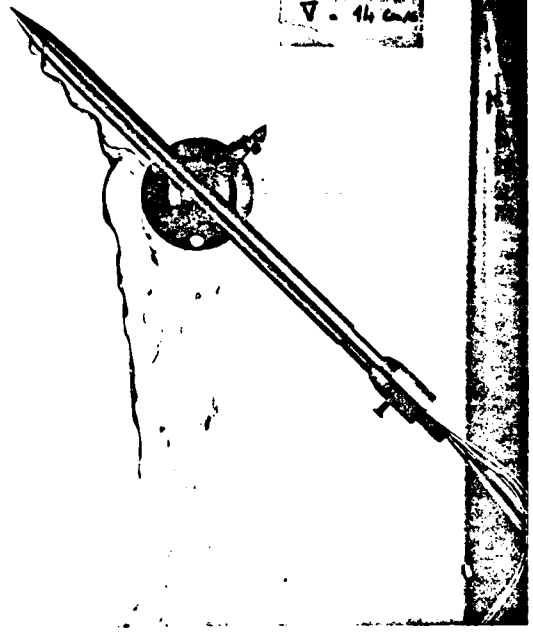


FIG. 33 - FLOW VISUALIZATION OVER A BLUNT NOSED BODY FOR $\alpha=35^\circ, 40^\circ, 45^\circ, 50^\circ$

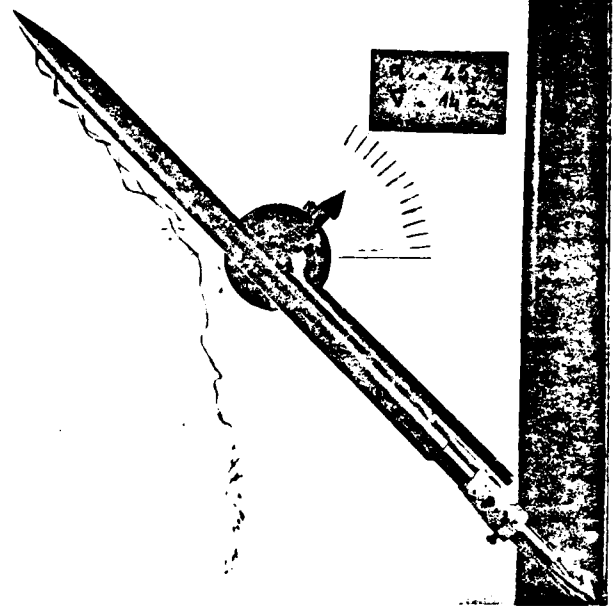
(a) $\alpha=45^\circ$, $Re_d=1250$

$\alpha = 45^\circ$
 $\nabla = 14 \text{ cm/s}$



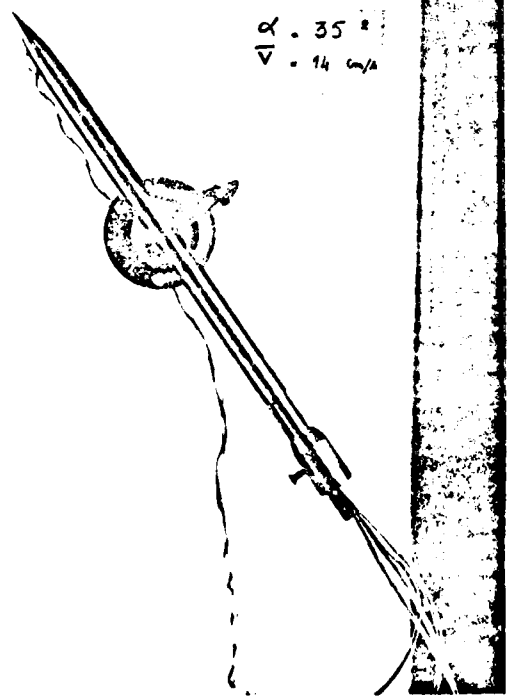
(b) $\alpha=45^\circ$, $Re_d=1250$

$\alpha = 45^\circ$
 $\nabla = 14 \text{ cm/s}$



(c) $\alpha=35^\circ$, $Re_d=1250$

$\alpha = 35^\circ$
 $\nabla = 14 \text{ cm/s}$



(d) $\alpha=35^\circ$, $Re_d=1250$

$\alpha = 35^\circ$
 $\nabla = 14 \text{ cm/s}$

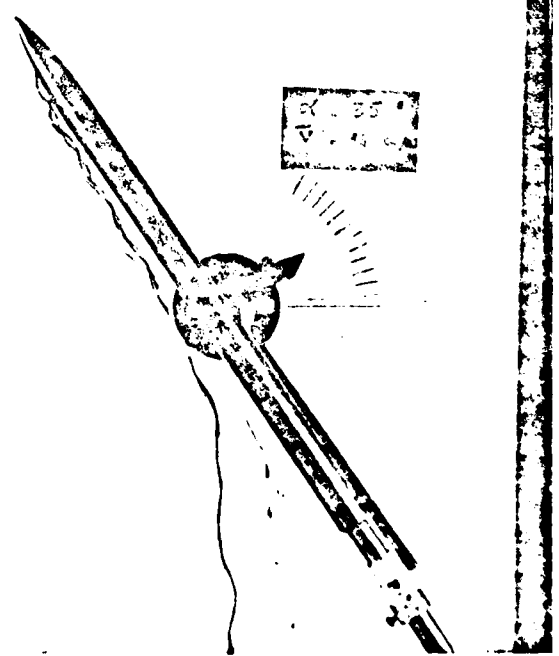


FIG. 34 - INVESTIGATION OF WALL EFFECT

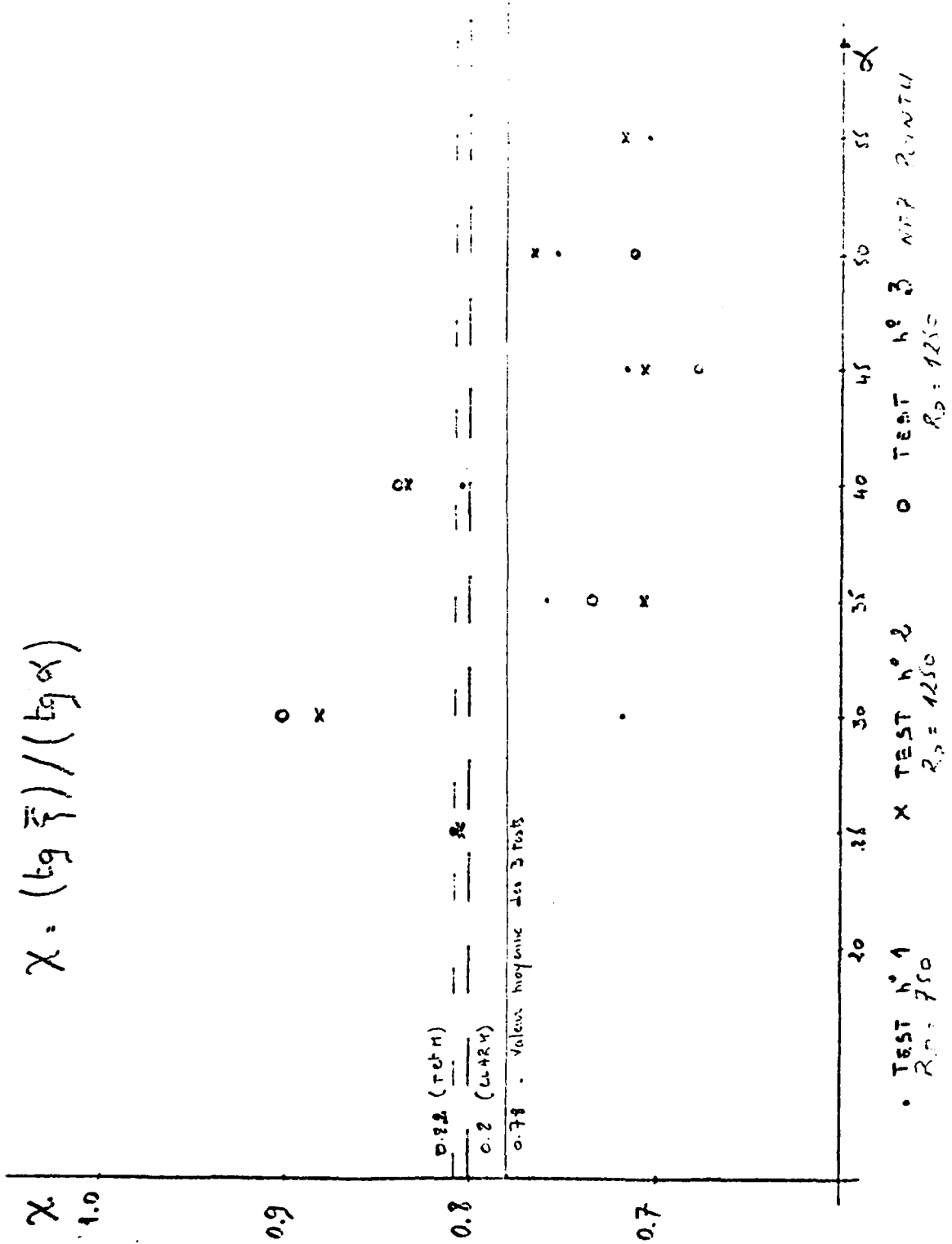


FIG. 35 - PARAMETER χ VERSUS ANGLE OF ATTACK AS DETERMINED FROM WATER TUNNEL INVESTIGATIONS (Ref. 45).

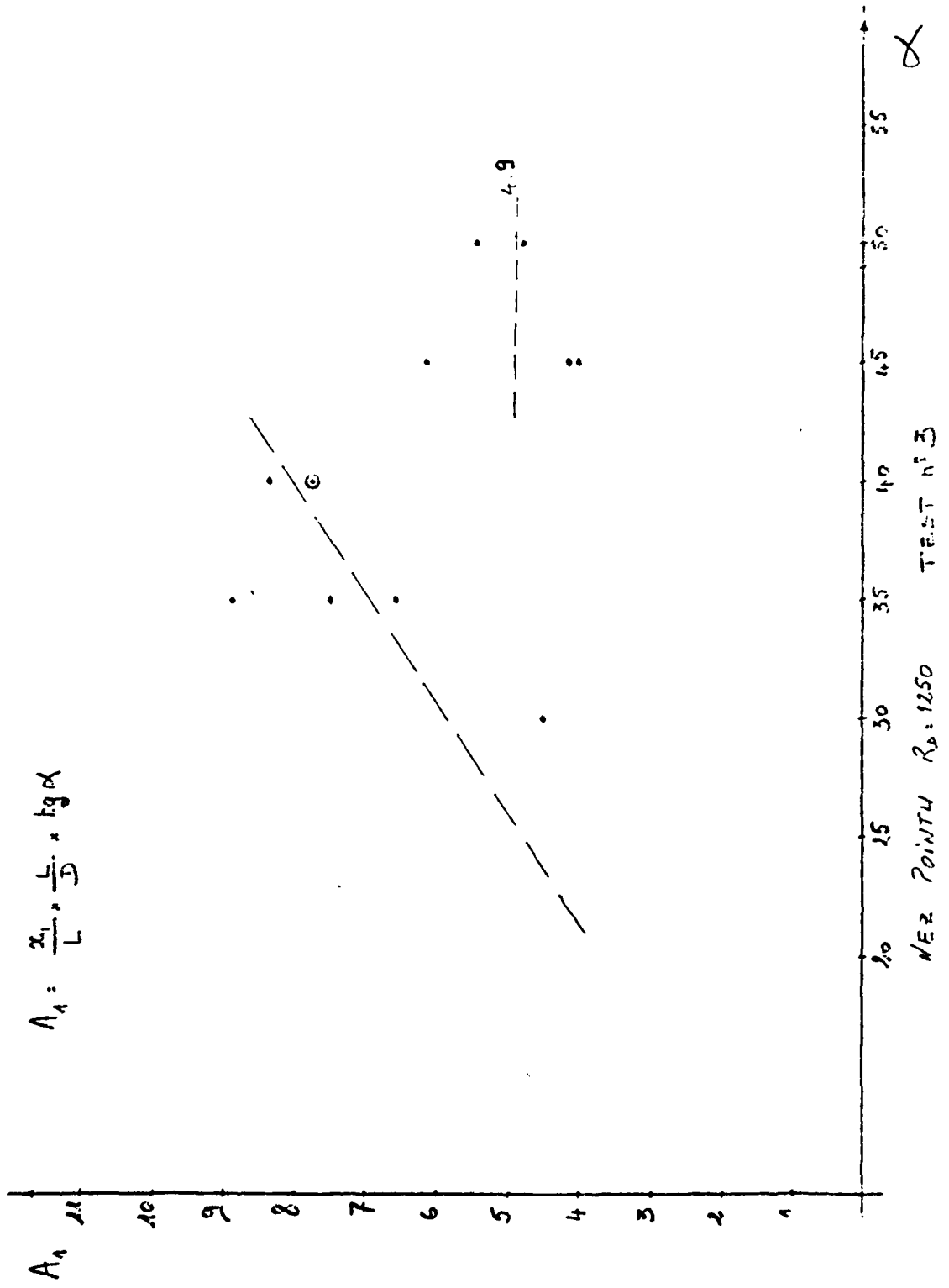


FIG. 36 - PARAMETER A_1 VERSUS ANGLE OF ATTACK AS DETERMINED FROM WATER TUNNEL INVESTIGATIONS (Ref. 45).

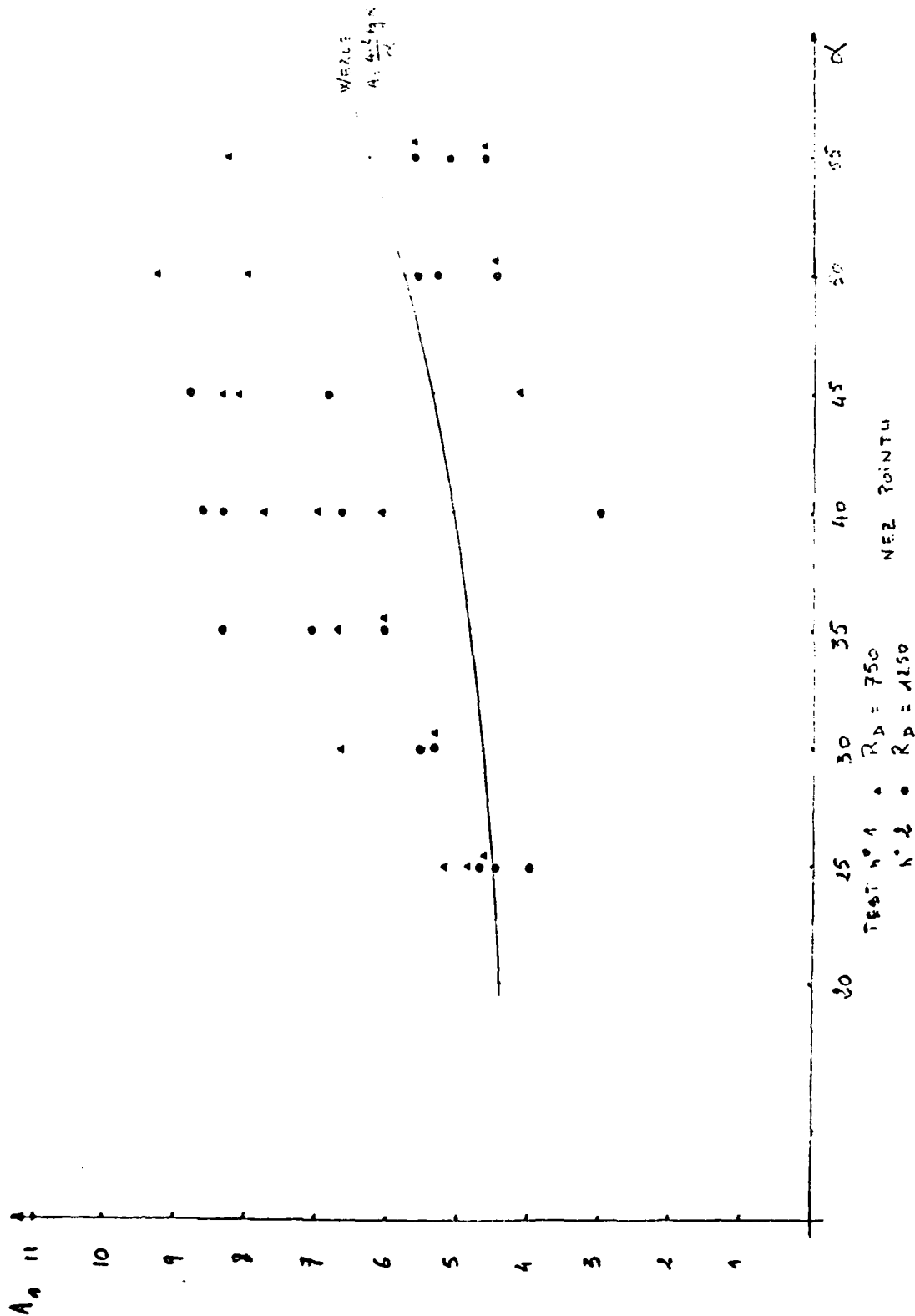


FIG. 37 - PARAMETER A_1 VERSUS α ; REYNOLDS NUMBER EFFECT (Ref. 45)

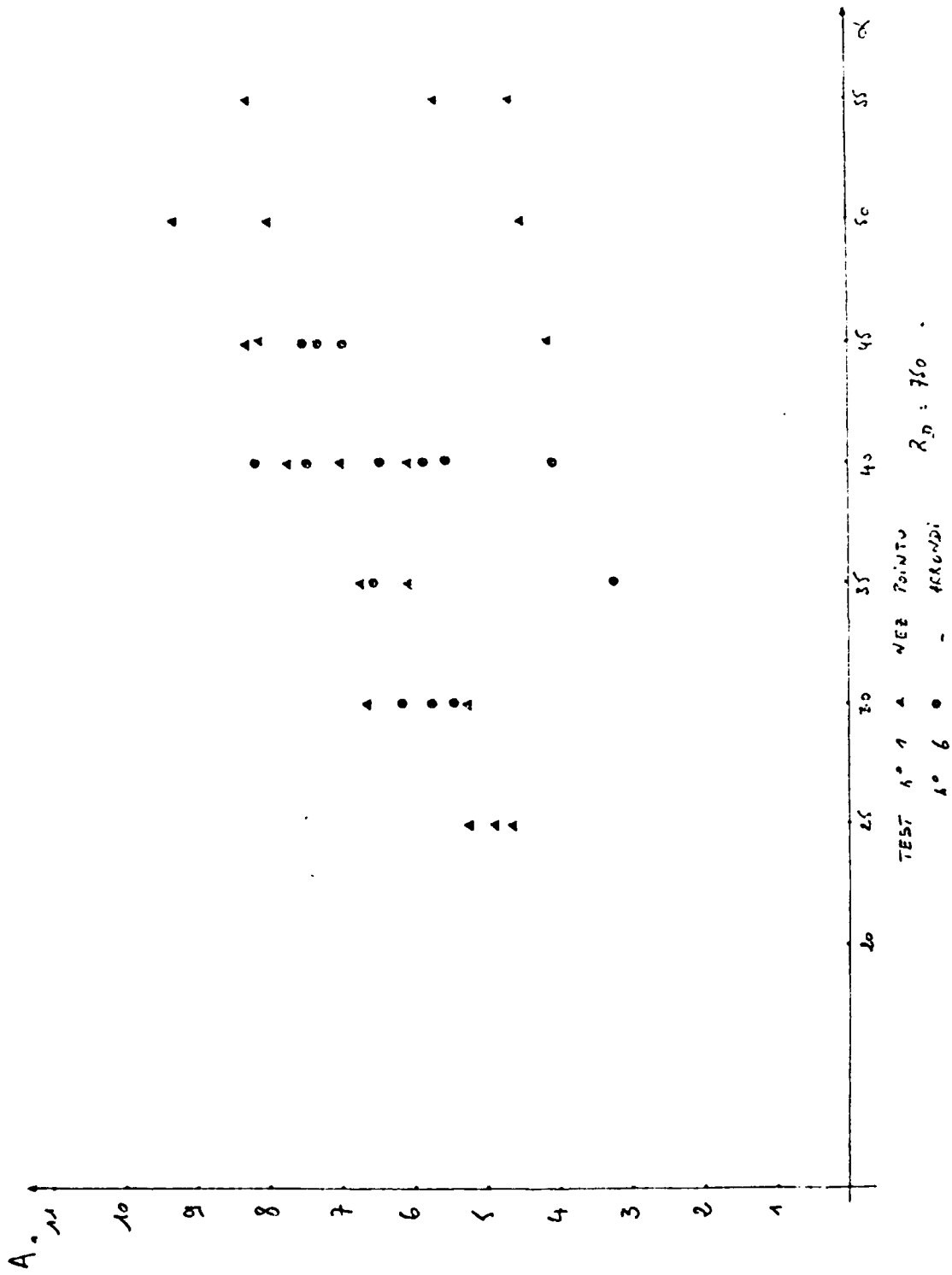


FIG. 38 - PARAMETER A_1 VERSUS α ; NOSE BLUNTING EFFECT (Ref. 45).

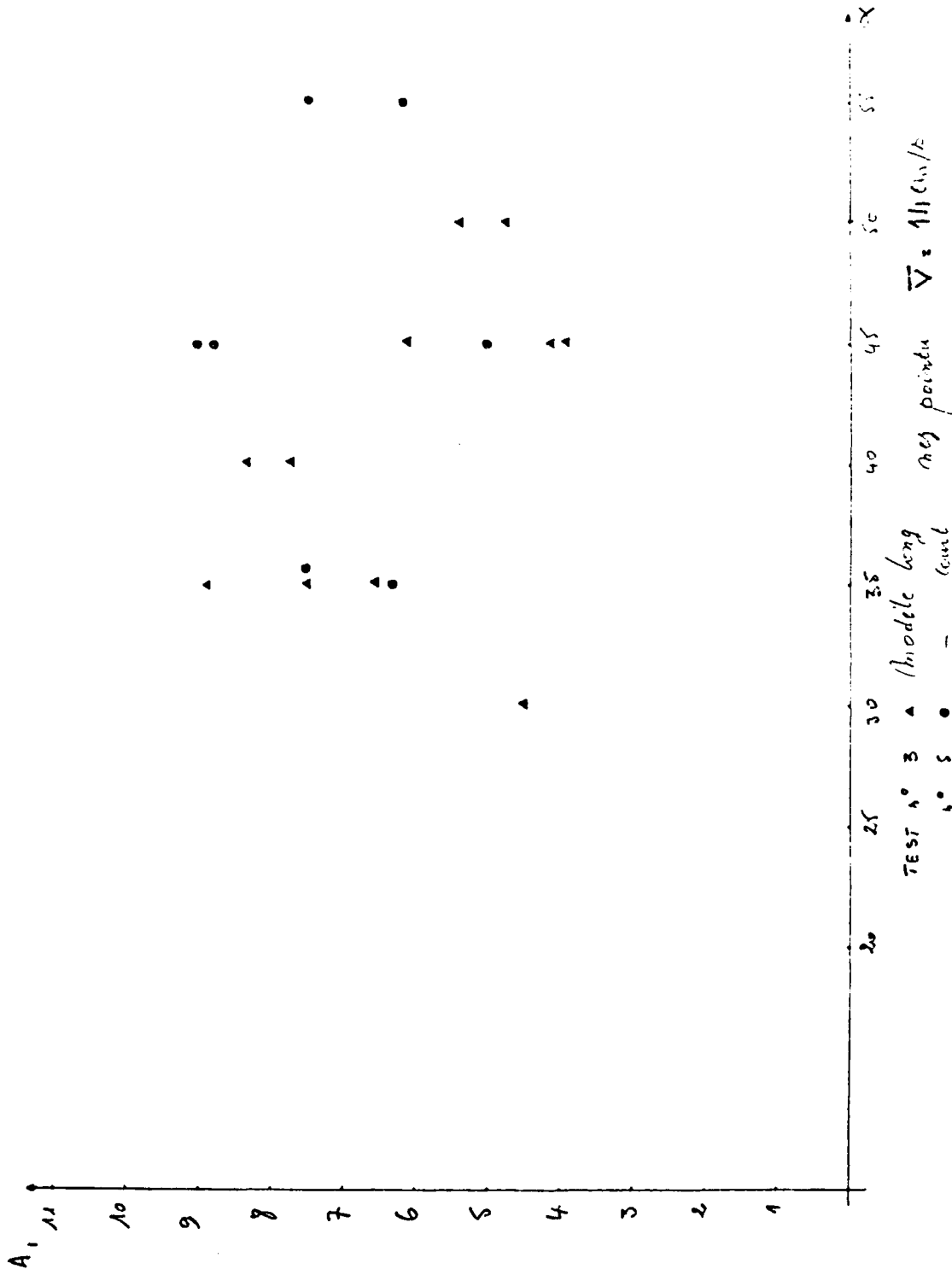


FIG. 39 - PARAMETER A₁ VERSUS α; WALL EFFECT (Ref. 45).

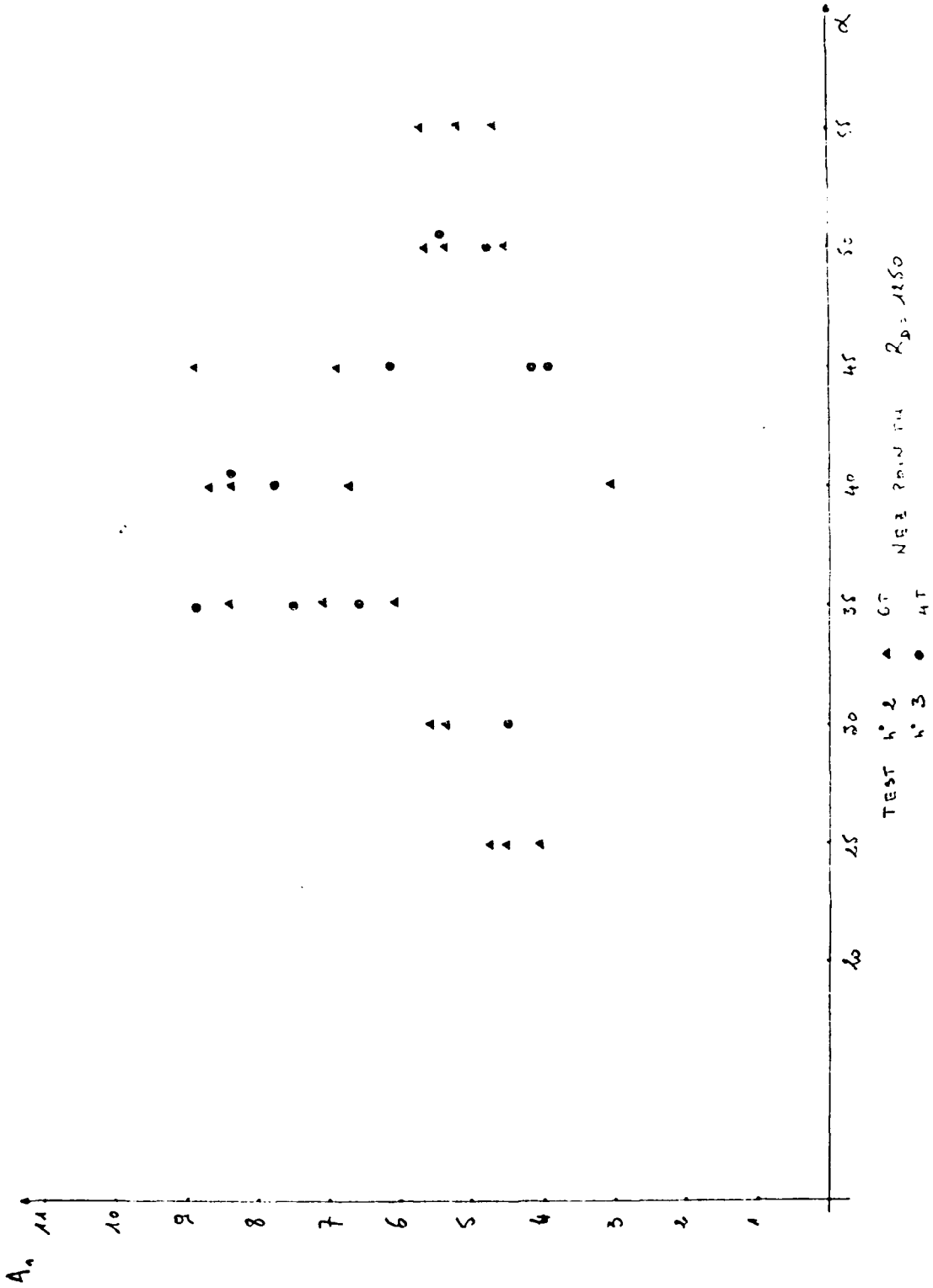
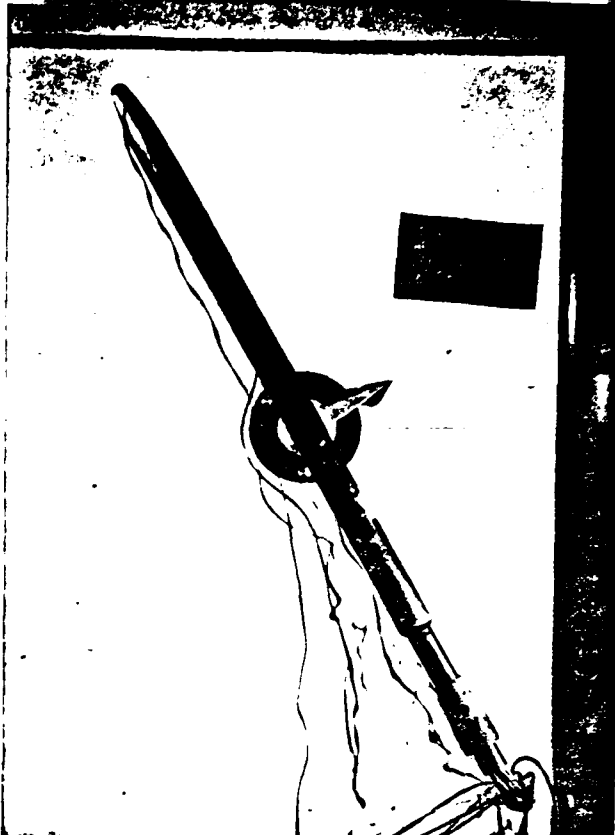


FIG. 40 - PARAMETER A_1 VERSUS α ; REARWARD DYE EJECTION HOLES EFFECT (Ref. 45).

$\alpha = 20^\circ; \bar{V} = 9 \text{ cm/s}$

- 100 -

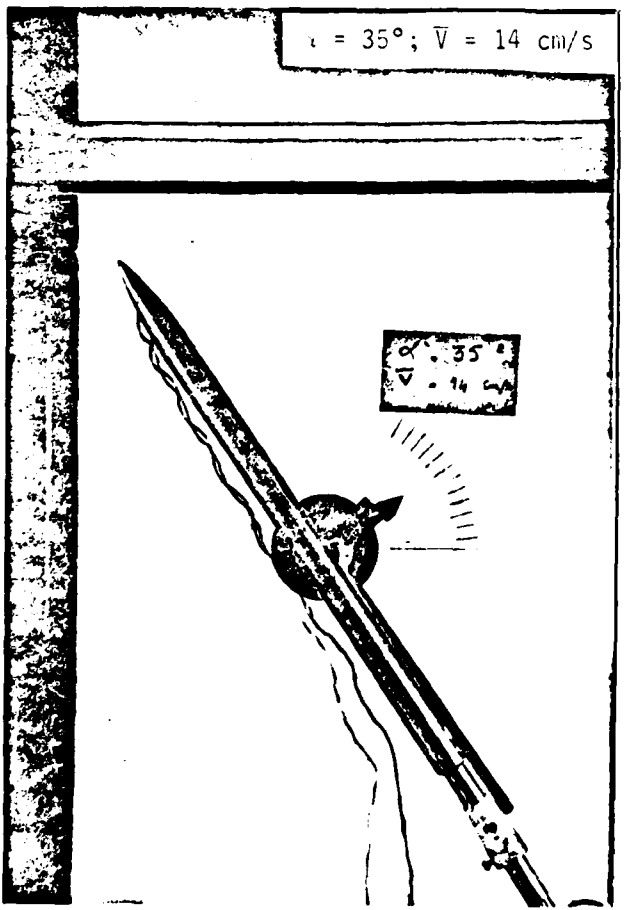
$\alpha = 30^\circ; \bar{V} = 9 \text{ cm/s}$



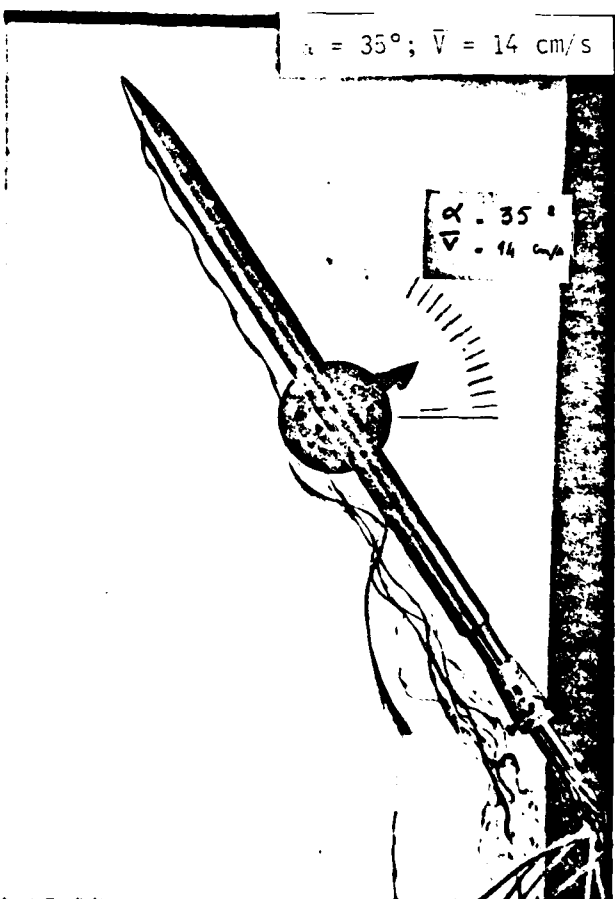
(a) dye ejection interference

(b) dye ejection interference

$\alpha = 35^\circ; \bar{V} = 14 \text{ cm/s}$



$\alpha = 35^\circ; \bar{V} = 14 \text{ cm/s}$



(c) support interference

(d) dye dispersion

FIG. 41 - PROBLEMS ENCOUNTERED IN FLOW VISUALIZATION TESTS

CN VS. ANGLE OF ATTACK

M = .417 SHARP NOSE

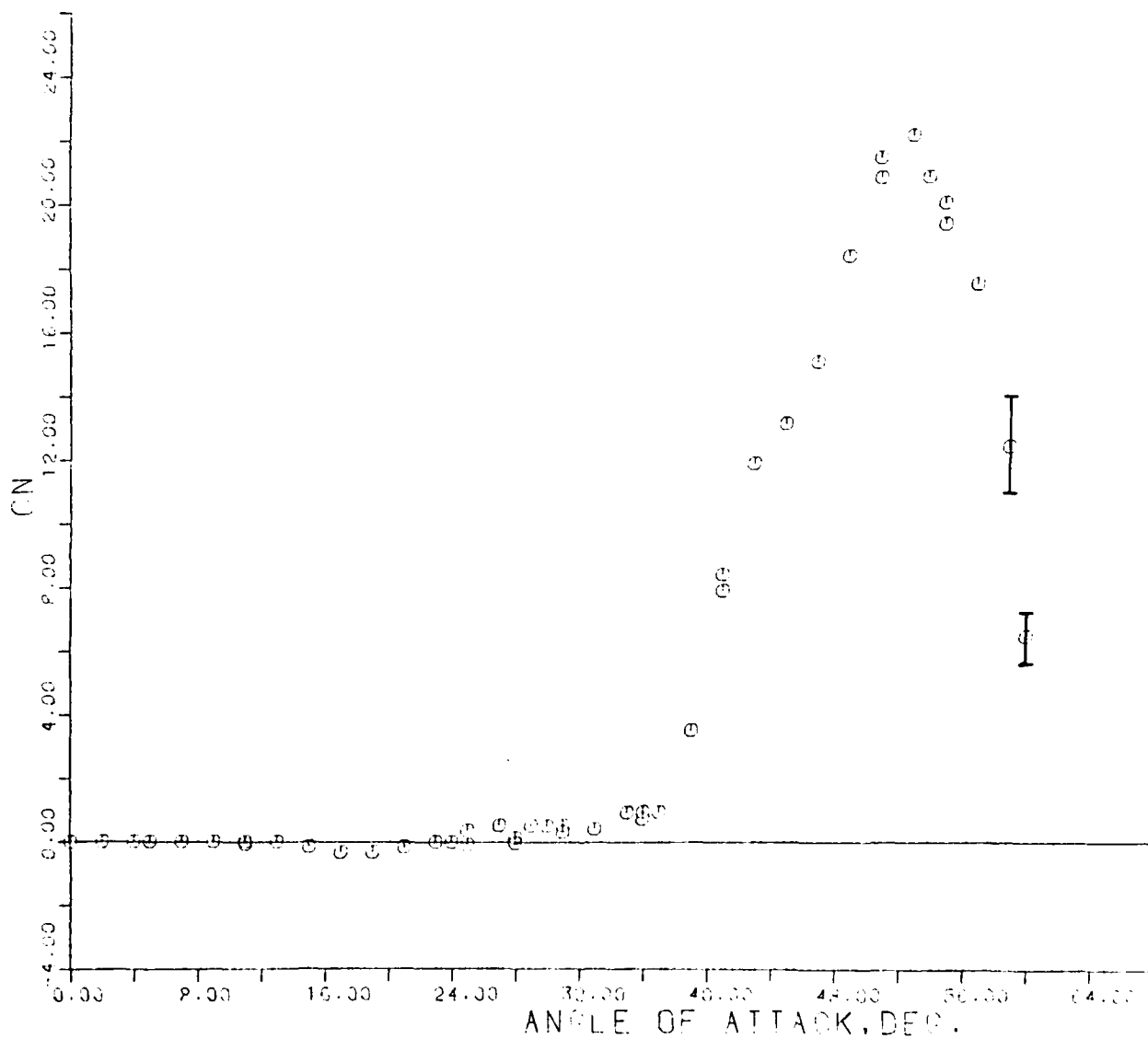


FIG. 42 - C_N VERSUS α ; $M = .417$ - SHARP NOSED BODY.

CZ VERSUS ANGLE OF ATTACK

M = .417 SHARP NOSE

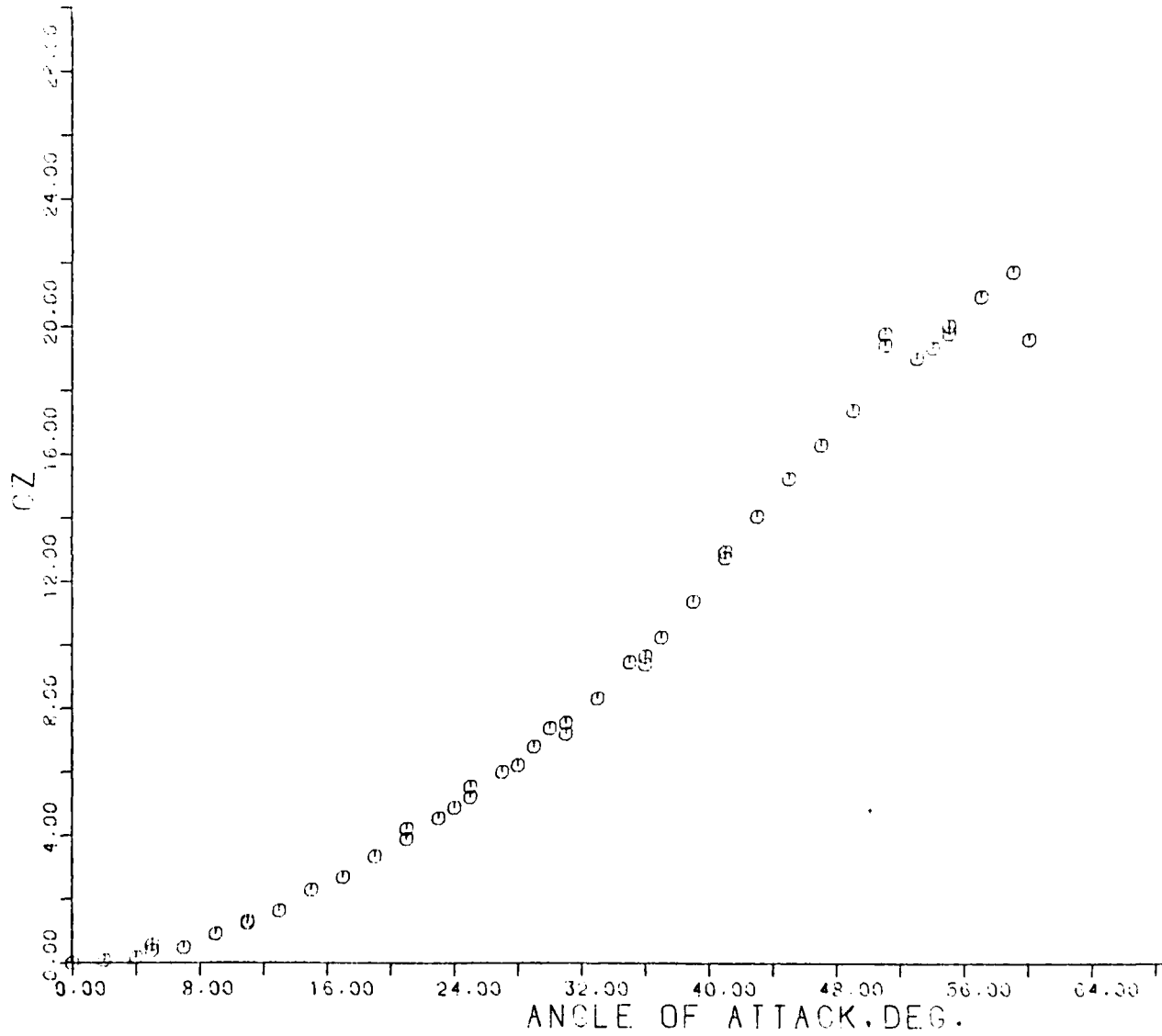


FIG. 43 - C_Z VERSUS α ; M = .417 - SHARP NOSED BODY.

CM VS. ANGLE OF ATTACK

M = .417 SHARP NOSE

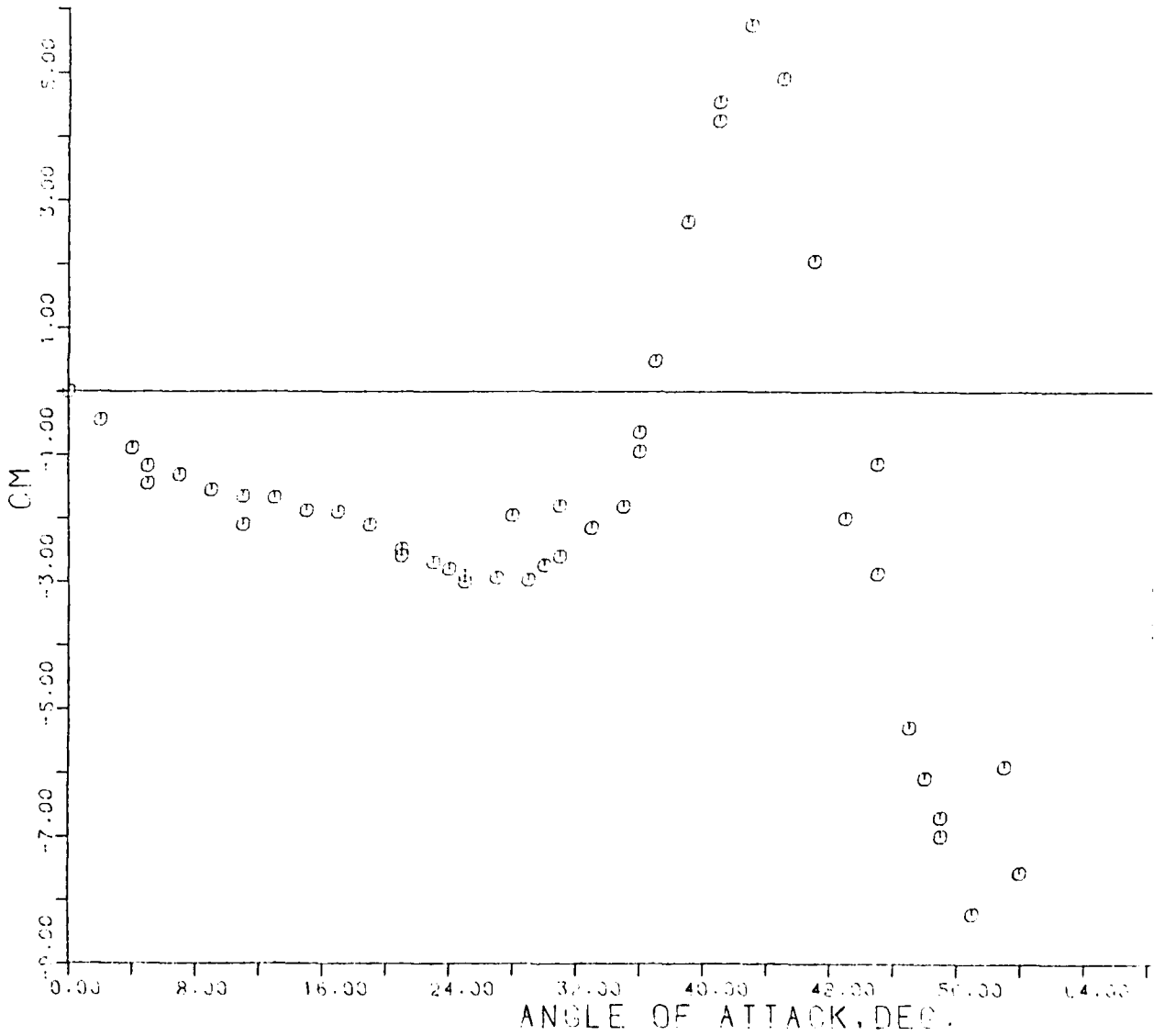


FIG. 44 - C_M VERSUS α ; M = .417 - SHARP NOSED BODY.

XCP/D VS. ALPHA FOR OZ

M = .417 SHARP NOSE

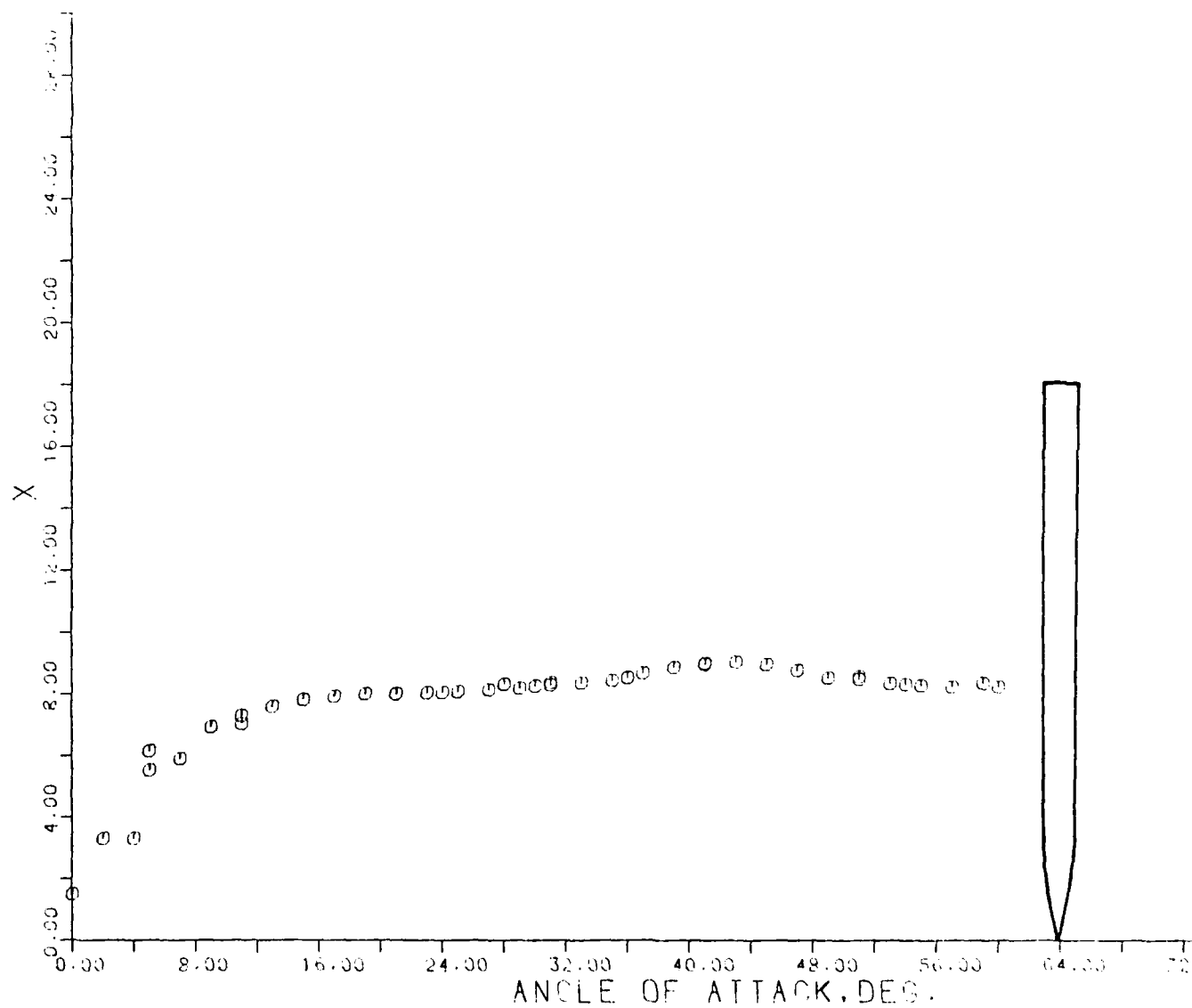


FIG. 45 - $(XCP/D)_Z$ VERSUS α ; M = .417 - SHARP NOSED BODY

CL VS. ANGLE OF ATTACK

M=.417 SHARP NOSE

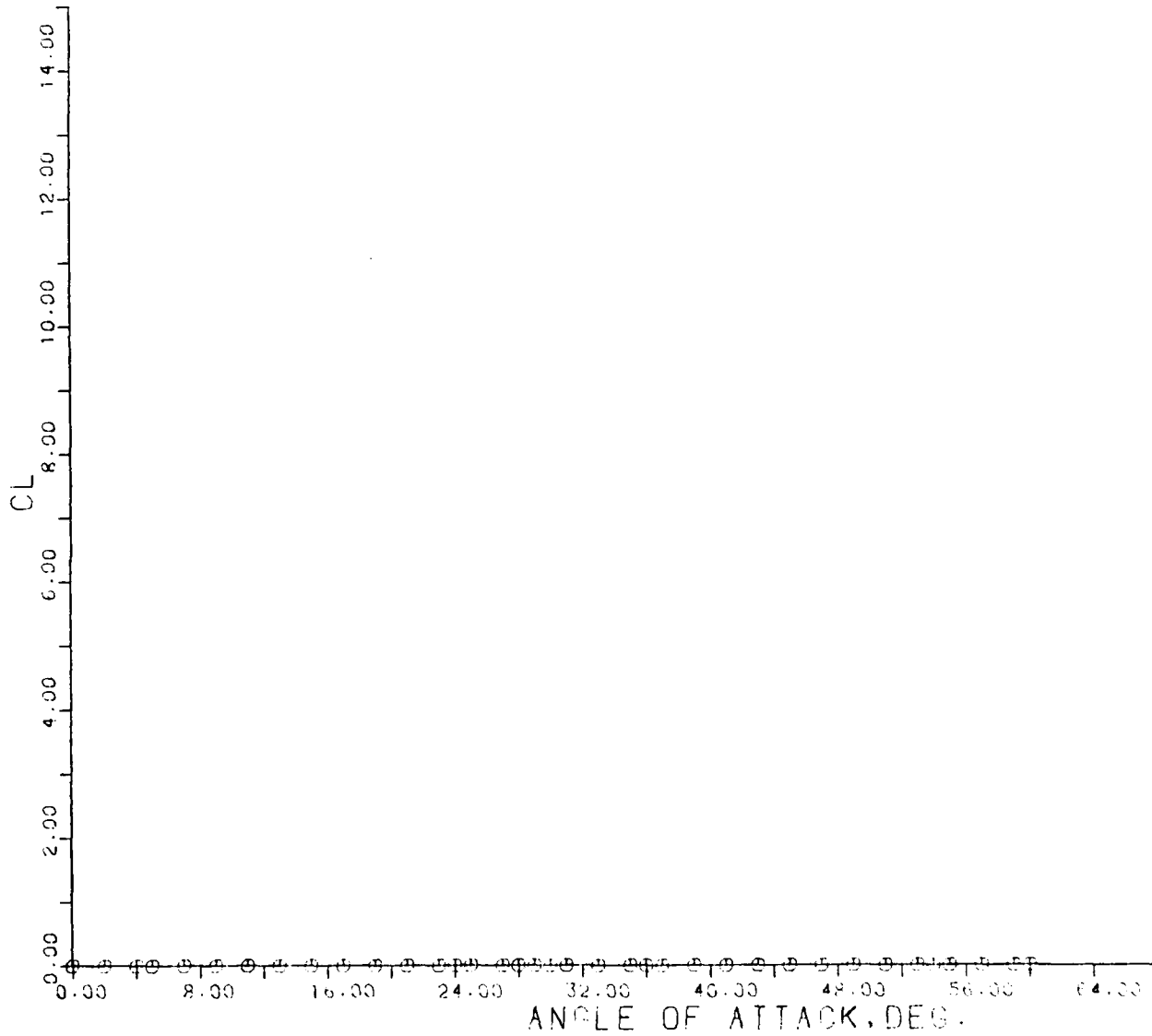


FIG. 46 - C_L VERSUS α ; M = .417 - SHARP NOSED BODY.

CN VS. ANGLE OF ATTACK

M = .617 SHARP NOSE

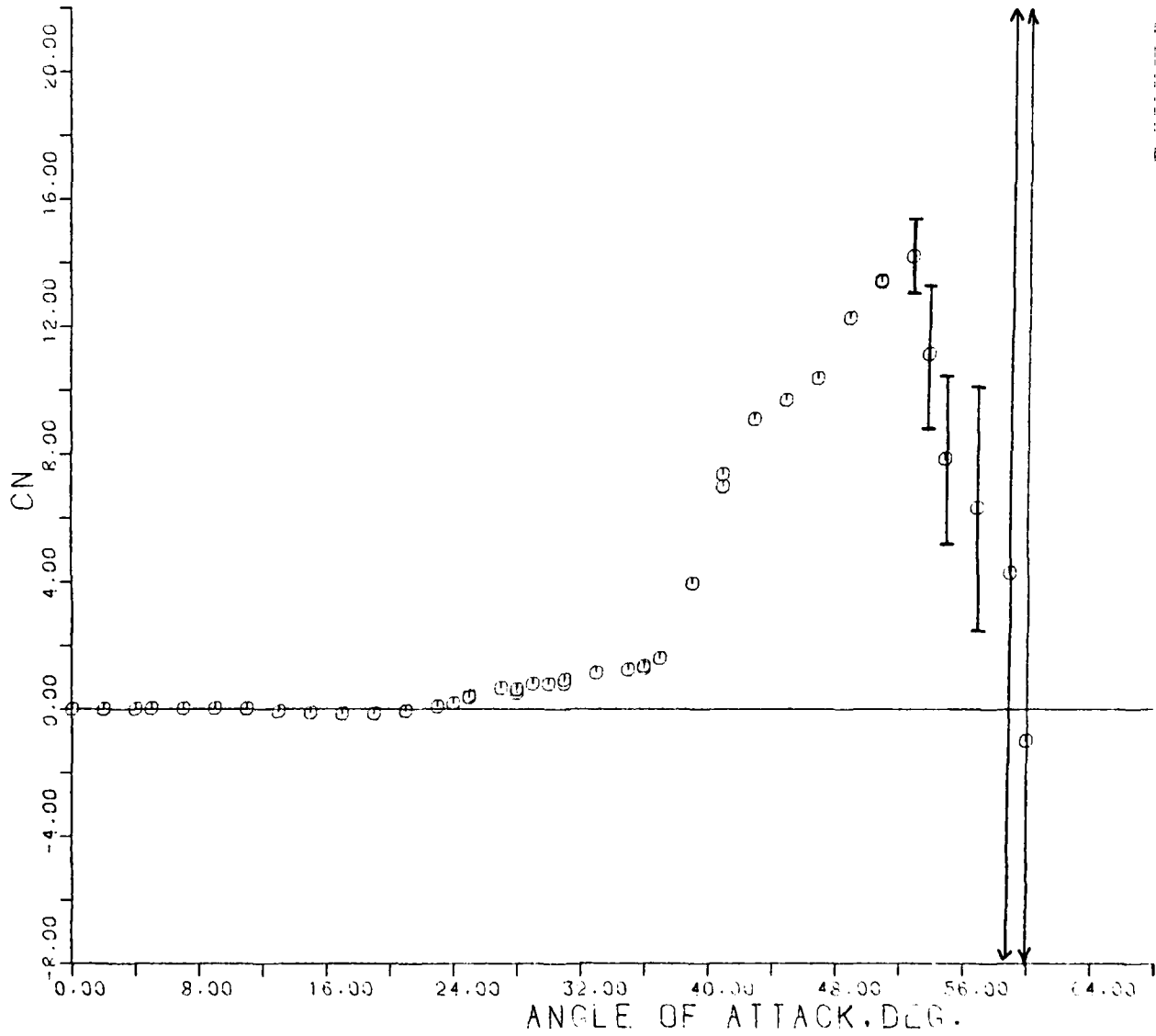


FIG. 47 - C_N VERSUS α ; M = .617 - SHARP NOSED BODY.

CZ VS. ANGLE OF ATTACK

M = .617 SHARP NOSE

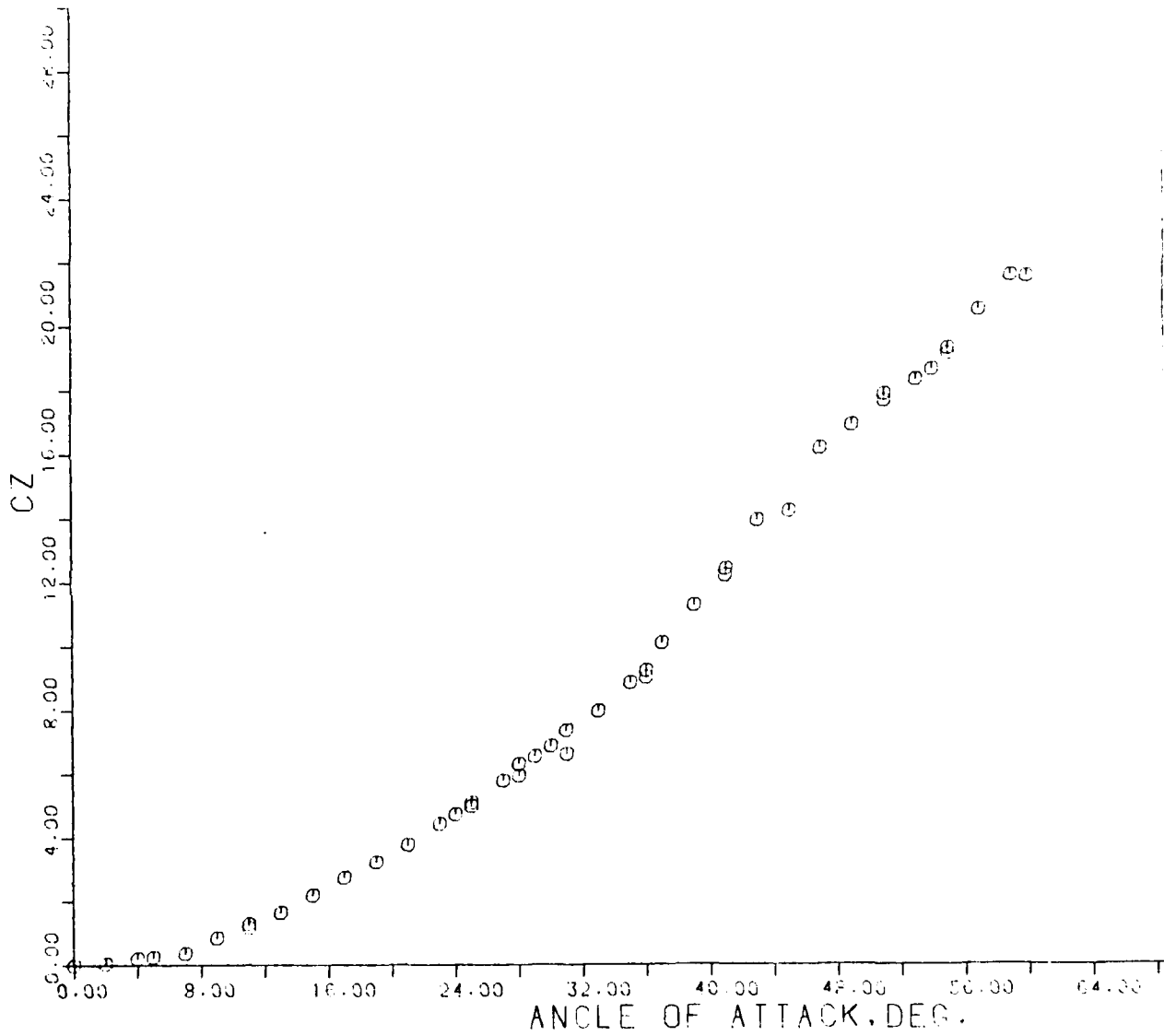


FIG. 48 - C_z VERSUS α ; $M = .617$ - SHARP NOSED BODY.

CM VS. ANGLE OF ATTACK

M = .617 SHARP NOSE

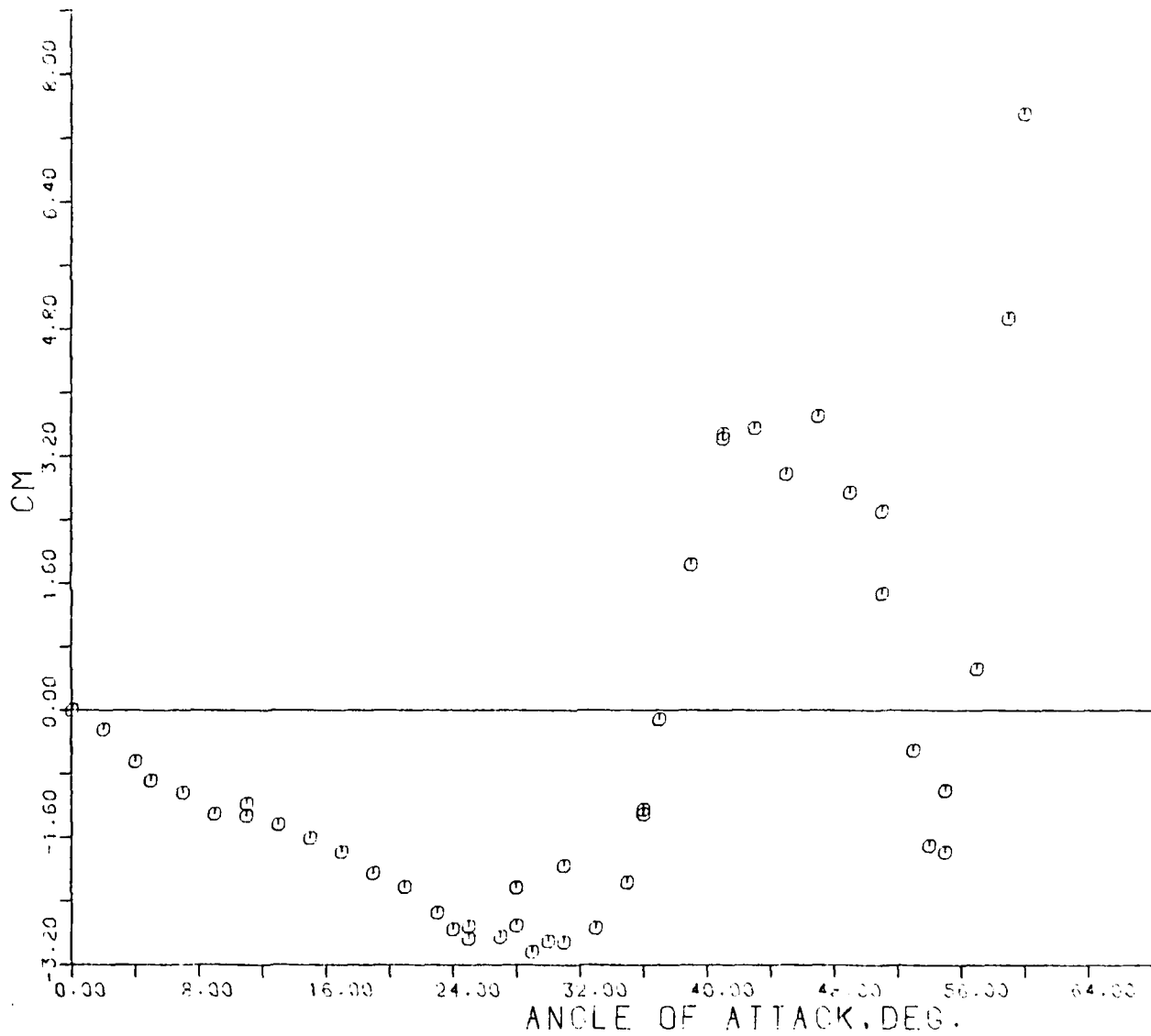


FIG. 49 - C_M VERSUS α ; $M = .617$ - SHARP NOSED BODY.

XCP/D VS. ALPHA FOR CZ

M = .617 SHARP NOSE

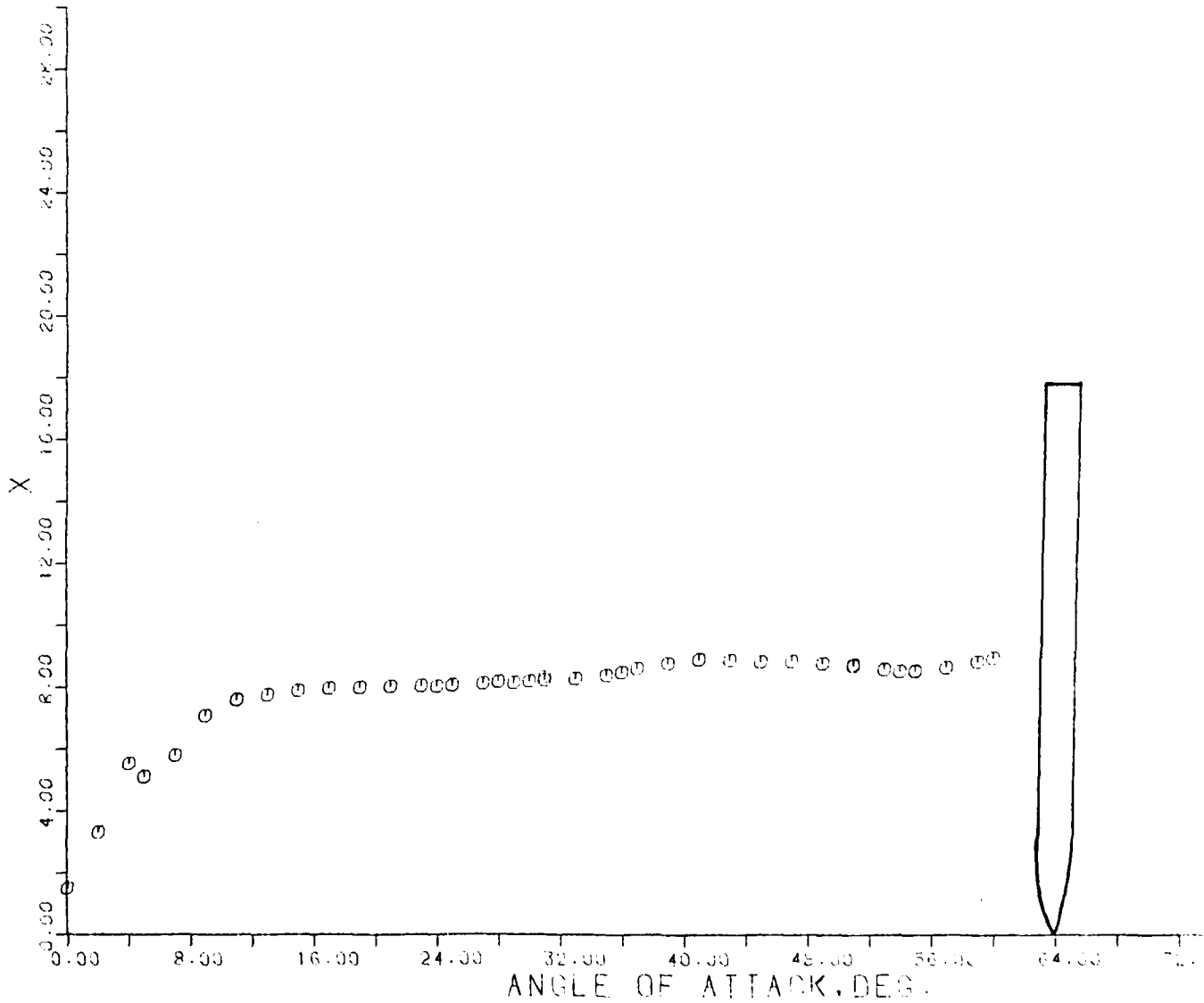


FIG. 50 - $(XCP/D)_Z$ VERSUS α ; M = .617 - SHARP NOSED BODY.

CL VS. ANGLE OF ATTACK

M = .617 SHARP NOSE

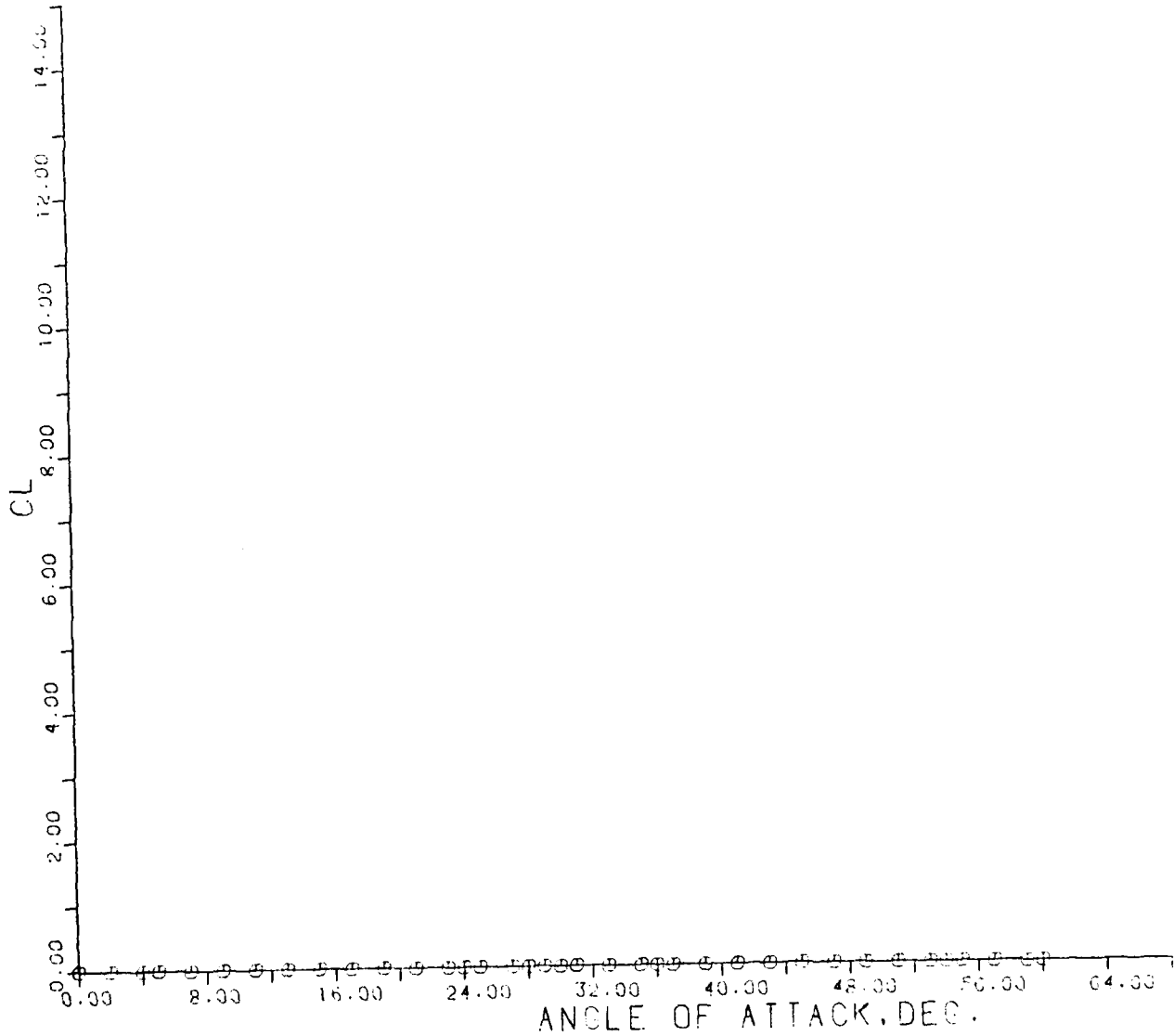


FIG. 51 - C_L VERSUS α ; M = .617 - SHARP NOSED BODY.

CN VS. ANGLE OF ATTACK

M = .695 SHARP NOSE

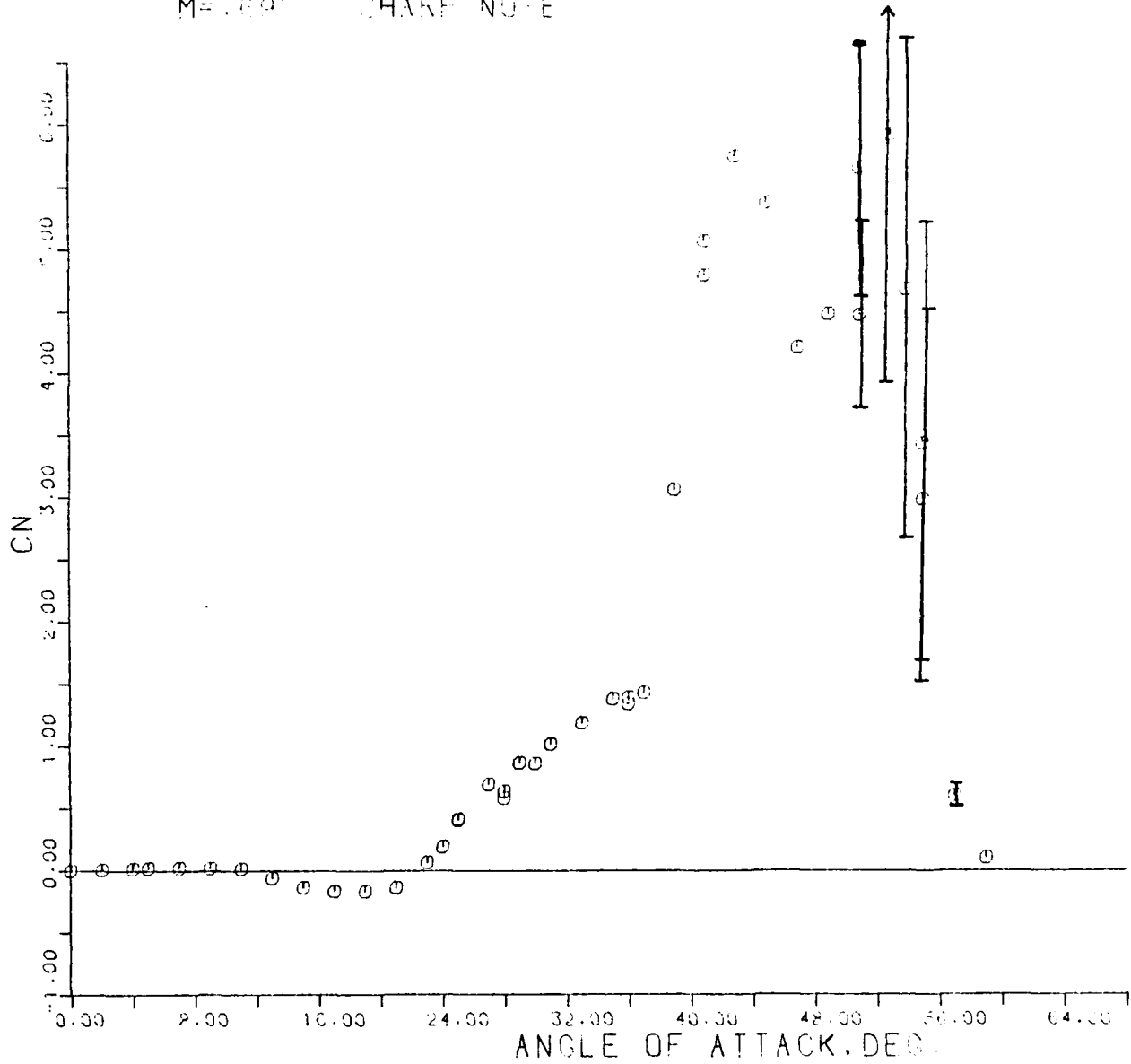


FIG. 52 - C_N VERSUS α ; M = .695 - SHARP NOSED BODY.

CZ VS. ANGLE OF ATTACK

M = 0.695 SHARP NOSE

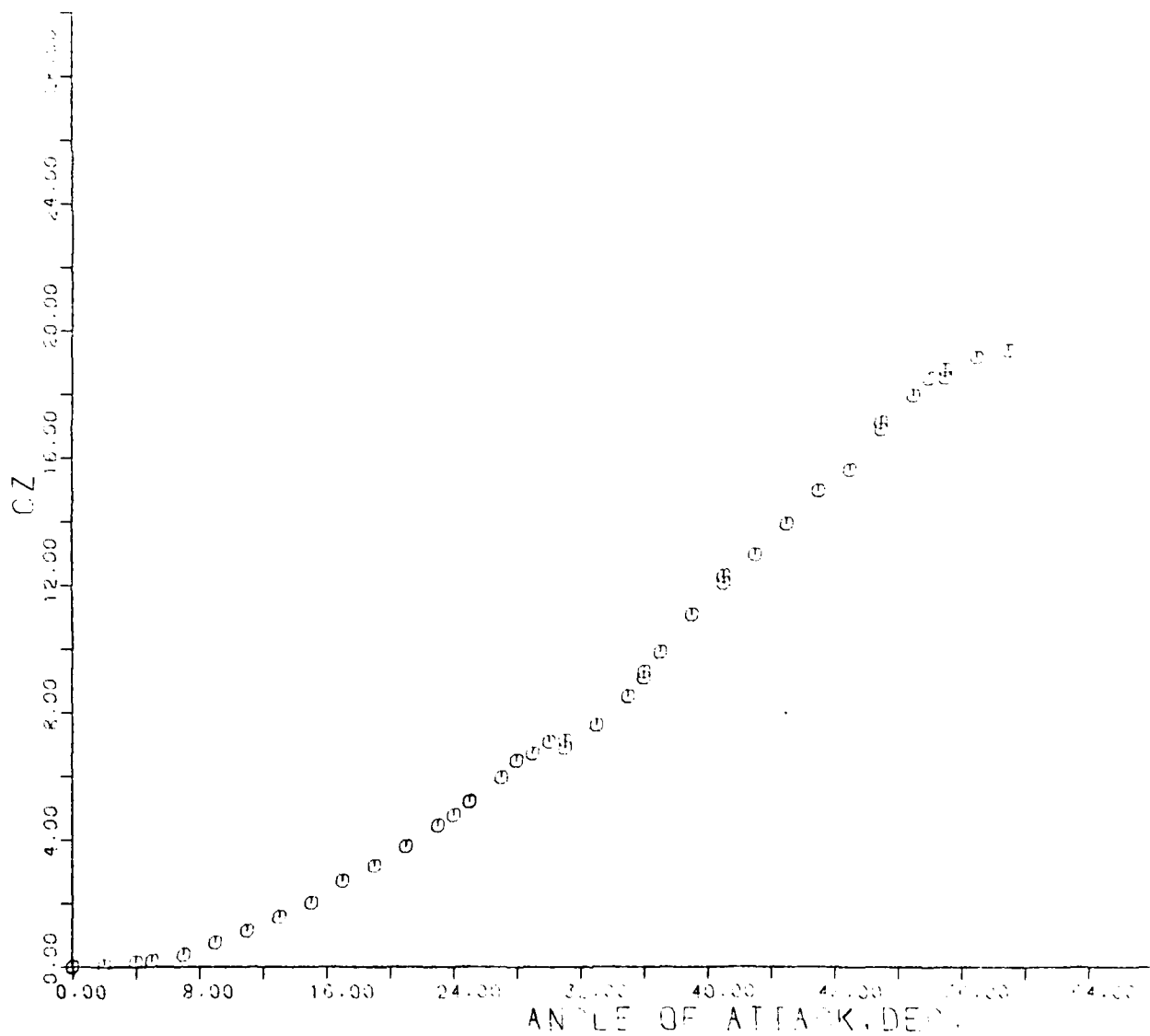


FIG. 53 - C_z VERSUS α ; $M = .695$ - SHARP NOSED BODY.

CM VS. ANGLE OF ATTACK

M = 0.695 SHARP NOSE

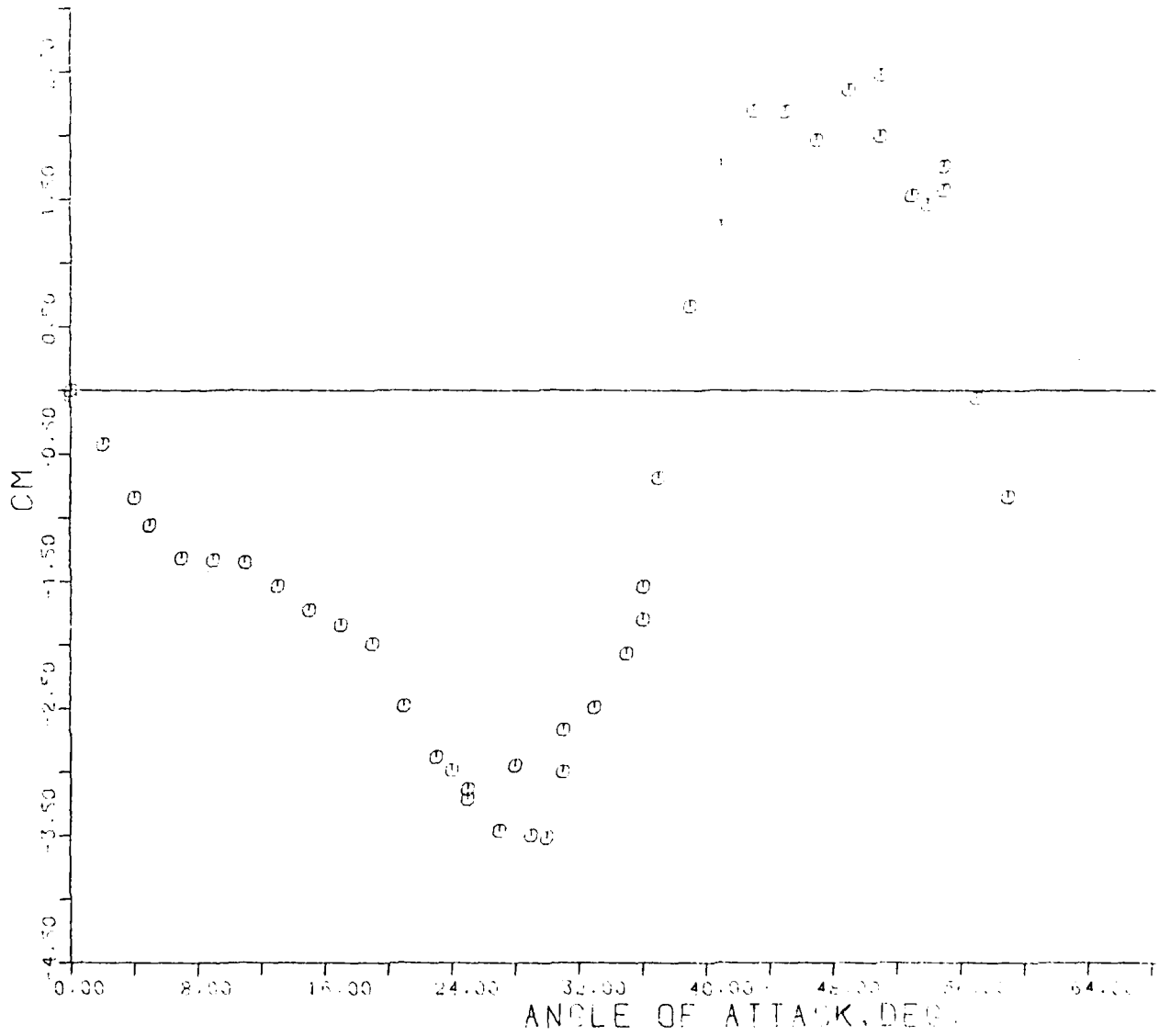


FIG. 54 - C_M VERSUS α ; $M = .695$ - SHARP NOSED BODY.

X CP/D VS. ALPHA FOR Z

M = .695 SHARP NOSED BODY

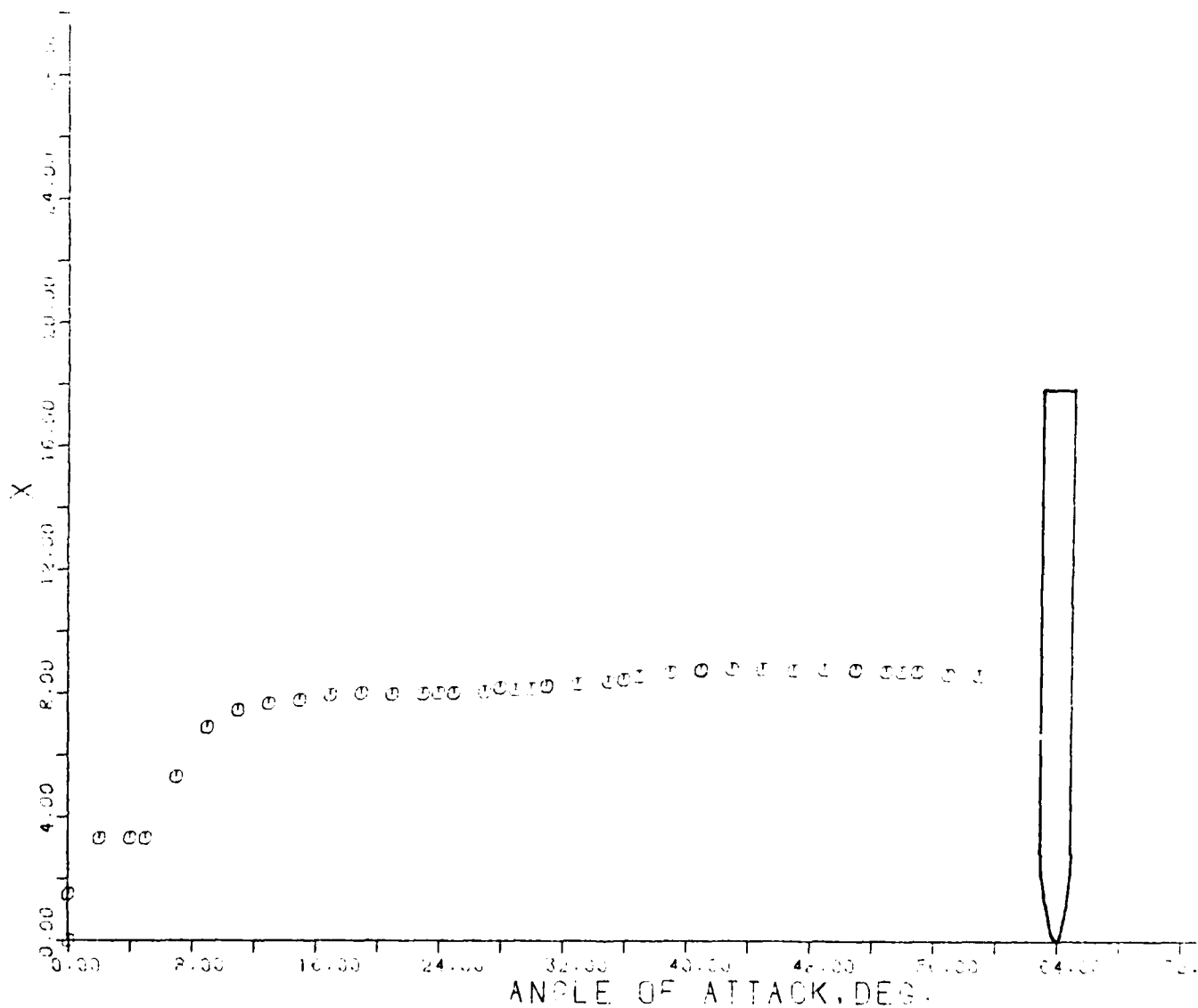


FIG. 55 - $(XCP/D)_Z$ VERSUS α ; $M = .695$ - SHARP NOSED BODY.

C_L VERSUS ANGLE OF ATTACK

NOSE SHARP NOSE

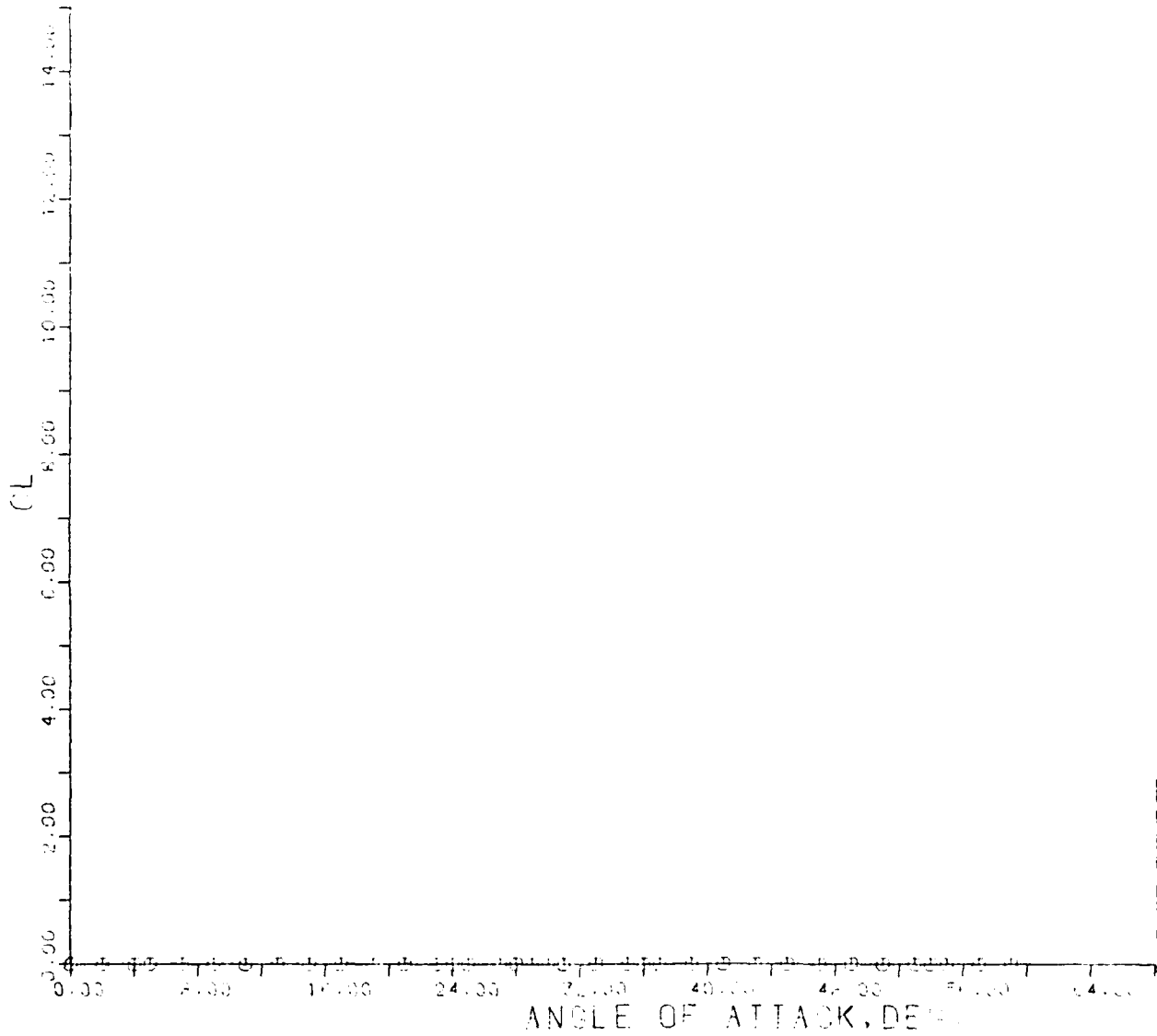


FIG. 56 - C_L VERSUS α ; M = .695 - SHARP NOSED BODY.

C_N VERSUS ANGLE OF ATTACK

MACH NUMBER = 0.796

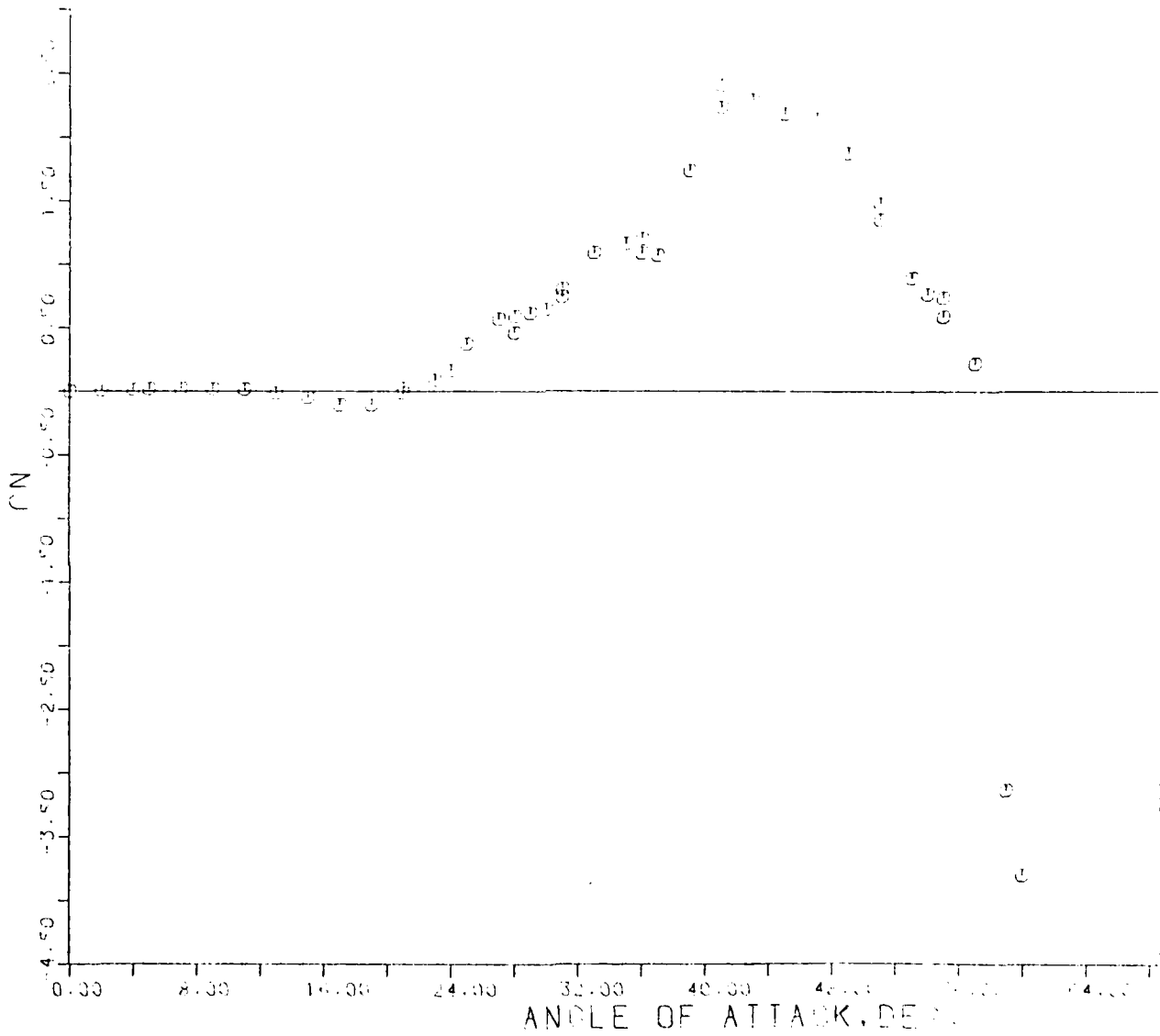


FIG. 57 - C_N VERSUS α ; M = .796 - SHARP NOSED BODY.

CZ VS. ANGLE OF ATTACK

M = .796 - SHARP NOSE

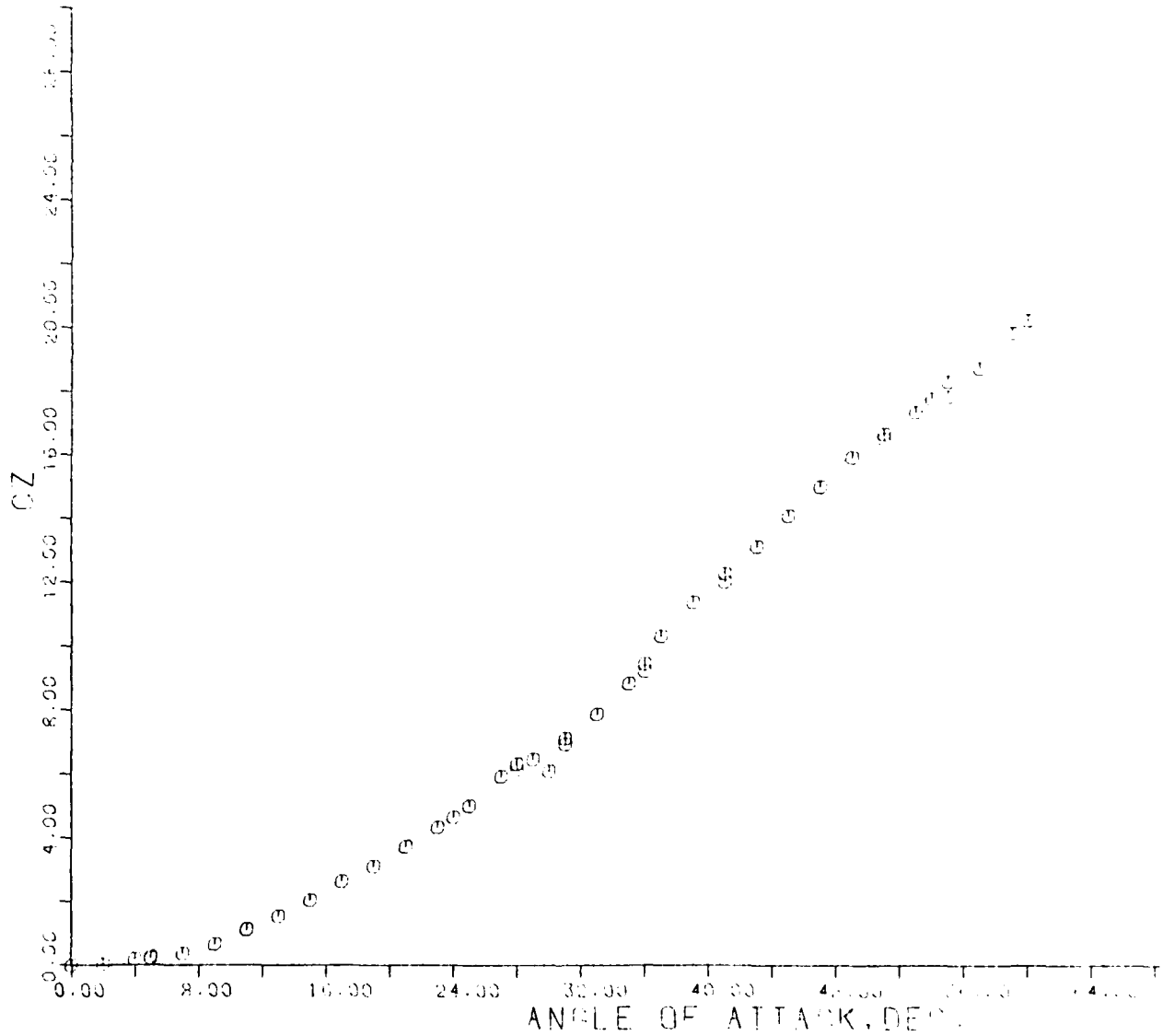


FIG. 58 - C_z VERSUS α ; $M = .796$ - SHARP NOSED BODY.

CM VS. ANGLE OF ATTACK

M = .796 SHARP NOSE

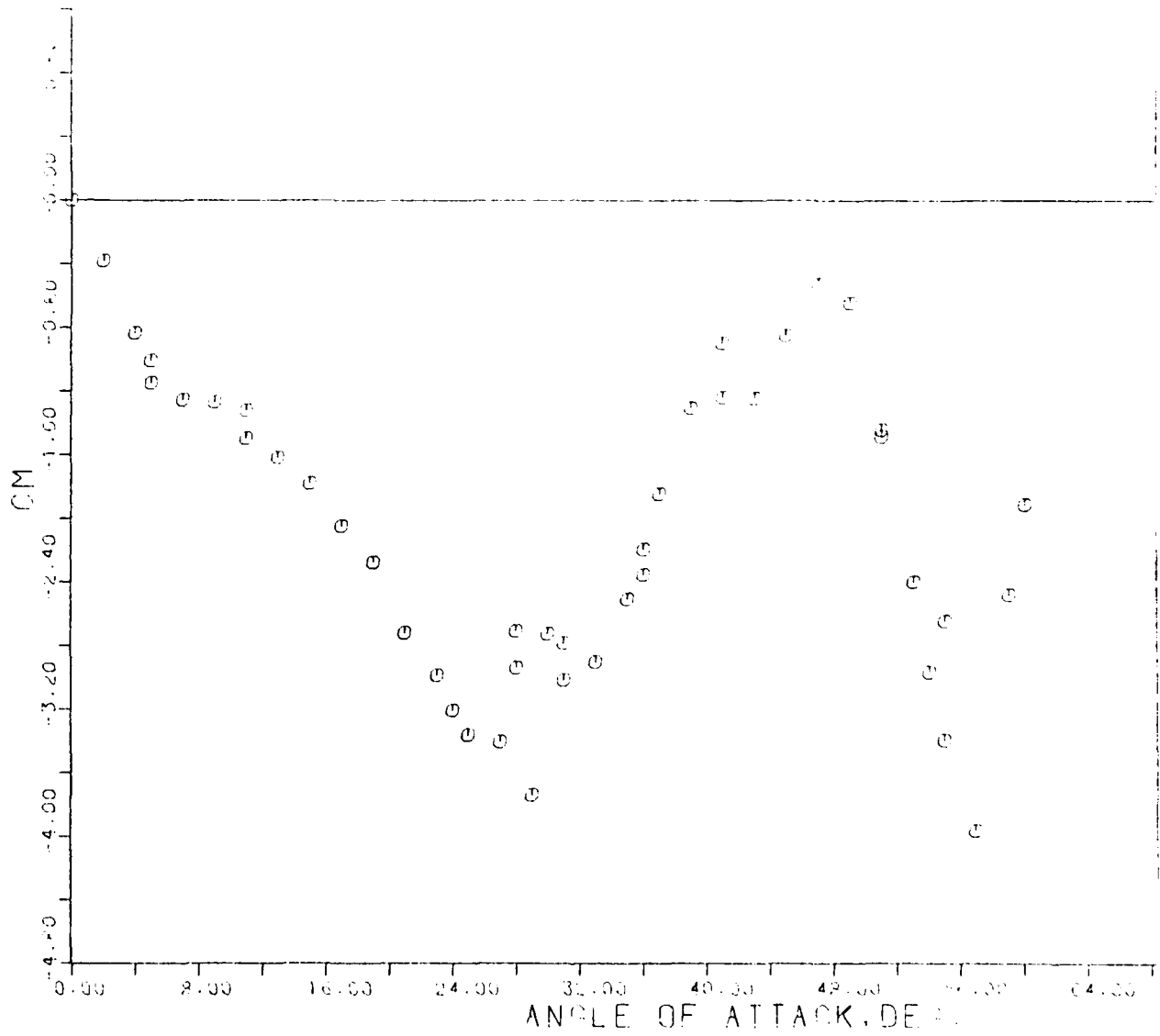


FIG. 59 - C_M VERSUS α ; $M = .796$ - SHARP NOSED BODY.

XCP/D VERS. ALPHA FOR OZ
M = .796 SHARP NOSE

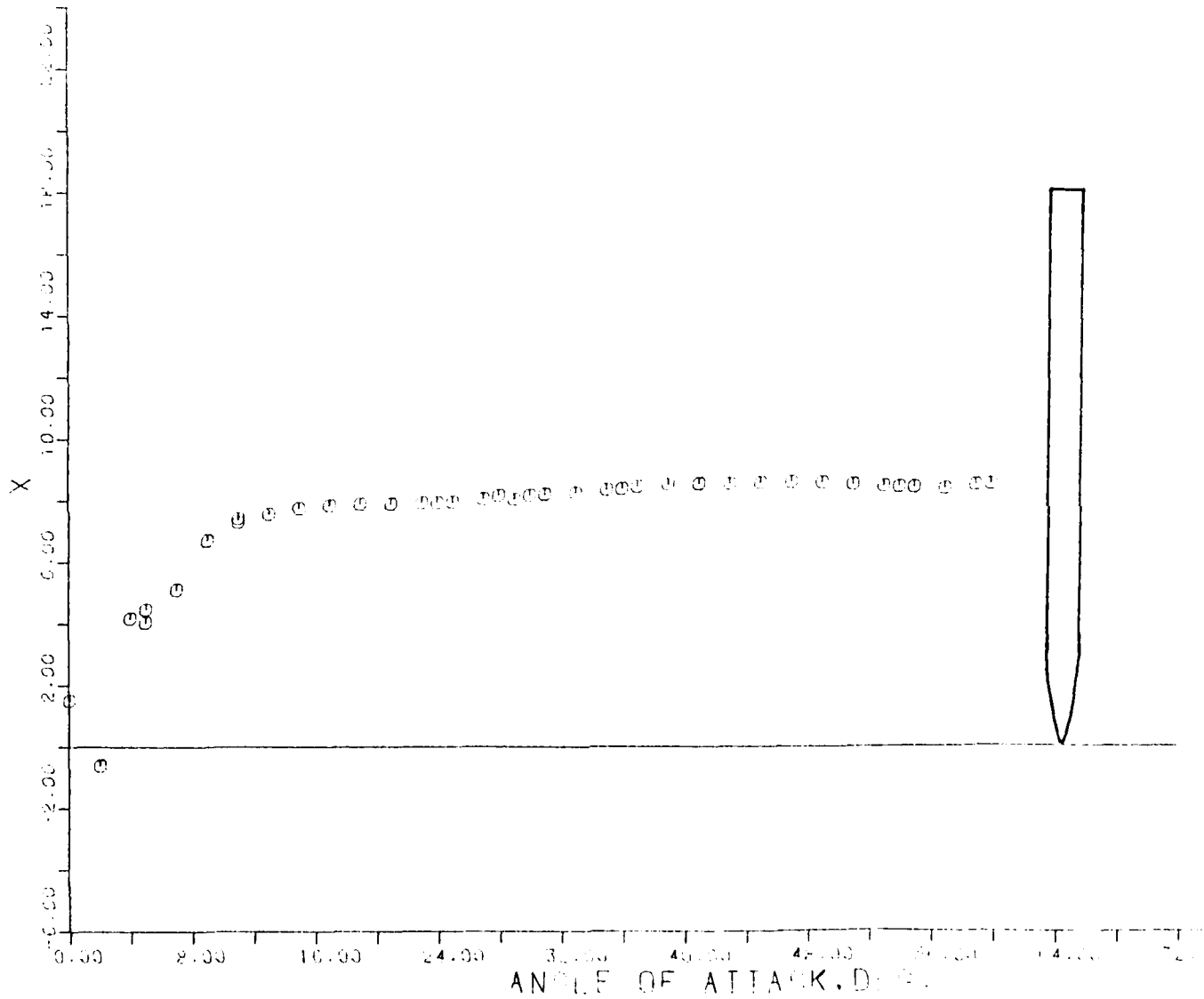


FIG. 60 - $(XCP/D)_Z$ VERSUS α ; $M = .796$ - SHARP NOSED BODY.

CL VS. ANGLE OF ATTACK

M = .796 SHARP NOSE

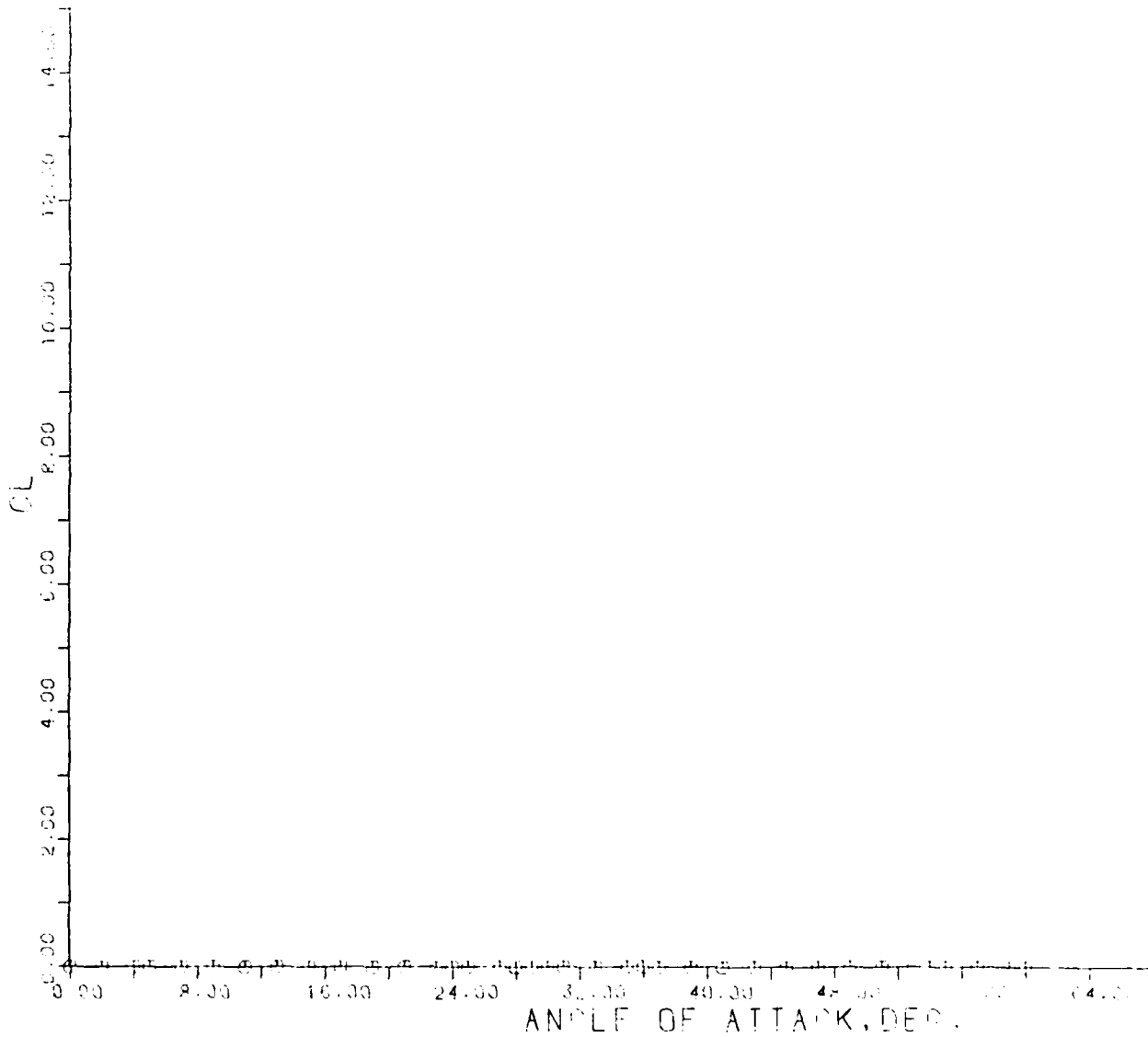


FIG. 61 - C_L VERSUS α ; $M = .796$ - SHARP NOSED BODY.

CN VS ANGLE OF ATTACK
M = .901 SHARP NOSE

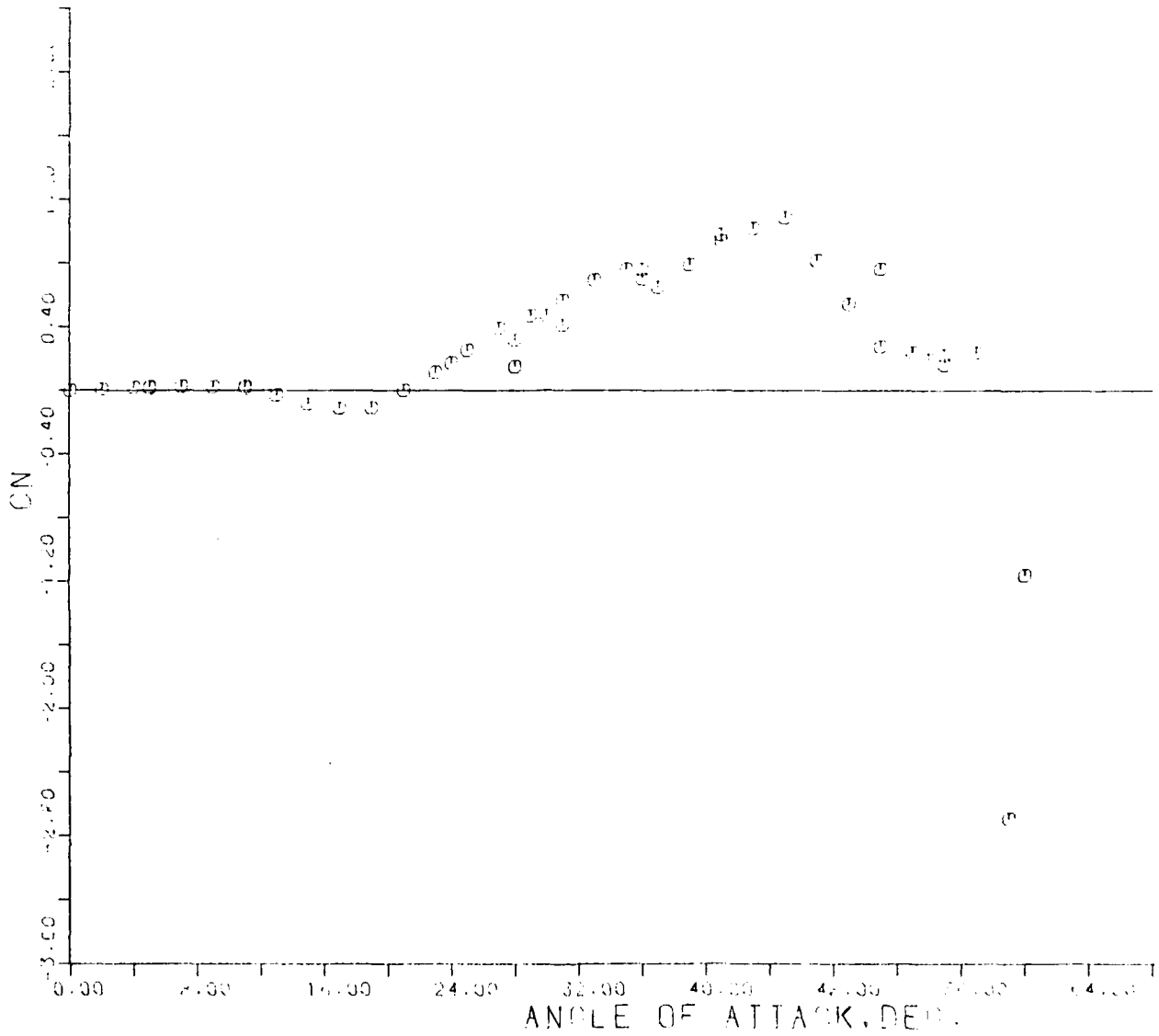


FIG. 62 - C_N VERSUS α ; M = .901 - SHARP NOSED BODY.

CZ VS. ANGLE OF ATTACK

M = 9.01 SHARP NOSED

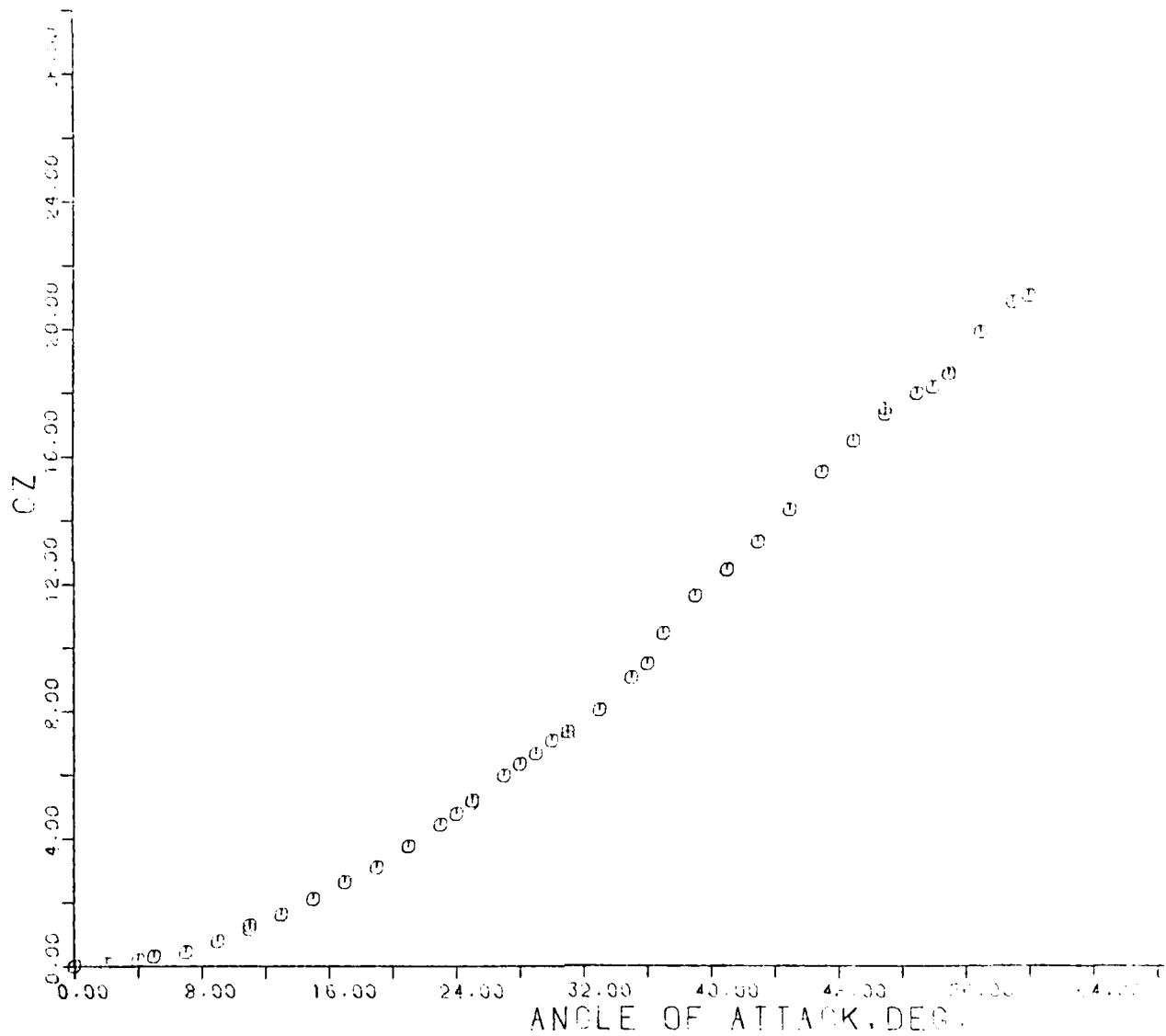


FIG. 63 - C_Z VERSUS α ; M = 9.01 - SHARP NOSED BODY.

C_M VERSUS ANGLE OF ATTACK

MACH .901 SHARP NOSED BODY

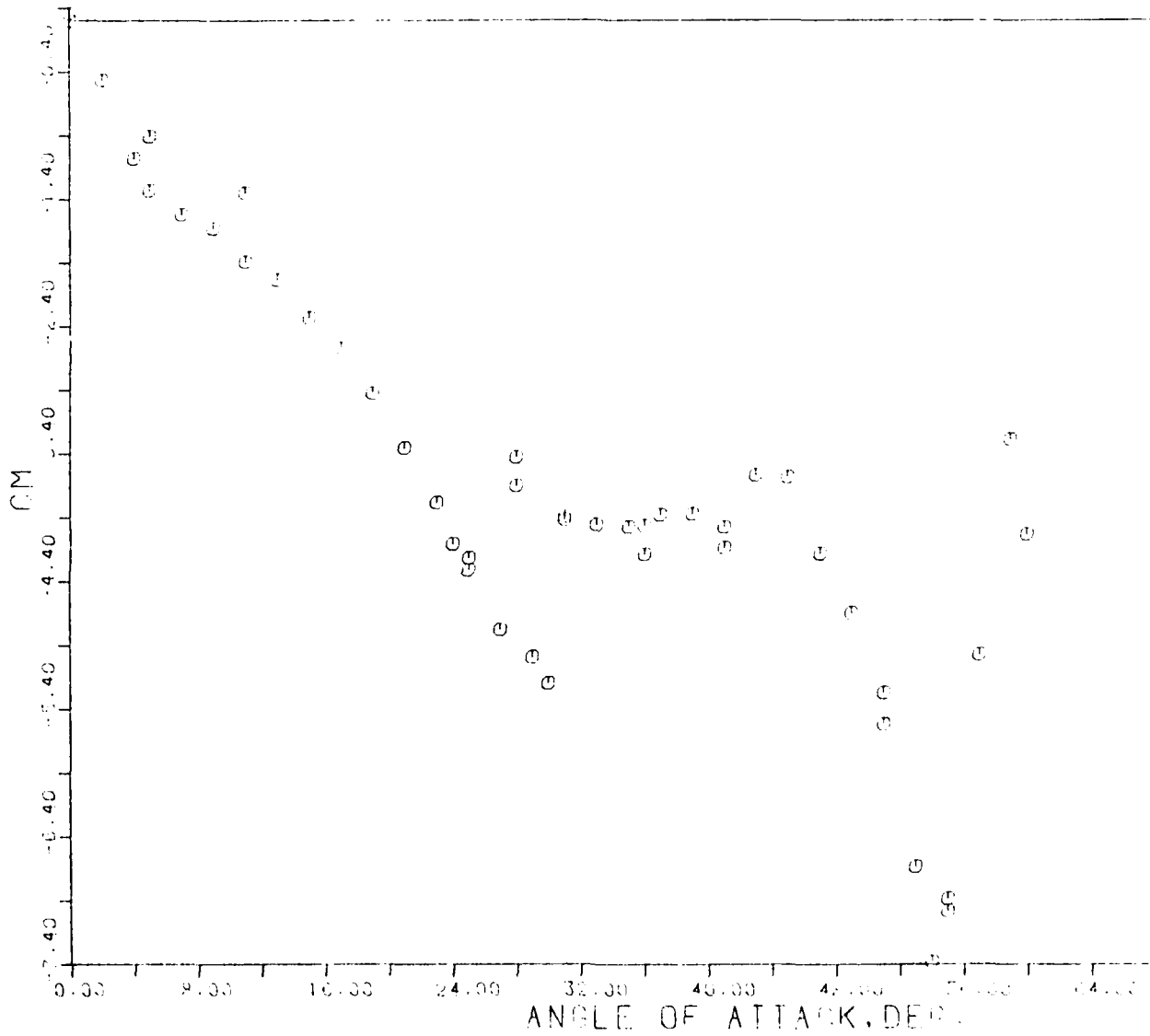


FIG. 64 - C_M VERSUS α ; M = .901 - SHARP NOSED BODY.

XCP/D V₂ ALPHA FOR CZ

M = .901 HARE NOSE

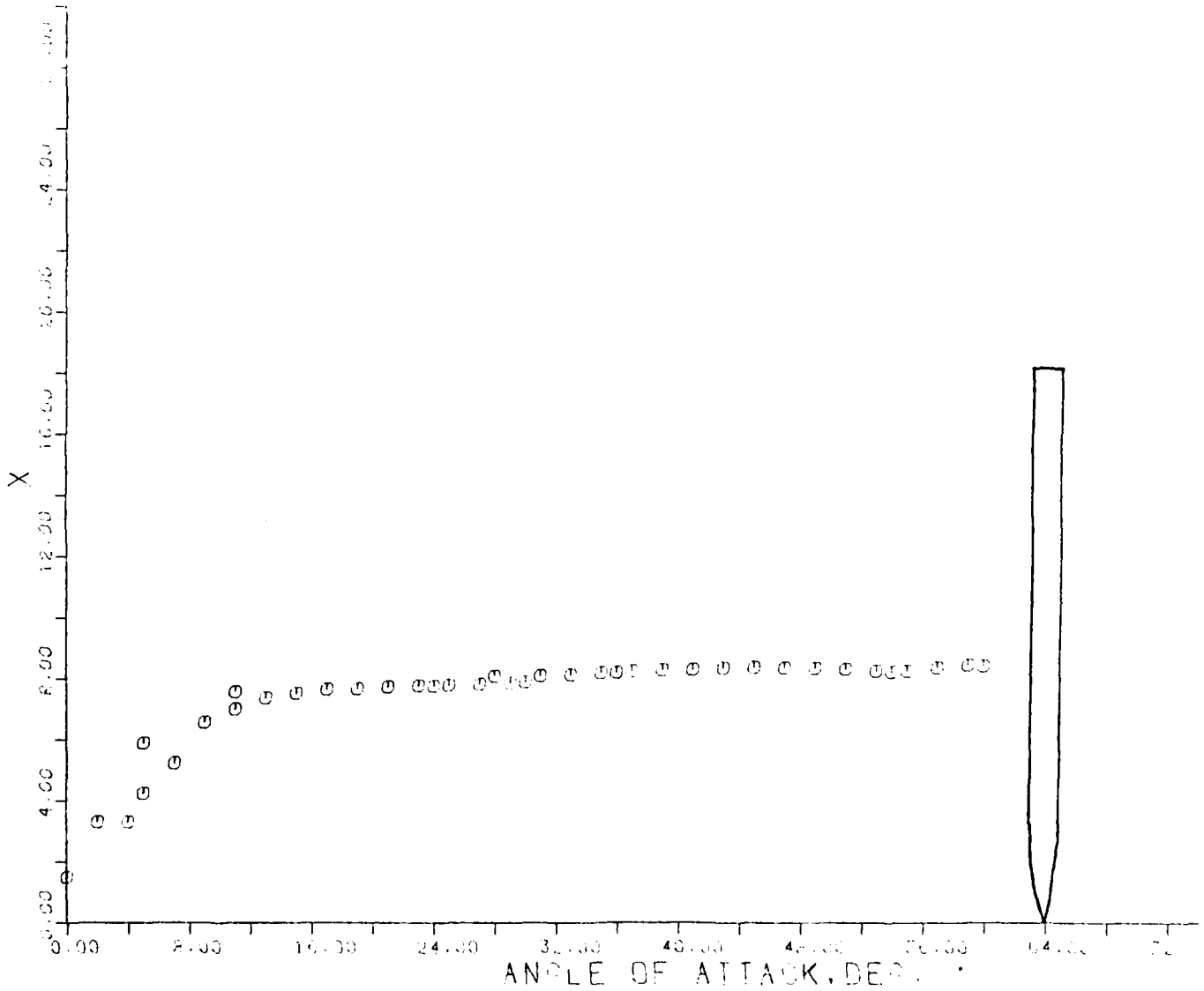


FIG. 65 - $(XCP/D)_Z$ VERSUS α ; M = .901 - SHARP NOSED BODY.

C_L VERSUS ANGLE OF ATTACK

M = .901 SHARP NOSED

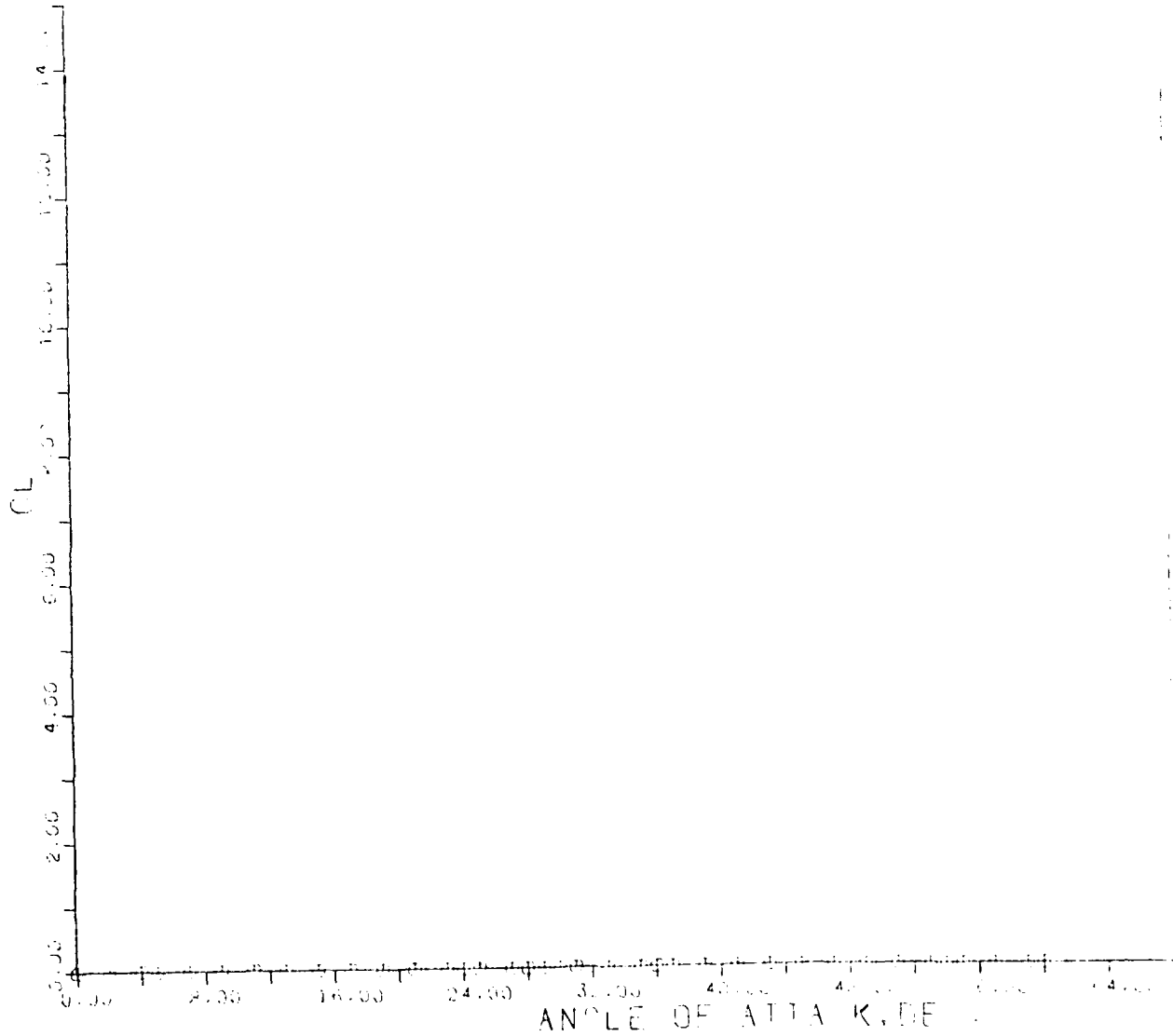


FIG. 66 - C_L VERSUS α ; M = .901 - SHARP NOSED BODY.

C_N VS. ANGLE OF ATTACK

M = .395 BLUNT NOSE

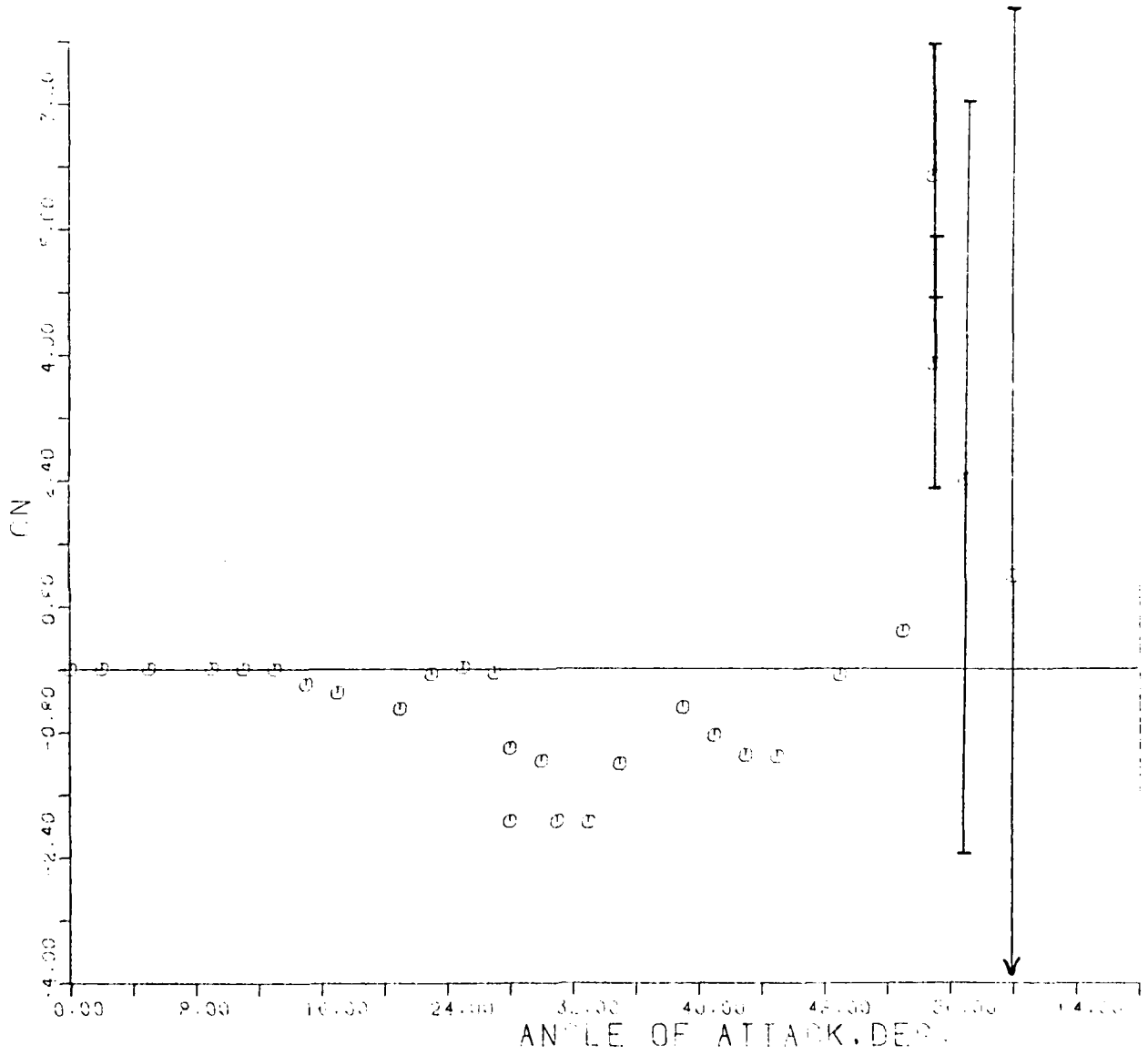


FIG. 67 - C_N VERSUS α ; M = .395 - BLUNT NOSED BODY.

C_Z VERSUS ANGLE OF ATTACK
M = .395 - BLUNT NOSED BODY

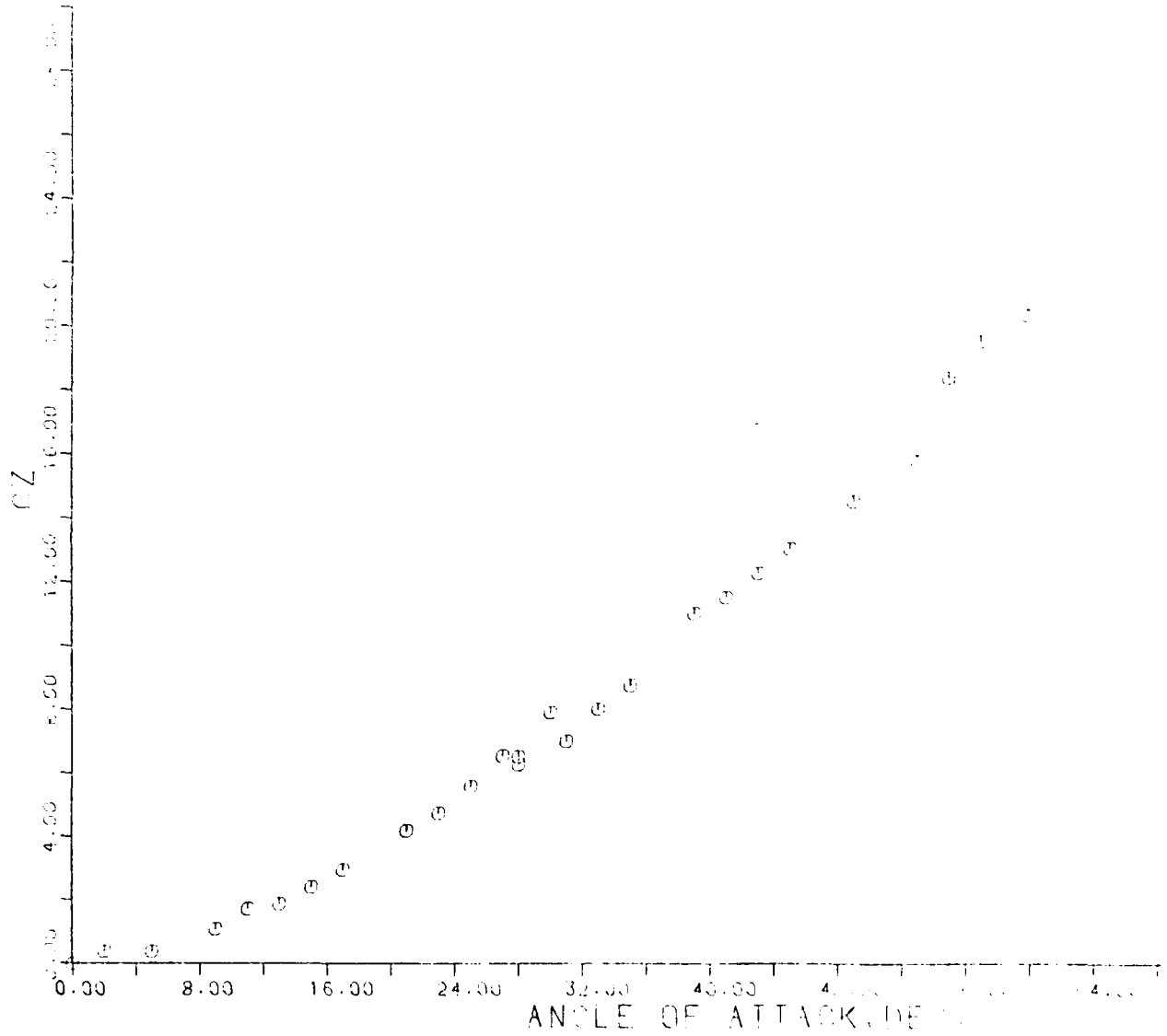


FIG. 68 - C_Z VERSUS α ; M = .395 - BLUNT NOSED BODY.

CM VERSUS ANGLE OF ATTACK
M = .395 - BLUNT NOSED BODY

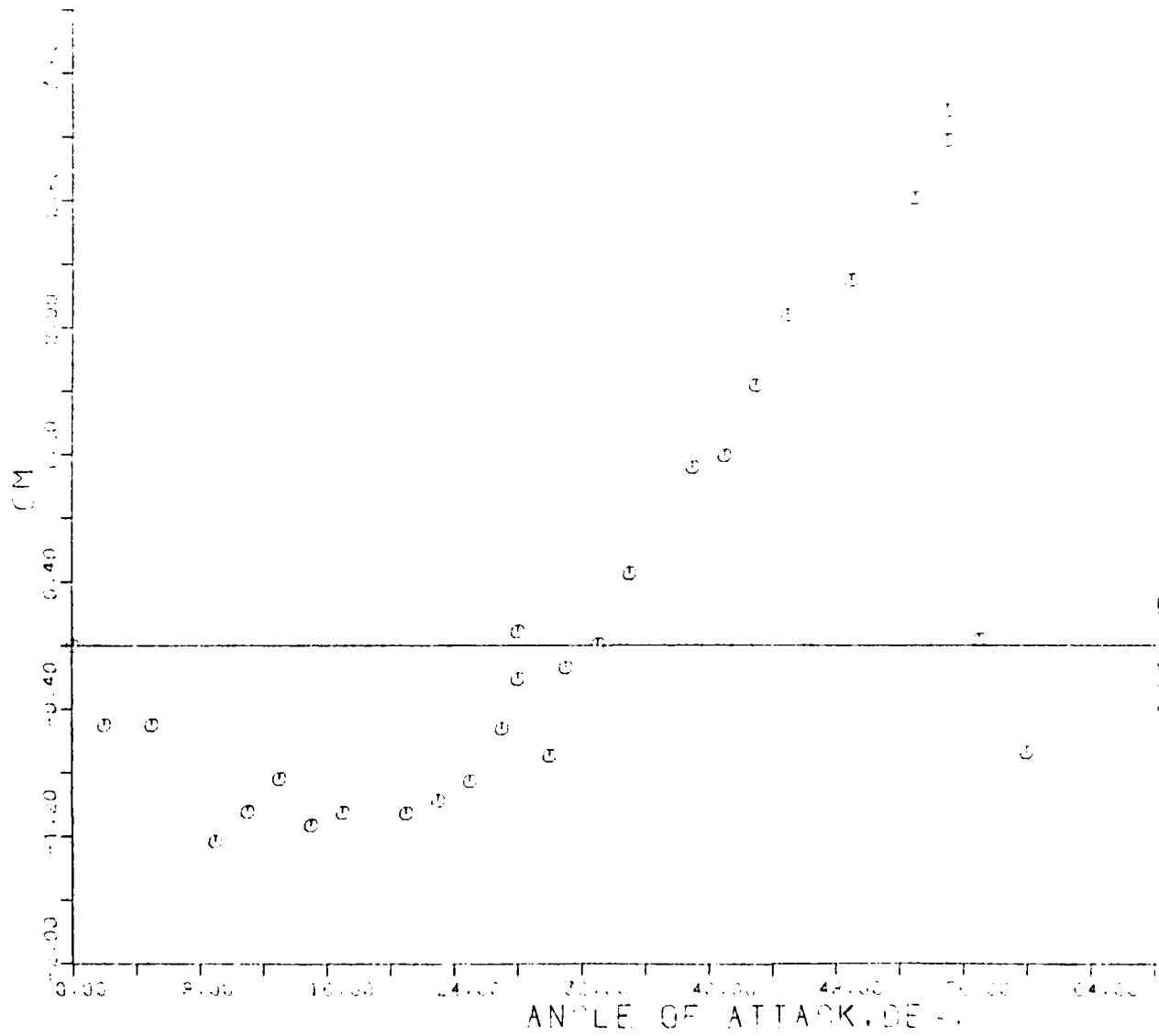


FIG. 69 - C_M VERSUS α ; $M = .395$ - BLUNT NOSED BODY.

XCP/D V. ALPHA FOR CZ
M = .395 - BLUNT NOSE

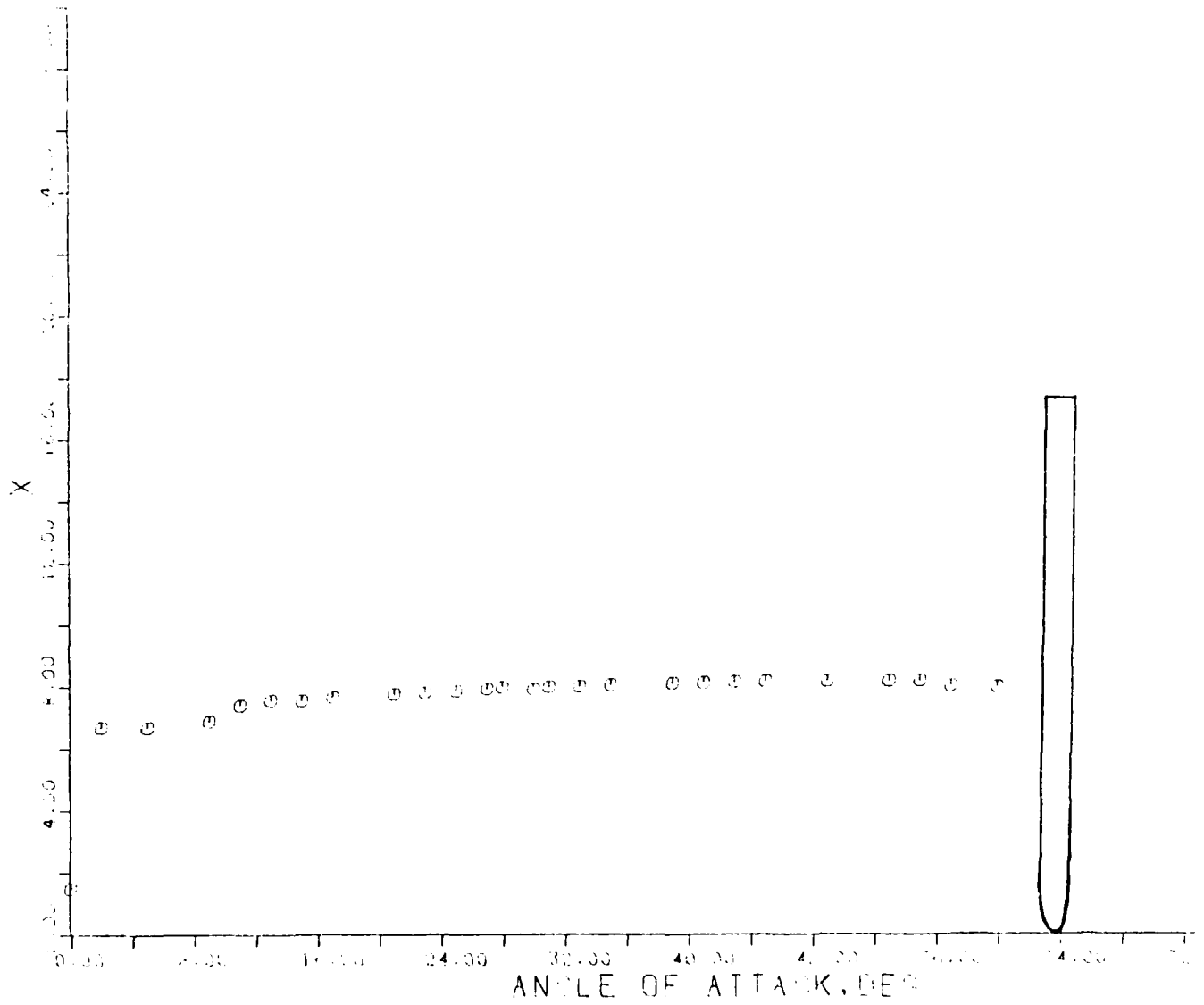


FIG. 70 - $(XCP/D)_Z$ VERSUS α ; $M = .395$ - BLUNT NOSED BODY.

CL VS. ANGLE OF ATTACK
M = .395 BLUNT NOSE

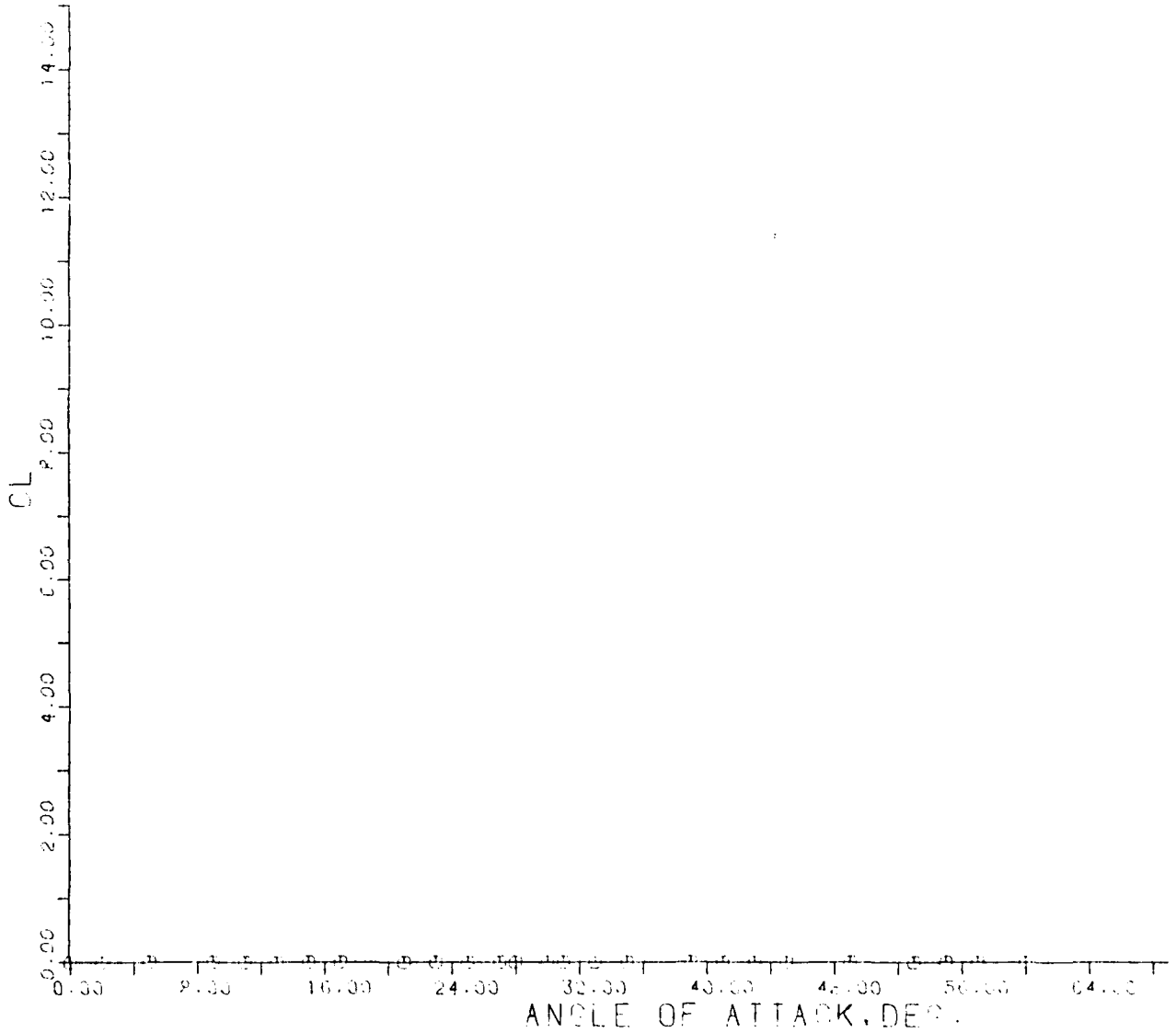


FIG. 71 - C_L VERSUS α ; $M = .395$ - BLUNT NOSED BODY.

CN VS. ANGLE OF ATTACK

M=.611 BLUNT NOSE

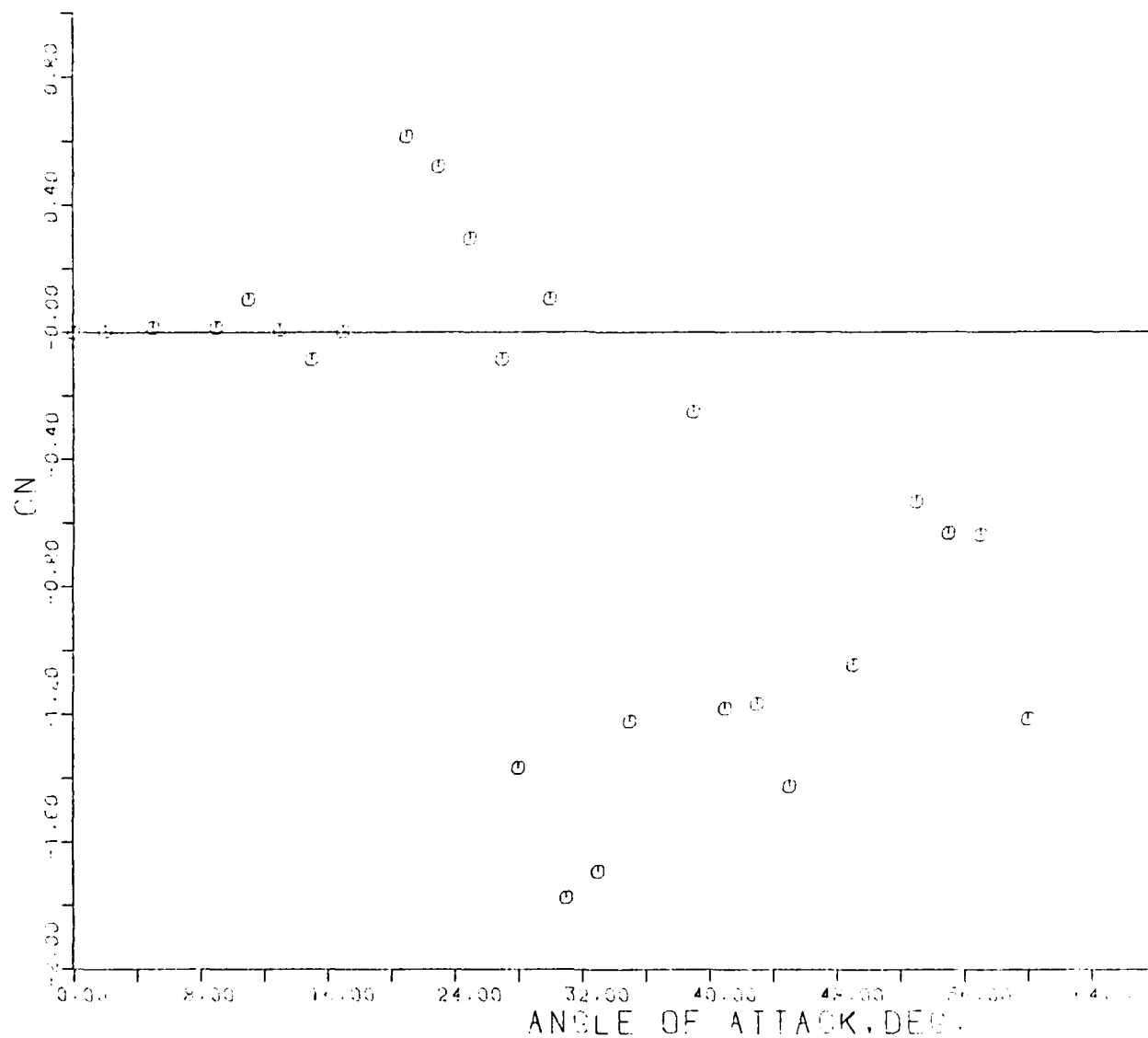


FIG. 72 - C_N VERSUS α ; $M = .611$ - BLUNT NOSED BODY.

CZ VS. ANGLE OF ATTACK
M = .611 BLUNT NOSE

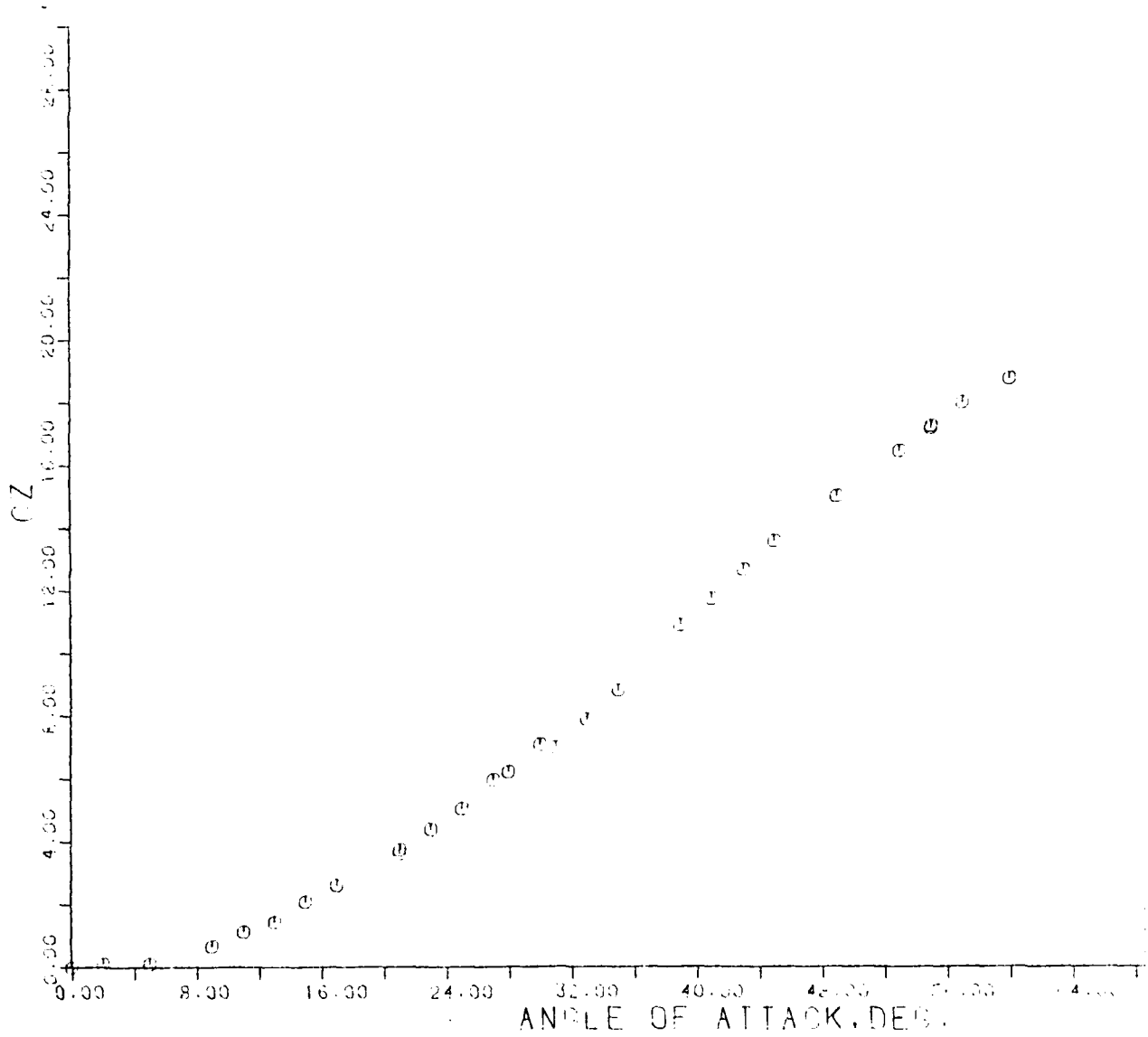


FIG. 73 - C_z VERSUS α ; $M = .611$ - BLUNT NOSED BODY.

CM VERS. ANGLE OF ATTACK

M = .611 BLUNT NOSE

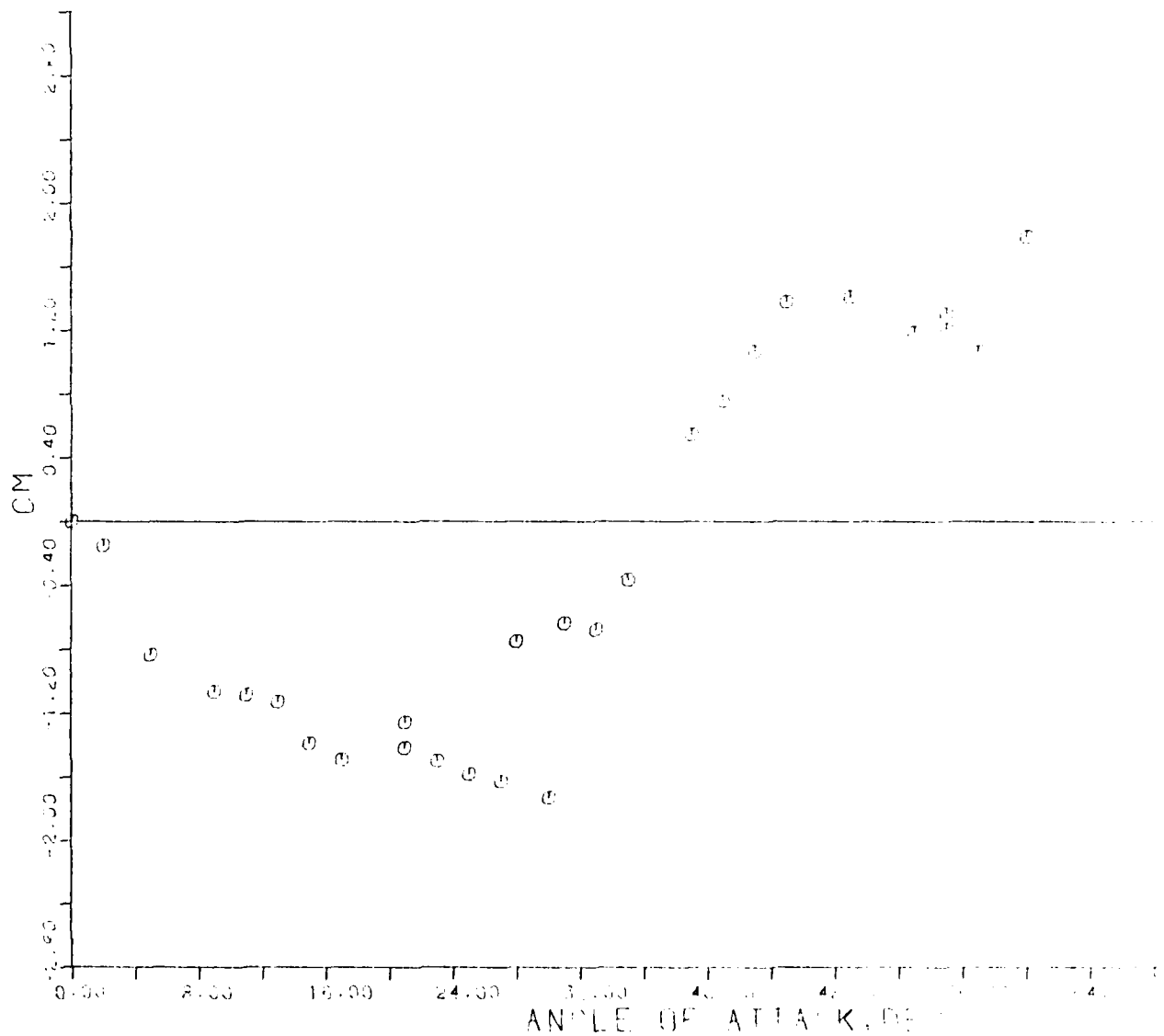


FIG. 74 - C_M VERSUS α ; $M = .611$ - BLUNT NOSED BODY.

XCP/D VS. ALPHA FOR Z
M=.611 BLUNT NOSE

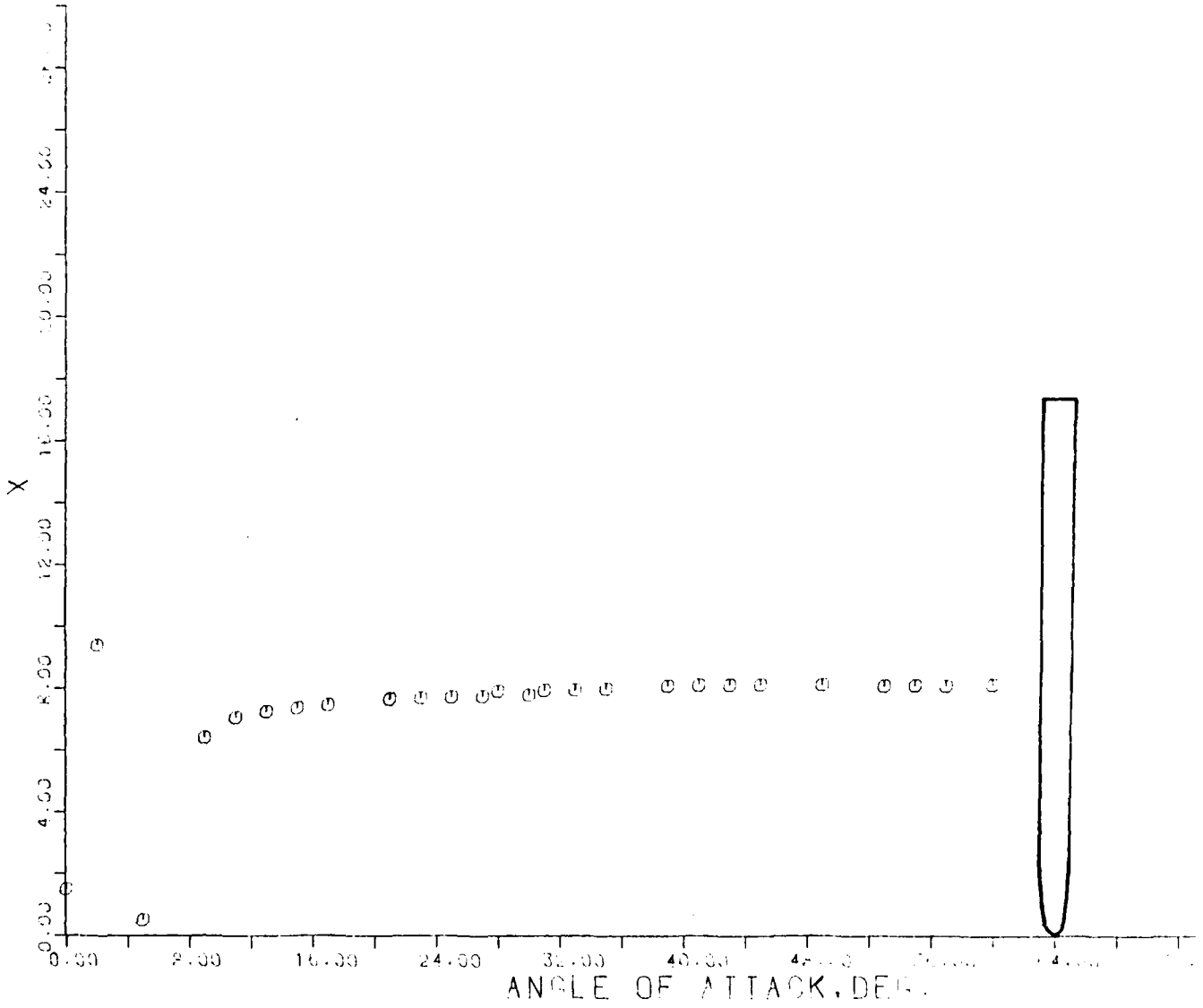


FIG. 75 - $(XCP/D)_z$ VERSUS α ; $M = .611$ - BLUNT NOSED BODY.

CL VS. ANGLE OF ATTACK
M=.611 BLUNT N. B.

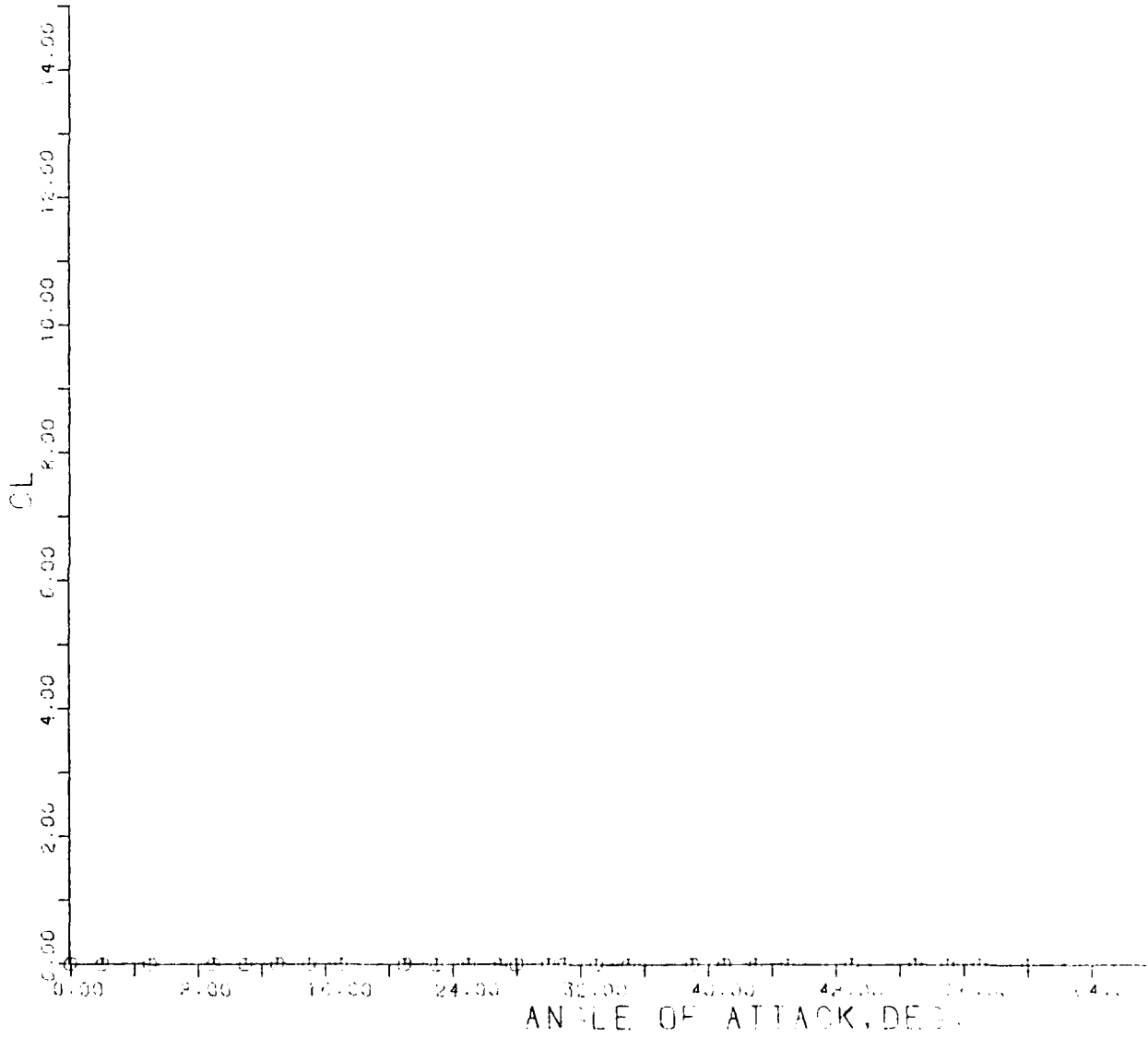


FIG. 76 - C_L VERSUS α ; $M = .611$ - BLUNT NOSED BODY.

CN VS. ANGLE OF ATTACK

M = .698 BLUNT NOSE

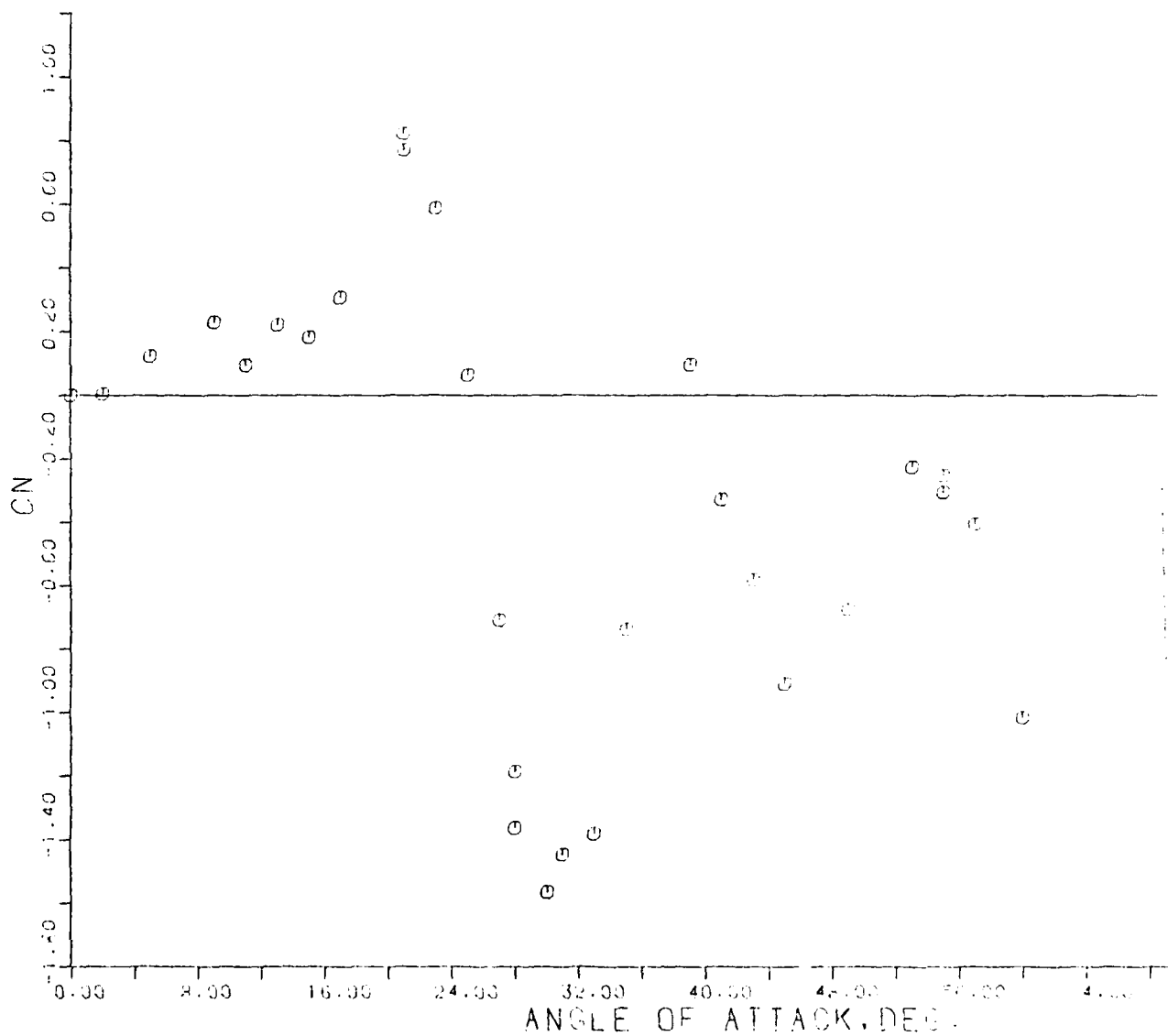


FIG. 77 - C_N VERSUS α ; M = .698 - BLUNT NOSED BODY.

CZ VS. ANGLE OF ATTACK

M = .698 BLUNT NOSE

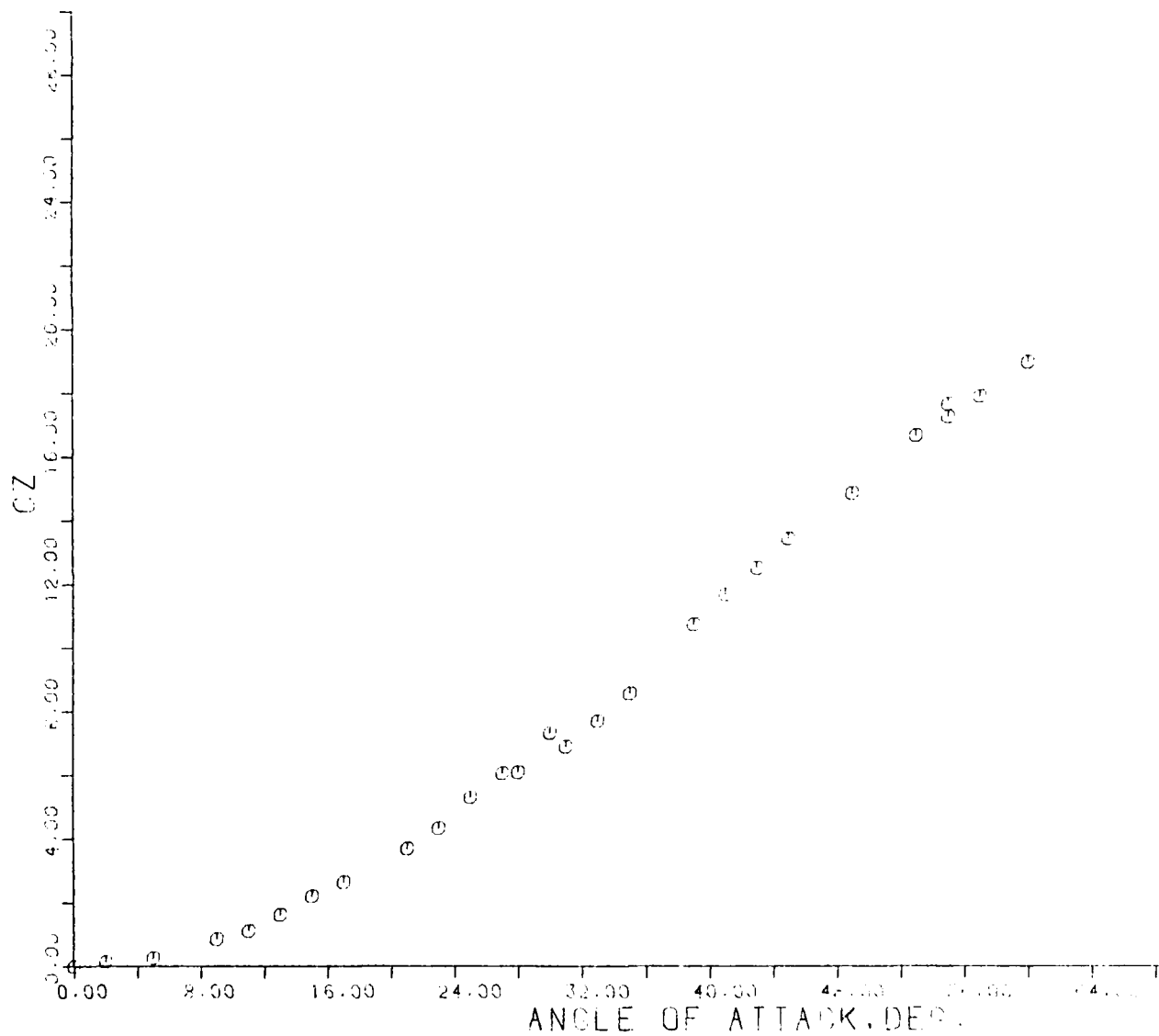


FIG. 78 - C_z VERSUS α ; $M = .698$ - BLUNT NOSED BODY.

CM VS. ANGLE OF ATTACK

M = 0.698 BLUNT NOSE

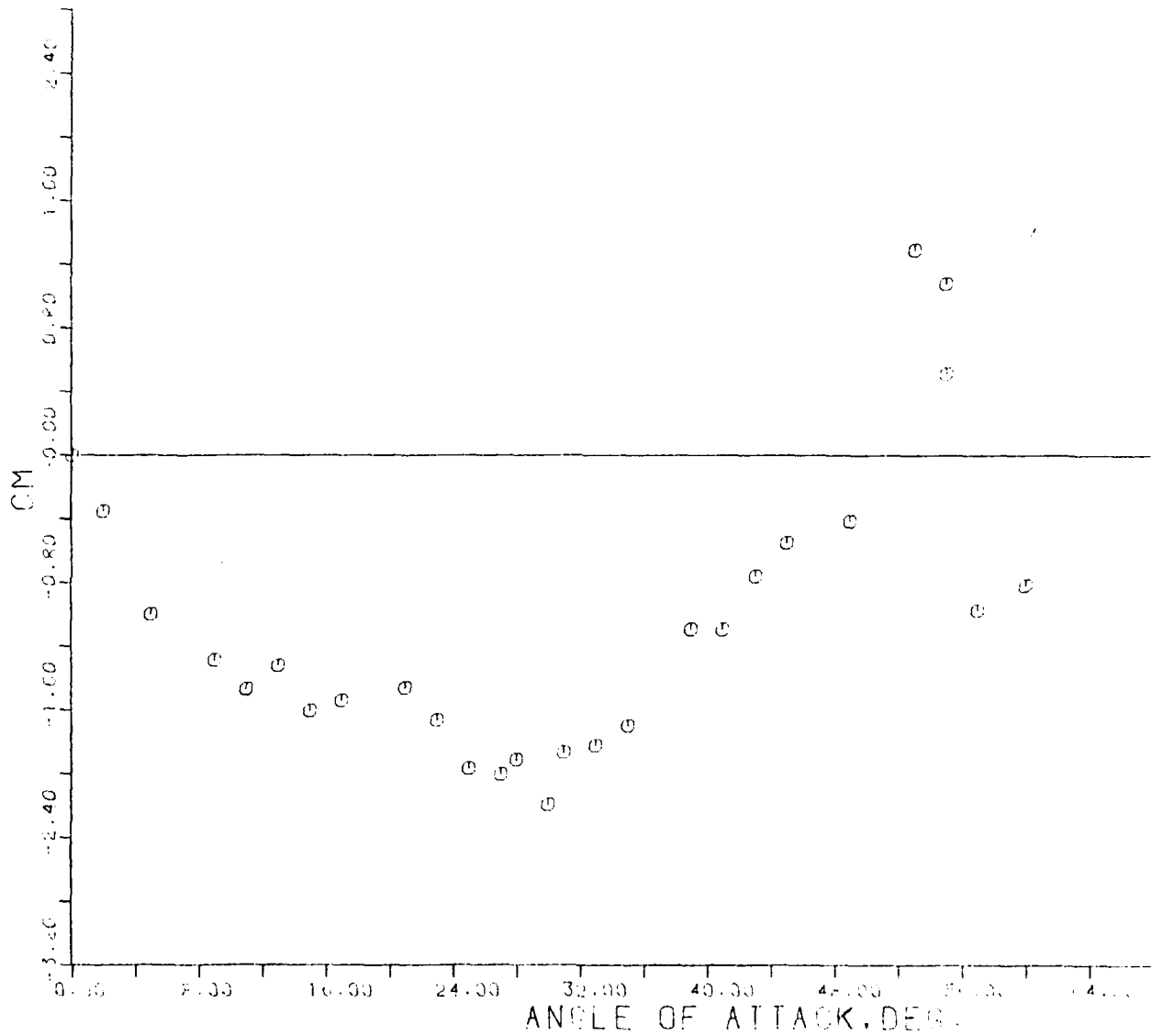


FIG. 79 - C_M VERSUS α ; $M = .698$ - BLUNT NOSED BODY.

XCP/D VS. ALPHA FOR CZ

M = .698 BLUNT NOSE

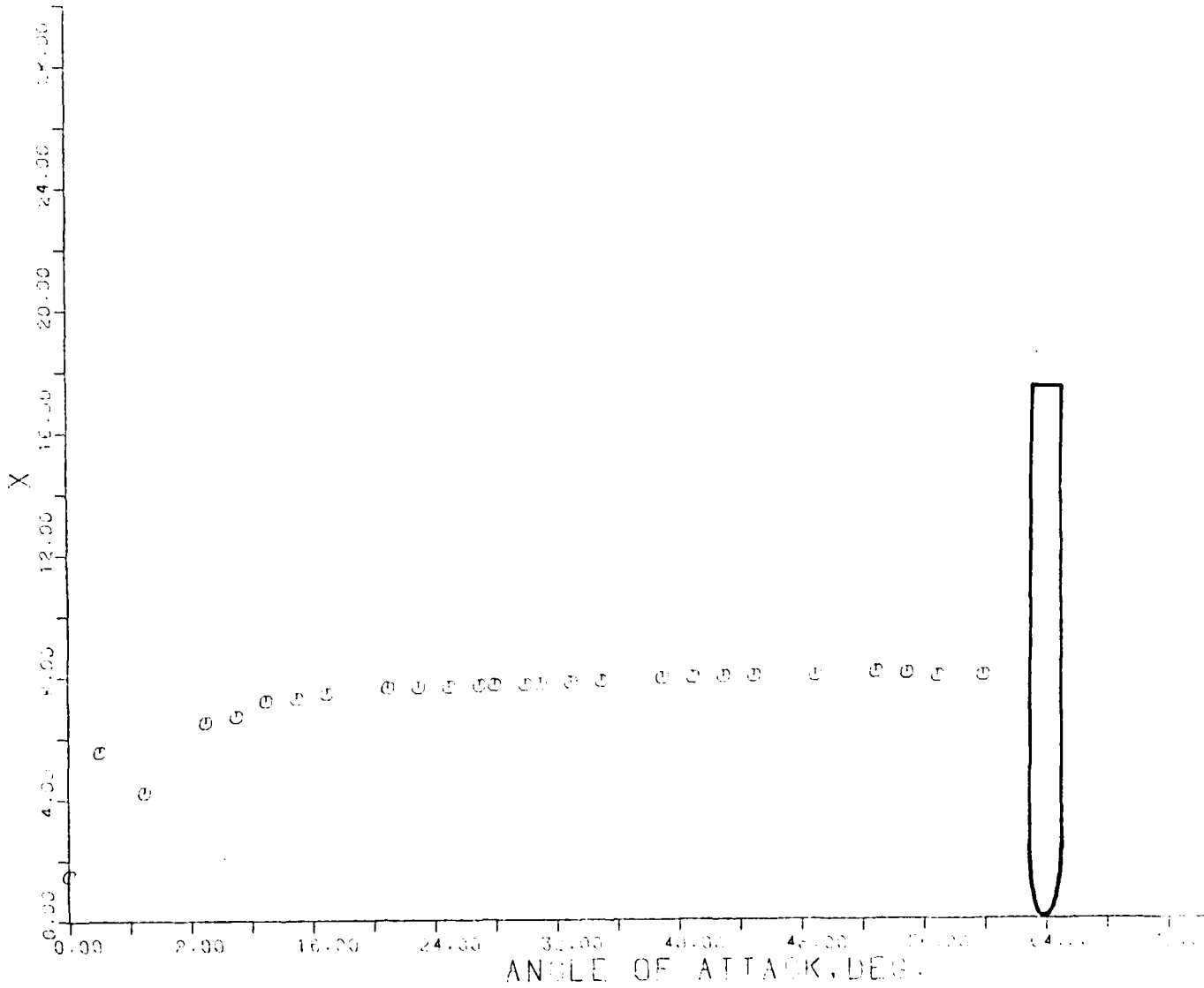


FIG. 80 $(X_{CP}/D)_Z$ α ; $M = .698$ - BLUNT NOSED BODY.

CL VS. ANGLE OF ATTACK

M = .698 - BLUNT NOSE

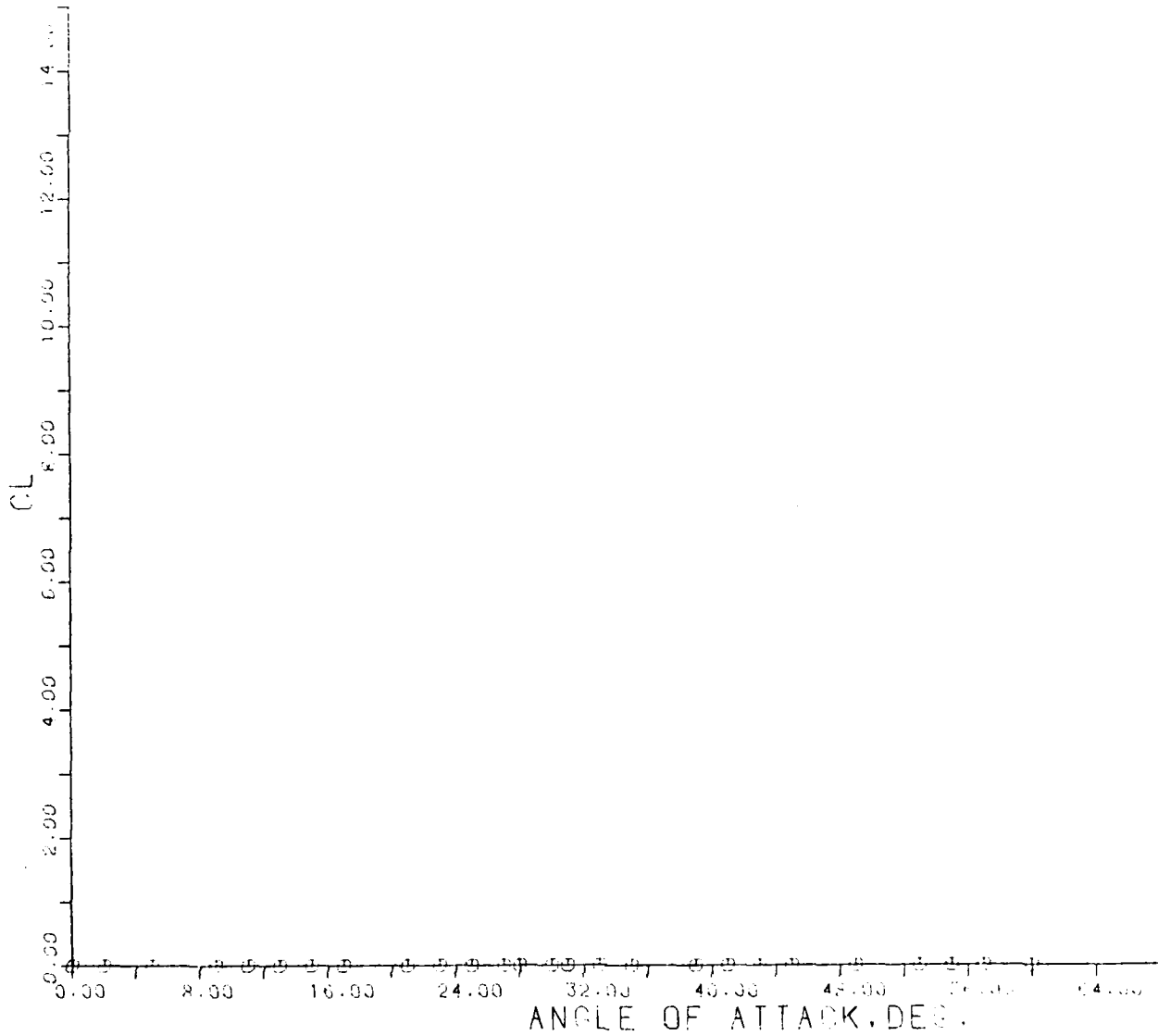


FIG. 81 - C_L VERSUS α ; $M = .698$ - BLUNT NOSED BODY.

CN VS. ANGLE OF ATTACK

M = .797 BLUNT NOSE

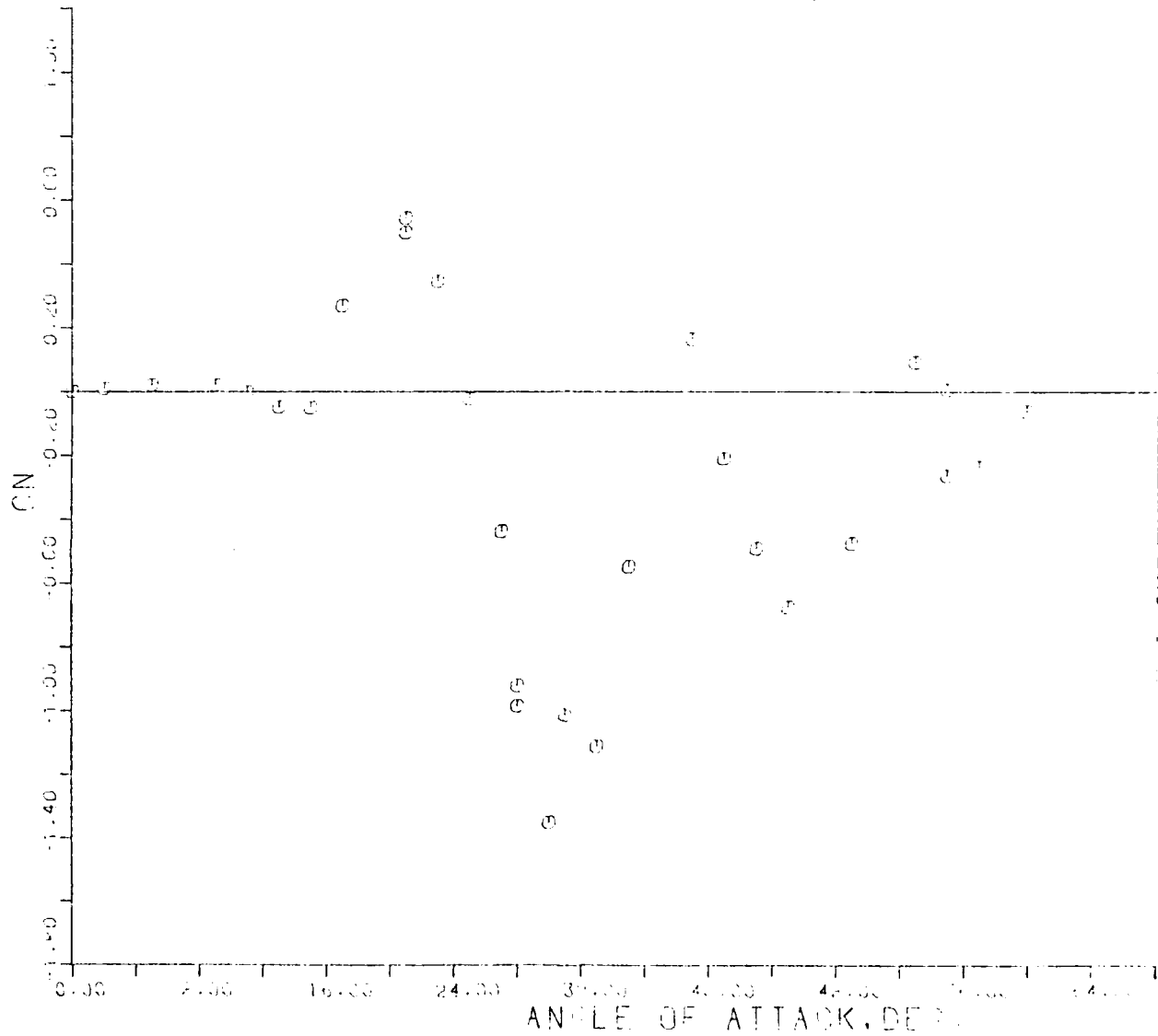


FIG. 82 - C_N VERSUS α ; M = .797 - BLUNT NOSED BODY.

C_Z VS. ANGLE OF ATTACK
NO. 77 BLUNT BODY

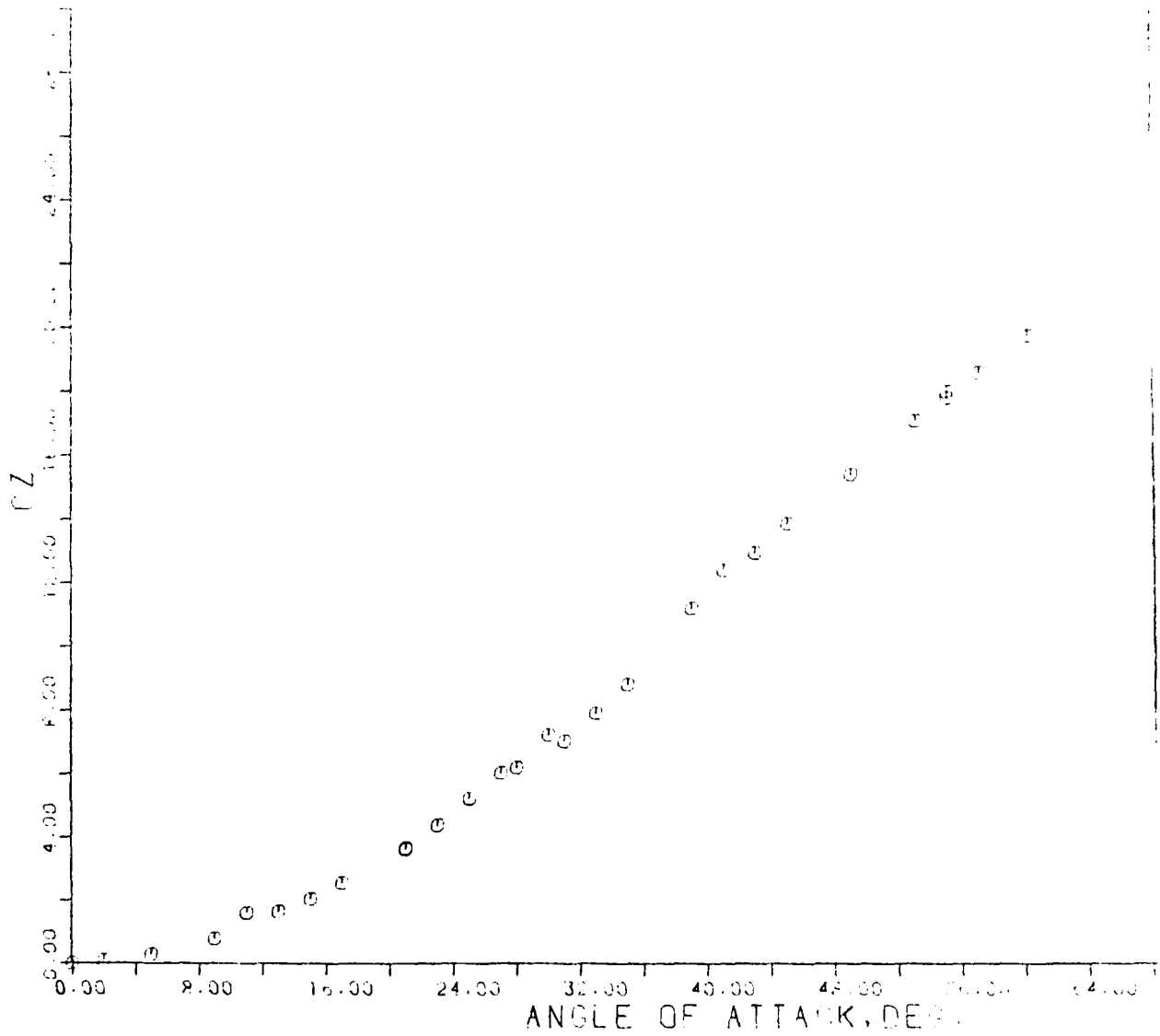


FIG. 83 - C_Z VERSUS α ; $M = .797$ - BLUNT NOSED BODY.

CM VS. ANGLE OF ATTACK

M = .797 BLUNT NOSE

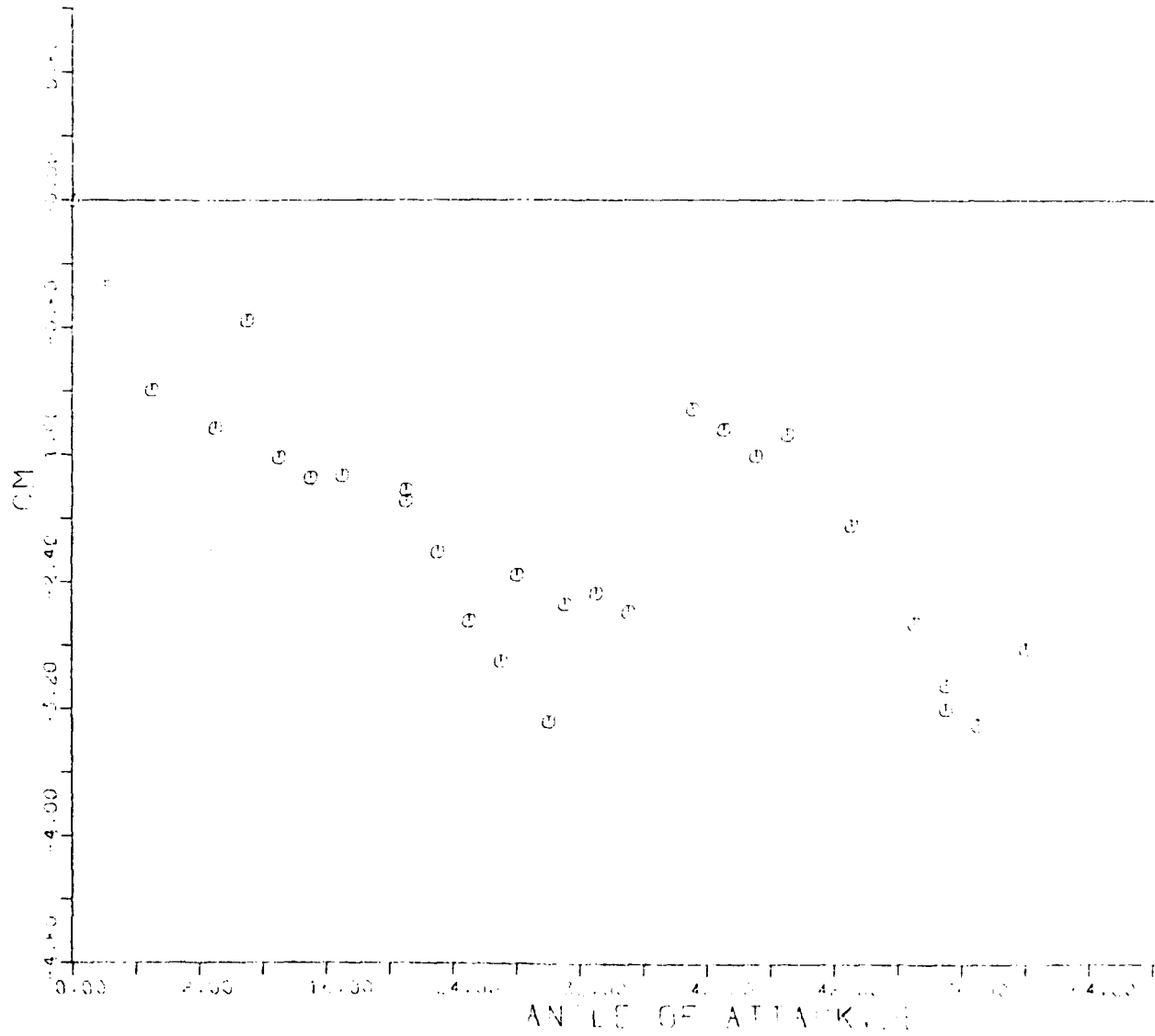


FIG. 84 - C_M VERSUS α ; $M = .797$ - BLUNT NOSED BODY.

XCP/D VS. ALPHA FOR OZ
M = .797 BLUNT NOSE

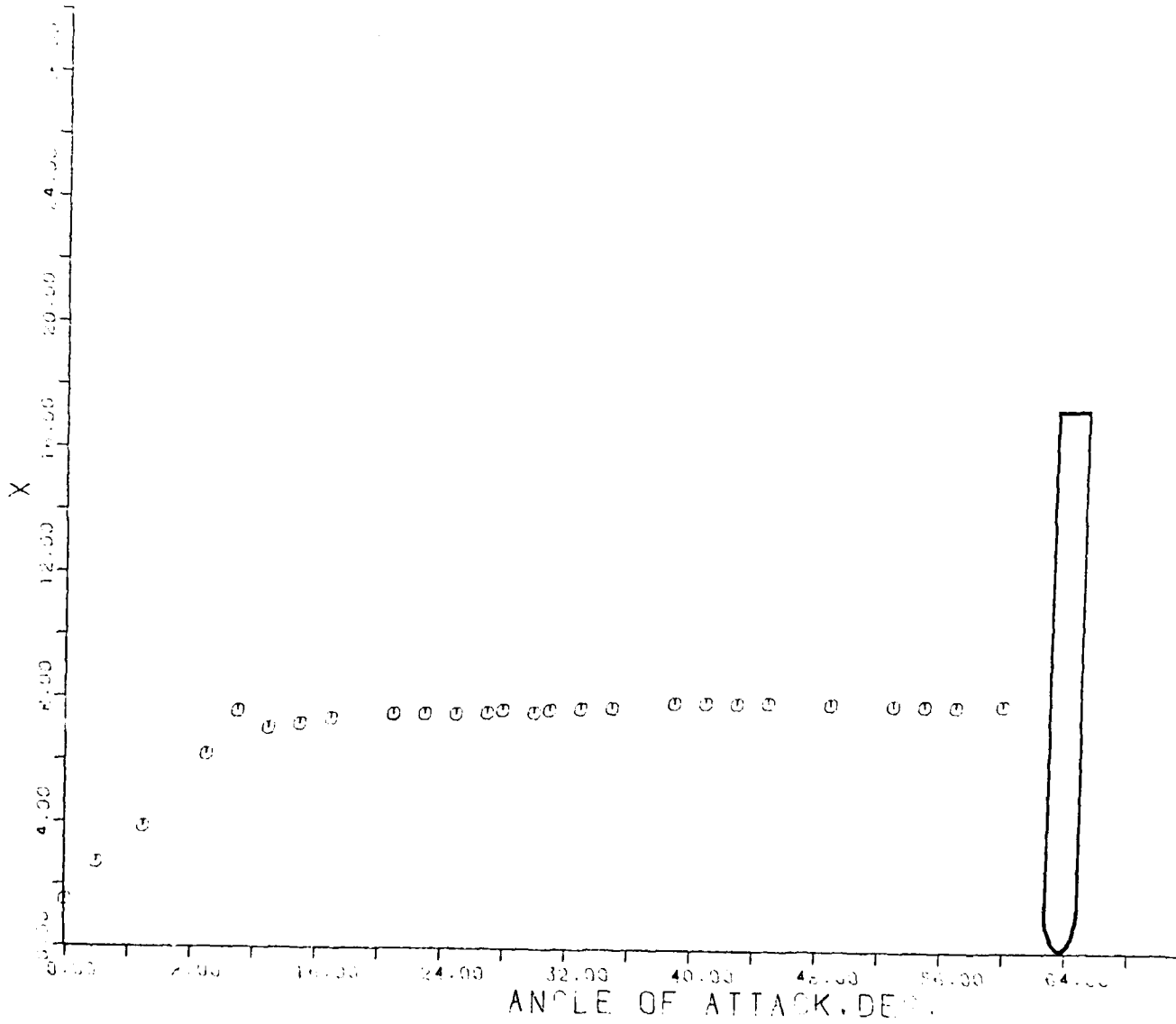


FIG. 85 - $(XCP/D)_Z = \alpha$; $M = .797$ - BLUNT NOSED BODY.

CL VS. ANGLE OF ATTACK

M = .797 BLUNT NOSE

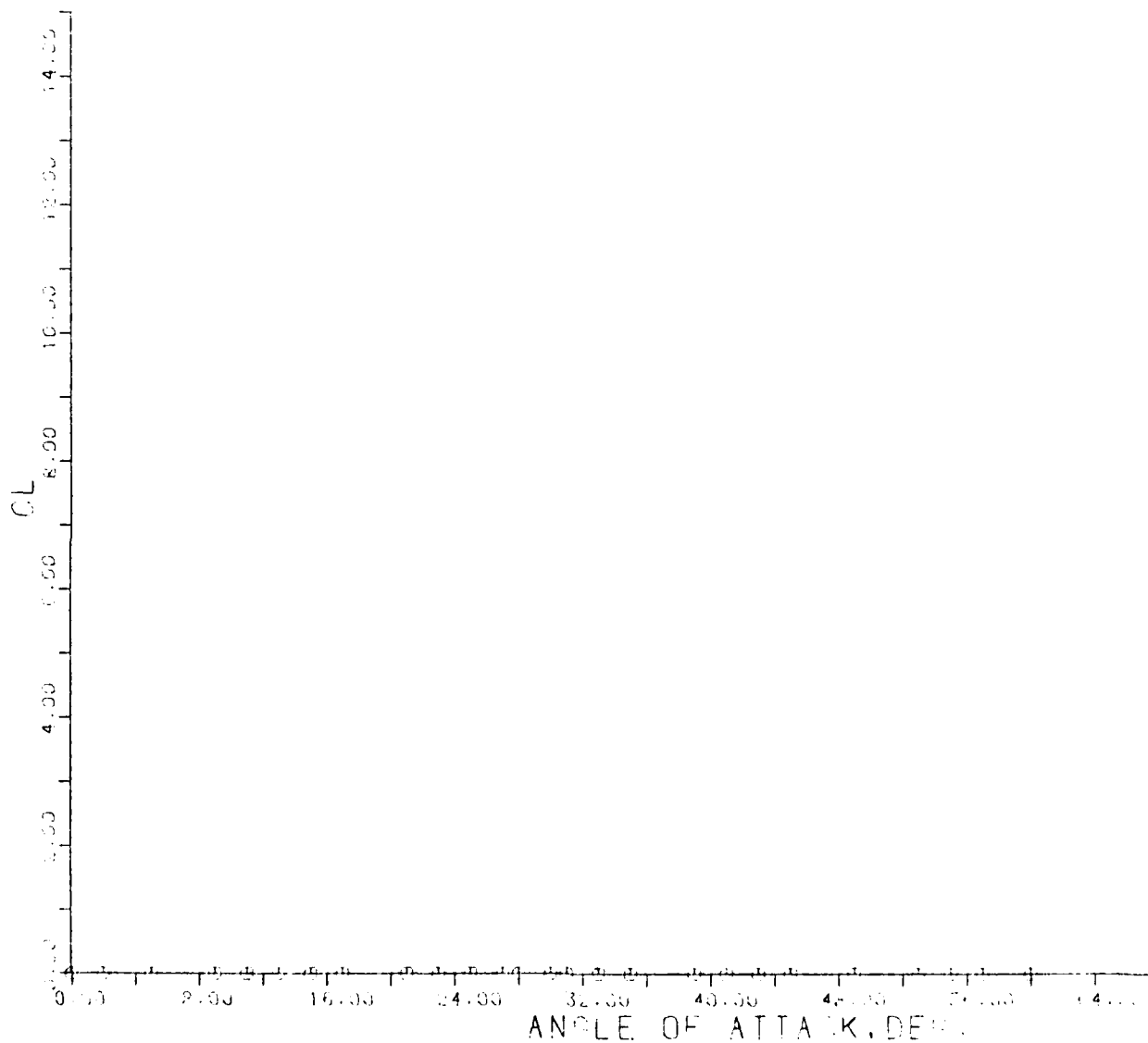


FIG. 86 - C_L VERSUS α ; $M = .797$ - BLUNT NOSED BODY.

C_Y VS. ANGLE OF ATTACK

M = .417 SHARP NOSE

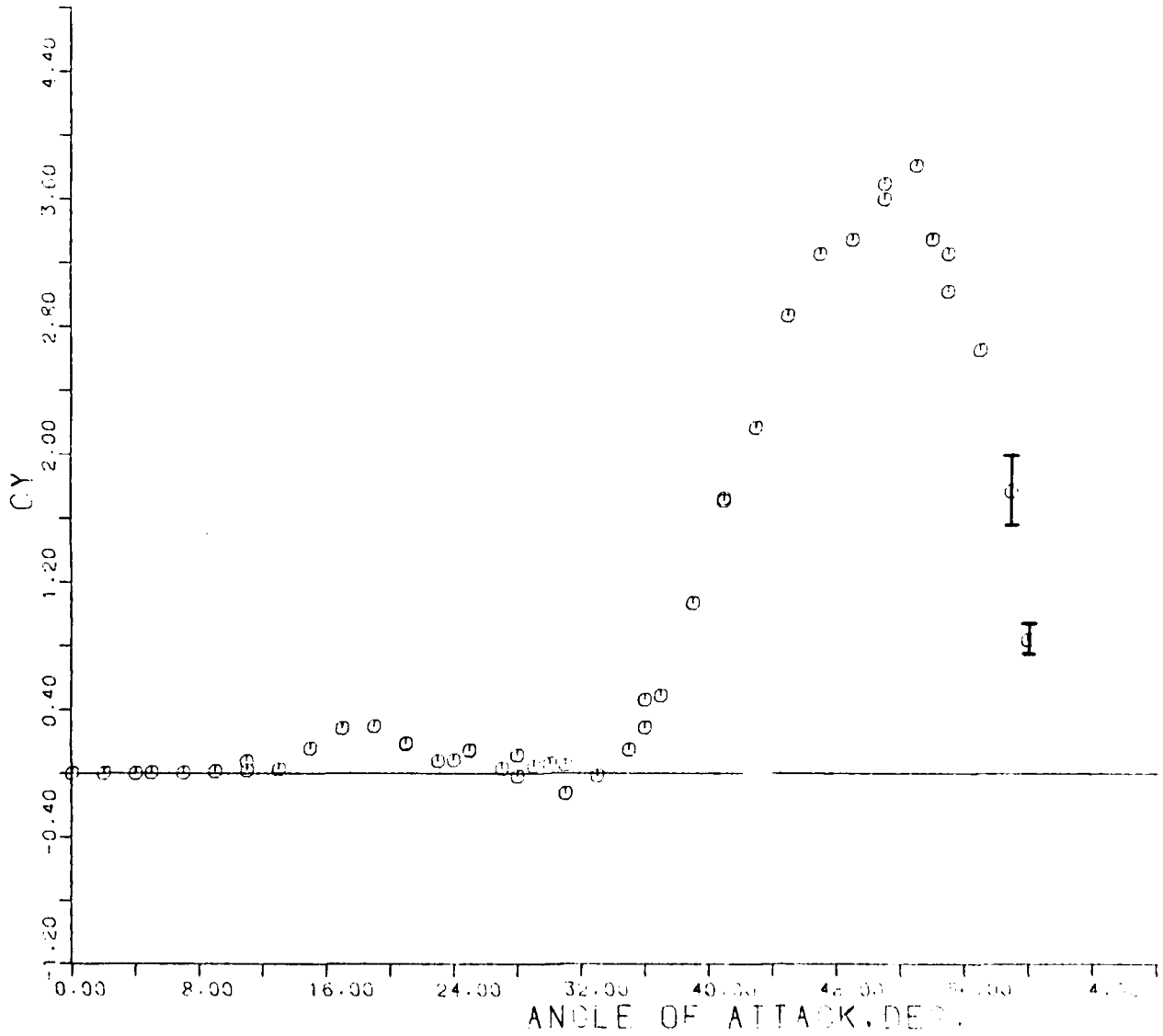


FIG. 87 - C_Y VERSUS α ; M = .417 - SHARP NOSED BODY.

XCP/D VS. ALPHA FOR CY
M=.417 SHARP NOSE

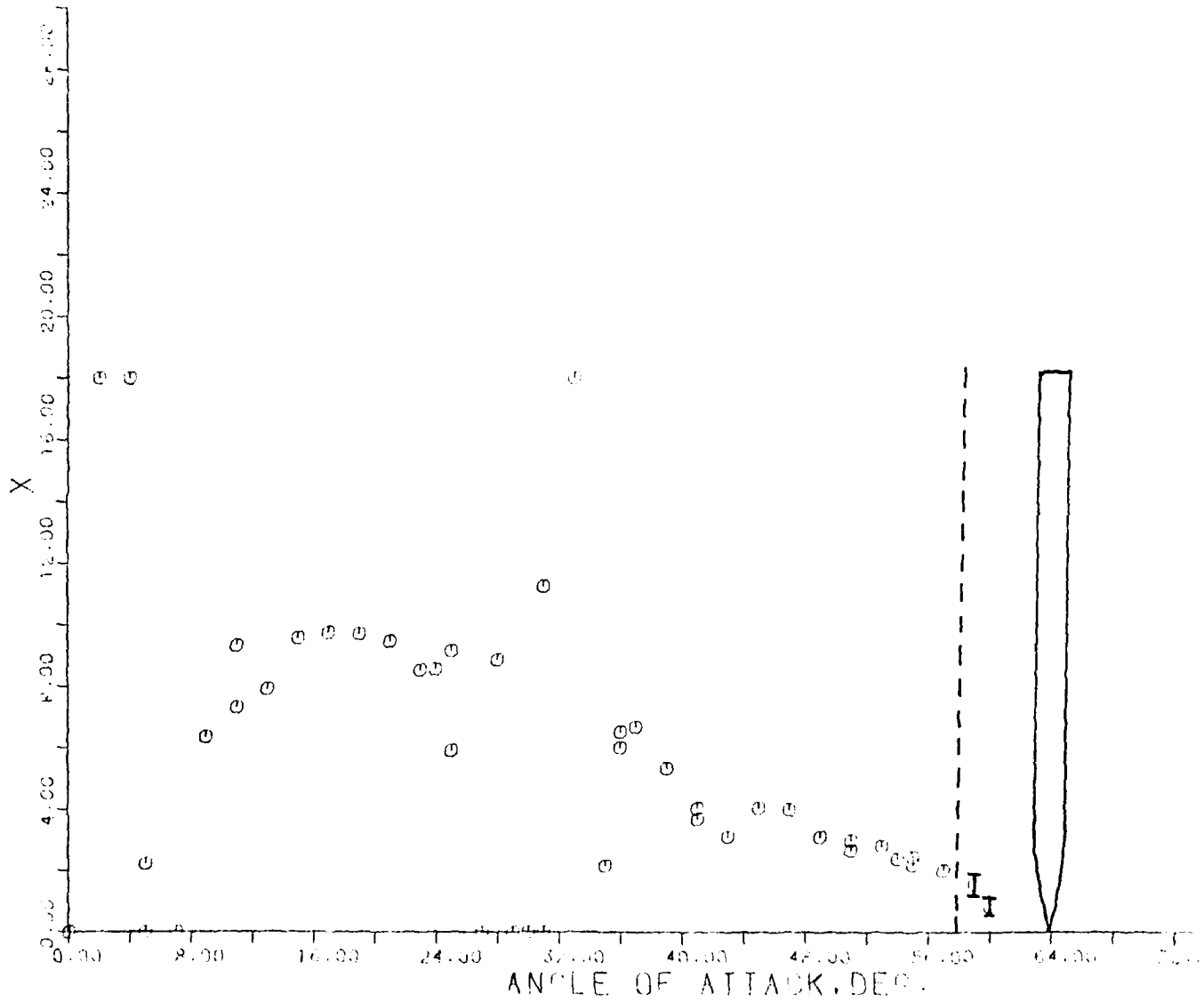


FIG. 88 - $(XCP/D)_y$ VERSUS α ; $M = .417$ - SHARP NOSED BODY.

CY VS. ANGLE OF ATTACK

M = .617 SHARP NOSE

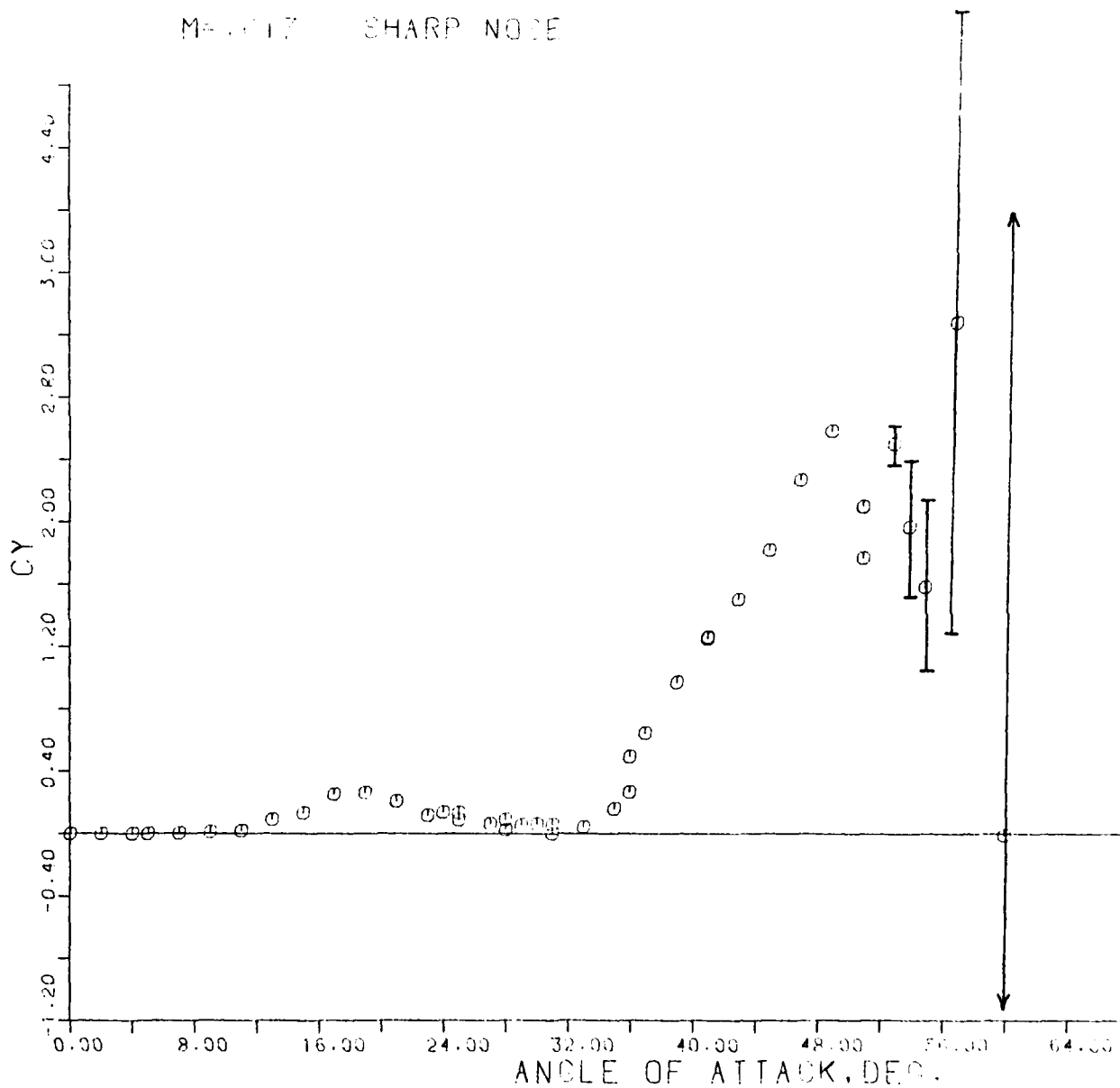


FIG. 89 - C_Y VERSUS α ; $M = .617$ - SHARP NOSED BODY.

XCP/D VS. ALPHA FOR CY

M=.617 SHARP NOSE

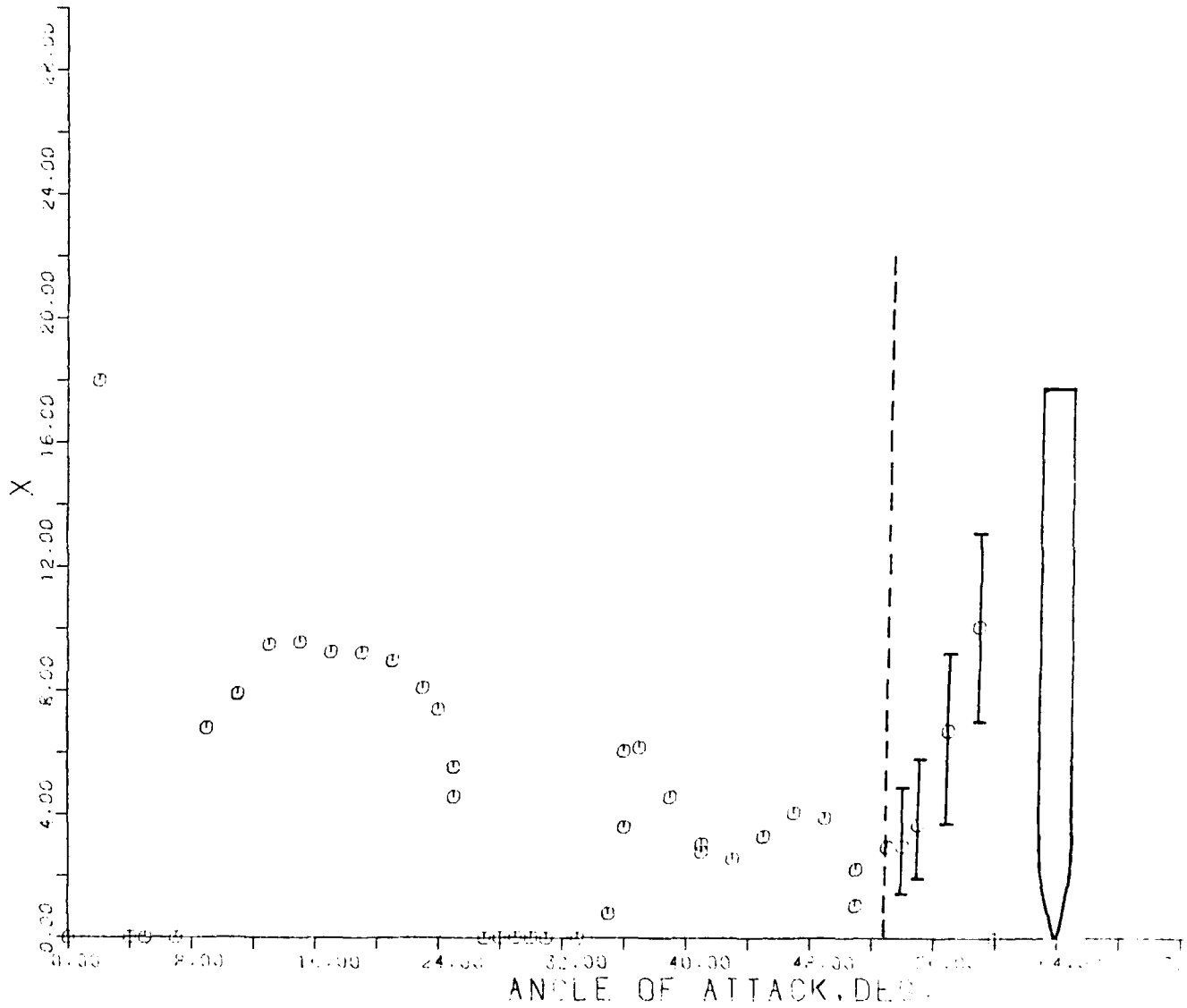


FIG. 90 - $(XCP/D)_Y$ VERSUS α ; M = .617 - SHARP NOSED BODY.

CY VS. ANGLE OF ATTACK

M = .695 SHARP NOSE

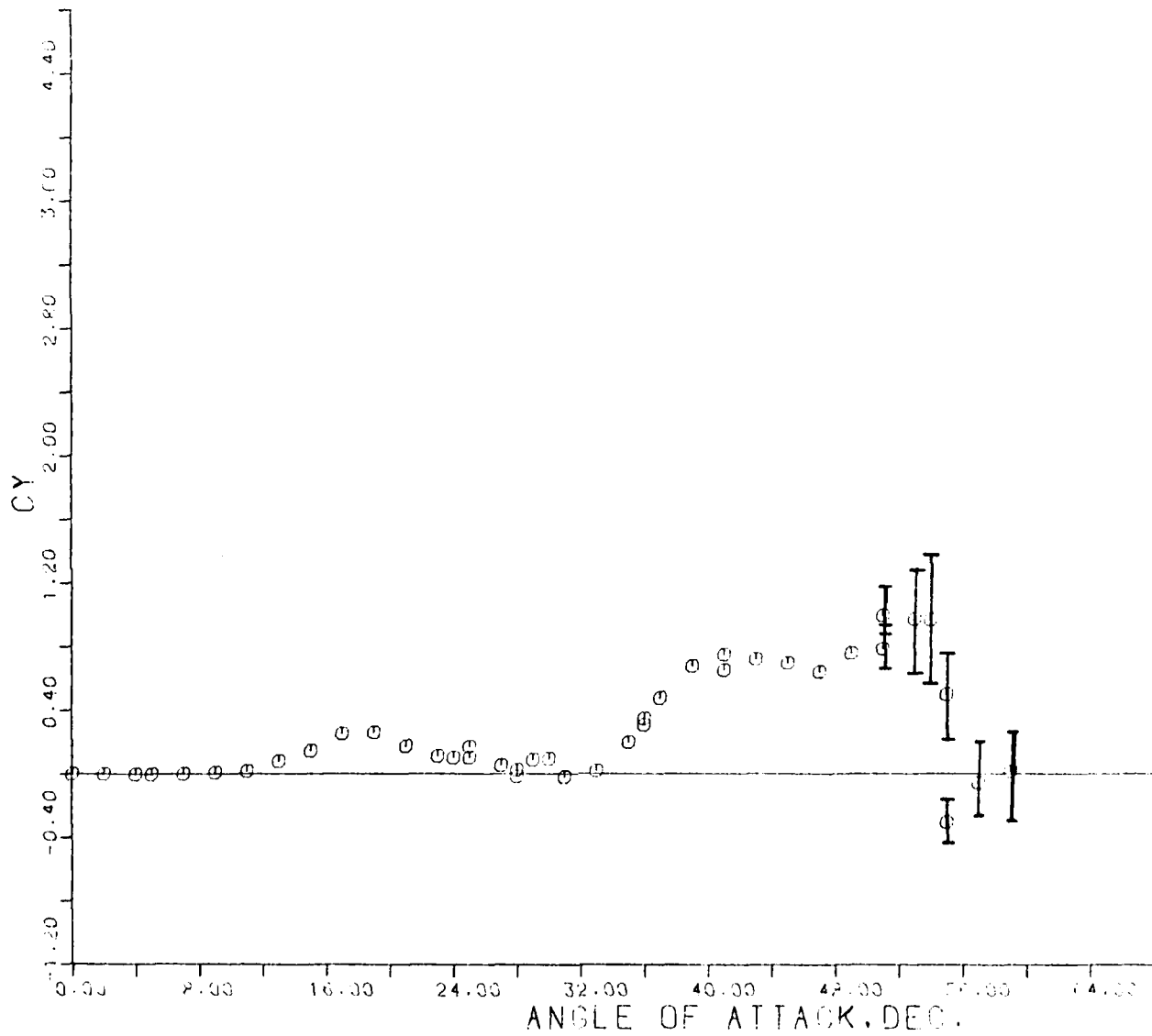


FIG. 91 - C_Y VERSUS α ; $M = .695$ - SHARP NOSED BODY.

XCP/D VS. ALPHA FOR CY

M = .695 SHARP NOSE

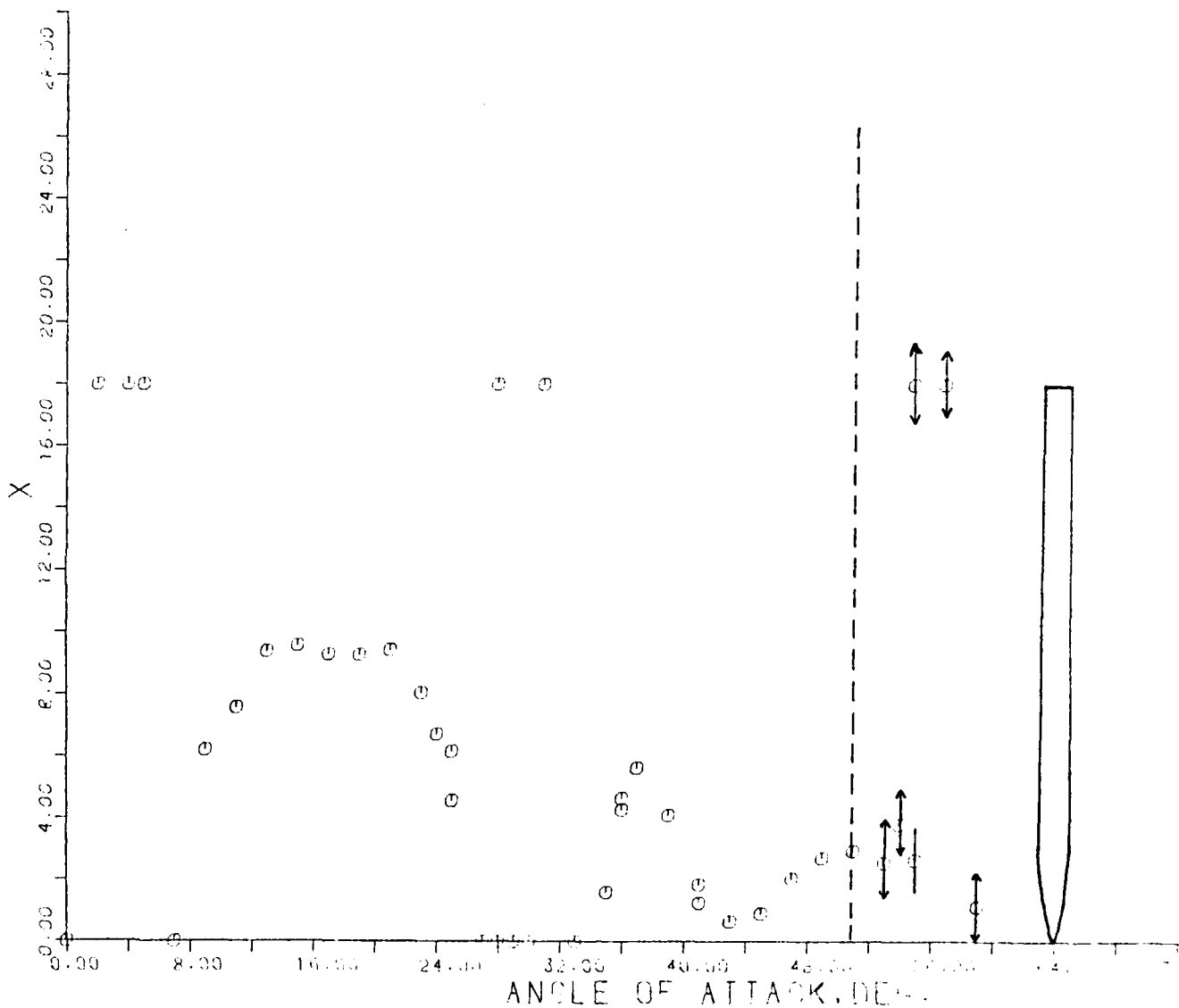


FIG. 92 - $(XCP/D)_\gamma$ α ; M = .695 - SHARP NOSED BODY.

CY VS. ANGLE OF ATTACK

M = .796 SHARP NOSE

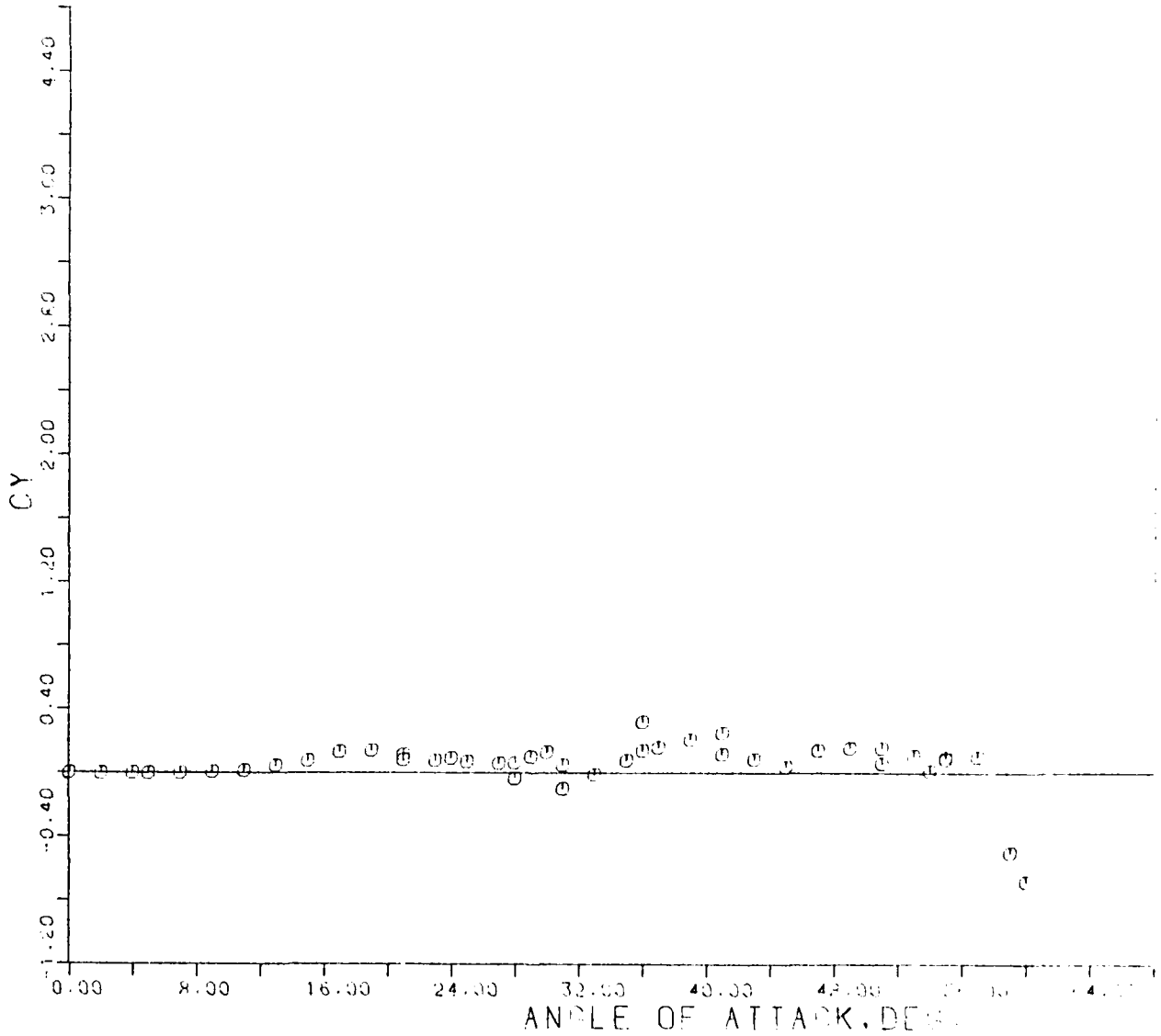


FIG. 93 - C_Y VERSUS α ; $M = .796$ - SHARP NOSED BODY.

XCP/D VS. ALPHA FOR CY

M = .796 SHARP NOSE

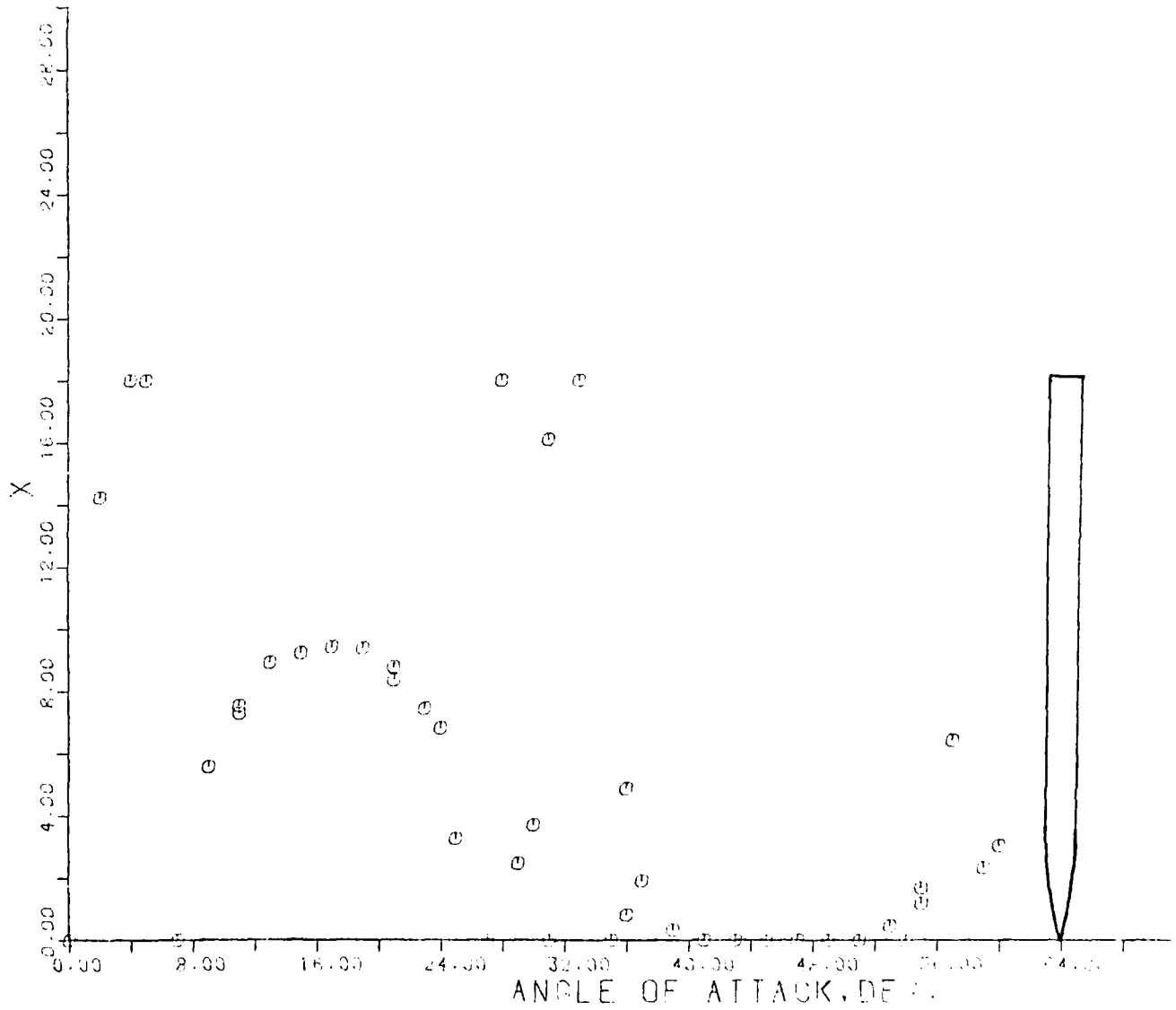


FIG. 94 - $(XCP/D)_y$ VERSUS α ; M = .796 - SHARP NOSED BODY.

CY VS. ANGLE OF ATTACK

M = .901 SHARP NOSE

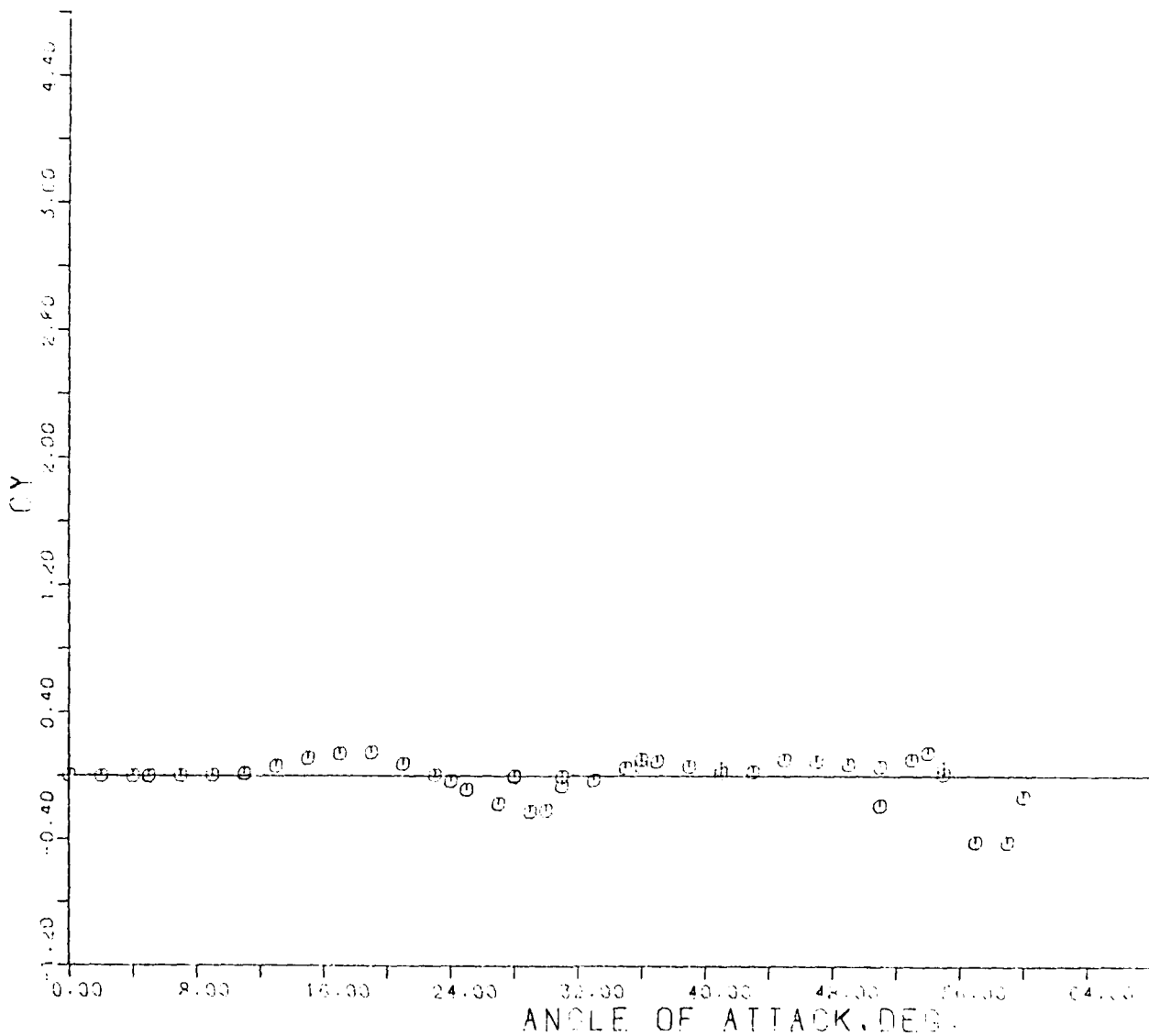


FIG. 95 - C_Y VERSUS α ; $M = .901$ - SHARP NOSED BODY.

XCP/D VS. ALPHA FOR CY

M = .901 SHARP NOSE

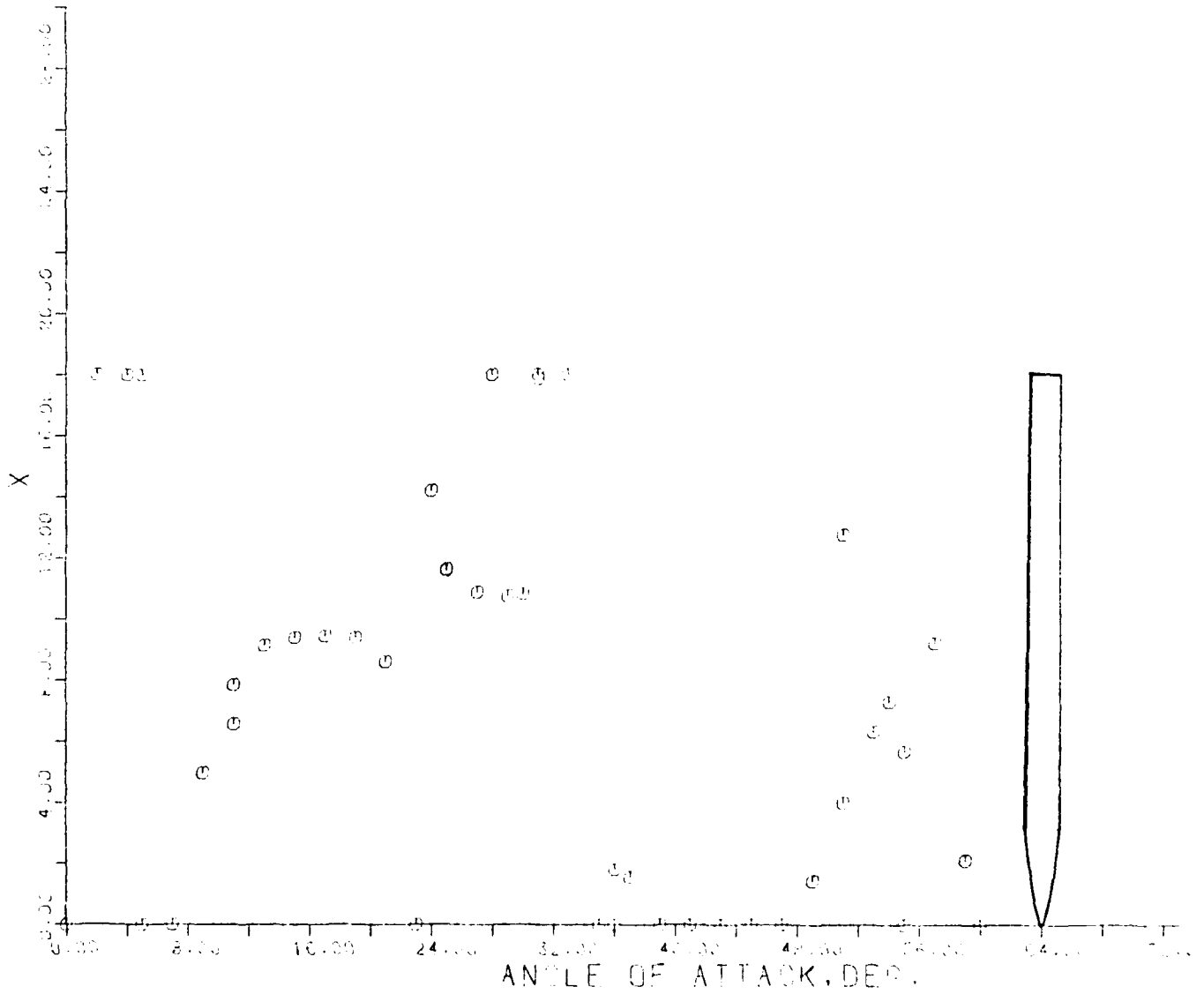


FIG. 96 - $(XCP/D)_Y$ VERSUS α ; M = .901 - SHARP NOSED BODY.

C_Y VERSUS ANGLE OF ATTACK

M = .395 BLUNT NOSED BODY

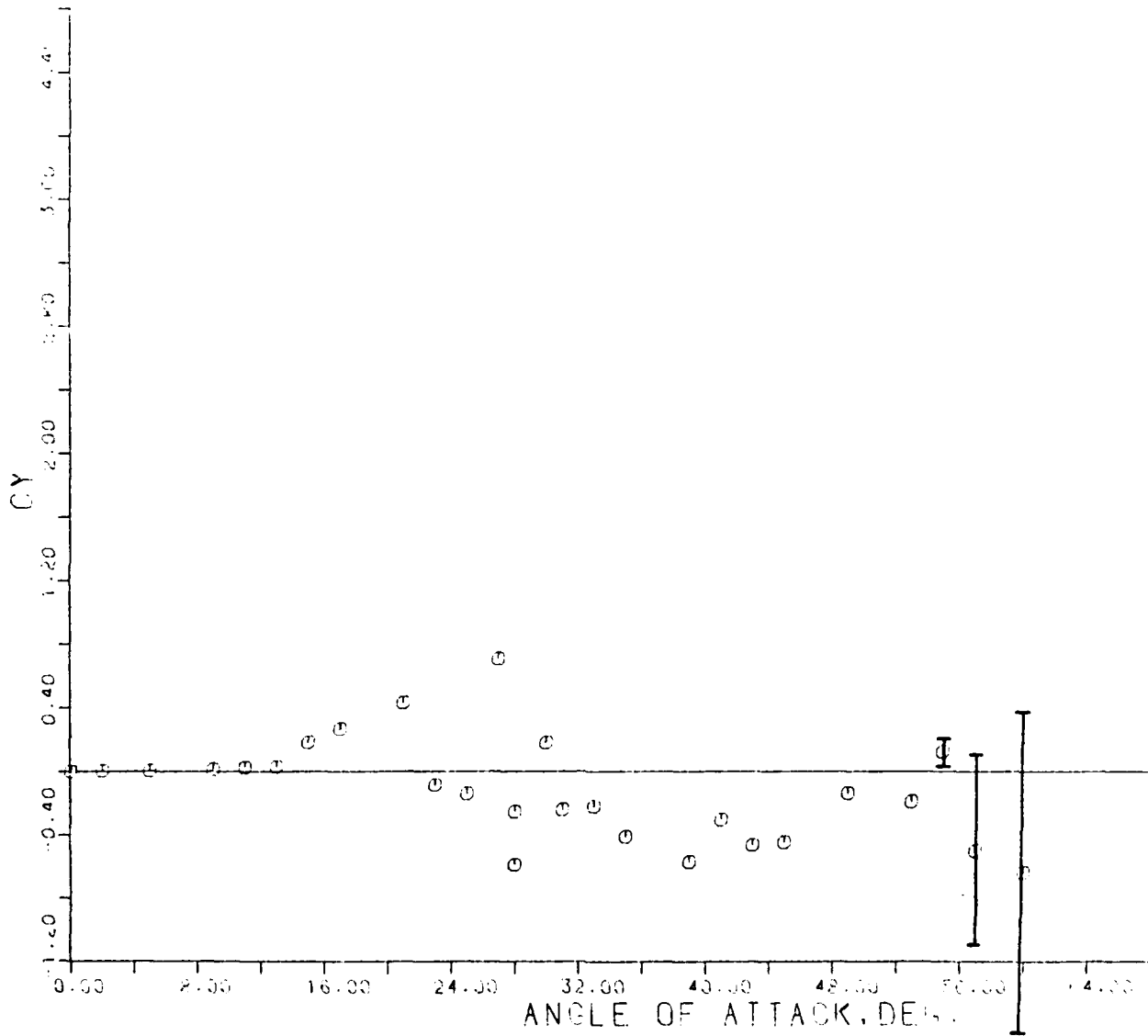


FIG. 97 - C_Y VERSUS α ; M = .395 - BLUNT NOSED BODY.

XCP/D VS. ALPHA FOR CY
M = .395 BLUNT NOSE

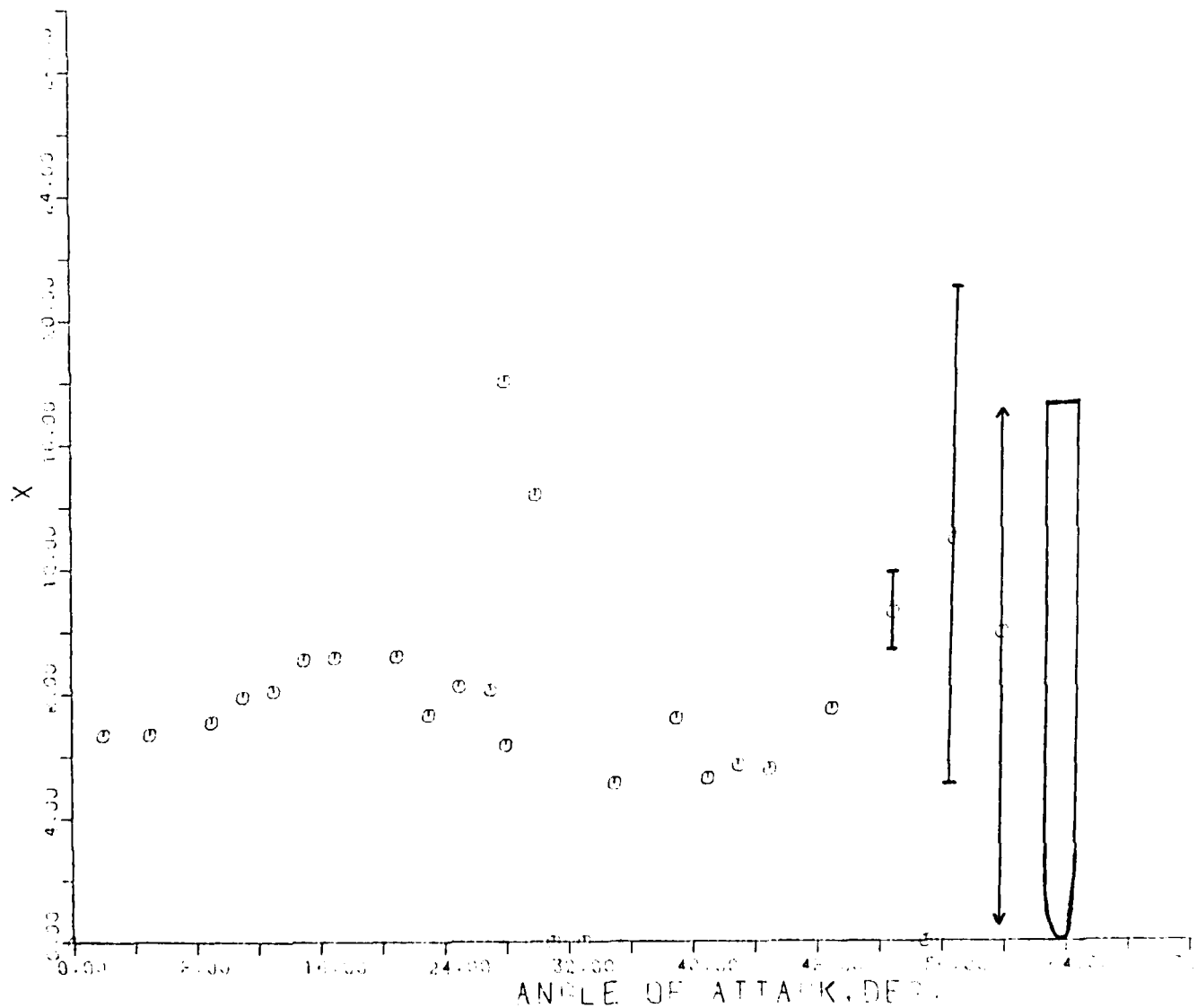


FIG. 98 - $(XCP/D)_Y$ VERSUS α ; $M = .395$ - BLUNT NOSED BODY.

C_Y VS. ANGLE OF ATTACK

M = .611 BLUNT NOSED

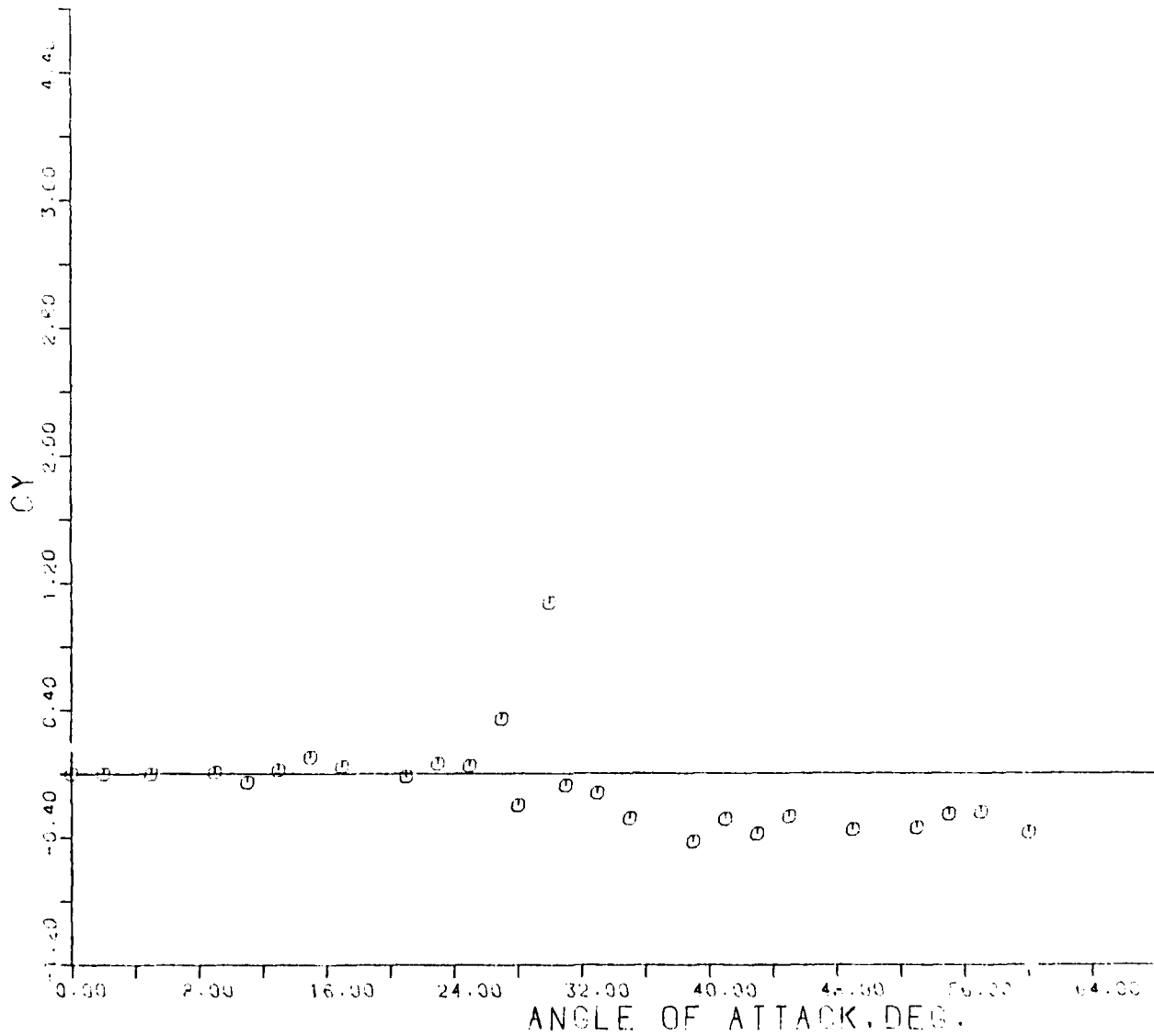


FIG. 99 - C_Y VERSUS α ; M = .611 - BLUNT NOSED BODY.

XCP/D VS. ALPHA FOR CY
M=.611 BLUNT NOSE

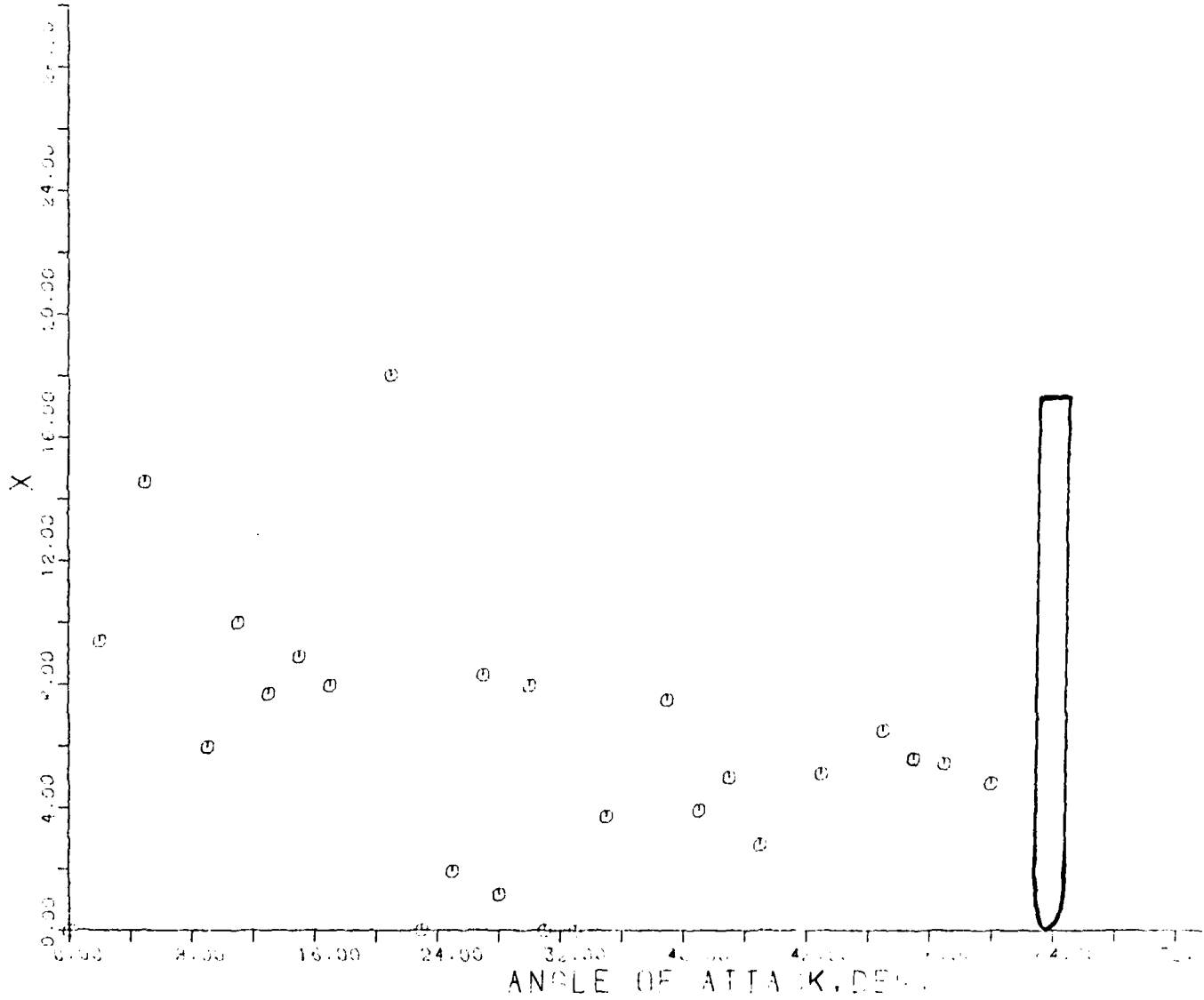


FIG. 100 - $(XCP/D)_y$ VERSUS α ; M = .611 - BLUNT NOSED BODY.

CY VS. ANGLE OF ATTACK

M = .698 BLUNT NOSE

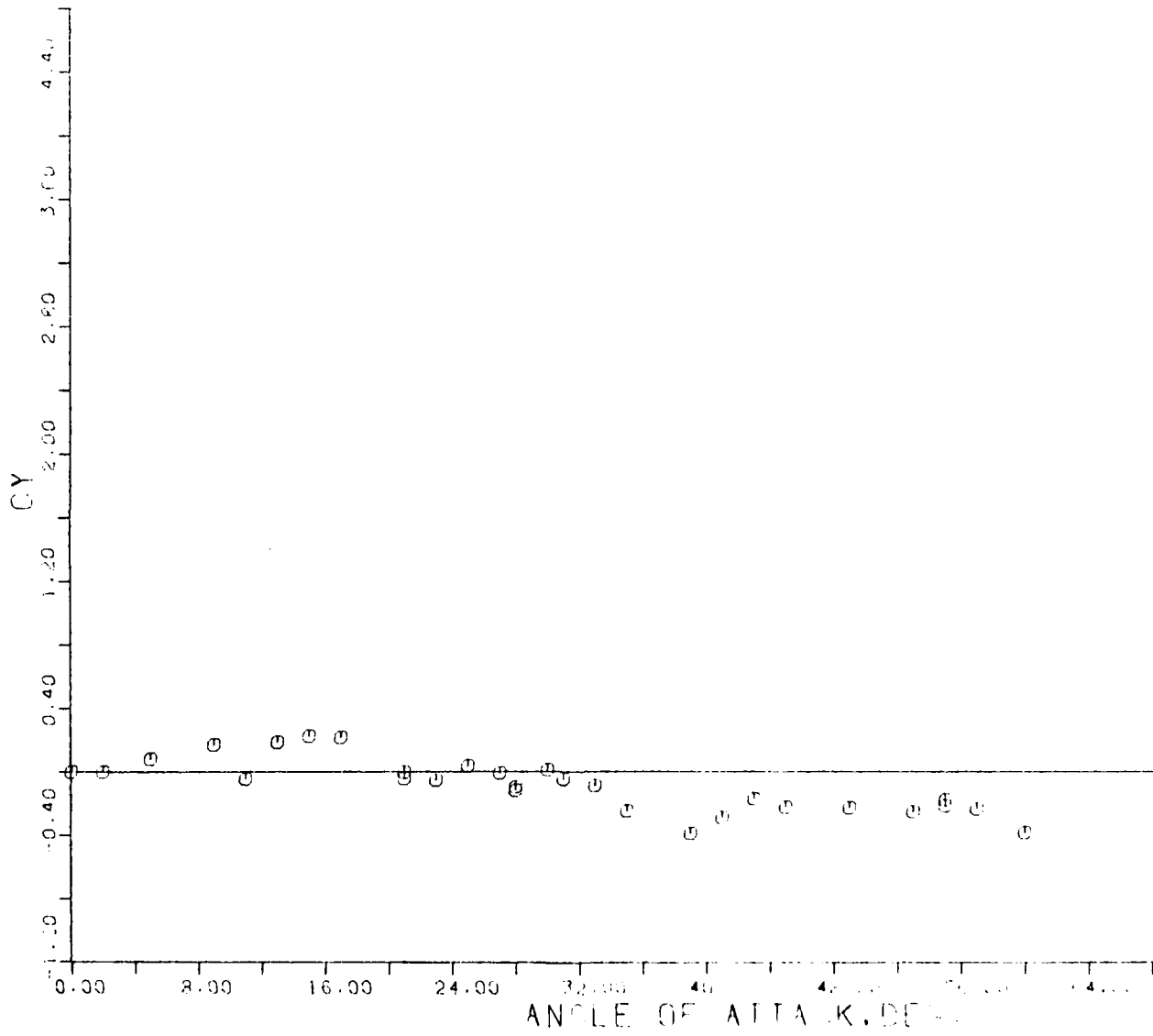


FIG. 101 - C_Y VERSUS α ; $M = .698$ - BLUNT NOSED BODY.

XCP/D VS. ALPHA FOR CY
M=.698 BLUNT NOSE

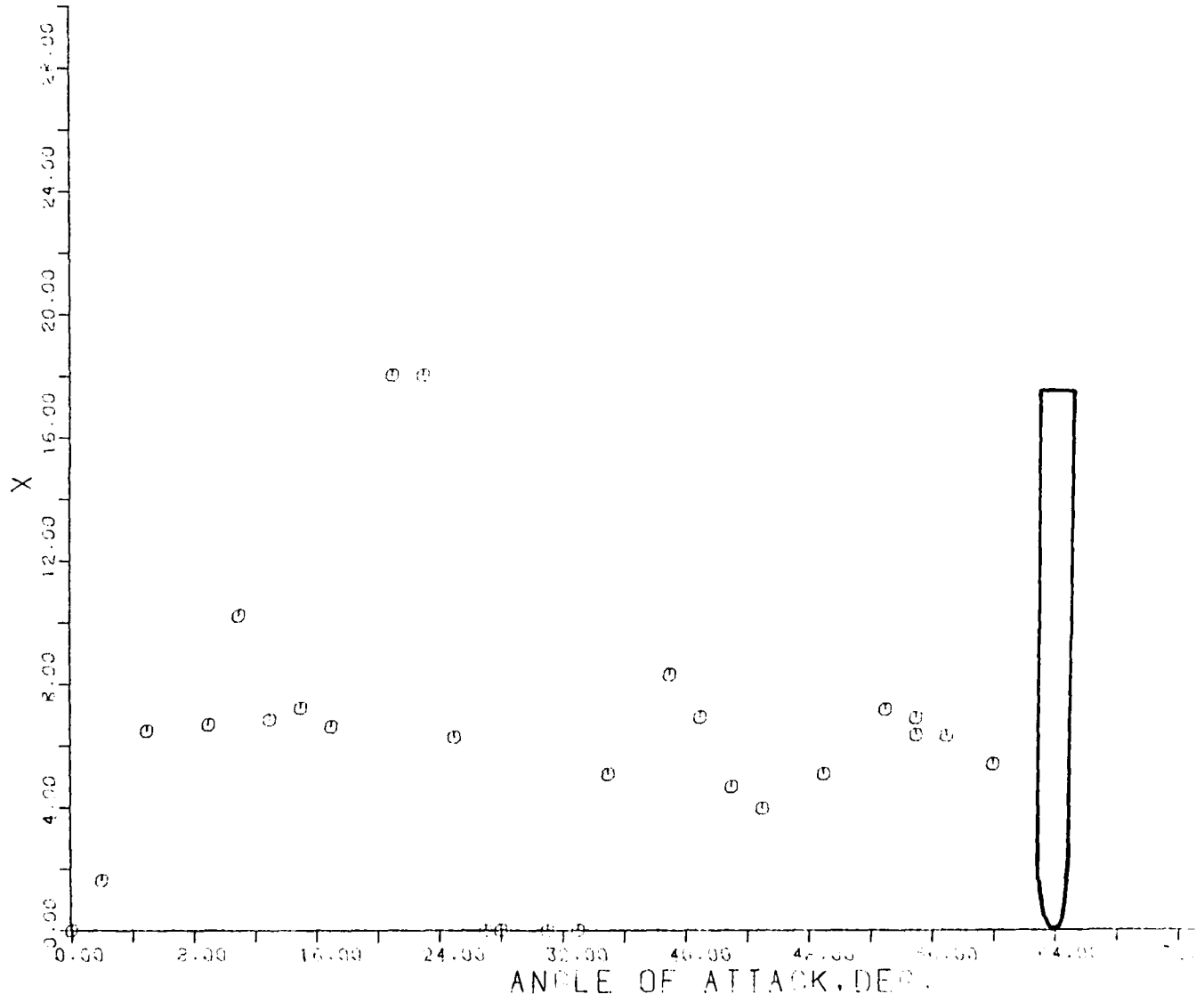


FIG. 102 - $(XCP/D)_\gamma$ VERSUS α ; $M = .698$ - BLUNT NOSED BODY.

C_Y VS. ANGLE OF ATTACK

M = .797 BLUNT N. B.

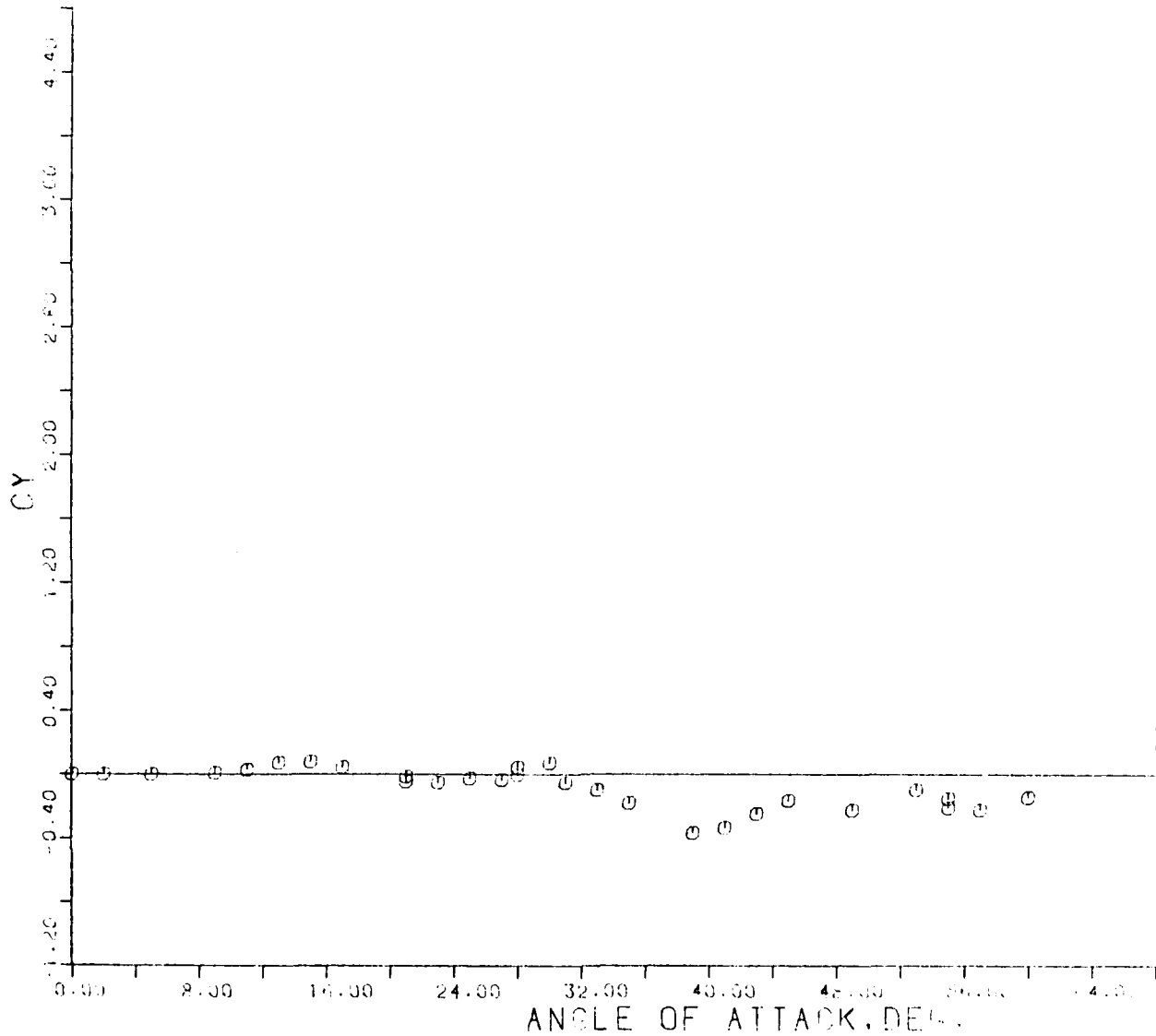


FIG. 103 - C_Y VERSUS α ; M = .797 - BLUNT NOSED-BODY.

XCP/D VS. ALPHA FOR CY

M = .797 BLUNT NOSE

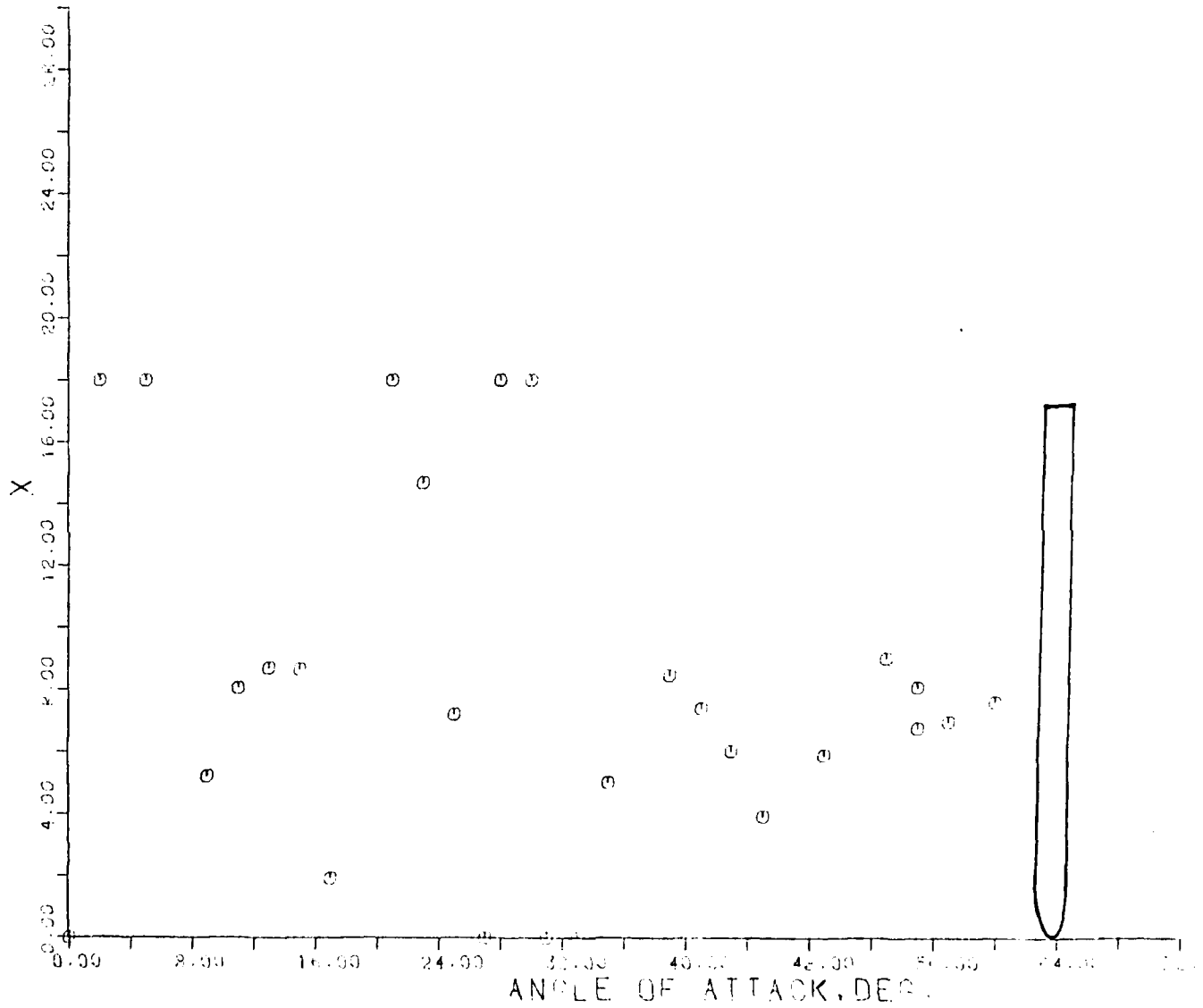


FIG. 104 - $(XCP/D)_Y$ VERSUS α ; M = .797 - BLUNT NOSED BODY.

$|C_{y_{max}}|$ vs. Mach Number

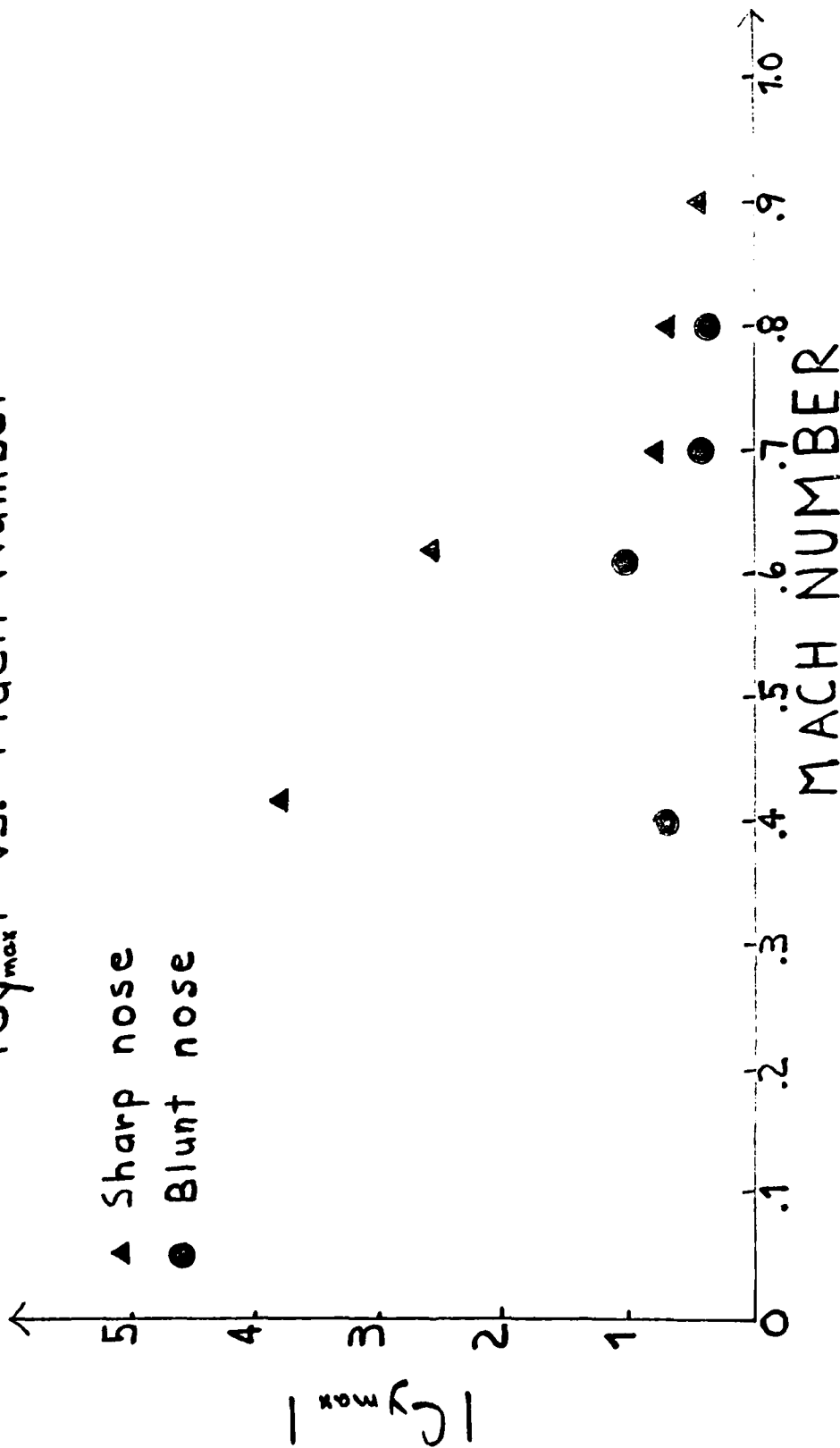


FIG. 105 - $|C_{y_{max}}|$ VERSUS MACH NUMBER FOR BOTH NOSE SHAPES.

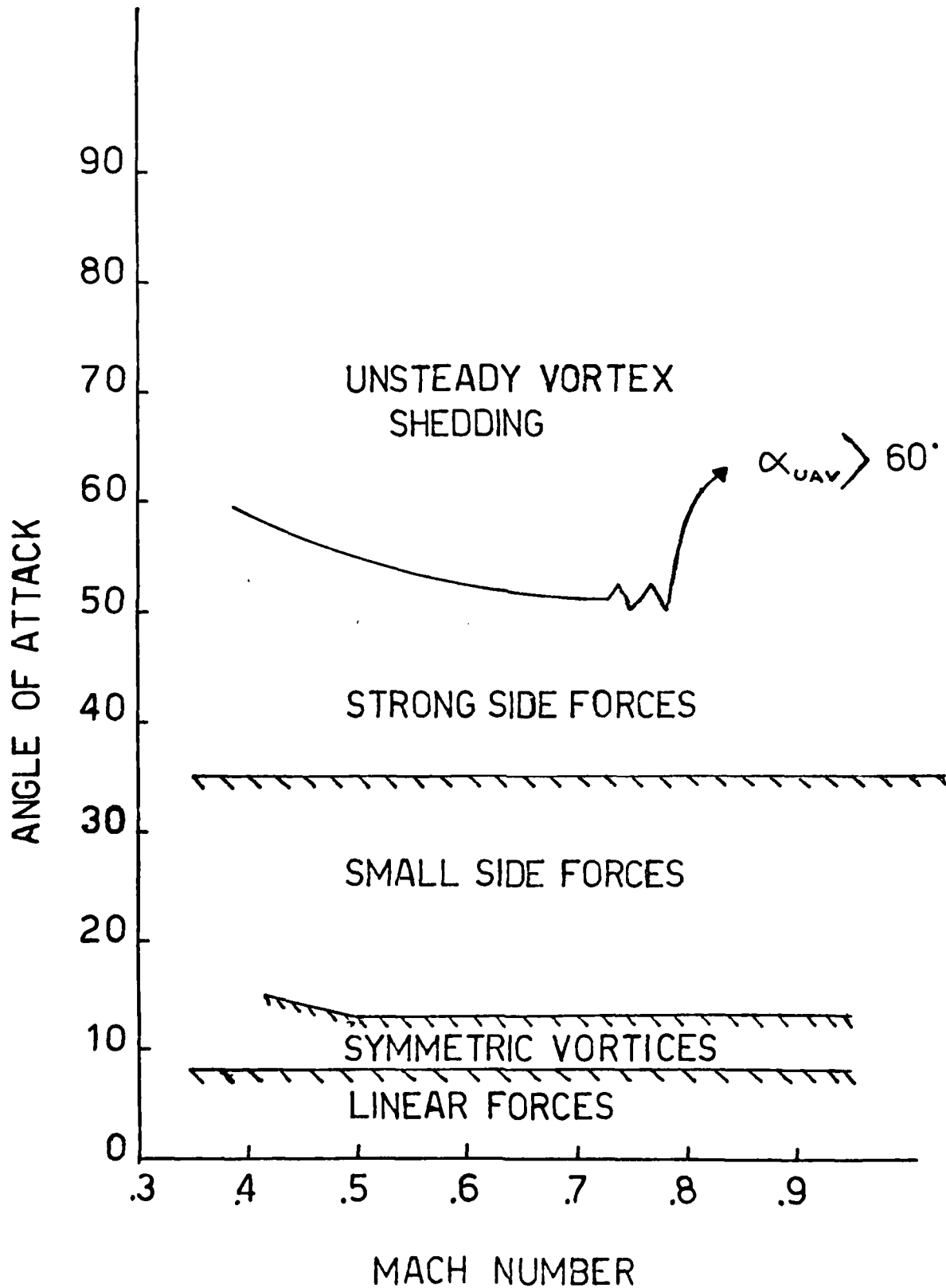


FIG. 166 - DIFFERENT FLOW REGIMES AS A FUNCTION OF MACH NUMBER.

Cy vs. Angle of Attack
for 2 Nose Shapes

M=0.407

Δ - Sharp

O - Blunt

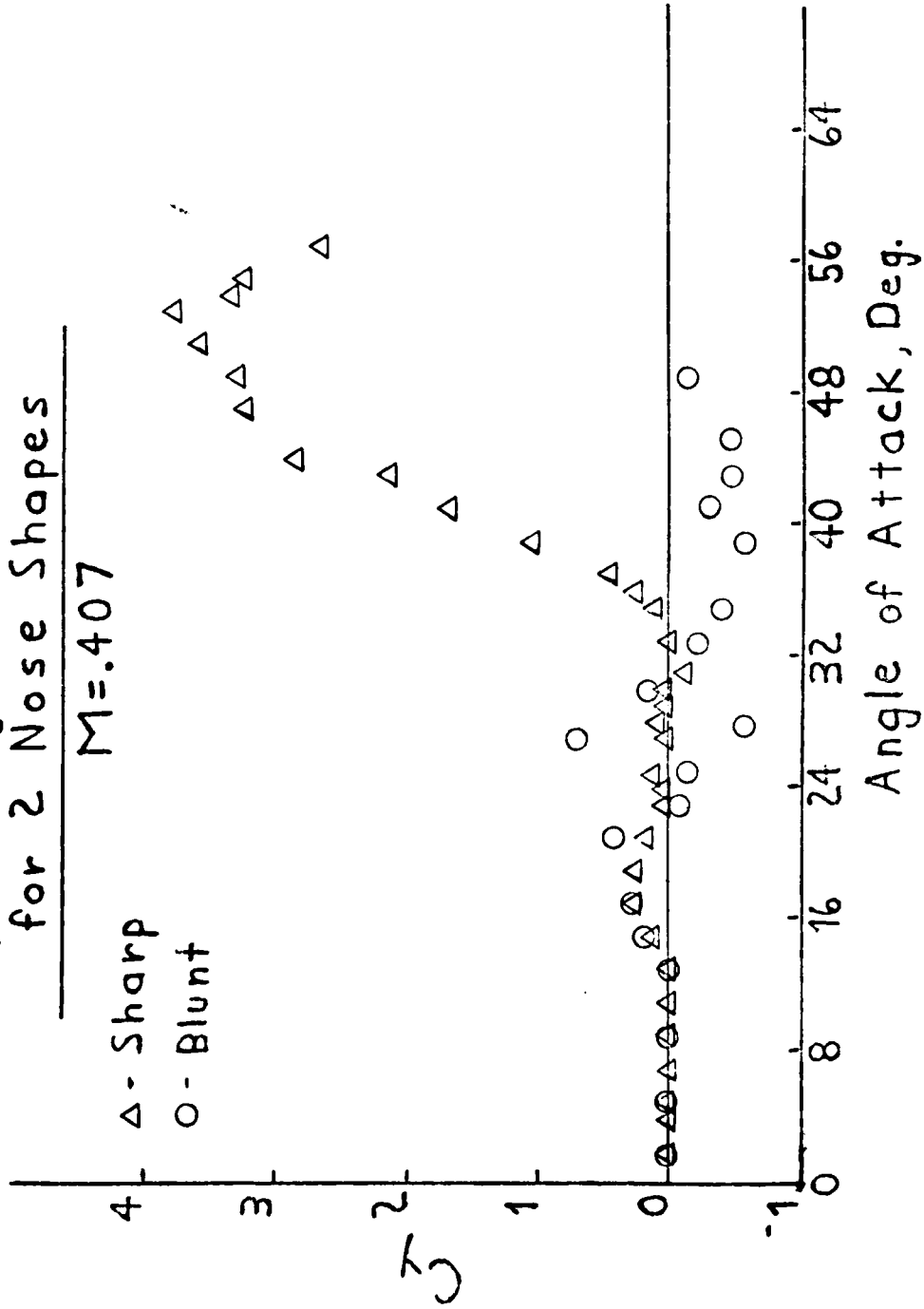


FIG. 133 - C_y VERSUS α FOR TWO NOSE SHAPES ; M = 0.407.

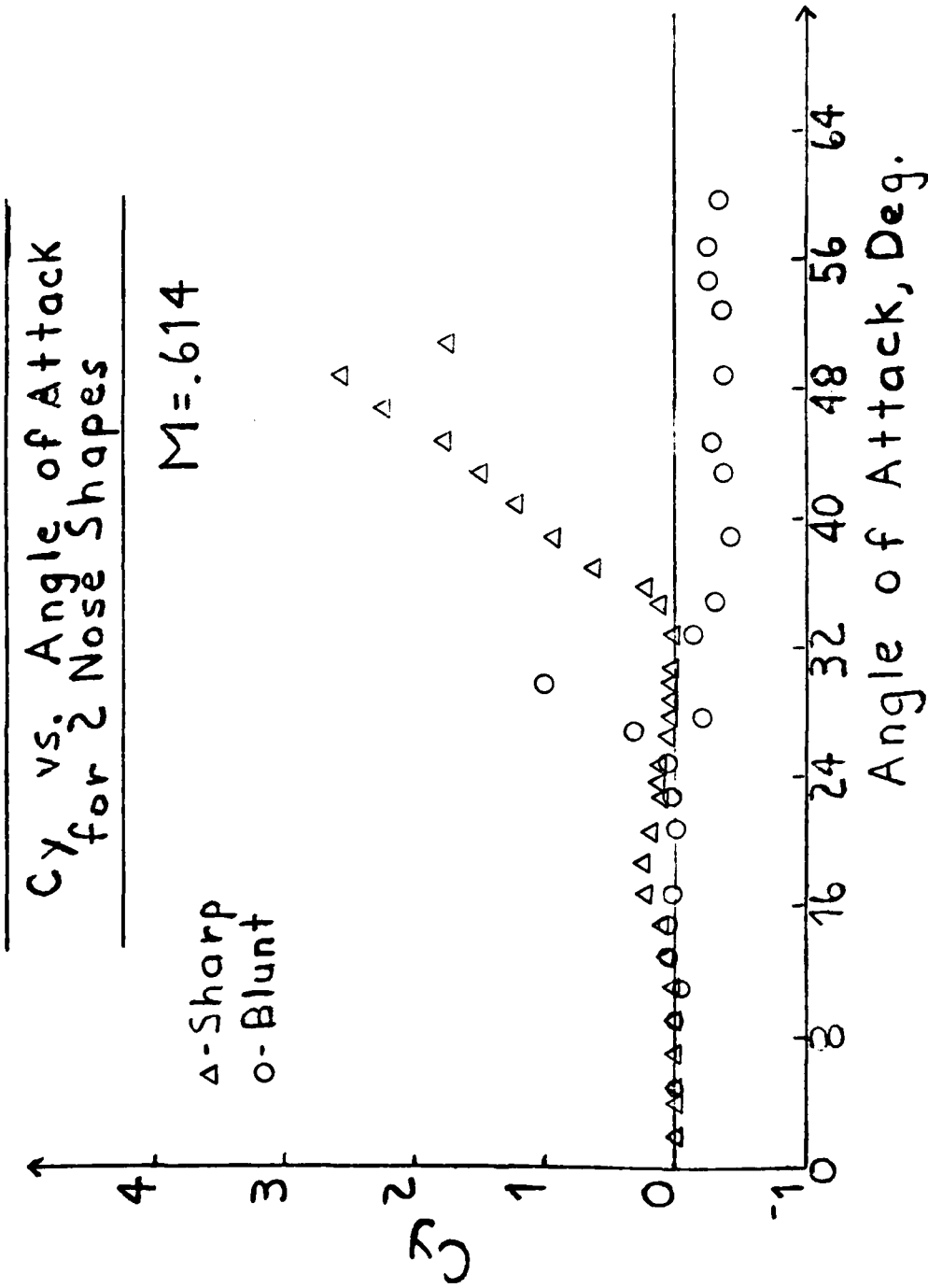


FIG. 109 - C_y VERSUS α FOR TWO NOSE SHAPES; $M = .614$.